Measuring and Modifying Temozolomide Delivery in Brain Tumours

A thesis submitted to The University of Manchester for a degree of Doctor of Philosophy in the Faculty of Biology, Medicine and Health.

2016

Ibrahim Khalil Djoukhadar

School of Health Sciences

Table of Contents

Abstract **15**

Declaration **16**

Copyright Statement **17**

Acknowledgement **19**

Author Biography **20**

Abbreviations **21**

Chapter 1 The Alternative Format Thesis **25**

1.1. Overview 25

1.2. Aims and objectives 25

1.3. Organisation and structure of the thesis 26

1.4. Research questions 28

Chapter 2 Brain Tumours: An Overview **29**

2.1. Introduction 29

2.2. Clinical features 29

2.3. World Health Organisation (WHO) classification of central nervous system tumours 30

2.4 Glioma biology overview 33

2.5 Imaging 35

2.5.1. Conventional MRI imaging in glioma *35*

2.5.2. Advanced MRI imaging techniques *36*

2.5.3. Clinical applications of MRI *41*

2.5.4. Positron emission tomography for gliomas *52*

2.6. Drug resistance in glioma tumours 55

2.7. Conclusions 56

Chapter 3 Blood-brain barrier: an overview **58**

3.1. Introduction 58

3.2 Historical aspects 58

3.3. Anatomy of the blood-brain barrier 59

3.4 Functions of the blood-brain barrier 61
3.4.1. Structural barrier proprieties *62*
3.4.2. Transport mechanisms in the blood-brain barrier *62*
3.5. Blood-brain barrier status in high-grade gliomas 65
3.5.1.The blood-tumour barrier *65*
3.5.2. P-glycoprotein and breast cancer resistance protein efflux transporter status in brain tumours *66*
3.6. Chemotherapy and brain tumours 67
3.6.1. Chemotherapy and brain tumours *67*
3.6.2. Strategies for enhancing drug delivery *69*
3.6.3. Methods for measuring drug delivery to the brain *72*
3.6.4. Efflux transporters: a potential solution *74*
3.6.5. Research aims *78*

Chapter 4 In-vitro studies: Temozolomide transport studies in a validated in-vitro blood-brain barrier model. 81

4.1. Abstract 81
4.2. Introduction 82
4.3. Materials and methods 83
4.3.1.Materials *83*
4.3.2.Isolation of porcine brain capillary endothelial cells *83*
4.3.3.Coating culture surfaces with collagen and fibronectin *84*
4.3.4.Culture of primary porcine brain endothelial cells *85*
4.3.5.Sub-culture of primary porcine brain endothelial cells into 96 well plates *85*
4.3.6.Measurement of P-glycoprotein functional activity *86*
4.3.7.Measurement of Breast Cancer Resistance Protein functional activity *87*
4.3.8.Assessment of Temozolomide Toxicity on Porcine Brain Endothelial Cells *87*
4.3.9.Assessment of Temozolomide inhibitory effect on P-glycoprotein functional activity *88*
4.3.10. Assessment of Temozolomide inhibitory effect on Breast Cancer Resistance Protein functional activity *89*
4.3.11. Culture of CTX-TNA2 astrocytes *90*
4.3.12. Generation of the blood-brain barrier model *90*
4.3.13. Measurement of transendothelial electrical resistance *92*

4.3.14. Measurement of permeability of porcine brain endothelial cell monolayers *93*
4.3.15. Detection of Temozolomide *93*
4.3.16. Temozolomide degradation studies *94*
4.3.17. Temozolomide transport experiments *94*
4.3.18. Statistical Analysis *95*
4.4. Results 96
4.4.1.Isolation of primary porcine brain cerebromicrovessels *96*
4.4.2.P-glycoprotein is functional in the porcine brain endothelial cells *96*
4.4.3.Breast cancer resistance protein is functional in the porcine brain endothelial cells 98
4.4.4.Temozolomide is not cytotoxic to porcine brain endothelial cells *98*
4.4.5Temozolomide does not inhibit P-glycoprotein-mediated transport *100*
4.4.6Temozolomide does not inhibit breast cancer resistance protein-mediated transport *101*
4.4.7Effects of puromycin pretreatment on the transendothelial electrical resistance of the porcine brain endothelial cells monolayer *102*
4.4.8Effects of the CTX-TNA2 rat astrocyte cell line on the transendothelial electrical resistance of the porcine brain endothelial cells monolayer *104*
4.4.9Effects of supplemented medium on the transendothelial electrical resistance of the porcine brain endothelial cells monolayer *105*
4.4.10Paracellular permeability of the in-vitro blood-brain barrier model *106*
4.4.11. Temozolomide detection and stability test *108*
4.4.12Effects of lowering pH on the integrity of the blood-brain barrier model *110*
4.4.13. Temozolomide transport studies *112*
4.5. Discussion and conclusions 115

Chapter 5 Preclinical *In-vivo* Imaging Study: Temozolomide is Transported by P-glycoprotein and Breast Cancer Resistance Protein Efflux Transporters at the Mouse Blood-Brain Barrier **121**
5.1. Abstract 121
5.2. Introduction 122
5.3. Materials and Methods 123
5.3.1. Chemicals *123*
5.3.2. Animals *123*

5.3.3. Experimental design *124*
5.3.4. Blood, plasma and brain metabolite analysis *125*
5.3.5. Small animal positron emission tomography *128*
5.3.6. Image reconstruction and analysis *130*
5.3.7. Brain uptake of [^{11}C]Temozolomide *131*
5.3.8. Statistical analysis *131*
5.4. Results 132
5.4.1. Plasma and brain radiolabelled metabolite analysis *132*
5.4.2. Ex-vivo brain experiments *139*
5.4.3. In-vivo PET experiments *142*
5.5. Discussion and conclusions 151

Chapter 6 Preclinical *In-vivo* Glioma Study: P-glycoprotein and Breast Cancer Resistance Protein Inhibition Can Enhance Temozolomide Efficacy in a Glioma Model. 157

6.1. Abstract 157
6.2. Introduction 158
6.3. Materials and methods 160
6.3.1. Materials *160*
6.3.2. Methods *160*
6.4. Results 173
6.4.1. No evidence of functionally active P-glycoprotein transporters in the U87 glioma cells *173*
6.4.2 Magnetic resonance imaging is a suitable tool for monitoring tumour growth in the U87 glioma model *174*
6.4.4. Combination therapy of Temozolomide and Tariquidar is superior to Temozolomide alone *176*
6.4.5. Tariquidar alone does not affect glioma growth *179*
6.4.6. Confirmation of the superior effect of combination therapy on glioma growth: *180*
6.4.7. In-vivo PET imaging study *182*
6.4.8. Plasma levels of Temozolomide are not different in the Temozolomide alone and combination therapy groups *185*
6.5. Discussion and conclusions: 188

Chapter 7: Imaging P-glycoprotein function in high-grade glioma patients 194

7.1. Abstract 194
7.2. Introduction 195
7.3. Methods 196
7.3.1. Patient recruitment 196
7.3.2. MRI acquisition 198
7.3.3. PET data acquisition 199
7.3.4. PET data processing 201
7.3.5.PET/MRI image-guided biopsy 206
7.3.6. Histopathological assessment 207
7.3.7. Statistical analysis 207
7.4. Results 209
7.4.1.Cerebral blood flow in glioma patients and healthy controls 211
7.4.2.Effects of Tariquidar on cerebral blood flow 214
7.3.3.Functional activity of P-glycoprotein 216
7.5. Discussion and conclusions 224
Chapter 8 Summary and Future Work 228
8.1. An overview 228
8.2. Critical appraisal of the work presented 230
8.2.1.Weakness of experimental design 230
8.2.2. Potential clinical applications of the work presented 231
8.3. Suggestions for future work 233
References 234
Appendix 277

Words count: 50422

Table of Figures

Figure 2. 1 Illustration of positron decay using ^{11}C 52
Figure 3. 1 Cellular components of the neurovascular unit. 60
Figure 3. 2 Location of P-glycoprotein (PGP) and breast cancer resistance protein (BCRP) efflux transporters in the brain endothelial cell. 64
Figure 3. 3 The normal blood-brain barrier and the blood-brain barrier in high-grade brain tumours. 67
Figure 3. 4 Hypothetical demonstration of chemotherapy delivery in brain tumours. 68
Figure 3. 5 Mechanism of temozolomide breakdown 69
Figure 4. 1 Co-culture *in-vitro* Blood-Brain Barrier model. 91
Figure 4. 2 Functional activity of P-glycoprotein in porcine brain enodthelial cells 97
Figure 4. 3 Functional activity of breast cancer resistance protein in porcine brain endothalial cells 98
Figure 4. 4 Temozolomide is not cytotoxic to porcine brain endothelial cells 99
Figure 4. 5 Temozolomide does not inhibit the functional activity of P-glycoprotein. 100
Figure 4. 6 Temozolomide does not inhibit the functional activity of Breast Cancer Resistance Protein. 101
Figure 4. 7 Treatment with Puromycin improves transendothelial electrical resistance 103
Figure 4. 8 Co-culture with rat astrocyte cell line CTX-TNA2 improves transendothelial electrical resistance. 104
Figure 4. 9 Supplemented medium improves transendothelial electrical resistance 106
Figure 4. 10 Apparent permeability coefficient of Lucifer Yellow. 107
Figure 4. 11 High performance liquid chromatography tandem-mass spectroscopy detection for Temozolomide at the different time points 108
Figure 4. 12 Stability of Temozolomide. 109

FIGURE 4. 13 STABILITY OF TEMOZOLOMIDE IS IMPROVED UNDER ACIDIC CONDITIONS. 109
FIGURE 4. 14 ACIDIC CONDITIONS REDUCE THE TRANSENDOTHELIAL ELECTRICAL RESISTANCE IN THE MONOLAYER OF PORCINE BRAIN ENDOTHELIAL CELLS. 110
FIGURE 4. 15 ACIDIC CONDITIONS INCREASE PERMEABILITY OF A MONOLAYER OF PORCINE BRAIN ENDOTHELIAL CELLS 111
FIGURE 4. 16 P-GLYCOPROTEIN AND BREAST CANCER RESISTANCE PROTEIN MEDIATED TRANSPORT OF TEMOZOLOMIDE. 112
FIGURE 4. 17 THE EFFECTS OF P-GLYCOPROTEIN AND BREAST CANCER RESISTANCE PROTEIN INHIBITION ON TRANSPORT OF TEMOZOLOMIDE. 113
FIGURE 4. 18 THE EFFECTS OF P-GLYCOPROTEIN INHIBITION ON THE TRANSPORT OF TEMOZOLOMIDE. 113
FIGURE 5. 1 CHEMICAL STRUCTURE OF RADIOLABELLED [^{11}C]TEMOZOLOMIDE 123
FIGURE 5. 2 REPRESENTATIVE CHROMATOGRAM OF TEMOZOLOMIDE AND ITS ACTIVE DAUGHTER METABOLITE MTIC IN MOUSE BRAIN 40 MINUTES POST [^{11}C]TMZ INJECTION. 128
FIGURE 5. 3 CHANGES IN THE RELATIVE PERCENTAGES OF THE PARENT COMPOUND [^{11}C]TMZ DETECTED IN THE PLASMA AND BRAINS OF WILD TYPE ANIMALS SOURCED FROM UK AND US 133
FIGURE 5. 4 CHANGES IN THE RELATIVE PERCENTAGES OF THE ACTIVE METABOLITE MTIC FOUND IN THE PLASMA AND BRAINS OF WILD TYPE ANIMALS SOURCED FROM THE UK AND THE US 134
FIGURE 5. 5 PERCENTAGES OF PARENT COMPOUND [^{11}C]TMZ AND THE ACTIVE RADIOLABELLED METABOLITE MTIC FOUND IN PLASMA AT 40 MINUTES AFTER RADIOTRACER ADMINISTRATION FOR WILD TYPE (UK), WILD TYPE (USA), P-GLYCOPROTEIN, BREAST CANCER RESISTANCE PROTEIN AND DUAL TRANSPORTER KNOCKOUT MICE. 136
FIGURE 5. 6 PERCENTAGES OF PARENT COMPOUND [^{11}C]TMZ AND THE RADIOLABELLED ACTIVE METABOLITE MTIC FOUND IN BRAIN EXTRACTS AT 40 MINUTES AFTER RADIOTRACER ADMINISTRATION FOR WILD TYPE (UK), WILD TYPE (USA), P-GLYCOPROTEIN, BREAST CANCER RESISTANCE PROTEIN AND DUAL TRANSPORTER KNOCKOUT MICE. 137
FIGURE 5. 7 PERCENTAGES OF PARENT COMPOUND [^{11}C]TMZ AND THE ACTIVE RADIOLABELLED METABOLITE MTIC FOUND IN PLASMA AND BRAIN EXTRACTS AT 60

minutes after radiotracer administration for wild type mice injected with vehicle and Tariquidar 138
Figure 5. 8 Brain-to-plasma ratios of radioactivity at 40 minutes after radiotracer injection for the different mouse types 140
Figure 5. 9 Brain-to-plasma ratios of radioactivity at 60 minutes after [^{11}C]Temozolomide injection in wild type mice injected with vehicle solution with Tariquidar. 141
Figure 5. 10 Significant positive correlation between the brain volumes segmented from the dynamic PET image and the brain weights in each mouse across all PET scans with [^{11}C]TMZ. 142
Figure 5. 11 Mean (± SD) whole-brain time-activity curves (SUV) in wild type, P-gp KO, BCRP KO, and dual transporter KO mice 143
Figure 5. 12 Plasma radioactivity concentrations (SUV) measured at 40 minutes after [^{11}C]TMZ injection in the different groups of mice from the metabolite analysis group 144
Figure 5. 13 Brain-to-plasma ratios of radioactivity at 40 minutes as measured with positron emission tomography after [^{11}C]Temozolomide injection for the different mouse groups 145
Figure 5. 14 Plasma radioactivity concentrations (SUV) measured at 40 minutes after [^{11}C]TMZ injection in the different mouse groups following correction for the fraction of the parent compound in plasma 146
Figure 5. 15 Brain-to-plasma ratios of radioactivity as measured with positron emission tomography at 40 minutes after [^{11}C]Temozolomide injection in the different mouse groups, corrected for the fraction of the parent compound in plasma 147
Figure 5. 16 Mean (± SD) whole-brain time-activity curves (SUV) for untreated wild type mice injected with a vehicle and with TQD.. 148
Figure 5. 17 Brain-to-plasma ratios of radioactivity at 60 minutes after [^{11}C]Temozolomide injection in wild type mice injected with a vehicle solution and TQD 149
Figure 6. 1 Photomicrograph of U87 glioma cells reaching approximately 70% confluence 161
Figure 6. 2 Outline of the first experiment with the human U87 glioma model. 166

FIGURE 6. 3 CHROMATOGRAM OF TMZ IN A PLASMA OF A MOUSE 4 HOURS FOLLOWING ADMINISTRATION OF TMZ BY ORAL GAVAGE.. 172
FIGURE 6. 4 LACK OF FUNCTIONAL ACTIVITY OF P-GLYCOPROTEIN IN U87 GLIOMA CELLS. 173
FIGURE 6. 5 FUNCTIONAL ACTIVITY OF BREAST CANCER RESISTANCE PROTEIN IN U87 GLIOMA CELLS..... 174
FIGURE 6. 6 REPRESENTATIVE T2-WEIGHTED CORONAL MAGNETIC RESONANCE IMAGES FROM A SINGLE MOUSE AT WEEKS 1, 2 AND 3 FOLLOWING IMPLANTATION OF U87 GLIOMA CELLS..... 175
FIGURE 6. 7 REPRESENTATIVE T1-WEIGHTED CORONAL MAGNETIC RESONANCE IMAGES FOLLOWING GADOLINIUM ADMINISTRATION FROM A MOUSE AT WEEKS 2 FOLLOWING IMPLANTATION OF U87 GLIOMA CELLS..... 175
FIGURE 6. 8 TUMOUR VOLUME MEASUREMENTS AT ONE, TWO AND THREE WEEKS POST IMPLANTATION OF U87 GLIOMA CELLS 177
FIGURE 6. 9 TUMOUR VOLUME MEASUREMENTS BEFORE ADMINISTRATION OF TREATMENT AND AFTER COMPLETION OF TREATMENT 177
FIGURE 6. 10 TUMOUR VOLUME MEASUREMENTS FROM WEEK 1 TO WEEK 12 POST IMPLANTATION OF U87 GLIOMA CELLS.. 178
FIGURE 6. 11 REPRESENTATIVE CORONAL T2-WEIGHTED IMAGES FOR EACH TREATMENT GROUP AT COMPLETION OF TREATMENT 179
FIGURE 6. 12 TUMOUR VOLUME MEASUREMENTS AT WEEKS 1, 2 AND 3 POST IMPLANTATION OF U87 GLIOMA CELLS IN CONTROL ANIMALS FORM THE FIRST AND SECOND STUDIES. 179
FIGURE 6. 13 TUMOUR VOLUME MEASUREMENTS AT WEEKS 1, 2 AND 3 POST IMPLANTATION OF U87 GLIOMA CELLS. 180
FIGURE 6. 14 SIGNIFICANT POSITIVE CORRELATION WAS FOUND BETWEEN THE BRAIN VOLUMES SEGMENTED USING THE LMA METHOD AND THE POST MORTEM BRAIN WEIGHTS ACROSS ALL PET SCANS WITH [^{11}C]TMZ. 182
FIGURE 6. 15 REPRESENTATIVE MAXIMUM INTENSITY PROJECTION IMAGE (LAST TEN MINUTES) ILLUSTRATING BRAIN UPTAKE OF [^{11}C]TEMOZOLOMIDE IN A DUAL-BED PET FOR ORTHOTOPIC GLIOMA MODEL IN THE TEMOZOLOMIDE ALONE (LEFT) AND TEMOZOLOMIDE PLUS TARIQUIDAR (RIGHT) TREATMENT GROUPS 183

FIGURE 6. 16 MEAN TIME-ACTIVITY CURVES (STANDARDISED UPTAKE VALUE (SUV) ± STANDARD ERROR OF THE MEAN [SEM]) OF [^{11}C]TMZ IN THE WHOLE BRAIN FOR ALL ANIMALS 184
FIGURE 6. 17 MEAN TIME-ACTIVITY CURVES (STANDARDISED UPTAKE VALUE (SUV) ± SEM) OF [^{11}C]TMZ IN THE HEMISPHERES FROM 0 TO 60 MINUTES AFTER RADIOTRACER INJECTION FOR ALL ANIMALS 184
FIGURE 6. 18 TMZ CONCENTRATION (MG/ML) IN PLASMA, AS MEASURED BY HIGH PERFORMANCE LIQUID CHROMATOGRAPHY WITH UV DETECTION 187
FIGURE 7. 1 EXAMPLE OF CO-REGISTRATION OF PET TO MRI 202
FIGURE 7. 2 DELINEATION OF REGIONS OF INTEREST IN PATIENT 5. 206
FIGURE 7. 3 PERFUSION AT BASELINE IN THE GREY MATTER AND WHITE MATTER FOR BOTH HEALTHY CONTROLS AND GLIOMA PATIENTS 212
FIGURE 7. 4 PERFUSION AT BASELINE IN THE DIFFERENT REGION OF INTERESTS IN THE FIVE GLIOMA PATIENTS.. 213
FIGURE 7. 5 CHANGES FROM BASELINE IN PERFUSION AFTER ADMINISTRATION OF 2 MG/KG OF TQD IN THE GREY AND WHITE MATTER FOR HEALTHY CONTROLS AND GLIOMA PATIENTS 214
FIGURE 7. 6 CHANGES FROM BASELINE IN PERFUSION AFTER ADMINISTRATION OF 2 MG/KG OF TQD IN THE DIFFERENT REGIONS OF INTEREST IN THE FIVE GLIOMA PATIENTS. 215
FIGURE 7. 7 CHANGES IN PERFUSION BETWEEN BASELINE AND TARIQUIDAR SCANS IN FOUR PATIENTS 216
FIGURE 7. 8 (R)-[^{11}C]VERAPAMIL UPTAKE AT BASELINE IN THE GREY AND WHITE MATTER FOR BOTH HEALTHY CONTROLS AND GLIOMA PATIENTS. 217
FIGURE 7. 9 (R)-[^{11}C]VERAPAMIL UPTAKE AT BASELINE IN THE DIFFERENT REGIONS OF INTEREST IN THE FIVE GLIOMA PATIENTS. 218
FIGURE 7. 10 CHANGES FROM BASELINE IN (R)-[^{11}C]VERAPAMIL K_1 AFTER ADMINISTRATION OF 2 MG/KG OF TQD IN THE GREY AND WHITE MATTER FOR HEALTHY CONTROLS AND GLIOMA PATIENTS 219
FIGURE 7. 11 CHANGES FROM BASELINE IN (R)-[^{11}C]VERAPAMIL K_1 AFTER ADMINISTRATION OF 2 MG/KG OF TQD IN THE DIFFERENT REGIONS OF INTEREST IN THE FOUR GLIOMA PATIENTS. 220
FIGURE 7. 12 (R)-[^{11}C]VERAPAMIL K_1 HISTOGRAMS IN GLIOMA PATIENTS. 221

FIGURE 7. 13 AXIAL T1-WEIGHTED IMAGE AND PARAMETRIC MAPS OF PERFUSION (CBF) AND (R)-[^{11}C]VERAPAMIL BRAIN UPTAKE AT BASELINE AND AFTER P-GLYCOPROTEIN INHIBITION IN PATIENT 2 2222
FIGURE 7. 14 A) BASELINE EXTRACTION FRACTION (E) OF (R)-[^{11}C]VERAPAMIL IN THE GREY AND WHITE MATTER FOR BOTH HEALTHY CONTROLS AND GLIOMA PATIENTS. 223

Table of Tables

TABLE 2. 1: SUMMARY OF THE WHO CLASSIFICATION FOR BRAIN TUMOURS. 32

TABLE 2. 2: SUMMARY OF THE MOST COMMONLY DERIVED MR IMAGING BIOMARKERS IN GLIOMA 37

TABLE 2. 3: SUMMARY OF THE CLINICAL DIFFERENCES BETWEEN DSC-MRI AND DCE-MRI 40

TABLE 2. 4: SOME OF THE COMMONLY IMPLICATRE MOLECULES IN THE DEVELOPMENT OF DRUG RESISTANCE IN PATIENTS WITH BRAIN TUMOURS. 56

TABLE 3. 1: EFFLUX TRANSPORTERS AND ANTICANCER DRUG SUBSTRATES. 74

TABLE 3. 2: EFFECTS OF DUAL P-GLYCOPROTEIN AND BREAST CANCER RESISTANCE PROTEIN INHIBITION ON THE BRAIN UPTAKE OF SOME ANTICANCER DRUGS 75

TABLE 3. 3: PET RADIOTRACERS THAT HAVE BEEN USED TO EVALUATE P-GLYCOPROTEIN AND BREAST CANCER RESISTANCE PROTEIN IN THE BRAIN. 78

TABLE 5. 1: CHARACTERISTICS OF UK SOURCED ANIMALS THAT UNDERWENT PLASMA AND BRAIN METABOLITE ANALYSIS FOLLOWING INJECTION WITH [^{11}C]TEMOZOLOMIDE. 126

TABLE 5. 2: CHARACTERISTICS OF USA SOURCED ANIMALS THAT UNDERWENT PLASMA AND BRAIN METABOLITE ANALYSIS FOLLOWING INJECTION WITH [^{11}C]TEMOZOLOMIDE. 126

TABLE 5. 3: CHARACTERISTICS OF ANIMALS THAT UNDERWENT PET SCANNING POSITRON EMISSION WITH [^{11}C]TEMOZOLOMIDE 129

TABLE 5. 4: PERCENTAGES OF PARENT COMPOUND [^{11}C]TMZ AND ITS METABOLITES FOUND IN PLASMA AT 10, 20, 40 AND 60 MINUTES AFTER RADIOTRACER ADMINISTRATION IN WILD TYPE (WT) ANIMALS 135

TABLE 5. 5: RELATIVE PERCENTAGES OF PARENT COMPOUND [^{11}C]TMZ AND ITS METABOLITES FOUND IN BRAIN EXTRACTS OF WILD TYPE (WT) ANIMALS AT 10, 20, 40 AND 60 MINUTES AFTER RADIOTRACER ADMINISTRATION IN WILD TYPE ANIMALS. 135

TABLE 5. 6: PERCENTAGES OF PARENT COMPOUND [^{11}C]TMZ AND ITS ACTIVE RADIOLABELLED METABOLITE MTIC FOUND IN PLASMA AND BRAIN EXTRACTS AT 40 MINUTES AFTER RADIOTRACER ADMINISTRATION. 136

TABLE 5. 7: PERCENTAGES OF PARENT COMPOUND [^{11}C]TMZ AND THE ACTIVE RADIOLABELLED METABOLITE MTIC FOUND IN PLASMA AND BRAIN EXTRACTS AT 60 MINUTES AFTER RADIOTRACER ADMINISTRATION FOR UNTREATED WILD TYPE MICE AND WILD TYPE MICE TREATED WITH TARIQUIDAR. 138

TABLE 6. 1: TREATMENT GROUPS AND DOSING REGIMENS 166
TABLE 6. 2: SUMMARY OF ANIMAL STUDIES. 168
TABLE 6. 3: CHARACTERISTICS OF ANIMALS THAT UNDERWENT PET SCANS WITH [^{11}C]TMZ. 170
TABLE 6. 4: SUMMARY OF THE FIRST *IN-VIVO* STUDY. 176
TABLE 6.5: VALUES OF THE CALCULATED AREAS UNDER THE CURVE FOR [^{11}C]TMZ UPTAKE IN EACH TREATMENT GROUP FOR THE DIFFERENT HEMISPHERES 185
TABLE 6. 6: SUMMARY OF BLOOD COLLECTION TIME POINTS, ISSUES ENCOUNTERED, AND TEMOZOLOMIDE CONCENTRATION IN PLASMA FOR THE DIFFERENT TREATMENT GROUPS. 186

TABLE 7. 1: DEMOGRAPHIC, CLINICAL AND SCAN DETAILS OF GLIOMA PATIENTS 209
TABLE 7. 2: DIFFERENT SEGMENTED ROIS WITHIN THE TUMOURS. 210
TABLE 7. 3: DEMOGRAPHIC AND SCAN DETAILS OF HEALTHY CONTROLS 201

Abstract

Institution	University of Manchester
Candidate	Ibrahim Khalil Djoukhadar
Degree title	Doctor of Philosophy
Thesis title	Measuring and Modifying Temozolomide Delivery in Brain Tumours
Date	December 2016

Glioblastoma (GBM) is the most common aggressive primary brain tumour in adults. Despite various recent treatment advances, prognosis and survival rates remain dismal. A potential explanation for such poor outcomes is the high invasive nature of glioma cells, which enable them to invade areas of the brain where the blood-brain barrier may still be intact. This could explain the frequently encountered tumour recurrences that occur at the edges of the original tumour or at the surgical resection margins. Another potential explanation for such poor outcomes is the blood-brain barrier (BBB), which prevents delivery of effective chemotherapy into the brain. Furthermore, efflux transporters at the BBB can also restrict drug delivery. P-glycoprotein (P-gp) and breast cancer resistance protein (BCRP) are two efflux transporters that work closely together as efflux pumps for a variety of anticancer drugs. Temozolomide (TMZ) is the central chemotherapy agent used in the treatment of malignant brain tumours but interestingly, its relationship with P-gp and BCRP remains poorly understood. The ultimate aim of this thesis is to develop an imaging method for measuring the effects of strategies modifying Temozolomide (TMZ) delivery into the brain and brain tumours.

An *in-vitro* BBB model was developed and validated. This was then used to conduct TMZ transport studies, which showed a trend for TMZ to be transported by P-gp and BCRP at clinically relevant concentrations.

In order to confirm these results, dynamic small animal positron emission tomography (PET) with [^{11}C]TMZ was also performed in wild-type and in mice lacking P-gp, BCRP or both transporters as well as in wild-type mice treated with the efflux transporter inhibitor Tariquidar (TQD). Scans confirmed higher delivery of [^{11}C]TMZ in mice lacking P-gp, BCRP and both transporters. Similar results were noted in wild type mice following the pharmacological inhibition of P-gp and BCRP.

A human glioma model in mice was derived by intracranial injection of human U87 glioma cells in thirty-five athymic female mice. Animals were treated with TMZ alone, TQD alone or combination therapy (TMZ and TQD). Response to treatment was evaluated by performing volumetric tumour measurement using MRI. Combination therapy was shown to be superior achieving significant early and sustained response in tumours when compared with TMZ alone treatment.

Finally, PET imaging was used with the known P-gp substrate (R)-[^{11}C]verapamil to demonstrate the functional activity of P-gp in five high-grade glioma patients. This approach was shown to be a suitable non-invasive imaging method for visualising P-gp function in patients with brain tumours and highlighted the heterogeneity of the functional activity of P-gp in these patients.

Declaration

No portion of the work referred to in the thesis has been submitted in support of an application for another degree or qualification of this or any other university or other instate of learning.

Copyright Statement

i. The author of this thesis (including any appendices and/or schedules to this thesis) owns certain copyright or related rights in it (the "Copyright") and s/he has given The University of Manchester certain rights to use such Copyright, including for administrative purposes.

ii. Copies of this thesis, either in full or in extracts and whether in hard or electronic copy, may be made **only** in accordance with the Copyright, Designs and Patents Act 1988 (as amended) and regulations issued under it or, where appropriate, in accordance with licensing agreements which the University has from time to time. This page must form part of any such copies made.

iii. The ownership of certain Copyright, patents, designs, trade marks and other intellectual property (the "Intellectual Property") and any reproductions of copyright works in the thesis, for example graphs and tables ("Reproductions"), which may be described in this thesis, may not be owned by the author and may be owned by third parties. Such Intellectual Property and Reproductions cannot and must not be made available for use without the prior written permission of the owner(s) of the relevant Intellectual Property and/or Reproductions.

iv. Further information on the conditions under which disclosure, publication and commercialisation of this thesis, the Copyright and any Intellectual Property University IP Policy (see http://documents.manchester.ac.uk/display.aspx?DocID=24420), in any relevant Thesis restriction declarations deposited in the University Library, The University Library's regulations (see http://www.library.manchester.ac.uk/about/regulations/) and in The University's policy on Presentation of Theses.

For my wife Hiba and daughters Farah and Hana

Thank you…

Acknowledgement

The work presented in this thesis would not have been possible without the input, intervention and support offered to me during the past few years.
I would like to express my sincere gratitude to Cancer Research UK and their donors for their generous funding and providing me with this opportunity to complete the research presented in this thesis. There are a number of people that I am indebted to for generously proving their time and support.

First and foremost, my profound thanks must go to my supervisors Professor Alan Jackson, Professor Kaye Williams, Dr Marie-Claude Asselin and Dr Jeffery Penny for continual encouragement, support and expert advice throughout my fellowship. You have provided the necessary framework and expertise upon which this research has been built. Words are never sufficient to express my gratitude to you. Special gratitude is extended to Professor Alan Jackson, my main supervisor and mentor, for his support and encouragement at the times when I needed it most.
I would like to thank my advisor, Professor Andrew King, for his advice and support.

I would like to thank a number of other individuals, whose roles are too diverse to mention. Their contributions have proven crucial to the completion of this work. Dr Calvin Soh, Pablo Torres, Dr Kenny Yu, Claire O'leary, Muhammad Babur, Duncan Forester, Alison Smigova, Elizabeth Barnett, Jose Anton, Adam Mcmahon, Brain Whitnall, Amy Watkins, Sujata Sridharan, Georgios Krokos, Miss Tina Karabatsou, Mr James Leggate, Dr Gerry Thompson, Dr Maria Feldmann and Anne Russell. A special thank you is extended to Alison Smigova for teaching and guidance, Dr Gerry Thompson and Dr Maria Feldmann for their help in patients' recruitment and Anne Russell for her amazing secretarial support.

I am also indebted to the amazing volunteers and patients who gave their time so generously. This work would have been impossible without you.

Thank you to my parents for their constant support. And finally, most of all, thank you to my wife Hiba for her unwavering support throughout this fellowship.

Author Biography

I have obtained my MB BS degree from Jordan University of Science and Technology in 2005. In 2006, I began my training as a foundation doctor in the West Yorkshire Training Scheme. During my neurosurgical rotation, I became interested in neurological diseases particularly brain tumours diagnosis and management. I joined the Leeds Radiology Academy in 2008 as a speciality radiology trainee and obtained the Fellowship of the Royal College of Radiology in 2012. In my fourth year of radiology training, I managed to secure funding from Cancer Research UK for this doctoral work at the University of Manchester, which was awarded at open competition in 2012.

I have been working as a clinical research fellow at the University of Manchester between 2013 and 2016. My research predominately focused on investigating the role of blood-brain barrier in limiting effective Temozolomide delivery in brain tumours. I returned to full time clinical work in 2016 and currently I am currently completing my final year of higher training in diagnostic neuroradiology at the Manchester Radiology Training Scheme.

Ultimately my career aspiration is to pursue the highest quality of neuroradiology practice with a commitment to research that will allow me to provide the best possible care to our patients.

Abbreviations

ABC	ATP binding cassette
ADC	Apparent diffusion coefficient
AGC	Automatic gamma counter
AJ	Adherens junctions
AIC	5-aminoimidazole-4-carboxamide
ANOVA	One-way analysis of variance
AQP-4	Aquaporin-4
AUC	Area under the curve
BBB	Blood-brain barrier
BCRP	Breast Cancer Resistance Protein
BEC	Brain endothelial cell
CNS	Central nervous system
CSF	Cerebral spinal fluid
CAM	Cell adhesion molecules
cAMP	Chlorophenylthio-cyclic adenosine monophosphate
CETA	Concentration Equilibrium transport assay
Cho	Choline
Cr	Creatine
DCE	Dynamic contrast enhanced
DMEM	Dulbecco's modified eagle medium
DSC	Dynamic susceptibility contrast
DTI	Diffusion tensor imaging

DWI	Diffusion weighted imaging
ECI	Electrospray Ionisation
EC50	Half-maximum-effect concentrations
EDTA	Ethylenediaminetetraacetic acid
FBS	Foetal bovine serum
FCS	Foetal calf serum
FDA	Food and Drug Administration
FDG	2-fluoro-2-deoxy-D-glucose
FDOPA	3,4-dihydroxy-6-[^{18}F]-fluoro-L-phenylalanine
FET	^{18}F-fluoroethyltyrosine
FLT	3L'deoxy-3L'-^{18}F-fluorothymidine
FLAIR	Fluid attenuated inversion recovery
fMRI	Functional magnetic resonance imaging
FOV	Field of view
FTIC	Fluorescein isothiocyanate
GSH/GST	Glutathione/glutathione-S-transferase
GBM	Glioblastoma multifome
GTM	Geometric transfer matrix
HIF- 1α	Hypoxia-inducible factor 1α
HPLC MS/MS	High performance liquid chromatography tandem-mass spectroscopy
IDH	Isocitrate dehydrogenase
LMA	Local means analysis
MDR	Multi-drug resistance
MET	Methyl-^{11}C-L-methionine

MGMT	O(6)-methylguanine-DNA methyltransferase
MR	Magnetic resonance
MRP	Multidrug-resistance-associated proteins
MRS	Magnetic resonance spectroscopy
MTIC	Monomethyl triazene 5-(3-methyltriazen-1-y1)-imidazole-4-carboxamide
MTT	3-(4,5-dimethyl-2-thiazoyl)-2,5-diphenyl-tetrazolium bromide
NAA	N-acetylaspartate
NVU	Neurovascular unit
OS	Overall survival
Papp	Apparent permeability coefficient
PBS	Phosphate-buffered saline
PET	Positron emission tomography
PDS	Plasma-derived serum
P-gp	P-glycoprotein
PKC	Protein kinase C
PWI	Perfusion weighted imaging
rCBV	Relative cerebral blood volume
RFU	Relative Fluorescence Unit
ROI	Region of interest
SEM	Standard error of the mean
SPE	Solid-phase extraction
STD	Standard deviation
SUV	Standardised uptake value
TAC	Time-activity curve

TEER	Trans-endothelial electrical resistance
TJ	Tight Junction
TQD	Tariquidar
TMZ	Temozolomide
UK	United Kingdom
US	United states of america
VEGF	Vascular endothelial growth factor
WHO	World Health Organisation
WT	Wild type
ZO-1	Zona occludens protein-1

Chapter 1 The Alternative Format Thesis

1.1. Overview

This thesis is presented in the alternative format. This allows a postgraduate doctoral or MPhil student to incorporate sections, which are in a format suitable for submission for publication in a peer-reviewed journal. Apart from the inclusion of such materials, the alternative format thesis must confer to the same standards expected for a standard thesis.

1.2. Aims and objectives

The aim of this thesis is to develop an imaging method for measuring the effects of strategies modifying Temozolomide (TMZ) delivery into the brain and brain tumours. In order to achieve this goal, a number of specific objectives were generated and tested:

1. Investigate the effects of P-glycoprotein (P-gp) and Breast cancer resistance protein (BCRP) inhibition on the transport of TMZ in-vitro.
An *in-vitro* blood-brain barrier (BBB) model that poses excellent barrier properties and expresses P-gp and BCRP was employed to conduct *in-vitro* transport studies, directly evaluating TMZ transport by P-gp and BCRP.

2. Evaluate the role of the P-gp and BCRP efflux transporters in the efflux of TMZ at the mouse BBB.
Small animal positron emission tomography (PET) scans were performed using radiolabelled [^{11}C]TMZ in wild type and genetic transporter knockout mice, as well as by using chemical inhibition of P-gp and BCRP.

3. Investigate the role of the P-gp and BCRP efflux transporters in limiting TMZ efficacy in brain tumours.
Glioblastoma (GBM) xenograft models were implanted into mice to evaluate how chemical inhibition of P-gp and BCRP mediated efflux affects the efficacy of TMZ.

4. Investigate the functional activity of P-gp in high-grade glioma patients.
PET imaging and (R)-[^{11}C]verapamil were utilised to non-invasively demonstrate the functional activity of P-gp in five patients with high-grade gliomas.

1.3. Organisation and structure of the thesis

Four experimental chapters are presented in scientific paper format. At the beginning of each experimental chapter, a brief abstract of the paper is provided. All experimental chapters have been written by the candidate with co-authors providing input on the draft versions that were incorporated in this thesis. The first two introductory chapters provide an overview of glioma tumours and the BBB to help establish the context and rationale for the research.

Chapter 2: *Glioma: An Overview.* This chapter provides a brief overview of glioma tumours and the current state of knowledge of the imaging techniques used in evaluating patients with brain tumours.

Chapter 3: *Blood-Brain Barrier: An Overview.* This chapter describes the role of the BBB and the role of the efflux transporters. Particular emphasis is placed on the role of P-gp and BCRP in limiting delivery of effective chemotherapy.

Chapter 4: *In-vitro studies: Temozolomide transport studies in a validated in-vitro blood-brain barrier model.* This is the first experimental chapter that investigates the relationship between TMZ and the efflux transporters P-gp and BCRP. In an effort to replicate the clinical settings, TMZ transport studies were conducted in a validated BBB model with high trans-endothelial electrical resistance (TEER) and proven functionally active P-gp and BCRP This experimental chapter provides the first direct evidence of active TMZ transport by both P-gp and BCRP.

Chapter 5: *Preclinical in-vivo study: Temozolomide is transported by P-glycoprotein and Breast Cancer Resistance Protein Efflux transporters at the mouse blood-brain barrier.* In this experimental chapter small animal PET imaging was used with

radiolabelled TMZ in groups of wild type and transporter knockout mice (P-gp, BCRP and dual transporter knockout) and in wild type mice that underwent efflux transporters inhibition with TQD. Brain uptake of the radiolabelled TMZ was determined by direct radioactivity concentration measurements using a gamma counter as well as PET imaging. The results of this chapter confirm that TMZ is transported by both P-gp and BCRP efflux transporters at the BBB of the mouse.

Chapter 6: *Preclinical in-vivo study: P-glycoprotein and Breast Cancer Resistance Protein inhibition enhances Temozolomide efficacy in a glioma model in mice.* After demonstrating that TMZ is transported by P-gp and BCRP, this chapter consisted of an efficacy study designed to investigate the effects of combination therapy of TMZ with P-gp and BCRP inhibition in an orthotopic glioma model in mice. Magnetic resonance (MR) imaging was used to assess tumour volume as a surrogate for tumour response. Combination therapy resulted in a quicker and more sustained tumour shrinkage when compared with TMZ alone therapy. Finally, several steps were taken in attempt to establish the mechanism for this response.

Chapter 7: *Clinical study: Imaging P-glycoprotein function in patients with high-grade gliomas.* The final experimental chapter describes a PET imaging study evaluating the functional activity of P-gp in patients with high-grade glioma tumours and comparing them to healthy volunteers. Heterogeneous P-gp functional activity was demonstrated amongst patients and within the different regions of individual tumours. This study also highlighted the importance of measuring cerebral perfusion to accurately measure P-gp function.

Chapter 8: *Summary and future work.* This chapter summarises the findings of the experimental chapters and discusses potential future work.

1.4. Research questions

The principle research question of the thesis is:

Can we develop a non-invasive imaging method for measuring and modifying TMZ delivery in patients with brain tumours?

Secondary questions arising from the primary question are:

1. What is the relationship between TMZ and the efflux transporter P-gp and BCRP?
2. Is efflux transporter inhibition in combination with TMZ treatment a suitable strategy for enhancing TMZ efficacy?
3. Is it possible to image the functional activity of P-gp in patients with high-grade glioma tumours?

Chapter 2 Brain Tumours: An Overview

2.1. Introduction

Brain tumours and other central nervous system (CNS) tumours are the eighth most common cancer in the United Kingdom (UK), responsible for approximately 3% of all cancer deaths. A significant proportion of these tumours are highly malignant, with GBM being the most common primary malignant tumour in adults, having a limited median survival time in England of only six months (Brodbelt et al., 2015).

This chapter will provide a brief overview of the clinical features, classification and biology of brain tumours, with a particular focus on the high-grade glioma tumours studied in this thesis.

2.2. Clinical features

Clinical manifestations of brain tumours are the result of multiple mechanisms, which include: raised intracranial pressure and direct brain tissue irritation or invasion. Raised intracranial pressure is usually the indirect consequence of a tumour mass, oedema or hydrocephalus. Brain tumours can cause hydrocephalus via either cerebrospinal fluid (CSF) overproduction or impairment of its circulation and resorption. The most commonly encountered manifestations of brain tumours include headache, nausea, vomiting, visual symptoms and altered mental status.

As with all neurological diseases of the brain, the clinical manifestations of brain tumours are directly related to the specific brain area that has been affected. Such local manifestations can be the result of direct irritation of the tumour-adjacent brain tissue via the mass effect or other metabolic processes (Tatter, 1999). Symptoms include seizures, altered sensation and progressive loss of function of the affected brain tissue.

The rate of tumour growth is another important factor. For example, a slow-growing, low-grade, infiltrative glioma can reach a late-stage size before causing symptoms. In contrast, rapidly-growing, high-grade tumours are more likely to become symptomatic and declare themselves earlier (Buckner, 2017).

2.3. World Health Organisation (WHO) classification of central nervous system tumours

The 2007 WHO classification of CNS tumours was recently revised in 2016 (Louis et al., 2016). The 2007 classification was based on the histological characteristics of the tumour's main cells of origin as well as their anatomical location (Louis et al., 2007). The 2016 update incorporates molecular markers such as a mutation in isocitrate dehydrogenase (IDH), integrating phenotypic (microscopic) and genotypic parameters for the clinical classification of brain tumours and making them more relevant to current clinical practice. Increased emphasis is placed on the genotype as the primary tool for determining a diagnosis, even in cases where there exists discordance between phenotypic and genotypic features. The classification also introduced the term "not otherwise specified - NOS" to allow for cases in which the molecular markers are not available or have not been identified.

Another important change in the new classification is the grouping of diffusely infiltrating gliomas, including tumours of both astrocytic and oligodendroglial cell origin. This grouping is based on the shared mutations in the *IDH1* and *IDH2* genes as well as their shared prognostic markers. Furthermore, both diffuse astrocytoma and anaplastic astrocytoma have been further divided into three categories: IDH-mutant, IDH-wildtype and NOS.

Oligodendroglioma and anapaestic oligodendroglioma tumours can only be diagnosed when both of the following genetic markers have been identified: IDH gene mutation and dual whole-arm losses of 1p and 19q (1p/19q co-deletion). For example, if a tumour has histological characteristics of an oligodendroglioma but lacks the molecular marker of 1p/19q co-deletion, it no longer can be diagnosed as an oligodendroglioma.

Finally, glioblastomas, the most aggressive form of tumour, have been divided into three categories: IDH-wildtype, IDH-mutant and NOS. IDH-wildtype represent the majority of the cases and is characterised as a primary glioblastoma (Yan et al 2009) (Cohen et al., 2013).

Histological grading is another tool that is used in the WHO classification. Tumours are assigned a grade from I to IV on the basis of their malignant features, such as nuclear atypia, mitotic activity, endothelial cell proliferation, cellularity and necrosis. This grading facilitates the prediction of biological behaviour and prognosis, and helps

guide clinical management. WHO grade I and II tumours constitute low-grade tumours, whilst grades III and IV represent high-grade tumours. Grade I and II tumours have relatively low cellular proliferative rates, but grade II tumours tend to be more infiltrative and have the potential to progress into higher grade tumours. Grade IV tumours represent the most malignant group, with the highest mitotic activity and necrosis and most aggressive infiltrative growth pattern (Louis et al., 2007). A summary of the updated WHO classification system is presented in Table 2.1.

Table 2. 1: Summary of the WHO classification for brain tumours.

1. Diffuse astrocytic and oligodendroglial tumours

- WHO grade II
  - Diffuse astrocytoma
    - IDH-mutant
    - *IDH-wildtype*
    - NOS
  - Oligoastrocytoma NOS
  - Oligodendroglioma
    - IDH mutant and 1p19q co-deleted
    - NOS

- WHO grade III
  - Anaplastic astrocytoma
    - IDH-mutant
    - *IDH-wildtype*
    - NOS
  - Anaplastic oligoastrocytoma, NOS
  - Anaplastic oligodendroglioma
    - IDH mutant and 1p19q co-deleted
    - NOS

- WHO grade IV
  - Glioblastoma
    - *IDH-Wildtype*
      - Giant cell glioblastoma
      - Gliosacroma
      - Epithelioid glioblastoma
    - IDH-mutant
    - NOS
  - Diffuse midline glioma, H3K27M-mutant

2. Other astrocytic tumours
3. Ependymal tumours
4. Other gliomas
5. Choroid plexus tumours
6. Neuronal and mixed neuro-glial tumours
7. Tumours of the pineal region
8. Embryonal tumours
9. Tumours of the cranial and paraspinal nerves
10. Meningiomas
11. Mesenchymal, non-meningothelial tumours
12. Melanocytic tumours
13. Lymphoma
14. Histiocytic tumours
15. Germ cell tumours
16. Tumours of the sellar region
17. Metastatic tumours

Adapted from (Louis et al., 2016). Tumours encountered as part of this thesis research belong to the first category; as such, detailed classification is provided.

2.4 Glioma biology overview

The Cancer Genome Atlas (TCGA) identified three main molecular pathways that are affected in a large number of GBM tumours. These include: (1) growth factor dysregulation, which can be achieved by activation of receptor tyrosine kinase (RTK) genes. (2) Activation of the phosphatidyl inositol-3- kinase (PI3K) pathway and finally (3) Cell apoptosis regulation via inactivation of the p53 and retinoblastoma-1 tumour suppressor pathways (TCGA, 2008). These findings shed some light on the complex biology of GBM and the various molecular pathways that are implicated in the growth of these tumours.

Another important molecular pathway in the development of GBM is IDH1 mutation, which has been first identified by a multi-group collaboration in 2008 (Parson et al., 2008). Mutations in the IDH1 and IDH2 genes have been commonly linked to the development of secondary GBM (Louis et al., 2016). The mutation appears to be a single amino acid missense mutation at the arginine 132. 2-hydroxyglutrate is the by-product of this mutation. Some authors suggested that IDH is an oncogene with 2-hydroxyglutrate being an oncometabolite. Furthermore, the TCGA initiative pointed to an association between IDH mutation and increased promoter methylation (G-CIMP).

A main differentiating characteristic of GBMs is their high microvascular proliferation, which is an essential requirement in facilitating the tumour growth (Fischer et al., 2005). Once the tumour size surpasses 1-2 mm, it starts to outgrow its blood supply, leading to necrosis and hypoxia. The tumour must then rely on angiogenesis to meet its increasing demands for nutrients and oxygen. This complex process is governed by multiple pro-angiogenic factors and begins with the expression of hypoxia-inducible factor 1α (HIF-1α). 2-hydroxyglutarate produced by mutant IDH can alter proline hydroxylation, which in turn, inhibits the degradation of HIF-1α. Thus IDH mutation can result in a microenvironment where HIF-1α protein levels are high (consistent with hypoxia) while oxygen tension is normal (Cohen et al., 2013). This has been referred to as “pseudo-hypoxia” and may play an important role in the biology of GBM tumours.

Furthermore, HIF-1α, in combination with stabilising genetic factors, facilitates the production of various pro-angiogenic factors, vascular endothelial growth factor (VEGF) being the main one (Folkman, 1992) (Plate et al., 1992). VEGF in turn

promotes the formation of immature blood vessels with increased endothelial permeability (Waggener and Beggs, 1976). The end result is the formation of a complex and highly heterogeneous vascular microenvironment in the tumour and around its growing edges.

A common feature of GBM is acidosis caused by hypoxia (low oxygen tension). Hypoxia essentially alters the cellular metabolism by shifting from oxidative phosphorylation to glycolytic metabolism generating a high acid load in the tumour microenvironment. As discussed previously, hypoxia induces the production of HIF-1α, which induces the expression of various intracellular pH-regulating mechanisms. The end result of this is tumour cells that are adapted and resistant to the toxic environment of acidosis.

The invasive nature of GBM is another hallmark of this tumour and a key reason preventing curative surgical resection. Scherer described the glioma invasion pathway, which occurs along the white matter tracts, neuronal tracts and vasculature (Scherer, 1940). Additionally, the tumour's aggressive invasive growth pattern appears to be directly linked to hypoxia, which drives the release of angiogenic factors at the tumour edges and in the adjacent brain tissue facilitating tumour growth and invasion (Zagzag et al., 2008). In fact, at the time of GBM diagnosis, it is accepted that tumoural cells have likely already spread to various areas of the brain, which may even appear macroscopically normal using conventional imaging techniques (Giese et al., 2003).

Finally, it is important to remember that tumoural heterogeneity is not limited to the vascular microenvironment but can also be seen in the tumours' genetic profiles as well as other biological factors such as cellular proliferation and metabolic activity. Heterogeneity can also be seen in different components of an individual tumour and is probably a major factor in the frequently observed differential response of these tumours to treatment. For example, hypoxic areas of the brain with low blood supply are likely to receive different concentrations of chemotherapy than the more solid portion of a tumour, hence showing a different response (Winkler et al., 2004).

2.5 Imaging

Imaging is integral to the management of patients with brain tumours, but its exact role is dependent on specific clinical indications (Ricci, 1999). Broadly speaking, the aims of imaging in patients with a brain tumour can be divided into four major categories: (1) establishing an underlying abnormality, (2) characterising the abnormality, (3) assisting in treatment planning, and finally (4) post-treatment evaluation.

The most commonly used imaging modalities for the assessment of neurologic disorders are computed tomography (CT) and magnetic resonance imaging (MRI). CT is mostly limited to hyper-acute clinical settings due to its low cost, wide availability, short imaging times and excellent ability to detect acute haemorrhage. MRI, on the other hand, offers improved anatomic delineation, increased sensitivity and access to a number of advanced imaging processes such as diffusion-weighted imaging. It is thus the modality of choice for the evaluation of brain tumours. In recent years, despite its complexity, expense and limited availability, PET use has been increasing, as it can provide unique additional information in specific clinical situations.

2.5.1. Conventional MRI imaging in glioma

Conventional MRI imaging protocols for use in cerebral malignancy include T1W, T2W, fluid attenuated inversion recovery (FLAIR), diffusion weighted imaging (DWI), T2*W gradient echo and post contrast T1W images. Despite the various advances in MRI imaging, conventional MRI still plays a dominant role in clinical practice and remains the mainstay of radiologic assessment of glial tumours. However, although conventional imaging protocols provide exquisite anatomic detail, it is important to note that, in many cases, they are not able to accurately identify the glioma's grade or cellular subtype. This is particularly important because these features have a major impact on treatment planning. For example, contrast enhancement, as well as certain morphologic features such as mass effect, necrosis and haemorrhage, are regarded as indicators of an aggressive, high-grade glioma. Contrast enhancement in particular has been suggested to correlate reliably with malignancy

(Pierallini et al., 1997). However, although a common feature of high-grade glioma, contrast enhancement remains nonspecific. For example, Scott et al. found that almost a third of high-grade glioma tumours showed no contrast enhancement, while White et al. noted that almost 50% of low-grade oligodendroglioma tumours demonstrated some enhancement (Scott et al., 2002) (White et al., 2005). Currently, no conventional MRI imaging features exist that can be reliably used to differentiate between the different glioma subtypes, such as grade II astrocytoma and oligodendroglioma (Upahday, 2011).

2.5.2. Advanced MRI imaging techniques

Conventional MRI imaging enables structural evaluation of tumour size, anatomic position and contrast enhancement patterns, but is limited in its use for evaluating pathophysiologic properties such as microscopic tumoural infiltration, microvascular characteristics, early response changes or the relationship of the tumour to eloquent cortical areas. The attempt to address these limitations led to the development of advanced MR imaging techniques able to evaluate the cellular, haemodynamic, metabolic and functional properties of gliomas.

The advanced MRI imaging techniques that are increasingly being employed in clinical practice include diffusion weighted imaging (DWI), diffusion tensor imaging (DTI), perfusion weighted imaging (PWI) including dynamic susceptibility contrast (DSC-MRI) and dynamic contrast enhanced (DCE-MRI) techniques, MR spectroscopy (MRS) and functional MRI (f-MRI). A summary of the most commonly utilised advanced MR imaging techniques and their derived imaging biomarkers is presented in Table 2.2.

***Table 2. 2**:* Summary of the most commonly derived MR imaging biomarkers in gliomas.

Technique	Biomarker	Correlation
DWI	Apparent diffusion coefficient	Cellular density
DSC-MRI	Relative cerebral blood volume Relative cerebral blood flow Mean transient time	Vascular proliferation
DCE-MRI	Relative cerebral blood volume Relative cerebral blood flow Contrast Transfer Coefficient (Ktrans)	Vascular proliferation Vascular permeability
ASL	Cerebral blood flow	Vascular proliferation
MRS	Various metabolites including Choline, Creatine, Lactate, Lipids and NAA	Surrogates for various physiological process
DTI	Fractional anisotropy of water molecules	White matter tracts
fMRI	Changes in deoxyhaemoglobin concentration	Surrogate for cortical activation

Abbreviations: DWI: diffusion weight imaging, DSC-MRI: dynamic susceptibility contrast MRI, DCE-MRI: dynamic contrast enhanced MRI, ASL: arterial spin labelling, DTI: diffusion tensor imaging, fMRI: functional MRI.

2.5.2.1 MRI Perfusion

As tumours grow they stimulate the development of new blood vessels, a process known as angiogenesis (Hanahan and Weinberg, 2000). These new vessels are characterised by a defective, permeable, blood brain barrier due to incomplete closure of endothelial tight junctions. In slowly growing tumours the process may result in regular, well-perfused, vascular beds with normal arterial, capillary and venous organisation. Where tumour growth outstrips the angiogenic process then tumour vasculature will be irregular with multiple blind ending vessels, arteriovenous shunts and areas of hypoperfusion and necrosis. The use of imaging biomarkers to quantify and characterise this abnormal microvascular environment provides a powerful tool in understanding individual variations in tumour biology.

There are two major groups of imaging techniques, which are used to derive quantified biomarkers that describe the tumour microvascular environment. The first, and most commonly used utilise dynamic imaging of the passage of a contrast agent (dynamic contrast enhanced imaging techniques), the second, arterial spin labelling (ASL) uses magnetic labeling of endogenous protons in blood to assess blood volume flow and flow rate.

Dynamic Contrast Enhanced Imaging Techniques

Dynamic contrast enhanced imaging techniques use a bolus injection of contrast agent (CA) and study its passage through the cerebral and tumoural vasculature in order to derive quantified metrics which describe the microvascular environment. This generic approach can be applied using dynamic CT or MR, and dynamic MR imaging can be performed using either T1 weighted or T2* weighted imaging.

Dynamic Susceptibility Contrast Enhanced-MRI (DSCE-MRI)

DSCE-MRI is widely used in clinical practice due to its relative ease and its contribution to diagnosis and therapy planning. A dynamic series of T2* weighted images is acquired, with a high temporal resolution, usually in the region of 4 to 5 seconds. During the dynamic acquisition bolus injection of paramagnetic contrast agent is administered via a peripheral vein using a power injector. The bolus retains integrity as it passes through the brain producing a relatively short-lived decrease in signal intensity reflecting intravascular contrast concentration. The signal change can, relatively simply, be transformed into a measure of contrast concentration allowing the generation of contrast concentration time course curves (CC-TCC). These dynamic images can be analysed using a number of algorithmic approaches. The area under the CC-TCC will be directly proportional to the regional percentage blood volume (rCBV). Absolute measurements of CBV can then be obtained by normalising rCBV to vascular values observed in large veins or normal white matter. In practice, estimation of CBF is complicated by broadening of the contrast bolus and regional delays in arrival due to vascular transit time. In addition, the contrast bolus will vary between subjects making it necessary to direct the estimate the size and shape of the bolus in the feeding arteries. The use of various mathematic deconvolution techniques to correct for variation in arterial bolus shape combined with approaches which correct for arrival time delay allows effective estimation of cerebral blood flow in normal vascular trees. Unfortunately, in tumoural vessels, characterised by tortuousity and abnormal flow patterns, the underlying assumptions of this model do not hold and estimates of CBF are likely to have significant inaccuracies.

Another limitation of DSCE-MRI is an assumption that CA remains intravascular with

no leakage into the extravascular extracellular space (EES). This assumption is, of course, incorrect where there is BBB breakdown. Such contrast leakage produces a strong and competing T1 contrast effect, also known as the "T1-shine through effect", which causes under estimation of CBV measurements. T1-shine through effects can be minimised by preloading the patient with a dose of contrast before acquiring the dynamic data (Jackson et al., 2002) (Boxerman et al., 2006). Other methods include the use of a low flip angle sequences and algorithmic correction of the individual CC-TCC curves (Cha et al., 2002) although the former has become unpopular due to the resulting decrease in signal-noise ratio.

Dynamic contrast enhanced MRI (DCE-MRI)

DCE-MRI uses dynamic T1 weighted sequences to measure changes in signal intensity during CA passage. The resulting changes in signal from intravascular and extravascular CA leakage are additive, which allows direct estimation of CA leakage and BBB permeability. In many clinical applications semi-quantitative analytic methods are applied, usually attempting to quantify the rate of change or degree of change of signal intensity relative to baseline (Jackson et al., 2014). These metrics are simple to measure and have been widely applied in many tumour types. However, in many applications, particularly in the brain, there has been a focus on the application of quantitative pharmacokinetic analytic algorithms that allow calculation of biomarkers that are believed to give greater physiologic specificity (Jackson, 2004).

The use of pharmacokinetic analysis techniques requires generation of CC-TCC from observed signal changes. For T1W data this requires accurate measurement of baseline T1 values prior to contrast passage. In most cases this is done using a gradient echo sequence with multiple flip angles. From the resulting dynamic images, CC-TCC can be derived for the feeding artery (arterial input function; AIF) and for each voxel in the tumour and normal tissues.

The most widely used analytic approach is a modified version of Tofts pharmacokinetic model which yields three main imaging biomarkers: estimates of the vascular fraction (*vp*), extravascular extracellular space fraction (*ve*) and the transfer contrast coefficient (K^{trans}) (Tofts and Kermode, 1991). K^{trans} derived using this model will be affected by both regional blood flow and the product of capillary endothelial permeability and surface area (PS). Where flow is low relative to leakage, K^{trans} will principally reflect flow whereas if leakage is low relative to blood flow then it will

principally reflect permeability (Tofts et al., 1999).

More complex analytic models can be implemented; however, these may be more sensitive to noise and require superior image acquisition strategies. Choosing the appropriate pharmacokinetic model is dictated by the requirements of the individual study as well as the available post processing hardware and local expertise (Tofts et al., 1999).

Differences between DSC-MRI and DCE-MRI are presented in table 2.3.

Table 2.3: Clinical differences between DSC-MRI and DCE-MRI.

	DSC-MRI	**DCE-MRI**
Advantages	Widely available in clinical practice	Most reliable
	Quick	Less artefact
Limitations	Susceptibility artefact	Requires complex modelling and post processing
	Permeability is not measured	Longer acquisition times

2.5.3. Clinical applications of MRI

Over the past 20 years, considerable research has been done on the use of advanced MRI for the characterisation of cerebral tumours. A number of specific clinical applications have emerged that will be discussed in this section. These applications include 1) grading of gliomas and identification of histologic subtypes, 2) identification of higher-grade transformation, 3) treatment planning and guidance, 4) assessment of treatment response, and 5) molecular characterisation.

2.5.3.1. Grading of gliomas and identification of histologic subtypes

Treatment strategies for gliomas differ greatly between low-grade gliomas (WHO grade I and II) and high-grade gliomas (WHO grade III and IV). High-grade glioma tumours such as GBM are classically treated with maximum surgical resection, followed by a combination of chemotherapy and radiotherapy (Stupp 2005). Low-grade tumour treatment strategies on the other hand vary greatly and may include: regular surveillance with imaging, surgical resection, chemotherapy or a combination of these approaches (Buckner, 2017).

Histologic grading remains the clinical gold standard, but in practice it is limited by sampling error, which can result in under-grading. In addition, cerebral tumours do not remain constant but evolve over time so that a biopsy showing a low-grade glioma may be under-graded or may simply dedifferentiate into a high-grade glioma following biopsy. In contrast, imaging is non-invasive, allows examination of the entire tumour and can be repeated to monitor tumour behaviour over time. Despite these limitations and in the absence of reliable imaging biomarkers, it is unlikely that imaging will replace histological assessment in current clinical practice.

A number of imaging biomarkers that quantify grade-related features of glioma biology have been described. High-grade glioma tumours are characterised by more rapid growth, higher proliferation, areas of hypoxia and necrosis and, consequently, higher angiogenic drive. High-grade glioma tumours are therefore characterised by a vascular microenvironment featuring high vessel density, disorganised vessel structure and abnormal capillary endothelial permeability. Several studies have reported a strong

positive correlation between tumour relative cerebral blood volume (rCBV) and grade (Law et al., 2004) (Maia et al., 2005) (Fan et al., 2006) (Yoon et al., 2014). Similarly K^{trans}, an imaging biomarker that reflects blood flow and endothelial permeability, is also independently related to tumour grade (Roberts et al., 2001) (Patankar et al., 2005) (Cha et al., 2006). However, perfusion-weighted imaging techniques are not without their limitations. For example, in an oligodendroglioma, rCBV can be elevated even in low-grade tumours (Cha et al., 2005). Furthermore, both DSC and DCE-MRI fail to reliably differentiate between grade III and IV tumours, presenting significant treatment implications.

Multiple studies have demonstrated that high-grade glioma tumours are associated with restricted diffusion, reflecting increased cellular density (Sugahara et al., 1999) (Kono et al., 2001) (Kitis et al., 2005). However, a significant overlap in apparent diffusion coefficient (ADC) values, a measure of magnitude of diffusion within tissues, exists between low-grade and high-grade glioma tumours, so that other researchers have been unsuccessful at applying ADC measurements to the prediction of grade (Lam et al., 2002). In practice, ADC is affected by a number of factors in addition to cellular packing. In particular, the presence of necrosis, which is a hallmark of GBM, is associated with very high ADC values. The summary metric mean ADC is therefore inappropriate to use as a measure of cellular density, since it will mask significant heterogeneity in ADC across the tumour. Despite these limitations, it is reasonable to view areas of restricted diffusion (low ADC) in a solid glial tumour as raising suspicion of higher histologic grade.

Low-grade and high-grade glioma tumours also show differences in metabolic profile that can evaluated by MRS. Measurement of a number of metabolite concentrations and metabolite ratios has been reported as useful for distinguishing between low- and high-grade tumours (Hourani et al., 2008). Many studies have demonstrated that high-grade glioma tumours are associated with an elevated Choline:Creatine (Cho:Cr) ratio (McBride et al., 1995) (Yang et al., 2002) (Sijens and Oudkerk, 2002) (Zeng et al., 2011). Similarly, low levels of N-acetylaspartate (NAA) and increased lactate have also been suggested as markers of higher-grade tumours (Negendank et al., 1996) (Murphy et al., 2002) (Howe et al., 2003) (Stadlbauer et al., 2006).

It is worth noting that combining different biomarkers improves the accuracy of predicting glioma grade. This has been demonstrated by multiple studies using combinations of DSCE-MRI, MRS and DWI (Bulakbasi et al., 2003) (Law et al.,

2003) (Di Costanzo et al., 2006) (Zonari et al., 2007).

The improved sensitivity of low-grade oligodendrogliomas to chemotherapy in comparison to low-grade astrocytomas makes the identification of these tumours a clinical priority. Low-grade oligodendrogliomas demonstrate lower ADC values (Tozer et al., 2007) and higher rCBV (Cha et al., 2005) compared with low-grade astrocytomas. However, these findings are non-specific, since they may also represent high-grade transformation occurring in low-grade astrocytomas.

2.5.3.2. Identifying malignant transformation in low-grade gliomas

Approximately two-thirds of low-grade glioma tumours will progress to high-grade by 4 to 5 years from onset. However, such malignant progression cannot be accurately predicted (Walker and Kaye, 2003) (Gudinaviciene et al., 2004) (Ohgaki and Kleihues, 2005), although imaging of tumour blood volume changes can identify an increased risk of malignant transformation. The disease follows a fatal course in virtually in all patients with malignant gliomas (Omuro et al., 2007). Prediction and early identification of malignant transformation are among the most important clinical goals in the management of low-grade gliomas, and current therapeutic strategies are largely based around active monitoring of disease progression using serial contrast-enhanced MRI. In conventional MRI, malignant transformation is suspected when a rapid increase in tumour size is seen or when new areas of contrast enhancement develop. Malignant dedifferentiation is associated with local foci of increased proliferation, with secondary increases in angiogenic activity, leading to increased vessel density and local blood brain barrier breakdown. DSC-MRI shows heterogeneous increases in rCBV, which appear to be an early marker of malignant transformation occurring 6-12 months before clear evidence of contrast agent leakage (Danchaivijitr et al., 2008) (Law et al., 2008).

2.5.3.3. Surgical treatment planning

Accurate surgical treatment planning can be aided by the correct identification of (1) tumour extent, (2) localisation of the aggressive component of the tumour, and (3) careful evaluation of the tumour's relationship to the surrounding eloquent brain cortex

and major white matter tracts.

Advanced MRI has become increasingly important in surgical planning, particularly for identification of optimal biopsy sites, as it provides improved demonstration of tumour extent and clearer demonstration of the relationship between the tumour and major white matter tracts and eloquent cortex.

Histology remains the gold standard for glioma grading, although the heterogeneity of glial cell tumours results in a significant risk of under-grading, particularly where tissue sampling is from biopsy. Identifying areas of high-grade dedifferentiation using DCE-MRI maps of CBV is now routinely done at many centres, and the use of spectroscopic imaging has also been shown to improve biopsy guidance (McKnight et al., 2007).

Another benefit of advanced MRI techniques is their ability to improve delineation of glioma margins and the extent of tumour invasion. This is important, as tumour cells frequently extend beyond the radiologic abnormality demonstrated by conventional MRI. A number of studies have shown that PWI, DWI and MRS can all provide clinically useful information regarding tumour infiltration and help to distinguish invasion from peripheral vasogenic oedema with an accuracy approaching 90% (Di Costanzo et al., 2006).

The relationship between the tumour and major white matter tracts can be demonstrated using diffusion tractography (Jellison et al., 2004) as well as assessing the degree of tumoural infiltration or displacement (Witwer et al., 2002) (Clark et al., 2003).

In recent years, fMRI has made the transition from the research setting to become an essential clinical tool. This was driven by the need to identify areas of the eloquent cortex and their relationship to the tumour and planned areas of resection. The clinical translation of fMRI was enabled by rapid technologic advances and the development and validation of multiple paradigms for mapping motor, language and visual areas. In clinical practice, mapping motor function is very reliable, showing excellent spatial correlation with intraoperative cortical stimulation. Conversely, language mapping has proved less reliable (Achten et al., 1999) (Fandino et al., 1999) (Roux et al., 2003). The impact of fMRI is reflected in various clinical, studies where it has been shown to facilitate surgical planning and to alter decision making (Lee et al., 1999), often enabling a more aggressive surgical approach and reducing operating times (Petrella et al., 2006) (Stippich et al., 2007).

2.5.3.4. Measuring and Predicting Therapeutic Response

2.5.3.4.1. Response assessment criteria

The WHO oncology response criteria, introduced in the 1980s, were designed to standardise clinical response assessment for research and clinical purposes (Miller et al., 1981). The criteria were designed for non-CNS tumours and in 1990, the Macdonald criteria for response assessment in gliomas were introduced (Macdonald et al., 1990). The current standard criteria for glioma response assessment are the RANO (Response Assessment in Neuro-Oncology) criteria, introduced in 2010. The RANO criteria allow for identification of target lesions (enhancing, greater than 10 mm diameter) and non-target lesions, which include FLAIR and T2 signal abnormalities indicative of a non-enhancing tumour. Clinical indicators, including changes in performance status and steroid usage, also are included (Wen et al., 2010).

Despite the development of revised response criteria, newer treatments can produce imaging changes that may be misleading. For example, following radiotherapy and TMZ, many patients with GBM demonstrate an increase in enhancement and progressive T2 signal abnormality. Follow-up scans, with no interval treatment, demonstrate improvement. This "pseudoprogression" which is seen in approximately 20% of patients two to six months after the start of therapy, is actually associated with a prolonged response. There appears to be a correlation between MGMT methylation status and pseudoprogression (Brandes, 2008). Both radiation necrosis, which typically occurs many months after the completion of radiation treatment, and pseudoprogression can be grouped under the umbrella term "treatment effect" to distinguish the associated enhancement from tumour-induced BBB breakdown. The clinical diagnosis of "pseudoprogression" is challenging and relies on accurate assessment of the clinical status as well as the radiological appearances.

Both radiation necrosis, which typically occurs many months after the completion of radiation treatment, and pseudoprogression can be grouped under the umbrella term "treatment effect" to distinguish the associated enhancement from tumour-induced BBB breakdown.

2.5.3.4.2. Differentiating true progression from pseudoprogression

Various advanced MR imaging techniques have been employed to achieve accurate identification of true tumour progression. DWI studies indicate that restricted diffusion favours increased cellularity, and therefore tumour progression, with authors suggesting various ADC cut-off values as a marker for progression (Matsusue et al., 2010) (Lee et al., 2012). Pseudoprogression also appears to be associated with lower rCBV values when compared with true progression. In a study by Larsen et al., lesions that regressed demonstrated a low CBV (less than 1.7 mL/100 g) and generally corresponded to a region of metabolic inactivity in 2-fluoro-2-deoxy-D-glucose-PET (FDG-PET) consistent with a treatment effect. Lesions that progressed demonstrated a high CBV (greater than 2.2 mL/100 g) and generally corresponded to a region of increased metabolic activity in FDG-PET compatible with tumour recurrence. The authors concluded that an absolute CBV threshold of 2.0 mL/100 g could be used to assess the regression or progression of a lesion, with a reported sensitivity and specificity of 100% (Larsen et al., 2013). Mangla et al. similarly evaluated rCBV values in patients with GBM before and 1 month after treatment. In patients with pseudoprogression, there was a 41% mean decrease in rCBV, while cases of true tumour progression showed a 12% increase in rCBV. ROC analysis revealed 76.9% sensitivity and 85.7% specificity (Mangla et al., 2010).

MRS may also be helpful in differentiating true progression from pseudoprogression. Despite the low number of participants in such studies, early results indicate that recurrent tumours are associated with elevated Cho-Cr and Cho-NAA ratios (Weybright et al., 2005) (Smith et al., 2009).

2.5.3.4.3. Identifying pseudoresponse and detection of non-enhancing tumours

Treatment regimes, including anti-angiogenic agents for glioblastoma patients, improve progression-free survival (PFS) but do not substantially affect overall survival (OS) (Gilbert et al., 2014). Anti-angiogenic therapy causes a rapid decrease in capillary endothelial permeability and consequent reduction in tumour enhancement, which has been described as a "pseudoresponse." Early identification of pseudoresponse is therefore important and relies on accurate identification of non-

enhancing tumours.

A non-enhancing tumour can be detected using conventional MRI sequences such as FLAIR. However, other pathologies such as gliosis and vasogenic oedema can induce similar imaging changes, and cannot be reliably differentiated from non-enhancing tumours. Conventional MRI alone is therefore limited in its ability to detect non-enhancing tumours.

Advanced MRI techniques such as DSC-MRI and DWI can play a complimentary role to conventional MRI in the assessment of pseudoresponse. In the ACRIN 6677 trial (Boxerman et al., 2013), development of progressive enhancement whilst receiving anti-angiogenic therapy was associated with poorer OS. However, when evaluating patients with improved or stable contrast enhancement, no differences in OS were detected. This unexpected observation may be due to the inability to differentiate true responses from pseudoresponses and highlights the limitations of conventional MRI.

In the same trial, DSC-MRI was superior to conventional MRI in the assessment of patients who demonstrated improved or stable enhancement. DSC-MRI demonstrated that decreased rCBV at two weeks after initiation of therapy was associated with longer OS (Boxerman et al., 2013); these findings were confirmed in a subsequent study (Schmainda et al., 2015).

Both DCE-MRI and DSC-MRI appear to be helpful for identifying areas of tumour infiltration, which is associated with higher perfusion parameters, in contrast to vasogenic oedema (Artzi et al., 2014) (Artzi et al., 2015).

DWI has also been investigated in patients receiving anti-angiogenic treatment. DWI exploits the theory that tumoural infiltration is associated with higher cellularity and therefore restricted diffusion (Gerstner et al., 2010), whilst free diffusion is the norm for simple vasogenic oedema. This is supported by a recent study from Lutz et al, in which the development of new areas of tumoural enhancement were associated with restricted diffusion (Lutz et al., 2014), which precedes the development of enhancement in some patients (Gupta et al., 2011).

It is important to note that DWI assessment is also limited by other factors. For instance, anti-angiogenic therapy may lead to the development of new areas of persistent restricted diffusion (Mong et al., 2012) (Rieger et al., 2010) (Farid et al., 2013) (Hesselink et al., 2014) as well as stroke-like lesions that can mimic non-enhancing tumours. Such limitations dictate the need for careful interpretation of DWI images in glioma patients receiving anti-angiogenic therapy.

2.5.3.4.4. Response prediction and early response detection

There is increasing interest in the identification of early response markers, which could be used to support personalised approaches to therapy by predicting poor response at baseline or very early in the therapy. One recent study evaluated the prognostic value of DWI by measuring ADC values in the enhancing portion of the tumour and found that tumours with low ADC values were more likely to progress at 6 months when compared to tumours with high ADC values (Pope et al., 2011). This finding was only true in patients who underwent treatment with an anti-angiogenic agent, illustrating the predictive, as opposed to prognostic, nature of this marker. Several studies also indicate a role for PWI in predicting response to anti-angiogenic agents (Hirai et al., 2008) (Sawlani et al., 2010). These studies indicate that perfusion-derived imaging biomarkers such as rCBV and rCBF partially predict the response to treatment. In another study, the authors introduced a novel biomarker (vascular normalisation index), which combines the DCE-MRI derived biomarker (K^{trans}) with microvessel volume and circulating collagen IV (serum biomarker), and found it to be predictive of overall and progression-free survival in the setting of anti-angiogenic therapy (Sorensen et al., 2009).

The functional parametric map (fPM), discussed above, is a relatively new concept that relies on measuring changes in single voxel values of measured parameters occurring over a short period during the early stages of treatment (Moffat et al., 2006) (Hamstra et al., 2008). Using careful coregistration of the tumours, measurement of the changes in single voxel parametric values can be acquired. Patterns of change in CBV and ADC have both been shown to have strong predictive value for response to treatment at a time when changes in mean/median values have not yet occurred (Hamstra et al., 2005) (Hirai et al., 2008) (Ellingson et al., 2010) (Sawlani et al., 2010).

2.5.3.5. Molecular characterisation with MRI

Recently there has been increasing emphasis on identifying the molecular and genetic features of glial tumours and incorporating them into tumour classification. This is becoming increasingly important, as specific mutations are increasingly being identified as independent prognostic factors capable of predicting treatment outcomes.

A few conventional MRI features, such as enhancement, necrosis and oedema, are known to be associated with poor outcome (Pope et al., 2005). Recently, there has been considerable interest in attempting to correlate these and other MR imaging features with relevant molecular and genetic features (Pope et al., 2008). In clinical practice, the most relevant mutations include 1p/19q co-deletion in oligodendroglioma tumours and the *IDH1* mutation and *MGMT* promoter methylation in GBM.

The co-deletion of 1p/19q in oligodendrogliomas is associated with improved response to chemoradiotherapy and improved outcome (Felsberg et al., 2004) (Walker et al., 2005). Certain conventional MRI features have been associated with 1p/19q co-deletion, including indistinct tumour borders on T1W and T2W images and heterogeneous signal intensity on T2 (Jenkinson et al., 2006a).

Texture analysis is an emerging imaging analysis approach that has been gaining increasing interest in recent years. It involves applying a post-processing step, which can be performed on MR images, in order to extract textural features of an image. Currently, the use of texture analysis remains largely limited to the research settings.

A study demonstrated that textural analysis of the T2 signal can predict co-deletion of 1p/19q with a sensitivity of 93% and specificity of 96% (Brown et al., 2008). Advanced MRI techniques such as PWI have also been used in similar studies, and co-deletion of 1p/19q is associated with higher rCBV as measured by DSC-MRI (Jenkinson et al., 2006b). Other advanced MRI imaging techniques such as MR spectroscopy have proven less promising in isolation but can be helpful if combined with perfusion imaging (Chawla et al., 2013).

An important gene mutation occurs at the active site of isocitrate dehdrogenase-1 (*IDH1*); this mutation has been implicated in gliomagenesis and is a feature of

secondary but not primary GBM (De Carli et al., 2009) (Nobusawa et al., 2009). Furthermore, a mutation in the IDH1 gene in patients with GBM and anaplastic astrocytoma is associated with improved survival (Yan et al., 2009). Conventional MR features may help in predicting *IDH1* mutational status. One study showed that GBM tumours harbouring the *IDH1* mutation are more likely to be located in the frontal lobe and to have a significant non-enhancing tumour volume (Carrillo et al., 2012). Similarly, grade II and III glioma tumours harbouring the *IDH1* mutation were found to be more likely to be located in a single lobe and to have less contrast enhancement (Qi et al., 2014). Low-grade gliomas that lack the *IDH* mutation tend to be larger in volume and demonstrate more infiltrative behaviour when compared with tumours having the *IDH* mutation (Metellus et al., 2010).

IDH1 mutations are associated with the production of 2-hydroxyglutarate (2-HG), which can serve as potential biomarker for differentiating between primary and secondary GBM as well as for monitoring treatment response. Unfortunately, serum levels of 2-HG are very low and cannot be detected clinically. Multiple researchers, however, have successfully employed 3T MR spectroscopy to detect 2-HG in glioma patients (Andronesi et al., 2012) (Pope et al., 2012). Whether 2-HG levels correlate with treatment response, tumour aggressiveness, or other correlates of malignancy remains to be determined.

Methylation of the *MGMT* repair enzyme is another important molecular feature of GBM; it is associated with improved response to TMZ therapy and improved survival (Hegi et al., 2004). A number of attempts to correlate MRI features with the status of the *MGMT* gene have been made. Several studies have reported that the pattern of enhancement in a tumour could reflect the underlying genetic status, with ring enhancement favouring an unmethylated *MGMT* promoter (Drabycz et al., 2010). It was also suggested that limited oedema is associated with improved prognosis in tumours with *MGMT* methylation (Carrillo et al., 2012). The results regarding tumour location are less convincing, with different studies suggesting different lobar predilection (Eoli et al., 2007) (Drabycz et al., 2010) (Ellingson et al., 2012).

Advanced MR imaging techniques have also been used in attempt to predict the *MGMT* promoter status of GBM tumours, but the results appear to be inconsistent. For instance, by using DWI and performing a 2-Gaussian curve fit of the histogram data from the enhancing component of GBM, a low median ADC of the lower curve that appeared to be associated with *MGMT* promoter methylation and better outcomes was

reported. However, this finding was not replicated in other studies using more clinically available analysis techniques based on the overall median ADC value (Moon et al., 2012) (Gupta et al., 2013) (Ahn et al., 2014). Similarly, rCBV measurements using DSC-MRI have yielded contradicting results, with some studies suggesting that *MGMT* methylated tumours have higher rCBV (Ryoo et al., 2013), and others not reproducing this finding (Moon et al., 2012). A recent study using DCE-MRI suggested that higher permeability, as measured by K^{trans}, is associated with *MGMT* methylated tumours (Ahn et al., 2014).

Although most of these studies were retrospective and looked at a relatively small number of patients, they highlight the potential role of novel non-invasive imaging biomarkers in predicting the molecular and genetic profile of glioma tumours. It is clear that further studies using larger cohorts are required before results can be translated into routine clinical practice.

2.5.4. Positron emission tomography for gliomas

2.5.4.1. Principles of positron emission tomography

PET is a molecular imaging technique that requires intravenous administration of a chemical in tracer amounts and its accumulation in the body is detected and quantified. Chemical tracers that bind to specific structures (receptors) or specific physiological process are usually preferred and referred to a ligand. The tracer or ligand is then labelled with a positron-emitting radioisotope to generate radiotracers and radiligands, for example ^{11}C, which has a $t_{1/2}$ of approximately 20 minutes. Other radioisotope with longer $t_{1/2}$, such radiolabelled Zicronium (^{89}Zr) that has a $t_{1/2}$ of 78.41 hours, are available but their clinical applications remain limited.

As the isotope decays, the positrons emitted collide with nearby electrons leading to the annihilation of both particles and the release of a pair of photons that travel in almost anti-parallel directions (Figure 2.1). The coincident detection of this photon pair by γ-detectors placed on opposite sides of a test subject allows the annihilation event to be recorded, and thus the spatial distribution of the radio-ligand to be reconstructed.

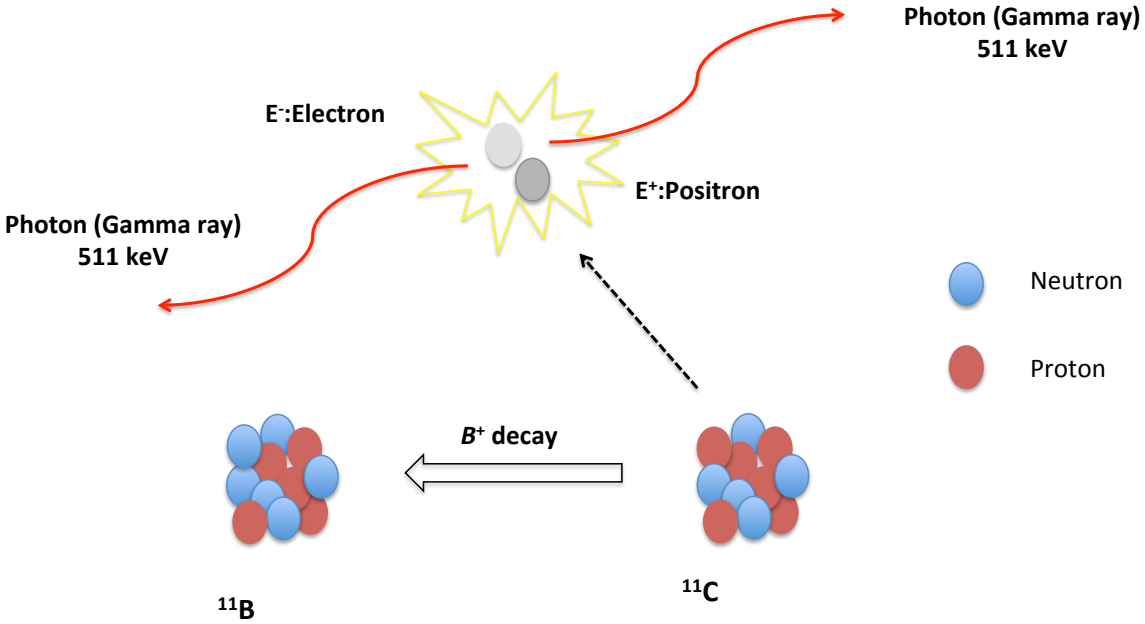

Figure 2. 1: Illustration of positron decay using ^{11}C as an example.

The introduction of tomographic techniques and PET scanners with a ring of detectors further improved the detection of photon emission. Furthermore, PET images can be co-registered with anatomical structural images obtained from a different imaging technique (MRI or CT), enabling the direct registration of the spatial distribution detected by PET onto the relevant structural anatomy. PET is now a well established clinical and research tool that can be utilised to investigate physiological functions, and not just as structural imaging tool.

2.5.4.2. Role of positron emission tomography in the management of gliomas

Over the last decade, there has been a substantial increase in studies reporting the utility of PET in the management of gliomas. PET imaging techniques can provide insight into a specific metabolic or molecular process by using designated radiotracers to target certain oncogenic pathways. In keeping with the advanced MRI techniques, PET has been evaluated for grade assessment, treatment planning, response prediction and treatment assessment.

Radiolabelled amino acids demonstrate high uptake in biologic active tumour tissue and low uptake in normal brain and have been of particular interest for the identification of brain tumour extent. The radiolabelled amino acids commonly used in clinical studies are methyl-^{11}C-L-methionine (MET), 3,4-dihydroxy-6-[^{18}F]-fluoro-L-phenylalanine (FDOPA) and ^{18}F-fluoroethyltyrosine (FET). Although it was originally postulated that amino acid uptake was related to increased proliferative activity in tumour cells, detailed pharmacokinetic analysis using L-2-^{18}F-fluorotyrosine showed that increased uptake in gliomas is caused by an increase in transport at the blood brain barrier (Wienhard et al., 1991). Increased uptake is present in most LGGs, despite apparently intact blood brain barriers. In high-grade glioma tumours, passive diffusion also contributes to amino acid uptake (Roelcke et al., 1996). Recent work has demonstrated that methionine uptake correlates closely with cell density. Despite this, there is clear evidence that methionine uptake can be low, even in the presence of significant tumour cell burden (Arita et al., 2012). MET-PET has been extensively studied as a diagnostic modality, grading tool, prognostic indicator and indicator of tumour extent for RT planning (Glaudemans et al., 2013). With tumour delineation using MET-PET, tumour volume definition was improved in 88% of low-grade and

78% of high-grade tumours (Sato et al., 1999) and the spatial extent of increased uptake was larger than seen with MRI in approximately 70% of cases and equal in the remaining 30% (Voges et al., 1997).

The use of ^{18}F-FET has gained significant popularity for clinical applications because of the longer half-life of the ^{18}F label. FET-PET, combined with MRI, improves the therapeutic assessment of patients with gliomas for both neurosurgery and RT planning. In histologic correlation studies comparing stereotactic brain biopsies to MRI and FET-PET, MRI had a sensitivity of 96% for detecting tumour tissue but a specificity of only 53%, while the combination of MRI and FET-PET yielded a sensitivity of 93% and a specificity of 94% (Pauleit et al., 2005). FET-PET has been studied as an indicator of post-surgical residual tumour volume and was found to have a strong prognostic impact on both overall survival and disease-free survival that was not demonstrated by tumour volume assessed using gadolinium-enhanced MRI (Piroth et al., 2011). However, a combination of MR and FET-PET adapted dose escalation in GBM, with a total dose of 72 Gray based on FET-PET, did not lead to any survival benefit, although no increase in acute or late toxicity was identified (Piroth et al., 2012). The exact cause for the failure of this approach is not clear. Interestingly, tumour recurrence patterns were very similar to a second prospective study that utilised FET-PET for treatment planning and showed improved outcome although it included lower numbers. A potential explanation is that a small volume of tumour cells, not reliably detected with PET, could have microscopically invaded beyond the detected radiological abnormality, and therefore was not included in the planned treatment field. Further studies are early needed before a definite conclusion can be made.

More recently, Kinoshita et al. developed a novel image analysis method using ^{18}F-FDG and MET-PET scans that allows for detection of tumour cell densities greater than 1,000/mm^2, with a sensitivity and specificity of 93.5% and 87.5%, respectively (Kinoshita et al., 2012).

FDOPA PET has been used to distinguish true progression from pseudoprogression. In a study looking at 110 glioblastoma patients, FDOPA PET achieved a diagnostic accuracy of 82% for this purpose (Herrmann et al., 2014). FDOPA PET also shows utility for identifying bevacizumab treatment failure prior to MRI-based RANO criteria and for predicting a favourable outcome following bevacizumab treatment

(Schwarzenberg et al., 2014). FDOPA PET also appears to be superior to FDG PET for assessing low-grade tumours for recurrence and distinguishing a tumour from radiation necrosis (Chen et al., 2006).

A high rate of cellular proliferation is a key feature of gliomas and other malignant tumours. Use of a thymidine analogue (3Ľdeoxy-3Ľ-^{18}F-fluorothymidine; FLT) provides high tumour-to-brain uptake ratios. FLT is a tracer that does not cross the BBB efficiently (Dohman et al., 2000) (Bendaly et al., 2002) but its uptake in gliomas has been shown to correlate closely with tumour grade and also provides significant prognostic information (Harris et al., 2012), with tumours that demonstrate higher proliferation resulting in shorter overall survival. FLT is a thymidine analogue, which reflects the activity of thymidine kinase-1. When FLT is phosphorylated by thymidine kinase-1 it leads to the intracellular entrapment of radioactivity; this process which is independent of the BBB.

2.6. Drug resistance in glioma tumours

Prognosis remains poor for patients with high-grade brain tumours despite the increasing list of chemotherapy agents used in the their treatment. The high failure rates encountered with chemotherapy have been largely attributed to the development of chemoresistance and the BBB. The development of chemoresistance is multifactorial and characterised by various complex molecular mechanisms, which enables tumour cells to develop a drug resistance phenotype. A summary of some of these mechanisms and some of the drugs involved is provided in Table 2.3.

Furthermore, brain tumours represent a unique challenge due to the presence of the BBB, as opposed to other systemic tumours, which prevents the delivery of effective chemotherapy. Efflux transporters are expressed by the BBB as well as glioma cells and as such have been implicated in limiting drug delivery as well as chemoresistance.

Table 2. 4: Some of the commonly implicated molecules in the development of drug resistance in patients with brain tumours.

Molecules	Drugs
MGMT	Temozolomide, Procarbazine, Dacarbazine, Nimustine, Carmustine, lomustine,fotemustine,
PKC	Vincristine, Etoposide, Teniposide, Carboplatne, Cisplatin, Nimustine, Carmustine, lomustine,
GSH/GST	Carboplatne, Cisplatin, Cyclophosphamide, Ifosfamide, Carmustine,
Efflux transporters MRP and P-gp	Vincristine, Etoposide, Teniposide

Abbreviations: MGMT: O6-methylguanine-DNA methyltransferase. PKC: protein kinase C, GSH/GST: reduced glutathione/glutathione-S-transferase. MRP: multidrug-resistance associated protein.

Imaging is the main modality used in the evaluating disease progression and response to a therapeutical intervention. As detailed previously, imaging relies on various imaging biomarkers that can be employed as secondary surrogate markers for the determining the success or failure of a particular treatment approach. None of the currently used imaging modalities in clinical practice allow for direct visualisation of drug delivery into the CNS and tumour microenvironment. Saleem et al successfully employed PET imaging to demonstrate *in-vivo* activation of TMZ in patients with brain tumours (Saleem 2003). Such imaging methods that can non-invasively demonstrate drug delivery and any changes in it, are clearly appealing and of paramount clinical importance.

2.7. Conclusions

The indications for, and utility of, imaging in the management of patients with brain tumours continues to expand. The combination of imaging and genetic markers has

furthered our understanding of tumour biology and behaviour, linking the microscopic and macroscopic levels. Quantitative and physiologic markers from advanced MRI have been increasingly validated as problem solving tools for identifying pseudoprogression, pseudoresponse and non-enhancing tumours. The integration of non-FDG PET with advanced MRI will improve our ability to accurately assess disease burden. Predictive and early response markers predicated on these techniques are areas where imaging may have a substantial impact on drug selection and other aspects of patient treatment, thereby improving patient outcomes.

Chapter 3 Blood-brain barrier: an overview

3.1. Introduction

Malignant brain tumours are one of the most devastating diagnoses in clinical practice, contributing to 2% of all cancer deaths. GBM represents the most aggressive subtype and is characterised by extensive mitosis, diffuse infiltration, neo-vascularisation and necrosis (Kleihues et al., 1993). Despite aggressive treatment approaches using a combination of surgery, radiation and chemotherapy, these tumours carry an extremely poor prognosis (Brodbelt et al., 2015). Furthermore, it is now known that all GBM tumours recur regardless of treatment approach, ultimately leading to patient demise (Wen and Kesari, 2008).

A possible contributing factor to the poor treatment outcome of GBM could be the BBB, which has been implicated as one of the major obstacles to effective chemotherapy delivery (Pardridge, 2005). In the last few decades, excellent progress has been made in understanding the structure and function of the BBB in both health and disease. This, in turn, should enable the enhancement of therapeutic strategies that target and modulate certain features of the BBB, leading to improved clinical outcomes.

3.2 Historical aspects

The first discovery relating to the BBB dates back to the late 19th century, around 1885, when German scientist Professor Paul Ehrlich first described the lack of brain staining following injection of dye into the peripheral vasculature, in contrast to the rest of the bodily organs. Ehrlich himself attributed this to an inherently low affinity of the brain for various dyes (Saunders et al., 2014).

The BBB concept and term as we know is believed to have been first introduced in 1900, when Lewandowsky observed that a lethal level of cocaine in animals can be achieved at much smaller levels when administered directly via the cerebrospinal fluid (CSF) rather than the systemic route (Saunders et al., 2014). This was shortly followed

by a further discovery in 1913, when Edwin Goldmann, a student of Paul Ehrlich, observed that the brain (with the exception of the choroid plexuses) was not stained following intravenous injections of Trypan blue. However, when the dye was injected directly into the CSF, it resulted in homogenous brain staining (Saunders et al., 2014).

Later, with the introduction of electron microscopy in the 1950s, Reese and Karnovsky localised the tight junctions (TJ) at the endothelium of the brain microvasculature (Reese and Karnovsky, 1967). They demonstrated that systematically administered horseradish peroxidase, a small enzymatic tracer, could not pass beyond the clefts of neighbouring endothelial cells. They also postulated the presence of metabolic pumps at the tight endothelial junctions that could allow for nutrients to enter the brain. This was probably one of the earliest descriptions that changed the perception of the BBB from a rigid structural barrier to its more dynamic and active reality.

3.3. Anatomy of the blood-brain barrier

The BBB is mainly composed of brain endothelial cells, astrocytes, pericytes and the basement membrane. The neurovascular unit (NVU) is a term used to reflect the intimate anatomic and functional relationship between these structures, which allows the BBB to carry out its functions (Figure 3.1) (Abbott, 2002) (Hawkins and Davis, 2005) (McCarty, 2009).

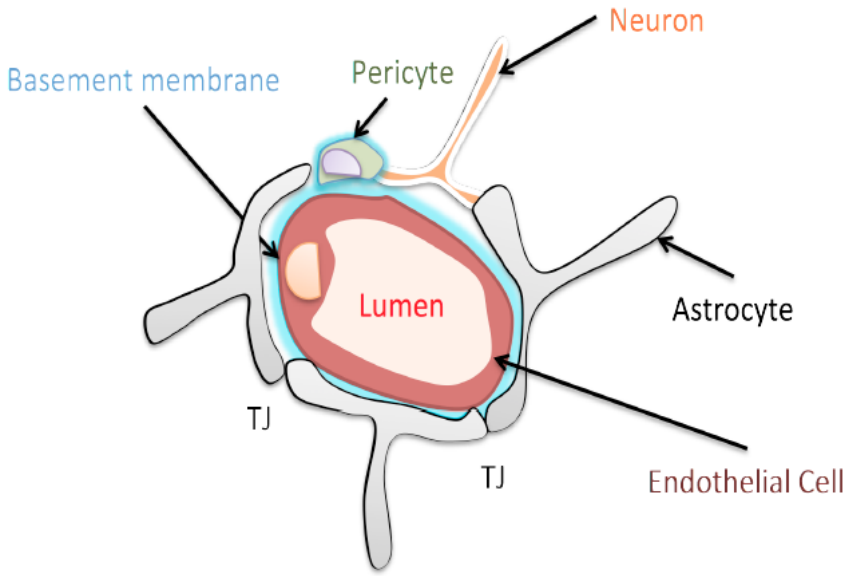

Figure 3. 1: Cellular components of the neurovascular unit. Adapted from (Abbott, 2002).

Brain endothelial cells (BECs) are considered the main contributor to the diffusion barrier properties of the BBB. BECs have specific structural and functional features that differ from the capillary endothelial cells present elsewhere in the body. They exhibit an increased number of mitochondria (Oldendorf et al., 1977) and TJ (Brightman and Kadota, 1992) and a scarce number of vesicles, resulting in a reduced rate of transcytotic activity (Nico and Ribatti, 2012).

Astrocytes are glial cells that are intimately associated with the endothelial cells; their astrocytic end feet cover more than 90% of the endothelial cell surface area (Hawkins and Davis, 2005). However, the exact mechanisms by which astrocytes help maintain BBB function remain a matter of debate. Extensive *in-vitro* and *in-vivo* studies have demonstrated the importance of astrocytes in maintaining BBB characteristics such as the induction of TJ formation in non-brain endothelia and their ability to decrease the permeability of endothelial cell monolayers *in-vitro* (Janzer and Raff, 1987) (Siddharthan et al., 2007). On the other hand, other studies have suggested that astrocytes are not essential for the maintenance of BBB function (Willis et al., 2004a) (Willis et al., 2004b). These conflicting findings have led some authors to suggest that astrocytes may well be implicated in inducing and maintaining the BBB's phenotypic features but that their exact role remains less well understood.

Pericytes are an integral component of the BBB, maintaining an intimate anatomical and functional relationship with the other cellular components of the neurovascular unit (Allt and Lawrenson, 2001). Multiple studies point to the role of pericytes in establishing the BBB's function, including the provision of mechanical support and role in modulation of transport (Nico and Ribatti, 2012).

The basement membrane, an important part of the NVU, comprises a heterogeneous mixture of proteins organised in a three-layer configuration. These proteins include structural proteins (mainly collagen type 4 and elastin), specialised proteins (fibronectin and laminin) and proteoglycans (Wolburg and Lippoldt, 2002). The adjacent endothelial cells, neurons and glial cells express complex matrix adhesion receptors and cell adhesion molecules (CAMs), which allow for extensive interaction with the basement membrane (Del Zoppo et al., 2006). Many diseases affecting the basement membrane, including glioblastoma tumours, result in increased BBB permeability (Rascher et al., 2002).

The role of neurons in maintaining the functional properties of the BBB is not completely understood. Recent studies have demonstrated the ability of neurons to alter BBB function. For example, Persidsky showed that neurons help regulate the blood supply to the neurovascular unit in response to metabolic changes in the endothelial cells (Persidsky et al., 2006). More recently, Minami demonstrated improved transendothelial electrical resistance (TEER) and barrier function when neurons where included in *in-vitro* BBB models, with co-culture resulting in increased TEER and barrier function (Minami, 2011).

Furthermore, it is now clear that close interaction and cross talk between the endothelial cells and the different elements of the neurovascular unit help modulate and maintain the barrier function (Abbott, 2002).

3.4 Functions of the blood-brain barrier

The function of the blood brain barrier is to control exchange between the brain and the cerebral circulation. Specific functions include:

1. Maintenance of brain homeostasis by regulating central nervous system composition, restricting access of most macromolecules to the brain (Wolburg and

Lippoldt, 2002).

2. Regulating the supply of nutrients via a variety of specific transport mechanisms (Persidsky et al., 2006).

3. Protection of the brain from harmful neurotoxins, including endogenous metabolites present in the systemic circulation (Weiss et al., 2009).

Our understanding of the BBB has evolved and it is now regarded as an ultra-dynamic interface between the brain parenchyma and the surrounding cerebral circulation, with highly specialised structural and functional properties that regulate the neural microenvironment.

3.4.1. Structural barrier proprieties

Junctional complexes between adjacent endothelial cells of the BBB are formed by TJs and adherens junctions (AJs). TJs form the main components of the BBB; these limit the passive diffusion between endothelial cells and through capillaries. Freeze-fracture studies have revealed TJs to be areas of apparent fusion on the luminal aspect of endothelial cells (Brightman and Reese, 1969), with highly complex transmembrane and cytoplasmic protein strands (Wolburg and Lippoldt, 2002). These complex features of TJs appear to be responsible for the high TEER and reduced vascular permeability associated with the BBB (Wolburg et al., 1994).

3.4.2. Transport mechanisms in the blood-brain barrier

The more dynamic and metabolically active aspect of the BBB relies on dedicated polarised transport mechanisms present on the luminal and abluminal sides of brain endothelial cells. Various transport mechanisms are responsible for allowing the entry of nutrients, while others restrict the access of harmful compounds. The list of transporters in the BBB is extensive, but can be broadly divided into two main categories: solute carriers and non-solute carriers, which include the ATP binding cassette (ABC) transporters and ion pumps (Shen and Zhang, 2010).

3.4.2.1. Drug efflux and ATP binding cassette (ABC) transporters

Some members of the ABC superfamily of efflux transporters appear to play a major role in excluding drugs from the brain parenchyma (Borst and Elferink, 2002) (Schinkel and Jonker, 2003) (Nies, 2007). Currently, 49 transporters have been identified and are grouped into 7 different subfamilies referred to as A, B, C, D, E, F and G. These transporters transport an array of drug substrates via an ATP-dependent mechanism (Dean et al., 2001) (Borst and Elferink, 2002). It is now recognised that expression of different transporters also varies widely between species (Warren et al., 2009).

In clinical practice and in the management of brain tumours, the transporters most commonly implicated in reducing drug efficacy are P-glycoprotein (P-gp, ABCB1 or *MDR1*), breast cancer resistance protein (BCRP or ABCG2) and multidrug-resistance-associated proteins (MRPs, ABCCs) (Agarwal 2013).

This thesis will focus on the P-gp and BCRP transporters.

3.4.2.2. P-glycoprotein (MDR1 or ABCB1)

Juliano and Ling first discovered P-gp in a Chinese hamster ovary cell line (Juliano and Ling, 1976). This finding was later followed by the discovery of P-gp in the BBB (Cordon-Cardo et al., 1989). A wide range of compounds are reported to be P-gp substrates; they are not necessarily chemically related to one another and include a large number of chemotherapy agents such as doxorubicin and vincristine, explaining these drugs' limited use in the treatment of brain tumours (Tsuji, 1998). P-gp is mainly expressed on the luminal side of endothelial cells (Figure 3.2) but is also located on the astrocytic foot processes and the abluminal surface of the endothelial cells, albeit in very small numbers (Golden and Pardridge, 1999) (Abbott et al., 2010). This arrangement facilitates the efflux of compounds from the cytoplasm into the circulation, thus reducing access to the brain parenchyma.

3.4.2.3. Breast cancer resistance protein (BCRP, ABCG2)

Since its discovery in 1998 (Doyle et al., 1998), BCRP has been one of the most extensively studied transporters. Similar to all the G-subfamily of ABC transporters, and in contrast to P-gp, BCRP is regarded as a "half-transporter," possessing one transmembrane domain and one nucleotide-binding domain (Schinkel and Jonker, 2003). Like P-gp, BCRP is expressed on the luminal domain of cerebromicrovascular endothelial cells in the human BBB, facilitating the drug efflux function (Cooray et al., 2002). It also has broad substrate specificity, overlapping with P-gp; substrates include anticancer drugs used in the treatment of brain neoplasms, such as erlotinib (Shen and Zhang, 2010). These features suggest a close functional relationship between P-gp and BCRP in mediating drug efflux (Breedveld et al., 2006).

The locations of the P-gp and BCRP efflux transporters in the brain endothelial cells are shown in Figure 3.2.

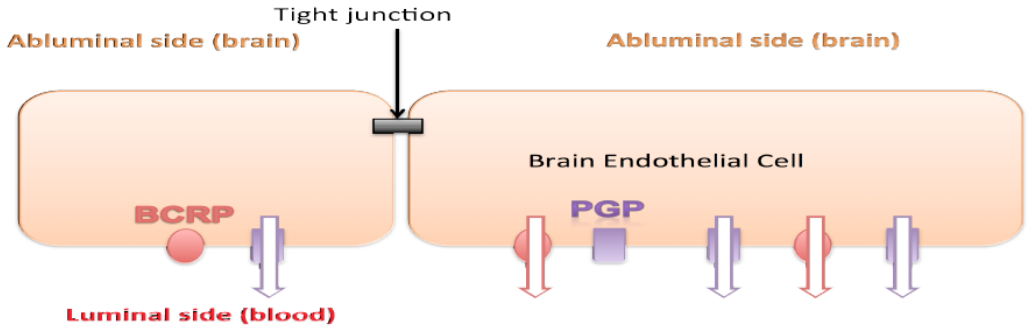

Figure 3. 2: Location of P-glycoprotein (PGP) and breast cancer resistance protein (BCRP) efflux transporters in the brain endothelial cell. Adapted from (Ribatti et al., 2006).

3.5. Blood-brain barrier status in high-grade gliomas

3.5.1. The blood-tumour barrier

Differences exist between the blood-tumour barrier (BTB) and the normal BBB. The BTB in high-grade gliomas such as GBM has been described as leaky, broken-down and even absent, with the morphological features of such tumoural vasculature described as early as 1970 (Long, 1970). These features include breakdown of the TJs with increased fenestration, increased numbers of mitochondria and increased thickness of the basal membrane accompanied by enlargement of the perivascular space (Long, 1970) (Hirano and Matsui, 1975). The end result of these changes is increased permeability corresponding to the contrast enhancement frequently seen in imaging (Steinhoff et al., 1978). In addition, there is a clear and direct association between the presence of those features, the grade of the tumour and BBB dysfunction. The higher the grade, the more apparent the morphological changes and the more severe the BBB dysfunction (Larsson et al., 1990). Such changes in permeability are variable and differ between the various tumour components, accounting for the heterogeneous enhancement patterns frequently encountered in clinical practice.

While the morphological changes affecting the BBB are well documented, the molecular changes responsible for this altered morphology are less clearly understood. Since TJs represent the main anatomic site for the physical properties of the BBB, researchers have tried to explore the molecular alterations that take place at this level (Liebner et al., 2000).

Other studies have focused on changes affecting the extracellular matrix (ECM) and its relation to the molecular components of TJs (Forsyth et al., 1999) (Groft et al., 2001) (Noell et al., 2012). More recently, another molecular component has been implicated in BBB dysfunction. Aquaporins are water channels present in astrocytes, with aquaporin-4 (AQP-4) being the most important (Papadopoulos et al., 2002) (Warth et al., 2004). In GBM and at the astrocyte end-feet contacting the basal lamina, increased expression of AQP-4 is found (Papadopoulos et al., 2001), although the full molecular mechanisms linking this finding with BBB dysfunction remain unclear.

3.5.2. P-glycoprotein and breast cancer resistance protein efflux transporter status in brain tumours

Many studies have examined ABC transporter expression in brain tumours, with the P-gp efflux transporter being the most widely investigated. For example, Toth et al. showed that P-gp was expressed by the new tumour-associated endothelial vasculature but not by the tumour cells themselves (Toth et al., 1996). Subsequently, Fattori et al. demonstrated increased P-gp expression in the tumour vasculature as well as in glioma cells (Fattori et al., 2007). These findings have been supported by others (Nabors et al., 1991) (von Bossanyi et al., 1997) (Demeule et al., 2001). Interestingly, numerous studies have failed to show any increase in P-gp expression in tumour cells (Spiegl-Kreinecker et al., 2002) (Decleves et al., 2002) (Fruehauf et al., 2006). Currently and despite these contradictory reports, the recent literature supports increased P-gp expression in glioma cells (Agarwal et al., 2011b). A possible explanation of the observed discrepancy in these studies is a heterogeneous expression of P-gp in brain tumours, which was observed in a study that contained small number of patients (Demeule et al., 2001).

The expression of P-gp as well as other proteins is collectively contributed to what is known as the multi-drug resistance (MDR) phenotype, which is one of the main mechanisms implicated in complex multi-drug chemoresistance (Loscher and Potschka, 2005b).

The BCRP efflux transporter has also gained increasing interest over the last few years. BCRP transporters have been linked directly to a side population of glioma cells, known as cancer stem cells, which are characterised by chemoresistance and increased BCRP expression (Dean et al., 2005). Using Hoechst, a high affinity BCRP substrate, Bleau et al. identified this side population of glioma cells and found increased ABCG2 expression on their plasma membranes (Bleau et al., 2009). Doyle and Zhou also reported similar results of increased BCRP expression in tumours (Zhou et al., 2001) (Doyle and Ross, 2003). Additionally, Zhang et al. demonstrated upregulation of BCRP expression in GBM vessels and adjacent parenchymal brain tissues (Zhang et al., 2003).

These studies suggest an apparent differential expression of both P-gp and BCRP

efflux transporters in brain tumours. However, the clinical impact of such expression patterns remains unclear.

Changes affecting the BBB in brain tumours are illustrated in Figure 3.3.

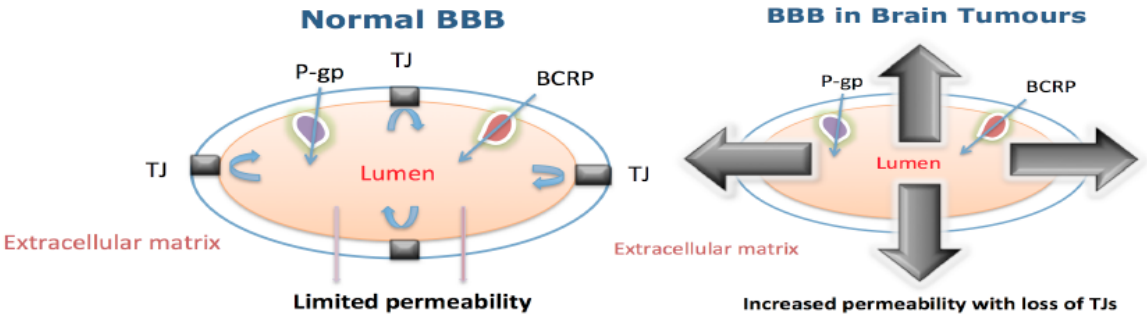

Figure 3. 3: The normal blood-brain barrier and the blood-brain barrier status in high-grade brain tumours. Adapted from (Agarwal et al., 2011a).

3.6. Chemotherapy and brain tumours

3.6.1. Chemotherapy and brain tumours

The BBB in the presence of a high-grade glioma is known to be dysfunctional. An important reflection of this compromised state is the concentrations of systematically administered drugs achieved within tumour tissues. A recent review article by Pitz et al. identified 18 studies that measured the concentrations of anticancer drugs in high-grade gliomas using surgical tissue sampling and microdialysis. These studies indicate that systematically administered anticancer drugs reach higher concentrations in the tumour core when compared to the tumour periphery (Pitz et al., 2011). These findings reflect the complex angiogenic process taking place in the tumour core, creating a leaky BBB (Jain et al., 2007), and the relatively more preserved barrier function at the growing edge of the tumour (Gilbertson and Rich, 2007). This is illustrated in Figure 3.4.

Figure 3. 4: Hypothetical demonstration of chemotherapy delivery in brain tumours. Region 1: Tumour core usually resected surgically. Region 2: Boundary of surgical resection. Region 3: Tissue surrounding the tumour core including normal brain tissue, which is not amenable to surgical resection and where tumour cells could reside.

High-grade glioma tumours such as GBM are characterised by invasive spread, which is a major factor preventing curative surgical resection. This invasive nature has resulted in acceptance of the fact that, at the time of GBM diagnosis, tumoural cells have likely already spread to various areas of the brain, which may even appear macroscopically normal via conventional imaging techniques (Giese et al., 2003).

TMZ became the main chemotherapeutic agent used in the treatment of newly diagnosed GBM following the introduction of Stupp therapy. Stupp et al. demonstrated an improved median survival time of 14.6 months using combined radiotherapy and TMZ versus a 12.2-month survival time with isolated radiotherapy (Stupp et al., 2005).

TMZ is an orally administered DNA alkylating agent of the imidazotetrazine family.

TMZ has excellent features such as high oral bioavailability due to stability in acidic conditions with rapid absorption achieving peak plasma concentrations in less than two hours (Baker 1999). It has also been shown to effectively penetrate the BBB (Baker 1999) (Saleem 2003). Despite this, it is important to remember that TMZ can only reach the CNS microenvironment in limited concentrations with previous neuropharmacokinetics studies showing a mean brain TMZ to plasma AUC ratio of

approximately 20%. This was seen in patients whom underwent microdialysis from peri-tumoural regions as well as CSF sampling (Ostermann 2004) (Synold 2009).

TMZ is a prodrug that is stable at acidic pH but when at alkaline pH spontaneously hydrolyses into the active component monomethyl triazene 5-(3-methyltriazen-1-y1)-imidazole-4-carboxamide (MTIC) (Denny et al., 1994). This is a particularly favourable feature, as brain tumours appear to have a higher pH than the surrounding normal tissue at the intracellular level (Rottenberg et al., 1984) (Vaupel et al., 1989). MTIC breaks down further into the inactive compound 5-aminoimidazole-4-carboxamide (AIC) and the active methyldiazonium cation responsible for cytotoxicity (Zhang et al., 2012). The active methyldiazonium cation methylates DNA at the N7 guanine, N3 adenine and O6 guanine positions to variable degrees (Tisdale, 1987) (Denny et al., 1994). There are multiple well-documented DNA repair mechanisms contributing to TMZ resistance; these include direct repair via the enzyme methylguanine-DNA methyltransferase (MGMT), DNA mismatch repair and base excision repair (Zhang et al., 2010) (Zhang et al., 2012). TMZ breakdown is depicted in Figure 3.5.

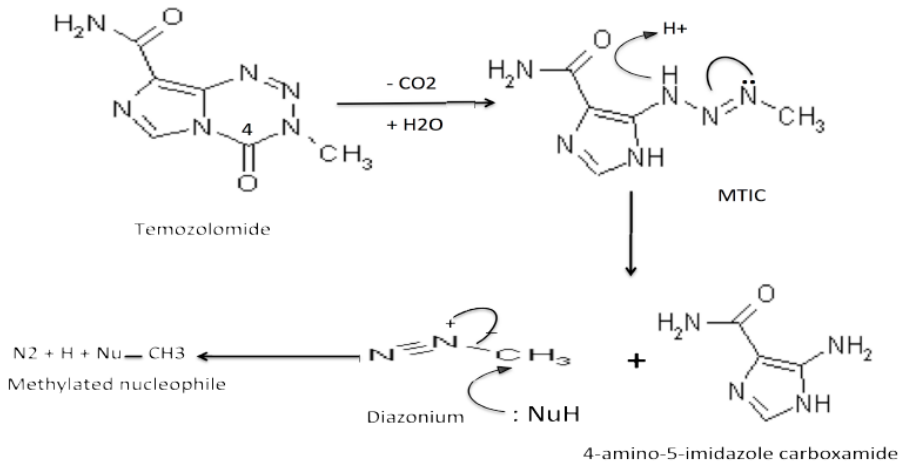

Figure 3. 5: Mechanism of temozolomide breakdown. Reproduced from (Villano et al., 2009).

3.6.2. Strategies for enhancing drug delivery

Oral and intravenous administrations are the classical routes for delivering therapeutic drugs when treating CNS pathologies. TMZ is a small lipophilic molecule and it

thought to cross the BBB (Newlands et al., 1997), many other chemotherapeutic agents lack the characteristics of TMZ, and therefore exhibit limited penetration into the CNS. As such, different strategies have been employed in an effort to circumvent the BBB and enhance the delivery of these agents. Some of the most commonly used methods are reviewed here.

3.6.2.1. Intra-arterial administration

The main concept behind intra-arterial administration of chemotherapy is that higher concentrations of the drug can be delivered directly to the tumour when compared with the intravenous route. This enables the use of lower doses to achieve similar local drug concentrations, which in turn reduces the systematic side effects (Yamada et al., 1987). The use of this approach has been evaluated in clinical studies (Fine et al., 1993) (Larner et al., 1995). Survival benefit, however, was not observed (Shapiro et al., 1992), and two further randomised clinical studies showed no significant improvement in outcome (Kochii et al., 2000) (Imbesi et al., 2006). These studies reported toxicity-related side effects. Furthermore, intra-arterial delivery requires conventional angiography to navigate the catheter to the appropriate feeding vessel. This is an invasive procedure, and as such is associated with risk factors such as stroke, infection and haemorrhage.

3.6.2.2. Intrathecal administration

Intrathecal administration bypasses the BBB by direct administration into the CSF space via various apparatuses (Bakhshi and North, 1995). Drugs administered intrathecally should be in their active form; this is best used in the treatment of tumours that line the CSF spaces, such as leptomeningeal tumoural seeding seen in glioblastoma tumours (Dardis et al., 2014), with methotrexate being one of the most widely used agents (Pinkel and Woo, 1994). One of the main limiting factors is the need for access to the CSF. Multiple methods have been used to achieve access, including repeated lumbar punctures and catheter placements (either into the ventricles or lumbar CSF spaces). All of these procedures are invasive and carry risks, including infection, haemorrhage and catheter malfunction (Chamberlain et al., 1997). Finally,

this method of administration has been proven ineffective in the treatment of brain tumours involving the parenchyma (Siegal and Zylber-Katz, 2002).

3.6.2.3. Direct tumoural delivery

The surgical implantation of biodegradable material containing a chemotherapeutic agent such as cisplatin and paclitaxel directly into the tumour has also been evaluated (Sheleg et al., 2002) (Vukelja et al., 2007). An example of such an approach is the use of Gliadel wafers, which consists of biodegradable materiel containing chemotherapy agent (carmustine). Brem et al. confirmed the efficacy of Gliadel wafers in a double-blinded study in 222 patients that showed improved overall survival, approximately 8 weeks, in patients with recurrent GBM whom received Gliadel in comparison to a placebo (Brem 1995).

Whilst this method avoids the BBB, it is clearly invasive and confers significant surgical risk. Furthermore, drug administered via this route relies on passive diffusion to reach the surrounding brain parenchyma, which in turn limits the drug's ability to reach tumour cells that are slightly distant from the implant (Strasser et al., 1995). The use of these devices remains limited in clinical practice.

3.6.2.4. Blood-brain barrier disruption

Mechanical disruption of the BBB has also been used; it is usually achieved by selective guidance of an intra-arterial catheter into the vessel feeding the tumour, which is then followed by administration of a hyperosmolar solution and the chemotherapeutic agent. Mannitol is one of the most widely employed osmotic agents; it causes disruption of the TJs, leading to increased permeability (Kroll and Neuwelt, 1998) (Zlokovic and Apuzzo, 1998). Enhanced, multiple-fold drug delivery has been established by this method (Miller, 2002). The major drawbacks of his procedure are the need for general anaesthesia and the risk associated cerebral angiography, possibly accounting for its limited use in clinical practice.

Other less invasive methods for disrupting the BBB are also under investigation. Focused ultrasound has been successfully utilised to cause temporary and reversible opening of the BBB in various preclinical in-vivo studies (Wang et al., 2009) (Huang et al., 2016). This method is currently under investigation in a clinical trial.

It is important to remember that to date, no randomised clinical studies have shown the BBB disruption approach to be effective.

3.6.3. Methods for measuring drug delivery to the brain

One of the main functions of the BBB is to restrict the entry of neurotoxins, including therapeutic drugs, into the CNS microenvironment. The consequences of this are well reflected by the large number of newly developed drugs that do not progress to clinical practice due to their poor ability to cross the BBB (Banks, 2009). Despite the disrupted status of the BBB in GBM, it is necessary to establish the ability of systematically administered therapeutic agents to gain access to the brain and tumours tissues. Additionally, many glioblastoma patients receive steroid treatments, which can reverse some of the BBB dysfunction. This partial reversal of dysfunction may well alter the ability of other drugs to penetrate the BBB (Claes et al., 2008).

Ideally, BBB function would be evaluated by measuring the concentration of a given drug in the brain and tumour tissues. Variable direct and indirect methods have been used to measure drug concentration in the brain and tumours in humans. Some of the most common methods are discussed below.

3.6.3.1 Direct sampling

Surgical sampling, either by biopsy or resection, enables the direct measurement of drug concentrations in the sampled tissue. Clearly, this is a highly invasive approach that should only be considered when tissue sampling is indicated clinically. Another important limiting factor is that these measurements reflect the concentration of a drug at a certain time point only and fail to provide any insight into the drug concentration in the adjacent tissues, where most tumour recurrence tends to occur.

An alternative direct method is micro-dialysis, which involves positioning small catheters into the desired targets. These catheters have semipermeable membranes that facilitate the sampling (Zhou and Gallo, 2005). This method is superior to surgical tissue sampling because it allows for sampling at different time points. Additionally, targets can be chosen to include tumour tissue as well as adjacent brain tissue. However, this technique remains technically demanding and invasive, requiring

surgery (Blakeley, 2008).

3.6.3.2 Indirect sampling

Drug levels in the CSF have been used as a surrogate marker for drug concentration in brain tissue. However, this method is not ideal, as it reflects the function of the blood-CSF barrier and not the BBB (Collins and Dedrick, 1983) (Pitz et al., 2011). Furthermore, there are important differences between plasma and CSF, such as lower pH in the CSF, which may affect drug breakdown, and lower protein concentration in the CSF, which may affect the amount of free drug (i.e. non-prtoein bound drug) available to interact at the target site. Finally, while CSF sampling by lumbar or ventricular access apparatus is safer than a surgical-based approach, it remains an invasive medical procedure with its own significant risks.

Until recently, imaging has been used as a biomarker to monitor disease response to therapy. Both conventional and more advanced MR imaging techniques have been utilised in this field. Such advanced imaging techniques provide useful biomarkers that are helpful in assessing responses to therapies, which may lead to changes in the BBB permeability (Provenzale et al., 2005) (Dhermain et al., 2010). Ultimately MR imaging techniques are well equipped to study the BBB permeability to a contrast agent but fail to provide any insight into the delivery of a systemically administered agent.

PET has also been successfully implemented for imaging GBM tumours (Bruehlmeier et al., 2004) (Swanson et al., 2009) (Dhermain et al., 2010). PET's main advantage over MRI is its ability to study the uptake of a particular drug by radiolabelling it as opposed to the secondary information on BBB permeability provided by MRI (Josserand et al., 2006) (Pike, 2009). For example, various clinical studies have utilised invasive sampling techniques to demonstrate increased TMZ concentration within the tumour core in comparison to the surrounding tissues (Pitz et al., 2011). This was also non-invasively demonstrated by Rosso et al., who used radiolabelled TMZ and PET to show higher TMZ uptake by the tumour core in comparison to the adjacent brain tissue (Rosso et al., 2009).

It is also important to remember that PET imaging is not without limitations. PET requires concurrent blood sampling, typically arterial, in order analyse using kinetic

models to estimate representative physiological cerebral parameters (Upton, 2007) (Pike, 2009). Beside other practical issues such as the need for expertise and a cyclotron on site, the only major scientific disadvantage of PET is its inability to differentiate between the drug administered and its radiolabelled metabolites (Upton, 2007).

3.6.4. Efflux transporters: a potential solution

For any anticancer drug to be effective in the treatment of glioma, it will need to achieve therapeutic concentrations in the tumour as well as in the surrounding areas where the BBB is intact but tumour cells are likely to have infiltrated. P-gp and BCRP are two efflux transporters that appear to work in tandem to drive efflux of many chemotherapeutic agents. For example, Polli et al. demonstrated a synergic effect achieved by dual P-pg and BCRP transporter knockout in mice, which increased brain uptake of a tyrosine kinase inhibitor (Lapatinib) when compared to both single transporter knockouts (Polli et al., 2009). De Vries et al. reported similar results for the anticancer drug topotecan (de Vries et al., 2007). Several studies have confirmed these findings with various anticancer drugs that are dual P-gp and BCRP substrates. This compensatory and mutual efflux mechanism of the P-gp and BCRP substrates probably explains the failure of tyrosine kinase inhibitors in clinical trials.

A summary of some of these studies is presented in Table 3.1. Examples of dual substrates and the effects of dual transporter inhibition are presented in Table 3.2.

Table 3. 1: Efflux transporters and anticancer drug substrates.

Transporter	Anticancer agent
P-glycoprotein	Doxorubicin, Epirubicin, Danorubicin, Docetaxel, Paclitaxel, Vinblastine, Vincristine, Etoposide, **Methotrexate**, **Topotecan**, **Sorafenib**, **Lapatinib**, **Mitoxantrone**
Breast Cancer Resistance Protein	Imatinib, Eriotinib, Gefitinib, **Methotrexate**, **Topotecan**, **Sorafenib**, **Lapatinib**, **Mitoxantrone**

Agents highlighted in bold reflects their dual P-gp and BCRP substrate status.

Table 3. 2: Effects of dual P-glycoprotein and Breast cancer resistance protein inhibition on the brain uptake of some anticancer drugs

Drug	Fold increase with P-gp KO	Fold increase with BCRP KO	Fold increase with Dual KO
Toptecan	1.5	1.5	12
Sorafenib	1	4	12
Lapatinib	4	1	42.5
Mitoxantrone	1.7	1.4	8

Fold increase represent the brain-to-plasma ratio in genetically transporter knockout (KO) mice in comparison to wild type animals. Adapted from (Agarwal et al., 2011a).

Furthermore, there has been increasing interest in the role of the ABC transporters in mediating resistance to anticancer drugs in GBM. However, while many studies have examined the role of P-gp and BCRP in mediating the efflux of a wide variety of anticancer drugs, very few studies have attempted to evaluate their relationship with TMZ directly.

For example, Ma et al. established a TMZ-resistant human glioma cell line (SF188-TR) by employing continuous TMZ exposure over a 6-month period. Subsequently, the authors found no significant difference between the TMZ-sensitive (SF188) and TMZ-resistant human glioma cell lines (SF188-TR) in the intracellular accumulation of TMZ and MRP1 expression. The authors concluded that TMZ resistance is unlikely to be mediated via efflux transporters, including P-gp (Ma et al., 2002).

Similarly, Luo et al. showed unaltered sensitivity to TMZ with the addition of a P-gp inhibitor, verapamil, in a melanoma cell line shown to overexpress P-gp (Luo et al., 2012). These findings suggest that TMZ is not a substrate for P-gp.

More recently, there has been an increase in the number of *in-vitro* studies attempting to investigate the relationship between TMZ and P-gp. However, these have focused on the transporter's role in the development of chemoresistance and its potential for enhancing TMZ's efficacy *in-vitro* (Zhang et al., 2014) (Munoz et al., 2015a). Munoz et al demonstrated in an *in-vitro* study that overexpression of P-gp was accoiated with increased chemoresistance to TMZ as shown by improved cell viability in two glioma cell lines by approximately 40% (Munoz et al., 2015b).

Zhang et al on the other hand employed photodynamic therapy in combination with

TMZ treatment in a preclinical *in-vivo* study in glioma model in rats. Their study demonstrated that photodynamic therapy lead to a decrease in P-gp expression, which was associated with higher TMZ concentration in glioma tissues and enhanced TMZ efficacy (Zhang 2014).

To date, only one preclinical *in-vivo* study has shown that TMZ is transported by P-gp (Goldwirt et al., 2014). The authors of this study administered high doses of TMZ via intravenous injection and performed pharmacokinetic studies in wild-type mice and mice lacking the P-gp efflux transporter. They demonstrated a minimal but significant increase in brain exposure to TMZ in animals lacking the P-gp efflux transporter.

Furthermore, the ability of TMZ to penetrate the BBB has been established in previous studies as previously discussed. More recently simulation software has been employed to evaluate the interaction between TMZ and P-gp. 3D modelling predicted that TMZ binds to P-gp and identified major residues involved in this interaction (Munoz 2015a).

Finally, Schaich et al. identified a single nucleotide polymorphism in the *MDR1* gene encoding for P-gp to be an independent predictor of the outcome of TMZ in GBM patients (Schaich et al., 2009). These findings appear to implicate the P-gp efflux transporter in the efflux of TMZ and the mediation of chemoresistance.

With regard to BCRP's affinity for TMZ, the data are even more scant. Chua et al. demonstrated increased ABCG2 expression in a side population of cells in a glioma cell line (U87-MG) following treatment with TMZ (Chua et al., 2008). Subsequently, Bleau et al. achieved comparable results and demonstrated the ability of TMZ to induce cell phenotypic changes in the side population of a glioma cell line (U87-MG), including overexpression of BCRP. The authors also performed *in-vitro* competition assays, in which TMZ, in contrast to the known BCRP substrate Hoechst, failed to cause a shift in the intracellular accumulation of mitoxantrone (Bleau et al., 2009). These two studies suggest that TMZ can induce over-expression of BCRP but do not shed any light on its substrate status.

PET provides an attractive, non-invasive imaging method that can be used to investigate the role of the ABC transporters. The most commonly followed approach to investigate possible transport of a drug by an efflux transporter is to perform a baseline PET scan following injection of the radiolabelled drug. Subsequently, a selective efflux transporter is injected, followed by administration of the radiolabelled

drug and performance of a second scan to assess for increased uptake (Liow et al., 2009). Alternatively, genetically modified animals with a transporter knockout are employed (Lazarova et al., 2008). Quantification in these studies is usually based on compartmental modelling, by calculating the rate of influx and efflux from one compartment to another (Kannan et al., 2009).

A wide array of preclinical *in-vivo* studies have utilised PET to evaluate the effects of P-gp inhibition in various radiolabelled substrates. For example, using [^{11}C]-verapamil and a P-gp inhibitor, Kuntner et al. successfully demonstrated increased P-gp activity in the cerebellum compared to the thalamus in healthy rats (Kuntner et al., 2010). This effect was also reported by Bankstahl et al. after status epileptics was induced in rats and a similar increase in P-gp activity was observed using radiolabelled verapamil (Bankstahl et al., 2011).

PET has also been utilised to evaluate BCRP function. In 2011, Yamasaki et al. radiolabelled topotecan, an anticancer drug known to be a substrate for both P-gp and BCRP, in a PET study. The authors used a combination of chemical and genetic P-gp and BCRP transporter knockout in mice and reported similar levels of increased topotecan-related radioactivity in the brain using both inhibition methods (Yamasaki et al., 2011). This study was not able to differentiate between the functions of those two transporters. In another study, Wanek et al. went a step further and successfully imaged the function of BCRP in mice (Wanek et al., 2012).

PET is a translational research tool and has been also applied in clinical imaging studies evaluating P-gp function. Careful interpretation of preclinical ABC transporter studies is needed prior to extrapolating findings to humans. This is particularly important due to clear interspecies differences. A study using three different radiolabelled compounds demonstrated such interspecies (human, primate and rodent) differences in P-gp's role in drug transport across the BBB (Syvanen et al., 2009). A similar conclusion was reached by Bauer et al., who found that humans and rats demonstrated comparable half-maximum-effect concentrations (EC50) for tariquidar, a third generation P-gp inhibitor, but significantly different [^{11}C]-verapamil-derived brain activity uptake. Here, tariquidar resulted in a 2.7-fold increase in humans compared to an 11-fold increase in rats (Bauer et al., 2012). In humans, the most abundant efflux transporters are, in order of abundance, BCRP, P-gp and MRP4 (Uchida et al., 2011). This may explain why multiple studies have demonstrated

greater effects of P-gp inhibition in small rodents in comparison to humans (Hsiao et al., 2006) (Bauer et al., 2012).

A summary of the radiotracers used in the evaluation of P-gp and BCRP efflux transporters is presented in Table 3.3.

Table 3. 3: PET radiotracers that have been used to evaluate P-glycoprotein and Breast Cancer Resistance Protein in the brain.

Tracer	Transporter Evaluated	Species
[11C]Erlotinib	P-gp and BCRP	Mouse
[11C]Gefitinib	P-gp and BCRP	Mouse
[11C]Elacridar	P-gp and BCRP	Mouse, rat and human
[11 C]-N-Desmethyl-loperamide	P-gp	Mouse, rat, primate and human
(R)[11C]Verapamil	P-gp	Mouse, rat and human
[11C]Tariquidar	P-gp and BCRP	Mouse, rat and human
[11C]Verapamil	P-gp	Mouse, rat, primate and human

Primate: non-human primate. Table adapted from (Langer, 2016).

Nonetheless, PET has been employed to study the efflux function of P-gp in multiple human studies (Table 3.3). Four different radiolabelled compounds known to be P-gp substrates were used, including N-desmethyl-loperamide (Kreisl et al., 2010), (R)-verapamil (Wagner et al., 2009) (Bauer et al., 2012) (Bauer et al., 2015), verapamil (Sasongko et al., 2005) (Arakawa et al., 2010) and tariquidar (Bauer et al., 2013a). The large majority of these studies were conducted in healthy volunteers, except for a small number of recent studies that evaluated P-gp functional activity in patients with epilepsy (Feldmann et al., 2013) (Bauer et al., 2014). To date, no clinical PET imaging studies have evaluated P-gp's functional activity in glioma patients or assessed the effect of the P-gp efflux function on a chemotherapeutic agent, including TMZ.

BCRP's functional activity in humans cannot be reliably assessed due to a lack of approved BCRP inhibitors.

3.6.5. Research aims

In summary, the relationship between TMZ and the efflux transporters remains poorly understood despite body of evidence pointing towards a role of P-gp in the transport of, or development of chemoresistance to TMZ. However, this relationship has not been fully evaluated. Additionally, P-gp and BCRP appear to work together as anticancer efflux transporters, with an overlap in their affinity for multiple anticancer drugs that are dual transporter substrates. Finally, PET imaging is a well-established research tool that has been successfully utilised to evaluate efflux transporter function in various preclinical and clinical settings, but not in the context of brain tumours.

This study is a pilot investigation of the role of P-gp and BCRP in the transport of TMZ and its role in human gliomas. The ultimate aim of this project was to develop a non-invasive imaging method to measure TMZ delivery to the brain and concentration in brain tumours. In order to achieve this goal, a number of specific objectives were generated and tested:

1. Investigate the effects of P-gp and BCRP inhibition on the transport of TMZ *in-vitro.*

An *in-vitro* BBB model that possesses excellent barrier properties and expresses P-gp and BCRP was employed to conduct *in-vitro* transport studies, directly evaluating TMZ transport by P-gp and BCRP.

2. Evaluate the role of the P-gp and BCRP efflux transporters in the efflux of TMZ at the mouse BBB.

Small animal PET scans were performed using radiolabelled [^{11}C]TMZ in wild type and genetic transporter knockout mice, as well as by using chemical inhibition of P-gp and BCRP.

3. Investigate the role of the P-gp and BCRP efflux transporters in limiting TMZ efficacy in brain tumours.

GBM xenograft models were implanted into mice to evaluate how chemical inhibition of P-gp- and BCRP-mediated efflux affects the efficacy of TMZ.

4. Study the functional activity of P-gp in high-grade glioma patients.

PET imaging and (R)-[^{11}C]verapamil were utilised to non-invasively demonstrate the functional activity of P-gp in five patients with high-grade gliomas.

Chapter 4 In-vitro studies: Temozolomide transport studies in a validated in-vitro blood-brain barrier model.

4.1. Abstract

Purpose: To investigate the relationship between TMZ and the efflux transporters P-gp and BCRP.

Methods: An *in-vitro* BBB model was derived from the co-culture of primary porcine brain endothelial cells with a rat astrocyte cell line. Key characteristics of the *in-vivo* BBB were established such as high trans-endothelial electrical resistance (TEER) and functionally active P-gp and BCRP efflux transporters.
An HPLC detection method for TMZ was developed. Concentration equilibrium transport assay were conducted over one hour period at clinically relevant concentrations of TMZ.

Results: Small but significant TMZ accumulation in the apical compartment of the *in-vitro* BBB model was detected (P = 0.015). This effect was not observed in the presence of P-gp and BCRP inhibitors.

Conclusions: Active TMZ transport indicates a potential role for P-gp and BCRP in the active efflux of TMZ. However, the limited evidence of active transport after one hour also suggests that TMZ is unlikely to be a strong substrate for these transporters.

4.2. Introduction

GBM is the most common primary brain tumour in adults (Holland, 2000) and is highly aggressive, leading to extremely dismal prognostic outcomes. The introduction of Stupp therapy (Stupp et al., 2005), which consists of combination treatment of TMZ, an orally administered alkylating agent which causes cell death by interfering with DNA replication (Marchesi et al., 2007), and radiotherapy improved median survival rates from 12.1 months for radiotherapy alone to 14.6 months for the combination therapy (Stupp et al., 2005). Since then, TMZ has remained the central chemotherapeutic agent used in the management of GBM patients.

The BBB represents a major obstacle to the delivery of effective chemotherapy, which in combination with the highly aggressive nature of GBM tumour cells, and their ability to develop chemoresistance, accounts for poor treatment outcomes with almost all tumours recurring (Wen and Kesari, 2008).

The BBB plays an important role in the homeostasis of the brain microenvironment via different transport mechanisms including the ABC efflux transporters. P-gp and BCRP are such efflux transporters, which have been implicated in the efflux of a wide range of chemotherapy agents (Loscher and Potschka, 2005a). Moreover, P-gp and BCRP appear to play an important role in the development of chemoresistance by limiting the intercellular accumulation of various chemotherapy agents in tumour cells (Szakacs et al., 2006) (Kusuhara and Sugiyama, 2007).

Recently, there is an increasing *in-vitro* body of evidence pointing towards a role for P-gp in the development of chemoresistance to TMZ (Munoz et al., 2014) (Munoz et al., 2015a) (Munoz et al., 2015b). However, the overall evidence remains poorly understood with many conflicting reports in the literature (Demeule et al., 2001).

Surprisingly, and despite extensive research work involving TMZ, on one hand and the efflux transporters P-gp and BCRP on the other, there are no robust published data on transport studies evaluating the relationship between TMZ and those efflux transporters. This study attempted to fill in this knowledge gap by employing an *in-vitro* BBB model that possesses excellent barrier properties and expresses both P-gp and BCRP transport proteins, simulating the *in-vivo* setting. Novel data is provided on the direct *in-vitro* transport of TMZ by P-gp and BCRP.

4.3. Materials and methods

4.3.1. Materials

Cell culture plasticware was obtained from Greiner Bio-one (Gloucestershire, UK). Rat-tail collagen type I and human fibronectin were obtained from Becton Dickinson (Oxford, UK). Dounce homogenisers were obtained from VWR (Lutterworth, UK). All cell culture reagents were purchased from Life Technologies (Paisley, UK), except plasma-derived serum (PDS) from First Link (Birmingham, UK). Rabbit anti-human Occludin, rabbit anti-human zona occludens protein-1(ZO-1) and Fluorescein isothiocyanate (FITC)-labelled mouse anti-rabbit IgG were obtained from Vector Laboratories (Peterborough, UK). All other remaining materials were purchased from Sigma-Aldrich (Poole, UK).

4.3.2. Isolation of porcine brain capillary endothelial cells

Cerebromicrovascular endothelial cell isolation was performed according to the methods detailed by Skinner et al with some modifications (Skinner et al., 2009). Ten to twelve porcine cerebral hemispheres were collected from the abattoir and inspected for lack of bruising, contusions or other obvious pathologies. The hemispheres were immediately placed in Dulbecco's modified Eagle medium (DMEM) supplemented with 1% (v/v) of Penicillin/Streptomycin mixture. The hemispheres were transported on ice to the laboratory in under 45 minutes.

The hemispheres were washed in ice-cold phosphate-buffered saline (PBS; 8 g sodium chloride, 0.2 g potassium chloride, 1.4 g sodium phosphate and 0.24 g of potassium dihydrogen phosphate were dissolved in 800 mL of sterile water. The pH was then adjusted to 7.4 and the solution was made up to 1 L with double distilled water containing 1% (v/v) of Penicillin/Streptomycin mixture). A watchmaker's forceps was then used to carefully resect the meninges. This was followed by careful resection of the white matter and the remaining grey matter was cut into small pieces that were passed through a sterile 50 mL syringe and collected in a sterile container containing DMEM. The cortical grey matter was then placed in a Dounce tissue grinder and manually homogenised using a loose-fitting pestle (89 − 127 μm clearance) for 17 strokes and a tight-fitting pestle (25 −76 μm clearance) for another 17 strokes. The

homogenate was filtered by applying negative pressure through a 150μm nylon mesh and subsequently through a 60 μm nylon mesh. The 60 μm mesh was placed in digest mix (210 units.ml^{-1} Collagenase, 114 units.ml^{-1} DNAase type I and 91 units.ml^{-1} Trypsin dissolved in 178 mL of M119 medium and filtered for sterilisation through a 0.22 μm filter). Subsequently, 20 mL of foetal bovine serum (FBS) and 2 mL of Penicillin/Streptomycin antibiotic mixture were added and mixed gently for one hour at 37ºC, and then direct pipetting used to wash off the material that was retained on the mesh. The digest mix containing the cerebromicrovessels was centrifuged at 22,700 x *g* for five minutes in a Hettich Universal 320 Centrifuge (Hettich, Germany). The supernatant was discarded and the pellet containing the cerebromicrovessels was resuspended in 10 mL of PBEC growth medium (DMEM low glucose without phenol red supplemented with 1% (v/v) of Penicillin/Streptomycin mixture, 1% L-glutamine, (v/v) 10% plasma derived serum and 125 μg.ml^{-1} heparin) and centrifuged again at 22,700 x *g* for five minutes. The supernatant was carefully aspirated and the resulting pellet was resuspended in foetal bovine serum:dimethyl sulfoxide (9:1). One-millilitre aliquots were placed into cryogenic vials and stored at −80ºC overnight. Vials were stored in liquid nitrogen until use. The isolation procedure resulted in approximately 16 − 20 vials.

Confirmation of the isolated PBECs was perfromed by evaluating the morphology and ultra-structural morphology of these cells using transmission electron microscopy. My colleague, Dr Pablo Toress, in our laboratory carried out further and more comprehensive characterisation including immunocytochemical detection of tight junction.

4.3.3. Coating culture surfaces with collagen and fibronectin

Culture surfaces were treated with collagen and fibronectin prior to culture of cells to facilitate attachment and proliferation. Each well in a six-well plate was treated with one mL of 100 μg.ml^{-1} rat tail collagen type 1 prepared in acetic acid and the plate agitated for two hours at room temperature. Subsequently, the collagen solution was removed and the wells were washed twice with one mL of PBS. The wells were then treated with one mL of 7.5 μg.ml^{-1} human fibronectin prepared in sterile water at 4ºC for 24 hours. The following day, fibronectin was aspirated and well washed twice with

one mL of PBS. To prevent drying of the collagen and fibronectin coated surfaces, the final fraction of PBS wash was left in the wells until cells were ready for seeding onto the surface.

The same method was followed for coating of the 96-well plates and Transwell® inserts but each well was treated with 32 µL and 500 µL of collagen and fibronectin respectively.

4.3.4. Culture of primary porcine brain endothelial cells

Six-well plates were agitated for one hour at room temperature, the fibronectin solution removed and the wells were washed twice with one mL warm PBS. The second wash was left in the wells until cell seeding. A single vial of the cryopreserved porcine brain capillary endothelial cells was thawed and immediately suspended in 10 mL of PBEC growth medium. This was subsequently centrifuged at 22,700 x *g* for five minutes and the supernatant carefully discarded. The pellet containing the cerebromicrovessels was resuspended in 6 mL of PBEC growth medium and one mL was added to each well. The plate was maintained in a humidified atmosphere for 24 hours at 37ºC and 5% CO_2.

Twenty-four hours post seeding, the cells were treated for 48 hours with 4 $\mu g.ml^{-1}$ Puromycin dihydrochloride prepared in PBEC growth medium. Thereafter the puromycin containing medium was replaced with a 1:1 (v/v) mixture of PBEC growth medium and DMEM supplemented with 10% (v/v) FBS and 1% (v/v) Penicillin/Streptomycin antibiotic mixture. Cells were routinely maintained in a humidified atmosphere at 37ºC and 5% CO_2 until confluent.

4.3.5. Sub-culture of primary porcine brain endothelial cells into 96 well plates

The medium was removed from the 6-well plates and discarded. The wells were then washed twice with one mL of warm PBS containing 0.2 mg/ml EDTA. Each well was subsequently treated with 0.3 mL of trypsin and incubated in a humidified atmosphere at 37ºC and 5% CO_2 for a maximum of ten minutes. The trypsin was then neutralised with 0.6 mL of 1:1 (v/v) mixture of PBEC growth medium and DMEM supplemented with 10% (v/v) FBS and 1% (v/v) Penicillin/Streptomycin antibiotic mixture.

Cells were then detached by continuous pipetting and collected into a universal tube. The suspension was centrifuged at 22,700 x *g* for five minutes and the supernatant carefully discarded. The pellet was resuspended in one mL of the 1:1 (v/v) mixture of PBEC growth medium and DMEM supplemented with 10% (v/v) FBS and 1% (v/v) Penicillin/Streptomycin antibiotic mixture. 20 µL of cell suspension was added to 20 µL of trypan blue solution and viable cell density calculated. Cells were then seeded onto 96-well plates to achieve a cell density of 20,000 cells per well.

4.3.6. Measurement of P-glycoprotein functional activity

Porcine brain endothelial cells were seeded in a 96-well plate pretreated with rat tail collagen type I and human fibronectin as described in section (4.3.3). Measurement of P-gp activity was carried out on confluent monolayers only (at least 2 days post plating onto 96-well plates). On the day of the experiment, the medium was discarded and the wells were washed with 200 µL of warm PBS. Subsequently, 100 µL of phenol red free DMEM supplemented with 1% L-glutamine were added to the wells and the plate incubated for 30 minutes at 37ºC and 5% CO_2. After this period, either 50 µL of the above DMEM (control condition) or 50 µL of the P-gp inhibitor verapamil hydrochloride at a concentration of 30 µM (final concentration 10 µM) were added to cells. Following 30 minutes of incubation, 50 µL of 2 µM calcein–AM (final concentration 0.5 µM) were added to all wells and the plate incubated for a further 30 minutes in a humidified atmosphere at 37ºC and 5% CO_2. After incubation, the medium was aspirated and the wells rapidly rinsed twice with 200 µL cold PBS and a further 100 µL cold PBS was added to the wells.

Intracellular calcein-AM accumulation was assessed by fluorescence spectroscopy using a Safire multiplate reader (Tecan, Germany) with an excitation wavelength of 490 nm and an emission wavelength of 530 nm. The fluorescence of the treated wells was calculated and expressed as a percentage of the fluorescence of the control wells (% of control). All fluorescence values were corrected for background fluorescence by subtracting the average fluorescence values of eight wells containing 100 µL of PBS. Seven independent experiments were performed with between five to eight replicates in each experiment.

4.3.7. Measurement of Breast Cancer Resistance Protein functional activity

Porcine brain endothelial cells were seeded in a 96-well plate pretreated with rat tail collagen type I and human fibronectin. Measurement of BCRP activity was carried out on confluent monolayers.

On the day of the experiment, the medium was discarded and the wells were washed with 200 µL of warm PBS. Subsequently, 100 µL of phenol red free DMEM supplemented with 1% L-glutamine were added to the wells and the plate incubated for 30 minutes at 37ºC and 5% CO_2. After this period, either 50 µL of the above DMEM (control condition) or control medium supplemented with 50 µL of the BCRP inhibitor KO143 at concentration of 1.5 µM (final concentration 0.5 µM) was added. Following 30 minutes of incubation, 50 µL of a 20 µM Hoechst 33342 (final concentration of 5 µM) were added to all wells and the plate incubated for a further 30 minutes in a humidified atmosphere at 37ºC and 5% CO_2. After the incubation, the medium was aspirated and the wells rapidly rinsed twice with 200 µL cold PBS and a further 100 µL cold PBS was added to the wells. Intracellular Hoechst 33342 accumulation was assessed by fluorescence spectroscopy using the Safire multiplate reader with an excitation wavelength of 370 nm and an emission wavelength of 450 nm. The fluorescence of the treated wells was calculated and expressed as a percentage of the fluorescence of the control wells (% of control). All fluorescence values were corrected for background fluorescence by subtracting the average fluorescence values of eight wells containing 100 µL of PBS. Seven independent experiments were performed with between five to eight replicates in each experiment.

4.3.8. Assessment of Temozolomide Toxicity on Porcine Brain Endothelial Cells

Cell viability was assessed using the MTT 3-(4,5-dimethyl-2-thiazoyl)-2,5-diphenyl-tetrazolium bromide) reduction assay. PBECs were seeded onto a 96-well plate at a density of 20,000 cells/well and the experiments were performed on confluent cell monolayers.

All solutions were prepared freshly on the day of the experiment. The MTT stock solution was prepared in sterile PBS at a concentration of 5 $mg.ml^{-1}$ and filtered through a 0.22 µm filter. TMZ was dissolved in DMSO at a concentration of 20 mM

and further diluted in phenol red free DMEM supplemented with 1% L-glutamine to produce concentrations range of 0.02, 0.2, 2, 20, 100 and 200 μM.

On the day of the experiment, the growth medium was discarded and the wells were washed with 200 μL of warm PBS. Subsequently, 100 μL of phenol red free DMEM supplemented with 1% L-glutamine were added to the wells and the plate incubated for 30 minutes at 37ºC and 5% CO_2. After this period, 100 μL of the above TMZ solutions were added to wells to achieve final concentrations of 0.01 μM, 0.1 μM, 1 μM, 10 μM, 50 μM and 100 μM, and the plates incubated for four hours. Subsequently, the medium was discarded and replaced with 200 μL of phenol red free DMEM supplemented with 1% L-glutamine, and 20 μL of the MTT stock solution was added. The plates were incubated for another two hours in a humidified atmosphere at 37ºC and 5% CO_2 to allow the formation of the formazan product. The supernatant was carefully removed and 100 μL of DMSO was added to each of the wells. The plates were gently agitated on a shaker to dissolve the purple formazan crystals for 15 minutes. Absorbance was measured at an excitation wavelength of 570 nm and an emission wavelength of 700 nm using the Safire multiplate reader. The results were expressed as a percentage of the absorbance measured for the control wells (% of control). All absorbance values were corrected for background absorbance by subtracting the average absorbance values of eight wells containing 100 μL of PBS. Four independent experiments were performed with five replicates in each experiment.

4.3.9. Assessment of Temozolomide inhibitory effect on P-glycoprotein functional activity

Porcine brain endothelial cells were seeded in a 96-well plate pretreated with rat tail collagen type I and human fibronectin. Measurement of P-gp activity was carried out on confluent monolayers.

All solutions were prepared freshly for each experiment. TMZ was dissolved in DMSO at a concentration of 20 mM and further diluted in phenol red free DMEM supplemented with 1% L-glutamine to produce concentrations range of 0.03 μM, 0.3 μM, 3 μM, 30 μM, 150 μM and 300 μM.

On the day of the experiment the medium was discarded and the wells were washed with 200 μL of warm PBS. Subsequently, 100 μL of phenol red free DMEM supplemented with 1% L-glutamine were added to the wells and the plate incubated

for 30 minutes at 37ºC and 5% CO_2. After this period, 50 µL of the above TMZ solutions (0.03 µM, 0.3 µM, 3 µM, 30 µM, 150 µM and 300 µM) were added to wells to achieve final concentrations of 0.01 µM, 0.1 µM, 1 µM, 10 µM, 50 µM and 100 µM, and the plates incubated for one hour. Additionally, as a positive control, a further set of wells was treated with 10 µM verapamil hydrochloride, a known P-gp inhibitor, for one hour.

After this period, the wells were incubated for a further 30 minutes with 50 µL of a 2 µM calcein-AM solution (final concentration 0.5 µM). Subsequently, the medium was aspirated and the wells rinsed twice with 200 µL cold PBS and a further 100 µL cold PBS was added to the wells. Intracellular calcein-AM accumulation was assessed by fluorescence spectroscopy using the Safire multiplate reader at an excitation wavelength of 490 nm and an emission wavelength of 530 nm. All fluorescence values were corrected for background fluorescence by subtracting the average fluorescence values of eight wells containing 100 µL of PBS. Four independent experiments were performed with at least five replicates in each experiment.

4.3.10. Assessment of Temozolomide inhibitory effect on Breast Cancer Resistance Protein functional activity

Porcine brain endothelial cells were seeded in a 96-well plate pretreated with rat tail collagen type I and human fibronectin. Measurement of BCRP activity was carried out on confluent monolayers.

All solutions were prepared freshly for each experiment. TMZ was dissolved in DMSO at a concentration of 20 mM and further diluted in phenol red free DMEM supplemented with 1% L-glutamine to produce concentrations range of 0.03 µM, 0.3 µM, 3 µM, 30 µM, 150 µM and 300 µM.

On the day of the experiment the medium was discarded and the wells were washed with 200 µL of warm PBS. Subsequently, 100 µL of phenol red free DMEM supplemented with 1% L-glutamine were added to the wells and the plate incubated for 30 minutes at 37ºC and 5% CO_2. After this period, 50 µL of the above TMZ solutions (0.03 µM, 0.3 µM, 3 µM, 30 µM, 150 µM and 300 µM) were added to wells to achieve final concentrations of 0.01 µM, 0.1 µM, 1 µM, 10 µM, 50 µM and 100 µM, and the plates incubated for one hour. Additionally, as a positive control, a further set

of wells was treated with 0.5 μM KO143, a known BCRP inhibitor, for one hour.

After this period, the wells were incubated for a further 30 minutes with 50 μL of a 20 μM Hoechst 33342 solution (final concentration 5 μM). Subsequently, the medium was aspirated and the wells rinsed twice with 200 μL cold PBS and a further 100 μL cold PBS was added to the wells. Intracellular Hoechst 33342 accumulation was assessed by fluorescence spectroscopy using the Safire multiplate reader at an excitation wavelength of 370 nm and an emission wavelength of 450 nm. The fluorescence of the treated wells was calculated and expressed as a percentage of the fluorescence of the control wells (% of control). All fluorescence values were corrected for background fluorescence by subtracting the average fluorescence values of eight wells containing 100 μL of PBS. Four independent experiments were performed with at least five replicates in each experiment.

4.3.11. Culture of CTX-TNA2 astrocytes

A single vial of the cryopreserved rat astrocyte cell line CTX-TNA2 (passages 12 − 26) was thawed and immediately suspended into 10 mL of DMEM supplemented with 10% (v/v) FBS and 1% (v/v) Penicillin/Streptomycin antibiotic mixture. This was subsequently centrifuged at 22,700 x *g* for five minutes and the supernatant carefully discarded. The pellet containing the CTX-TNA2 cells was resuspended in 12 mL of DMEM supplemented with 10% (v/v) FBS and 1% (v/v) Penicillin/Streptomycin antibiotic mixture and one mL was added to each well of a 12 well plate. The plate was maintained in a humidified atmosphere for 24 hours at 37ºC and 5% CO_2.
Upon reaching confluency (typically in 48 −72 hours), the medium was collected and filtered for sterilisation through a 0.22 μm filter and stored in −20ºC. This is referred to as CTX-TNA2 astrocyte conditioned medium (CTX-TNA2 ACM)

4.3.12. Generation of the blood-brain barrier model

Transwell® polycarbonate inserts (surface area 1.2 cm^2; pore size 0.4 μm) were coated with rat tail collagen type I and human fibronectin as described in section (4.3.3) but each Transwell® insert was treated with 500 μL of collagen and fibronectin. PBEC

subculturing was performed as in section (4.3.5) but cells were seeded at a density of 80000 cells per 500 µL per Transwell® insert. Cells were seeded onto the upper (donor) compartment of the Transwell® polycarbonate insert while the abluminal (basal) side faced the receiver compartment. Transwells® and inserts were maintained overnight in a humidified atmosphere for 24 hours at 37ºC and 5% CO_2.

48 hours post seeding, Transwell® inserts were transferred to a new 12-well plate containing confluent CTX-TNA2 astrocytes. Media was aspirated and replaced with a 1:1 (v/v) mixture of PBEC growth medium and CTX-TNA2 ACM (Figure 4.1). Media was replaced every 48 hours and cultures were maintained in a 1:1 (v/v) mixture of PBEC growth medium and CTX-TNA2 ACM. On day six, 24 hours prior to conducting a transport experiment, Transwell® inserts were transferred to a new 12-well plate without astrocytes and cells were maintained in supplemented media which consisted of serum-free DMEM supplemented with 1% (v/v) Penicillin/Streptomycin antibiotic mixture, 1% (v/v) L-glutamine, 125 µg/mL heparin, 312.5 µM 8-4-chlorophenylthio-cyclic adenosine monophosphate (cAMP), 7.5 µM 4-(3-Butoxy-4methoxyphenyl)methyl-2-imiadzolidone (RO-20-1724) and 55 µM hydrocortisone. This helped maintain and enhance the Transendothelial Electrical Resistance (TEER) of the model (Rubin et al., 1991).

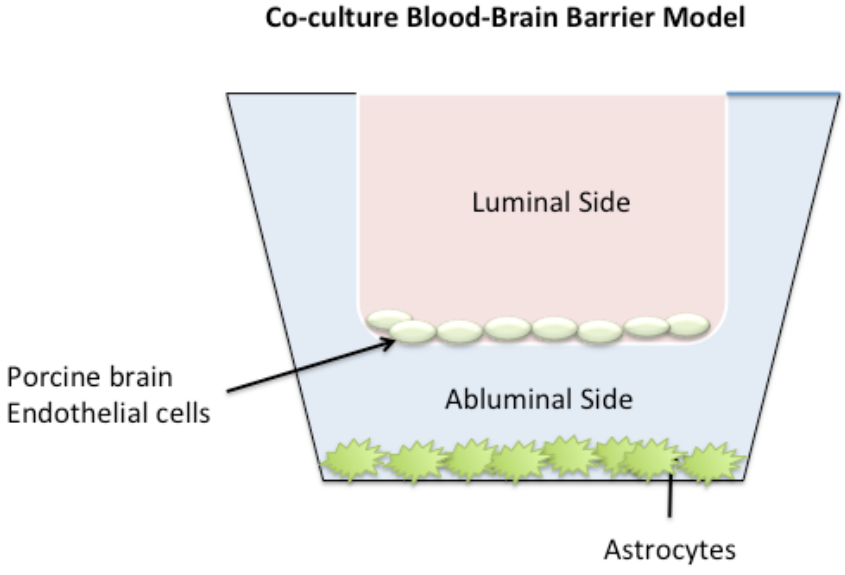

Figure 4. 1: Co-culture *in-vitro* Blood-Brain Barrier model.
A diagram demonstrating PBECs containing Transwells® co-cultured with CTX-TNA2 astrocyte cell line.

4.3.13. Measurement of transendothelial electrical resistance

TEER of the Transwell® inserts was recorded on alternate days from day one post seeding to the day of the experiment. TEER was measured manually using EVOM chopstick electrodes (World Precision Instruments, Sarasota, FL, USA). All measurements were performed under sterile conditions.

The TEER of control Transwell® polycarbonate insert filters lacking cells were initially recorded. In order to calculate the final TEER of the Transwell® inserts containing PBEC cells, the control TEER was subtracted from filters with cells and final resistance corrected for surface area (1.2 cm^2).

All cultures used for transport experimentation demonstrated a minimum of 300 $\Omega.cm^2$ above control Transwell® inserts.

4.3.14. Measurement of permeability of porcine brain endothelial cell monolayers

Permeability studies across the PBEC monolayers were performed as described by Mark and Miller (Mark and Miller, 1999), with some modifications. Paracellular permeation was quantified by measuring the apparent permeability coefficient (P_{app}) of Lucifer Yellow (Mr 457.24). Lucifer Yellow was added to the donor (apical) compartment of the Transwell® insert to achieve a final concentration of 50 μM. 100 μL samples were taken from the donor and receiver compartments at 0 and 3 hours. Samples were placed in a 96-well plate and Lucifer Yellow permeability was assessed by fluorescence spectroscopy using the Safire multiplate reader with an excitation wavelength of 425 nm and an emission wavelength of 515 nm. The fluorescence of the treated wells was calculated and expressed as a percentage of the fluorescence of the control wells (% of control). All fluorescence values were corrected for background fluorescence by subtracting the average fluorescence values of eight wells containing 100 μL of PBS. P_{app} was calculated using the following equation (Artursson, 1990):

$P_{app}(cm/sec) = dc/dt \times V \div A\ C_0$

dc/dt: changes in the concentration of the donor compartment over time ($mol.L^{-1}.sec^{-1}$)

V: volume in the reservoir of the receiver compartment (cm^3)

A: Surface area of the membrane (1.2 cm^2)

C_0: Initial concentration of the donor compartment ($mol.L^{-1}$)

Four independent experiments were performed with at least six replicates in each experiment.

4.3.15. Detection of Temozolomide

TMZ concentration was quantitated using a high performance liquid chromatography tandem-mass spectroscopy (HPLC/MS/MS) method that was developed and validated locally at the Biomolecular Analysis facility in the Faculty of Life Sciences at the University of Manchester. In brief, 5μL samples were applied to a mobile phase, which consisted of 5% (v/v) acetonitrile with 0.1% (v/v) formic acid. Separation was achieved on an Agilent C18, 2.1 x 100 mm, 1.8 μm column (828700-902). After one

minute the gradient was increased to 95% (v/v) acetonitrile over six minutes and held for three minutes before returning to equilibrium. Data were collected in positive Electrospray Ionisation (ESI) in separate runs on a previously tuned and calibrated Agilent 6520 QTOF (Agilent Technologies) operated between 100 and 1700 m/z. During analysis two reference masses 195.063 ($C_6H_6N_6O_2$) and 217.045 ($C_6H_6N_6O_2$ .NA) were assessed continuously with MS/MS between three to six minutes using collision energy of 5. The capillary voltage was set at 3500V with a scan rate of 1 spectrum per second and the drying gas flow rate was 8 L/min.

Data were analysed using Agilent MassHunter software (Agilent Technologies) to manually extract peak areas and Waters Progenesis QI software (Waters Corporation) to automatically compare samples.

4.3.16. Temozolomide degradation studies

All solutions were prepared freshly on the day of each experiment. TMZ was dissolved in DMSO at a concentration of 20 mM and 1 mL aliquots were then generated by diluting samples in phenol red free DMEM to achieve a final concentration of 50 μM, as this represents the clinically relevant dose. Separate 1 mL samples were prepared similarly but with the addition of 8.5% (v/v) phosphoric acid (30 μL to 1mL).
To investigate TMZ stability over time, samples were analysed at various time points (0, 1, 2, 3, 4 and 5 hours) as detailed in section (4.3.15).
Four independent experiments were performed with at least eight replicates in each experiment.

4.3.17. Temozolomide transport experiments

A Concentration equilibrium transport assay (CETA) was utilised to evaluate the effects of P-gp and BCRP inhibition on the transport of TMZ. The final volume in these assays was 600 μL in the donor (apical) compartment and 1500 μL in the receiver (basal) compartment.
Transport experiments were conducted on day 7 post seeding of PBEC onto Transwell® inserts. TEER values were documented prior to starting the experiment and

only Transwell® inserts that demonstrated TEER above 300 Ω.cm^2 (after subtracting the background value of a blank Transwell® insert) at the end of the experiment were included in the analysis. Additionally, monolayers that demonstrated >15% drops in TEER were also excluded.

All solutions were prepared on the day of the experiment and warmed to 37 ºC. Transport medium was aspirated and replenished one-hour prior to start of the experiment with an initial volume of 200 µL and 500 µL in the donor and receiver compartments respectively. Following this period, 200 µL and 500 µL of the BCRP inhibitor KO143 (concentration of 1.5 µM) and of the P-gp inhibitor verapamil hydrochloride (concentration of 30 µM) were added to the donor and receiver compartment respectively. While 200 µL and 500 µL of transport medium was added to the donor and receiver compartment respectively as a control.

Following 30 minutes incubation at 37ºC and 5% CO_2, 200 µL and 500 µL of TMZ at a concentration of 150 µM were added to the donor and receiver compartment respectively achieving final concentrations of 50 µM for TMZ, 0.5 µM of the BCRP inhibitor KO143 and 10 µM of the P-gp inhibitor verapamil hydrochloride. Aliquots of 100 µL samples were taken from the donor and receiver compartment at 0 and one hour time points. Collected samples were stored at -20ºC and analysed within 48 hours.

Results for individual transport assays in CETA are presented as the percentage of the drug loading concentration versus time. Transport by P-gp and BCRP efflux transporters was indicated by increase in drug concentration over time in the donor compartment compared with the receiver compartment.

Four independent experiments were performed with at least five replicates in each experiment.

4.3.18. Statistical Analysis

All data are expressed as mean ± standard deviation (SD) and analysed using either Student's *t*-test for comparison between two groups or one-way analysis of variance (ANOVA) for multiple groups. A *P* value of <0.05 was considered to be statistically significant.

4.4. Results

4.4.1. Isolation of primary porcine brain cerebromicrovessels

Cerebromicrovessels were successfully isolated from freshly harvested porcine brains and cerebromicrovessel fragments were stored at −80 ºC. Capillaries were revived and seeded onto a 6-well plate that had been coated with collagen and fibronectin. In the first to third day post seeding, PBECs grew and began to form islands of cells, which continued to differentiate with time. Typically by the seventh day post seeding, a confluent monolayer of PBECs was formed.

4.4.2. P-glycoprotein is functional in the porcine brain endothelial cells

The functional activity of P-gp was confirmed in PBECs by using an intracellular calcein-AM accumulation assay. Calcein-AM is a P-gp substrate and a molecular probe that when metabolised by intracellular esterases produces the fluorescent calcein and as a result intracellular calcein retention is increased when P-gp function is inhibited (Eneroth et al., 2001). Intracellular calcein retention was measured by fluorescence and was found to be seven fold higher in cells pretreated with verapamil hydrochloride, a P-gp inhibitor at 10μM, when compared with vehicle treated control cells (696 ± 204 Relative Fluorescence Unit (RFU) and 100 ± 15 RFU, respectively) (Figure 4.2).

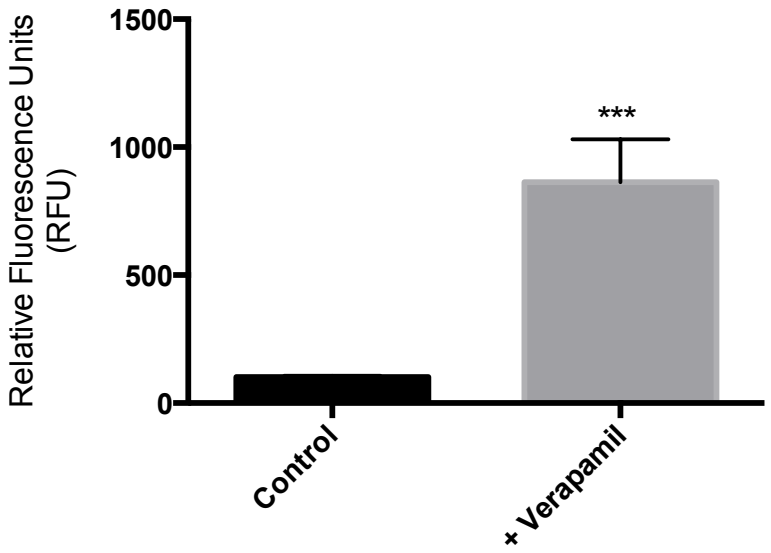

Figure 4. 2: Functional activity of P-glycoprotein in porcine brain enodthelial cells as assessed by the intracellular accumulation of calcein-AM.
Cells were pre-incubated for 30 min at 37 °C in growth medium or growth medium containing 10 μM verapamil. Intracellular accumulation of calcein was measured by spectrofluorometry (excitation λ 490 nm, emission λ 520 nm). Data are expressed as relative fluorescent units and are mean ± SD of 12 replicates (n = 5). *** indicates statistical significance of $p<0.001$ compared to respective control by Student's t-test.

4.4.3. Breast cancer resistance protein is functional in the porcine brain endothelial cells

The functional activity of BCRP was measured in PBECs by using Hoechst 33342 assay. Hoechst 33342 is a molecular probe that is known to be a BCRP substrate and can be easily measured by fluorescence (Kim et al., 2002). Intracellular Hoechst 33342 retention was measured by fluorescence and was found to be significantly (2.7 fold) higher ($p<0.001$) in cells pretreated with KO143, a selective BCRP inhibitor at 0.5μM, when compared with vehicle treated control cells (273±61 RFU and 100±15 RFU, respectively; Figure 4.3).

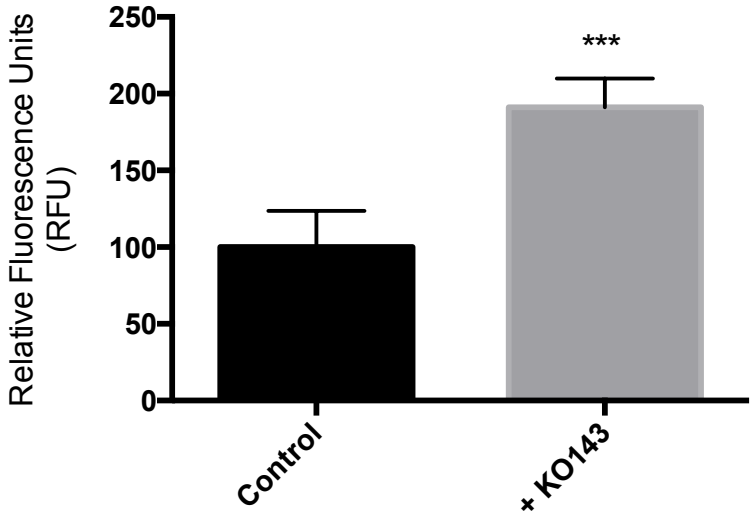

Figure 4. 3: Functional activity of breast cancer resistance protein in porcine brain endothalial cells as assessed by the intracellular accumulation of Hoechst 33342.
Cells were pre-incubated for 30 min at 37 °C in growth medium or growth medium containing 0.5 μM KO143. Intracellular accumulation of Hoechst 33342 was measured by spectrofluorometry (excitation λ 370 nm, emission λ 450 nm). Data are expressed as relative fluorescent units and are mean ± SD of 12 replicates (n = 7). *** indicates statistical significance of $p<0.001$ compared to respective control by Student's t-test.

4.4.4. Temozolomide is not cytotoxic to porcine brain endothelial cells

The MTT cell viability assay was used to test a series of concentrations of TMZ for four hours. It is important to note that the four hours time window is significantly shorter than the usual 24 hours window that used for determining cytotoxicity effect. However, the four hours time point was chosen as it includes the whole duration of the

planned drug transport studies.

This tested concentrations of TMZ ranged from 0.01 μM to 100 μM and includes the clinically relevant plasma concentration which approximately equates to a dose of 50 μM (Ostermann et al., 2004) (Barazzuol et al., 2012).

The MTT assay is used for assessing the metabolic activity of cells; in this assay metabolically active cells can reduce tetrazolium MTT dye to the insoluble formazan. This reduction relies on NAD(P)H-dependent oxidorecutase enzymes.

TMZ had no apparent effect on endothelial cell viability over the 4 h exposure time even at the highest concentration of 100 μM (Figure 4.4). This result confirms that TMZ is not cytotoxic to PBEC at the tested concentrations and under our experimental conditions.

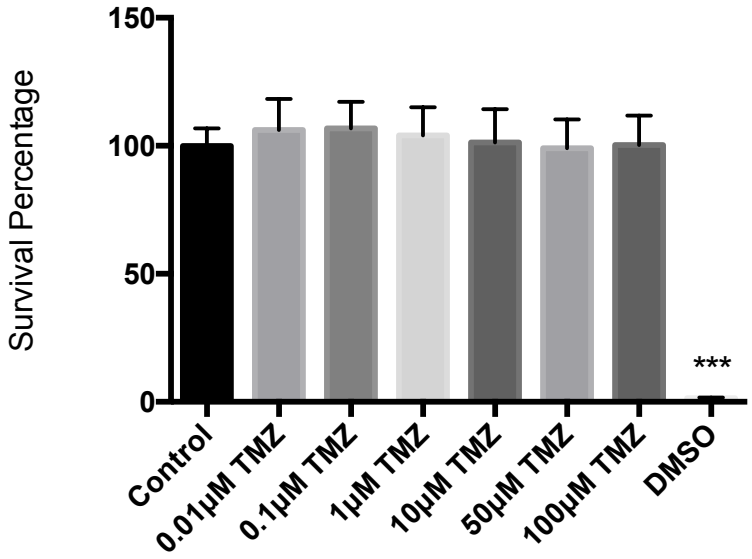

Figure 4. 4: Temozolomide is not cytotoxic to porcine brain endothelial cells .
MTT cell viability assays were performed by treating the cells with the indicated concentrations of TMZ for four hours. Survival is expressed as a percentage of untreated cells (control) after subtracting background absorbance from all values. DMSO was also added to an empty well as a negative control. A total of four independent experiments were carried out in five replicates. *** indicates statistical significance of $p<0.001$ compared to respective control by Student's t-test.

4.4.5 Temozolomide does not inhibit P-glycoprotein-mediated transport

In order to investigate if TMZ inhibits the P-gp efflux transporter, calcein-AM assays were repeated following a 30-minute preincubation period with different doses of TMZ ranging from 0.01 μM to 100 μM. Additionally, as a positive control, cells were treated with verapamil hydrochloride, a widely used P-gp inhibitor at 10μM. TMZ did not exert any inhibitory effect on P-gp efflux transporter function at the concentrations tested, contrary to verapamil hydrochloride. These results indicate that, in our experimental studies with PBECs, TMZ does not inhibit P-gp activity (Figure 4.5).

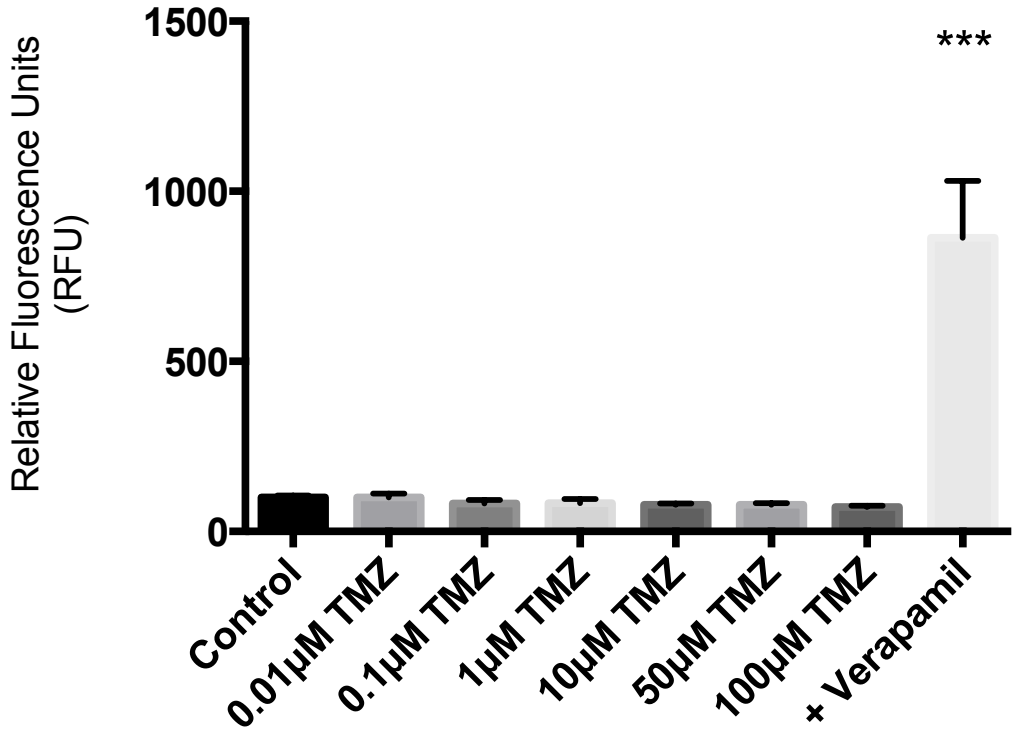

Figure 4. 5: Temozolomide does not inhibit the functional activity of P-glycoprotein. Intracellular accumulation of fluorescent calcein in control cells and cells pretreated with either TMZ at the indicated concentrations or P-gp inhibitor Verapamil hydrochloride (10 μM). Data are expressed as a percentage of the control after subtracting background fluorescence from all values and are a mean ± SD of four different experiments with at least five replicates in each. Statistical significance was determined using t-test (2 tailed). *** Indicates a P value of < 0.001.

4.4.6 Temozolomide does not inhibit breast cancer resistance protein-mediated transport

The effects of TMZ on BCRP functional activity were evaluated by measuring intracellular accumulation of the BCRP substrate Hoechst 33342. As a positive control, cells were treated with KO143, a selective BCRP inhibitor at 0.5μM. The efflux of Hoechst 33342 was not significantly altered by TMZ treatment, in contrast to the KO143 treated cells (Figure 4.6).

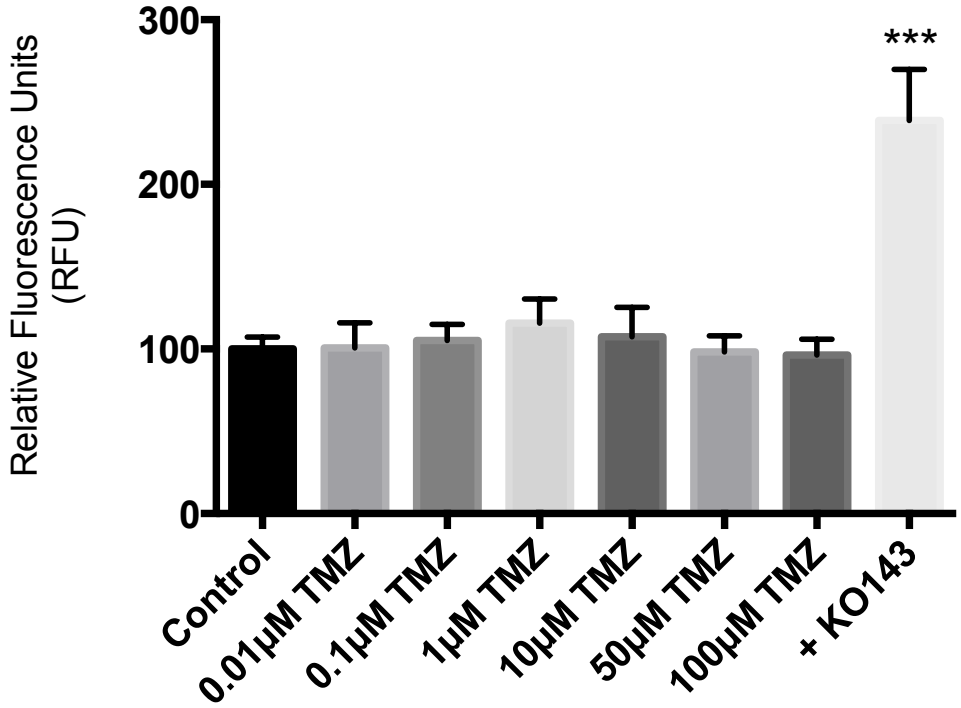

Figure 4. 6: Temozolomide does not inhibit the functional activity of Breast Cancer Resistance Protein.
Intracellular accumulation of fluorescent Hoechst 33342 in control cells and cells pretreated with either TMZ at the indicated concentrations or BCRP inhibitor KO143 (0.5 μM). Data are expressed as a percentage of the control after subtracting background fluorescence from all values and are a mean ± SD of four different experiments with at least five replicates in each. Statistical significance was determined using t-test (2 tailed). *** Indicates a P value of < 0.001.

4.4.7 Effects of puromycin pretreatment on the transendothelial electrical resistance of the porcine brain endothelial cells monolayer

One of the limiting factors affecting the integrity of an *in-vitro* blood brain barrier model is the purity of the brain endothelial cells used to form a monolayer. Contaminating cells such astrocytes and pericytes greatly reduce the integrity of the BBB model limiting the reproducibility of any drug transport studies (Perriere et al., 2005).

PBECs can resist pretreatment with puromycin, a P-gp substrate, due to the high expression of P-gp, which allows the cells to actively efflux puromycin. Contaminating cells on the other hand express low levels of P-gp and thus cannot actively efflux puromycin, which causes toxicity and death.

PBECs that were pretreated with puromycin before subculturing onto the Transwells® and subsequently co-cultured with CTX-TNA2 astrocytes demonstrated significantly higher ($p<0.001$) TEER ($379 \pm 14.61\ \Omega.cm^2$) when compared with untreated PBECs that were subcultured onto the Transwells® ($108 \pm 5.42\ \Omega.cm^2$). These results suggest that pretreatment with puromycin enhances the purity of PBECs enabling it to form a more confluent monolayer and improving the integrity of the *in-vitro* BBB model (Figure 4.7).

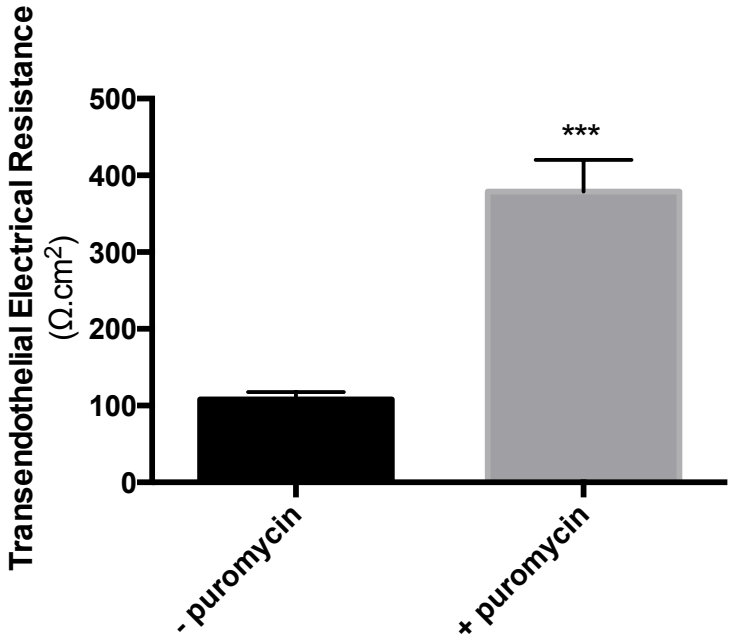

Figure 4. 7: Treatment with Puromycin improves transendothelial electrical resistance. Porcine brain endothelial cells were maintained in culture for 48 h with (grey) or without (black) 4 μ g.ml^{-1} puromycin. Subsequently PBECs, 80,000 cells/well, were seeded onto Transwell® inserts and maintained for 4 days in growth medium (DMEM containing 10 % (v/v) plasma-derived serum, 100 U.ml^{-1} Penicillin, 100 μ g. ml^{-1} Streptomycin, 2 mmol. l-1 glutamine and 125 mmol. l-1 heparin). At day 4 post seeding monolayers were grown in the presence astrocytes and maintained in growth medium. At day 6 post seeding growth medium was supplemented with 312.5 μM cAMP, 17.5 μM RO20-1724 and 55 nM hydrocortisone; TEER was measured on day 7. Net mean TEER values (background subtracted) are shown, n=6. Statistical significance was determined using two-way ANOVA analysis, *** = $p < 0.001$.

4.4.8 Effects of the CTX-TNA2 rat astrocyte cell line on the transendothelial electrical resistance of the porcine brain endothelial cells monolayer

Many studies reported improvement of morphological and physiological characteristics of endothelial cells when cultured in the presence of glial cells such as astrocytes (Cantrill et al., 2012). Furthermore, the inclusion of astrocytes in the BBB model brings it closer to the *in-vivo* setup where endothelial cells and astrocytes are in close contact.

Similar results were demonstrated in these experiments where PBECs were co-cultured for 48 hours with the rat astrocyte cell line CTX-TNA2 from day four post seeding onto Transwell® inserts. The TEER of PBEC monolayers co-cultured with CTX-TNA2 demonstrated significantly higher ($p<0.001$) TEER at day six (401.81 ± 12.6 $\Omega.cm^2$) when compared with PBEC monolayers maintained in the absence of astrocytes (214.6 ± 6.1 $\Omega.cm^2$ Figure 4.8).

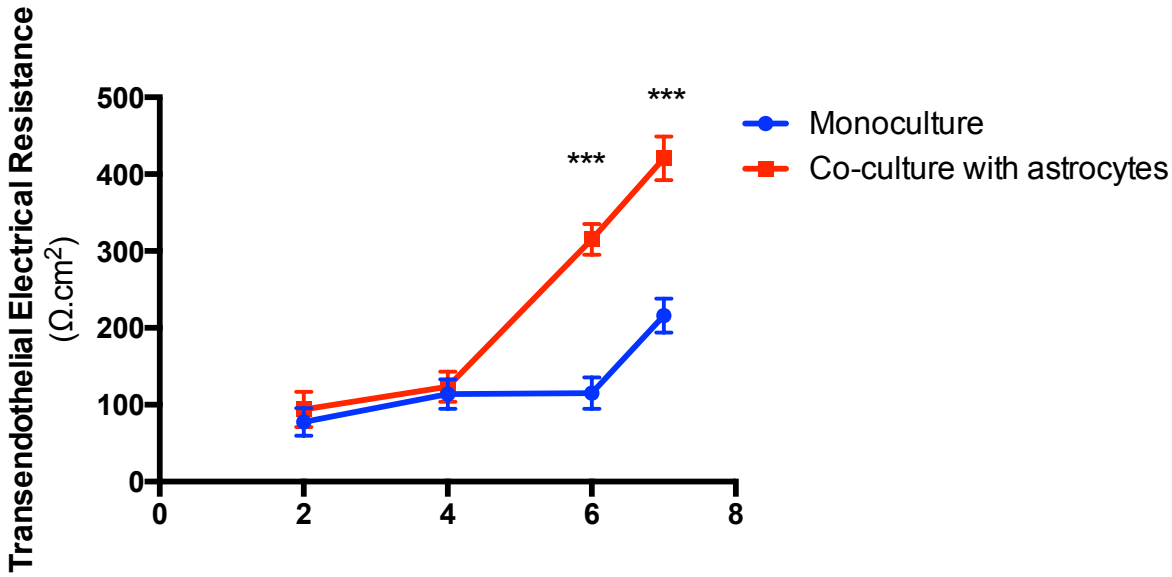

Figure 4. 8: Co-culture with rat astrocyte cell line CTX-TNA2 improves transendothelial electrical resistance.

Porcine brain endothelial cells were maintained in culture for 48 h with 4 µ $g.ml^{-1}$ puromycin. PBECs, 80,000 cells/well, were seeded onto Transwell® inserts and maintained for 4 days in growth medium (DMEM containing 10 % (v/v) plasma-derived serum, 100 $U.ml^{-1}$ penicillin, 100 µ g. ml^{-1} streptomycin, 2 mmol. l-1 glutamine and 125 mmol. l-1 heparin). At day 4 post seeding monolayers were grown in the presence (red) or the absence (blue) of astrocytes and maintained in growth medium. At day 6 post seeding growth medium was supplemented with 312.5 µM cAMP, 17.5 µM RO20-1724 and 55 nM hydrocortisone; TEER was measured on day

2, 4, 6 and 7. Net mean TEER values (background subtracted) are shown, n=8. Statistical significance was determined using two-way ANOVA analysis, *** = $p < 0.001$.

4.4.9. Effects of supplemented medium on the transendothelial electrical resistance of the porcine brain endothelial cells monolayer

Supplemented medium consisted of DMEM serum-free media supplemented with 1% (v/v) Penicillin/Streptomycin antibiotic mixture, 1% (v/v) L-glutamine, 125 µg/mL heparin, 312.5 µM/L cAMP, 17.5 µM/L RO-20-1724 and 55 µM/L hydrocortisone. Few studies reported that the addition of serum-free supplemented media could help maintain and improve the TJ integrity and therefore improve the barrier properties of the BBB model (Rubin et al., 1991) (Cantrill et al., 2012).

The effect of supplemented medium on the TEER of PBEC monolayers was also investigated. Supplemented medium consisted of DMEM serum-free media supplemented with 1% (v/v) Penicillin/Streptomycin antibiotic mixture, 1% (v/v) L-glutamine, 125 µg/mL heparin, 312.5 µM/L cAMP, 17.5 µM/L RO-20-1724 and 55 µM/L hydrocortisone. The addition of supplemented medium to the PBEC monoculture at day four post seeding onto Transwell® inserts resulted in a significant increase ($p<0.001$) in TEER from (114.1 ± 8.5 $\Omega.cm^2$) to (200.7 ± 6.1 $\Omega.cm^2$). Such rise in the TEER was lacking in the PBEC monolayers that were not exposed to supplemented medium. Additionally, it is important to note that the rise in TEER in the PBEC monoculture model was only temporary as drops in TEER were detected the following day (Figure 4.9).

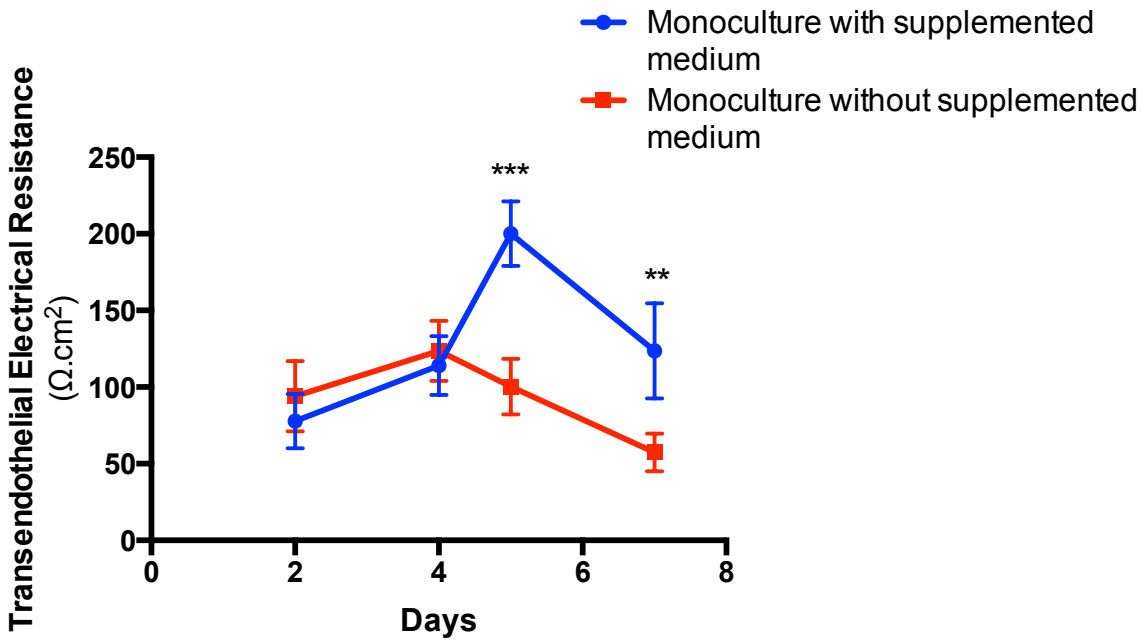

Figure 4. 9: Supplemented medium improves transendothelial electrical resistance. Porcine brain endothelial cells were maintained in culture for 48 h with 4 µ g.ml^{-1} puromycin. PBECs, 80,000 cells/well, were seeded onto Transwell® inserts and maintained for 4 days in growth medium (DMEM containing 10 % (v/v) plasma-derived serum, 100 U.ml^{-1} penicillin, 100 µ g. ml^{-1} streptomycin, 2 mmol. l^{-1} glutamine and 125 mmol. l-1 heparin). At day 4 post seeding growth medium was either supplemented with 312.5 µM cAMP, 17.5 µM RO20-1724 and 55 nM hydrocortisone (blue) or simply replaced with fresh growth media (red); TEER was measured on day 4, 5, 6 and 7. Net mean TEER values (background subtracted) are shown, n=8. Statistical significance was determined using two-way ANOVA analysis, *** = $p < 0.001$.

4.4.10. Paracellular permeability of the *in-vitro* blood-brain barrier model

Permeability of paracellular compounds gives an added indicator of the restrictive nature of the BBB model as dictated by the formation of the tight junctions. In agreement with the measured TEER values, the apparent total permeability of Lucifer Yellow, a small molecular weight compound that is transported via the paracellular pathway, was measured at 7.3 ± 0.76 x 10^{-6} cm.s^{-1}. Comparatively the apparent permeability of the control Transwell® inserts (no PBEC monolayer) was significantly higher at 49.2 ± 17.4 x 10^{-6} cm.s^{-1} (Figure 4.10). This result demonstrates the restrictive nature of the *in-vitro* BBB model and reinforces its suitability for conducting transport studies.

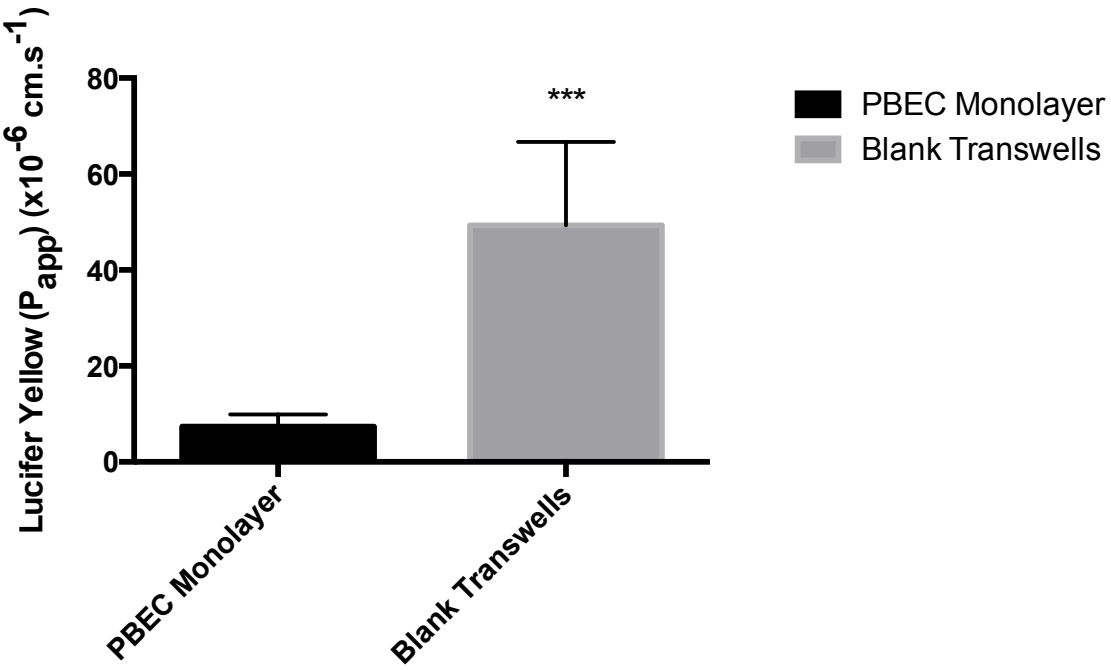

Figure 4. 10: Apparent permeability coefficient of Lucifer Yellow.
Porcine brain endothelial cells were maintained in culture for 48 h with 4 μg.ml^{-1} puromycin. PBECs, 80,000 cells/well, were seeded onto Transwell® inserts and maintained for 4 days in growth medium (DMEM containing 10 % (v/v) plasma-derived serum, 100 U.ml^{-1} penicillin, 100 μ g. ml^{-1} streptomycin, 2 mmol. l-1 glutamine and 125 mmol. l-1 heparin). At day 4 post seeding monolayers were grown in the presence of astrocytes and at day 6 post seeding growth medium was supplemented with 312.5 μM cAMP, 17.5 μM RO20-1724 and 55 nM hydrocortisone; On day 7 Lucifer Yellow (50 μ M) was added to the donor (apical compartment) at t=0 and samples,100 μl, removed from the donor and receiver compartments at 0, 1 h and 3 h. Lucifer yellow (excitation 425 nm and emission 535 nm) were quantified by spectrofluorometry. *** denotes statistical significance of P_{PBEC} vs. P_{filter} to assess contribution of PBEC monolayer. Data are mean ± standard deviation (n=4, 12 replicates for P_{PBEC} and 8 replicates for P_{filter}).

4.4.11. Temozolomide detection and stability test

TMZ can be clearly detected using HPLC/MS/MS (Figure 4.11). In this example, the signal intensity of transition of 50 µM TMZ in the cell culture medium of the *in-vitro* BBB model showed a significant drop with time, reflecting the poor TMZ stability.

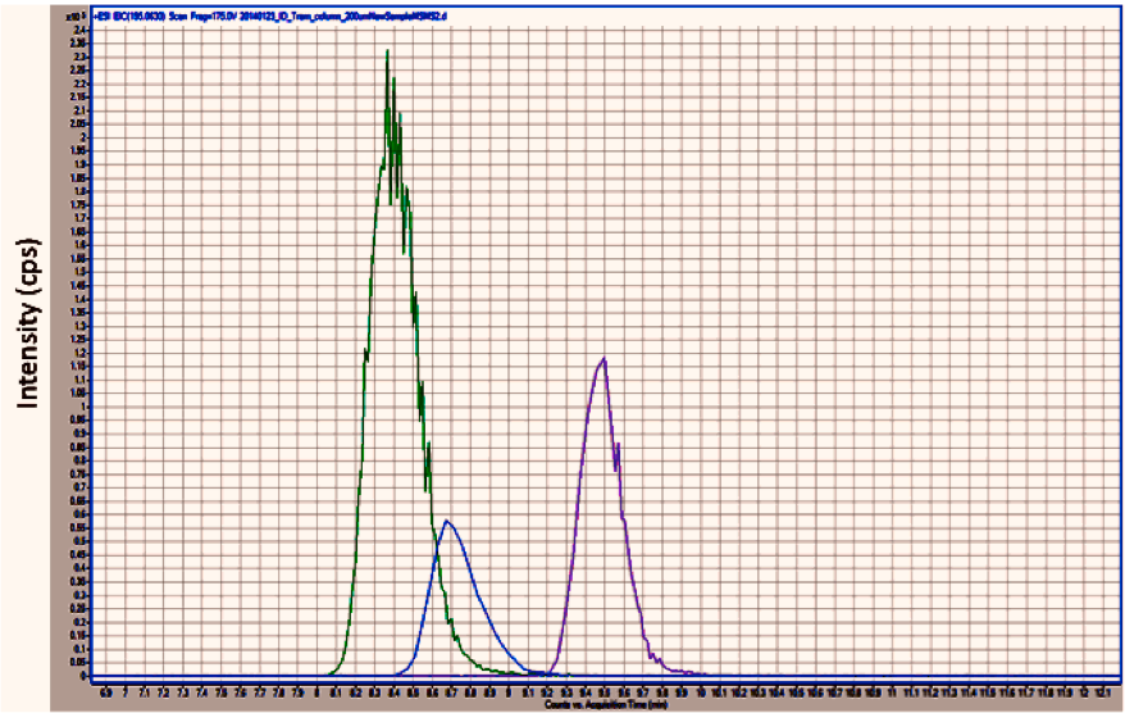

Figure 4. 11: High performance liquid chromatography tandem-mass spectroscopy detection for Temozolomide at the different time points: point 0 (green), 1 hour (purple) and 2 hours (blue). cps, counts per second.

TMZ is a prodrug that is known to undergo rapid breakdown under alkaline conditions to the pharmacologically active product 5-(3-methyltriazen-1-yl)imidazole-4-carboxamide (MTIC) and the non-active product 4-amino-5-imidazole-carboxamide (AIC). Drug transport studies assessing active efflux mechanisms are classically performed over a four-hour window to minimise the effects of passive diffusion and to allow for the detection of weak substrates. Thus, the assessment of TMZ stability over time is particularly important prior to proceeding to *in-vitro* transport studies.

In these experiments, and as reported in the literature, TMZ undergoes rapid breakdown in pH neutral transport experimental settings (Figure 4.12). The degradation was rapid and led to significant loss of signal, which rendered TMZ

detection by HPLC/MS/MS unreliable after two hours. This is a significant limitation, which precludes the use of standard drug transport experiments.

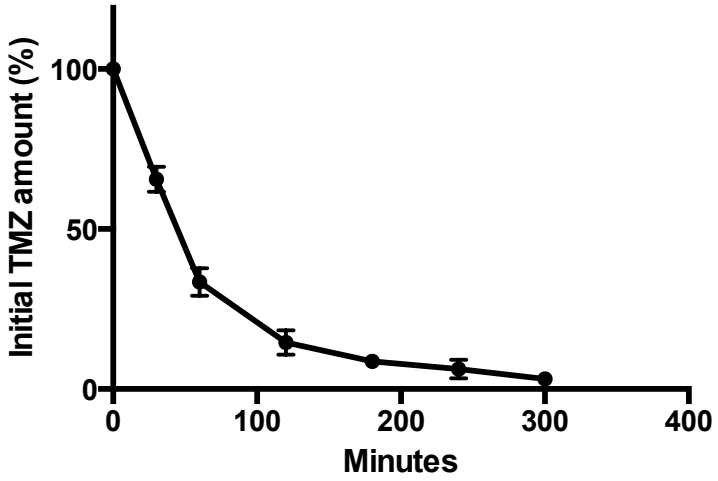

Figure 4. 12: Stability of Temozolomide.
Temozolomide was added to DMEM cell culture medium at a pH of 7.4 and 37ºC. Data are mean ± standard deviation (n=4 with 8 replicates).

A potential solution was to perform the transport studies under slightly more acidic pH conditions. The addition of 8.5% (v/v) phosphoric acid to DMEM cell culture medium to reduce the pH below 6 significantly improved the stability of TMZ and prevented its rapid degradation (Figure 4.13).

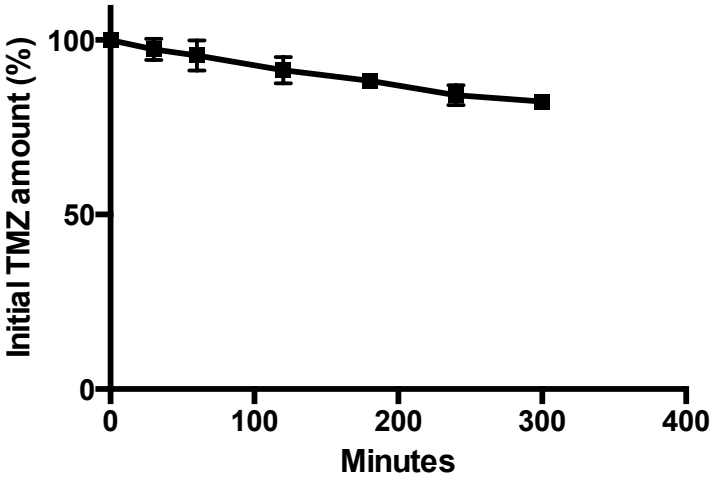

Figure 4. 13: Stability of Temozolomide is improved under acidic conditions.
Temozolomide was added to DMEM cell culture medium containing phosphoric acid at a pH lower than 6 and a temperature of 37ºC. Data are mean ± standard deviation (n=4 with 5 replicates).

4.4.12 Effects of lowering pH on the integrity of the blood-brain barrier model

Once the stability of TMZ under acidic conditions was confirmed, it was essential to assess the impact of lowering pH on the integrity of the *in-vitro* BBB model. Monolayers of PBECs that were exposed to 8.5% (v/v) phosphoric acid demonstrated a significant ($p<0.001$) drop in TEER after four hours of exposure. Comparatively, there was no significant drop in TEER in the monolayers of PBECs that were not exposed to 8.5% (v/v) phosphoric acid (Figure 4.14).

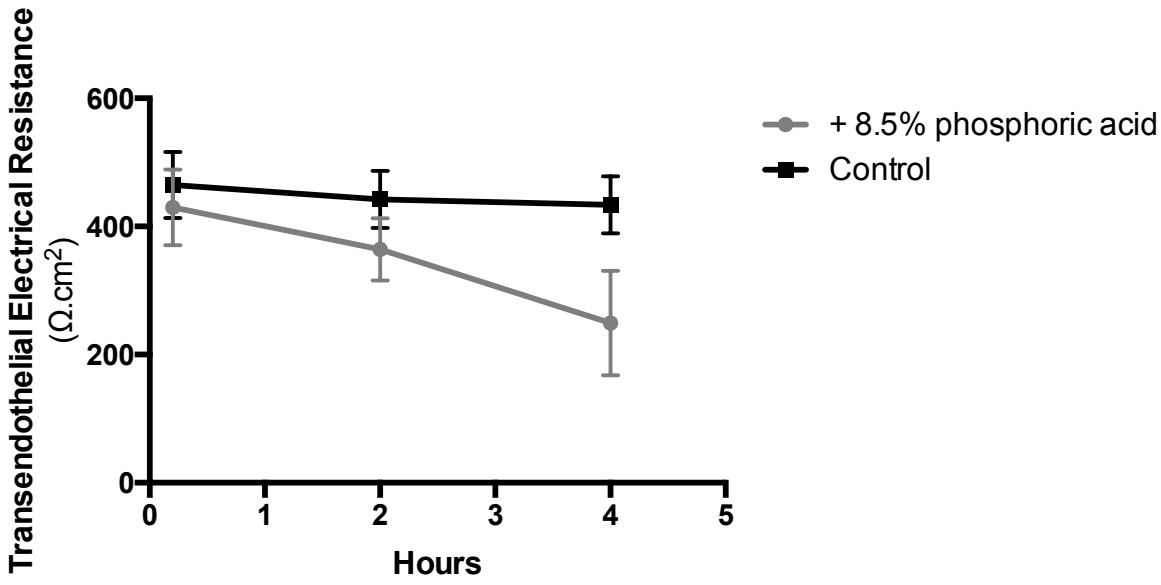

Figure 4. 14: Acidic conditions reduce the transendothelial electrical resistance in the monolayer of porcine brain endothelial cells.
Porcine brain endothelial cells were maintained in culture for 48 h with 4 μg.ml^{-1} puromycin. PBECs, 80,000 cells/well, were seeded onto Transwell® inserts and maintained for 4 days in growth medium (DMEM containing 10 % (v/v) plasma-derived serum, 100 U.ml^{-1} penicillin, 100 μ g. ml^{-1} streptomycin, 2 mmol. l-1 glutamine and 125 mmol. l-1 heparin). At day 4 post seeding monolayers were grown in the presence of astrocytes and at day 6 post seeding growth medium was supplemented with 312.5 μM cAMP, 17.5 μM RO20-1724 and 55 nM hydrocortisone; On day 7, 8.5% (v/v) phosphoric acid was added to the cell culture medium to create **acidic conditions** (reduce the pH below 6) in some Transwells® while others were maintained in the standard **control** conditions. TEER was measured prior to the addition of the acid, 2 and 4 hours subsequently. Data are mean ± standard deviation (*n* = 5 with 12 replicates).

Similarly, the paracellular permeability of PBEC monolayers was significantly ($p<0.005$) increased as evident by the higher permeability to Lucifer Yellow (Figure

4.15). These results indicate loss of integrity in the *in-vitro* BBB model where PBEC monolayers have been exposed to phosphoric acid. Therefore, it is not possible to conduct TMZ transport studies under acidic conditions.

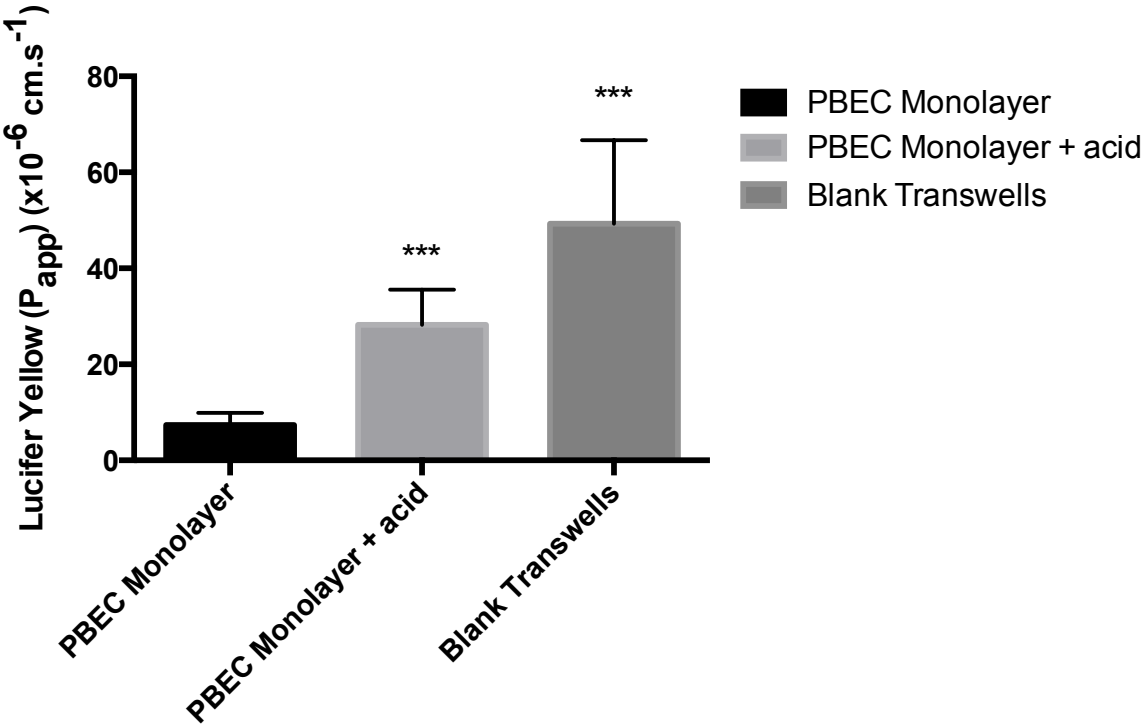

Figure 4. 15: Acidic conditions increase permeability of a monolayer of porcine brain endothelial cells as measured by the apparent permeability coefficient of Lucifer Yellow.
Porcine brain endothelial cells were maintained in culture for 48 h with 4 μg.ml^{-1} puromycin. PBECs, 80,000 cells/well, were seeded onto Transwell® inserts and maintained for 4 days in growth medium (DMEM containing 10 % (v/v) plasma-derived serum, 100 U.ml^{-1} penicillin, 100 μ g. ml^{-1} streptomycin, 2 mmol. l-1 glutamine and 125 mmol. l-1 heparin). At day 4 post seeding monolayers were grown in the presence of astrocytes and at day 6 post seeding growth medium was supplemented with 312.5 μM cAMP, 17.5 μM RO20-1724 and 55 nM hydrocortisone; On day 7 and one hour before the addition of Lucifer Yellow, some PBEC monolayers were treated with 8.5% phosphoric acid to lower the pH. Lucifer Yellow (50 μ M) was added to the donor (apical compartment) at t=0 and samples,100 μl, removed from the donor and receiver compartments at 0, 1 h and 3 h. Lucifer yellow (excitation 425 nm and emission 535 nm) were quantified by spectrofluorometry. *** denotes statistical significance of P_{PBEC} vs. P_{filter} to assess contribution of PBEC monolayer. Data are mean ± standard deviation (n=4, 12 replicates for PBEC monolayer, 12 replicates for PBEC monolayer treated with phosphoric acid and 8 replicates for control Transwell® inserts).

4.4.13. Temozolomide transport studies

The rapid TMZ breakdown encountered in this study renders bidirectional permeability studies challenging as detection of small but significant amounts of active transport may prove difficult. An alternative method is the CETA, where identical concentrations of TMZ are added to both the apical and basal compartments, either in the presence or absence of P-gp and BCRP inhibitors. This method minimises passive diffusion and reduces the effects of TMZ breakdown, as the drug will degrade to an identical degree in both apical and basal compartments that have identical composition. Therefore, it was felt that detailed pharmacokinetics analysis of TMZ breakdown in the apical and basal compartments was not required in this instance.

CETA demonstrates that in the control transwells®, there was a trend for TMZ to accumulate in the apical compartment, which was statistically significant ($P = 0.0153$; Figure 4.16).

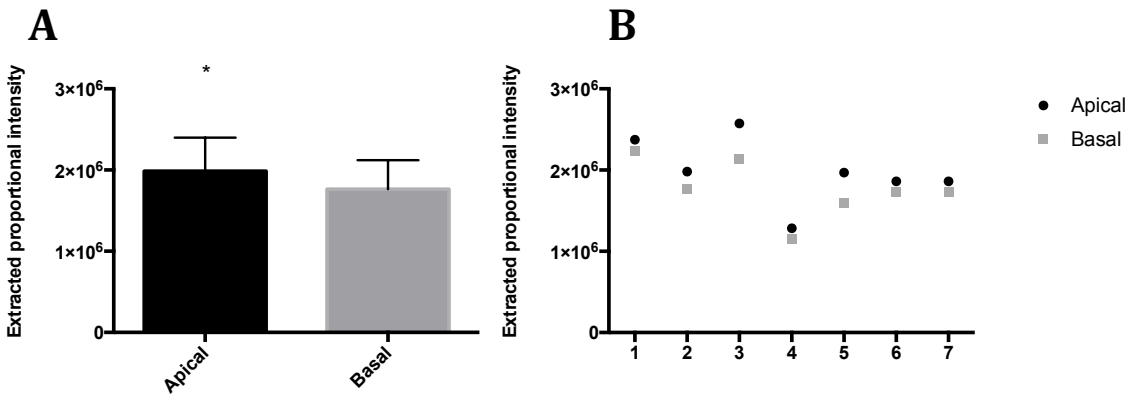

Figure 4. 16 : P-glycoprotein and breast cancer resistance protein mediated transport of Temozolomide.
Temozolomide was added to both compartments at a final concentration of 50 μM. 100 μL samples were withdrawn at 60 minutes from both compartments and analysed immediately with HPLC/MS. Data presented for three separate experiments in (A) with a representative example of individual Transwells® in (B). Data are mean ± standard deviation (n=3, 7-8 replicates). Statistical significance was determined using paired t-test. * Indicates a P value of < 0.05.

Comparatively, Transwells® in which TMZ was incubated with dual P-gp and BCRP inhibition (Figure 4.17) or P-gp inhibition only (Figure 4.18) failed to show any difference in the final measured concentration of TMZ between the apical and basal

compartments.

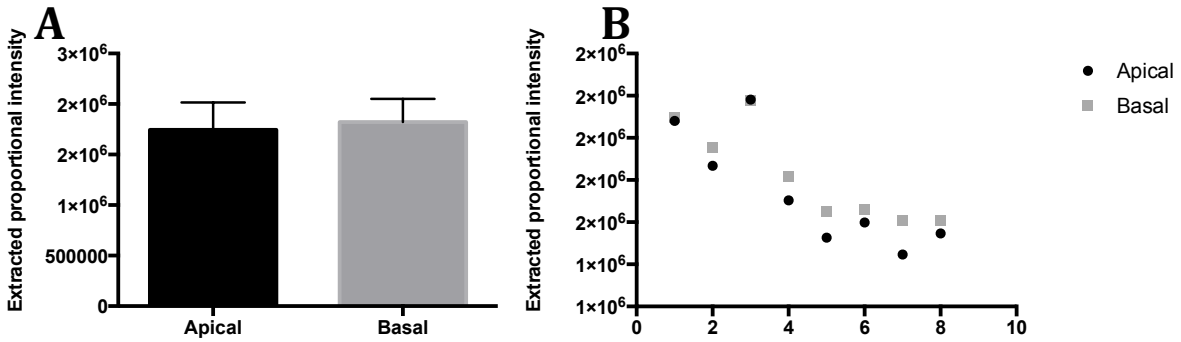

Figure 4. 17: The effects of P-glycoprotein and breast cancer resistance protein inhibition on transport of Temozolomide.
30 minutes before conducting Temozolomide transport study transwells® were incubated with the P-glycoprotein inhibitor verapamil and breast cancer resistance protein inhibitor KO143 to make final concentrations of 10 μM and 0.5 μM respectively. Temozolomide was then added to both compartments at a final concentration of 50 μM. 100 μL samples were withdrawn at 60 minutes from both compartments and analysed immediately with HPLC/MS. Data presented for three separate experiments in (A) with a representative example of individual Transwells® in (B). Data are mean ± standard deviation (n=3, 7-8 replicates). Statistical significance was determined using paired t-test.

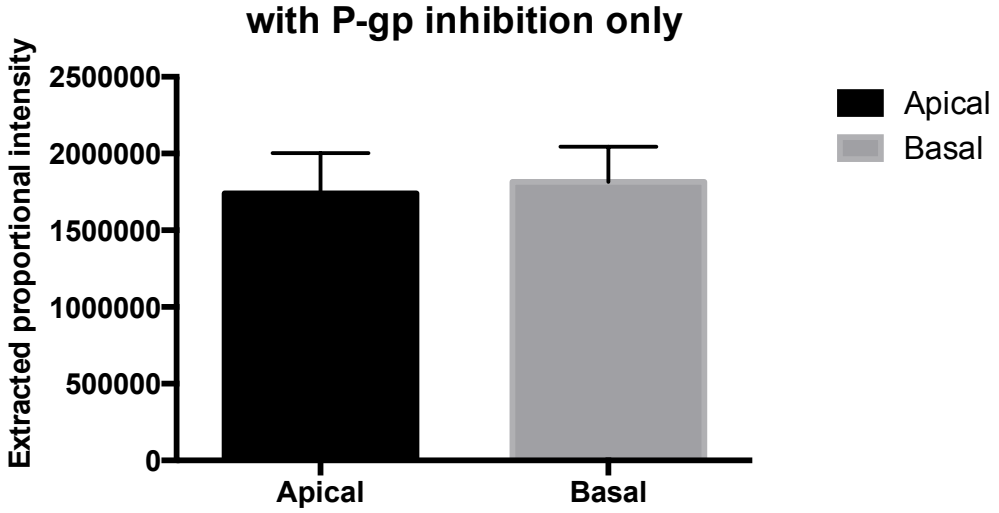

Figure 4. 18: The effects of P-glycoprotein inhibition on the transport of Temozolomide.
30 minutes before conducting Temozolomide transport study Transwells® were incubated with the P-glycoprotein inhibitor verapamil (final concentrations of 10 μM).

Temozolomide was then added to both compartments at a final concentration of 50 μM. 100 μL samples were withdrawn at 60 minutes from both compartments and analysed immediately with HPLC/MS. Data are mean ± standard deviation (n=3, 7-8 replicates). Statistical significance was determined using paired t-test.

These results suggest active TMZ transport in the absence of a concentration gradient and indicate a potential role for P-gp and BCRP in the active efflux of TMZ. However, the limited evidence of active transport after one hour also suggests that TMZ is unlikely to be a strong substrate for these transporters.

4.5. Discussion and conclusions

One of the main functions of the BBB is to protect the brain from harmful substances in systemic circulation. This includes cytotoxic agents that are commonly used in the treatment of high-grade brain tumours. The contribution of the BBB may appear less critical in the settings of a high-grade glioma tumour, especially as disruption of the BBB integrity is to be expected (Larsson et al., 1990). Furthermore, the treatment of high-grade glioma includes radiotherapy, which can impair the BBB integrity and increase its permeability. Multiple studies demonstrated that systematically administered chemotherapy agents reach higher concentration in the tumour core when compared with the adjacent brain tissue (Pitz et al., 2011). This includes Temozolomide which is the only frontline chemotherapy treatment approved by the Food and Drug Administration (FDA) for glioblastoma multiforme.
Despite this, treatment outcomes for glioblastoma multiforme remain poor with a median survival rate of 14.6 months (Stupp et al., 2005). A possible explanation for such poor outcomes could be the fact that chemotherapy agents fail to reach the edges of the growing tumour, where tumoural cellular infiltration of the normal brain precedes disruption of the BBB. Furthermore, the endothelial cells of the BBB express various efflux transporters such as P-gp and BCRP, which serve as efflux pumps mediating the transport of drugs from the endothelial cells back into the blood stream.

Additionally, the development of chemoresistance of glioma cells to TMZ remains a major limiting factor in the effective treatment of glioma patients. One of the important mechanisms for developing this chemoresistance is the up regulation of efflux transporters, such as P-gp. The role of P-gp in mediating chemoresistance remains controversial and poorly understood. However, there is increasing evidence pointing towards a relationship between the over expression of P-gp and the development of chemoresistance. For example, Zhang et al. demonstrated that photodynamic therapy enhanced TMZ effects in a glioma model in rats by limiting the expression of P-gp in the intact BBB and in the glioma cells (Zhang et al., 2014). In a more recent study, Munoz et al. indirectly demonstrated that TMZ, at high concentrations, competes for P-gp, and that P-gp expression mediated the development of chemoresistance (Munoz

et al., 2015b). Furthermore, this study showed enhanced TMZ anti-tumuoral effects when combined with P-gp inhibition (Munoz et al., 2015b). The relationship between TMZ and P-gp was also evaluated in genetically modified mice that lacked P-gp, where P-gp lacking mice showed small increases in TMZ transport into the brain (Goldwirt et al., 2014).

It is important to note that the clinical translation of these studies proved more challenging with only a single study suggesting a solitary *MDR1* single nucleotide polymorphism (which encodes for P-gp) capable of predicting TMZ treatment outcomes in patients with GBM tumours (Schaich et al., 2009). However, other studies failed to observe the same finding. For example, Demeule et al. reported that *MDR1* expression was higher than normal brain in only three GBM patients while three had similar and four had even lower expression than the normal brain (Demeule et al., 2001).

The majority of the available literature on *in-vitro* studies attempts to indirectly evaluate the relationship between TMZ and P-gp and they clearly point towards a relationship between the two. However, only a solitary study attempted to examine directly TMZ transport by P-gp (Goldwirt et al., 2014). It is important to note that in this study TMZ accumulation in the brain of mice was measured after freezing and storing the brain samples in −20ºC. Storing brain samples at −20ºC can slow, but does not eliminate, spontaneous TMZ degradation, which can cloud the finding of limited P-gp mediated transport of TMZ.

Moreover, when evaluating novel compounds it is becoming increasingly important to evaluate P-gp and BCRP efflux transporters simultaneously. This holds especially true, as these transporters are known to work in tandem in effluxing many anticancer drugs. This is well documented in multiple studies highlighting limited BBB penetration of a given agent with solitary (P-gp or BCRP) efflux transporter inhibition, but demonstrating that much greater BBB penetration was achieved with dual inhibition of these transporters (de Vries et al., 2007) (Polli et al., 2009) (Kodaira et al., 2010) (Agarwal et al., 2011c). The relationship between TMZ and the efflux transporters P-gp and BCRP has never been evaluated in a single unifying study. This study is believed to be the first to directly investigate the effects of P-gp and BCRP inhibition

on the transport of TMZ at clinically relevant concentrations.

Measuring drug concentration in brain tissue in a clinical study is not feasible and also unethical. The use of CSF as a surrogate marker has been suggested, however, the blood-CSF barrier is highly permeable and does not represent a suitable surrogate for the brain. Given these challenges and limitations, the use of an *in-vitro* BBB model for TMZ transport studies was felt to be justified.

An essential step in conducting drug transport experiments is the development and validation of a reproducible *in-vitro* BBB model that replicates the *in-vivo* settings. Our *in-vitro* non-contact co-culture BBB model uses PBECs and the immortalised rat astrocyte cell line CTX-TNA2. The use of PBECs in the development of *in-vitro* BBB models is well established (Franke et al., 1999) (Zhang et al., 2006) (Cohen-Kashi Malina et al., 2009) (Skinner et al., 2009). The use of the CTX-TNA2 cell line has also been described previously and is known to induce and maintain key features of the *in-vivo* BBB (Cantrill et al., 2012).

In the present model the measured TEER consistently achieved values of 400 $\Omega.cm^2$, which is lower than previously described by Cantrill et al. (Cantrill et al., 2012). However, it is important to note that the TEER values are still higher than many of the reported models (Zhang et al., 2006) and are at least three times as high as the recommended values by FDA for transport studies (Luna-Tortos et al., 2008). Additionally, here, Transwell® inserts that demonstrated TEER lower than 300 $\Omega.cm^2$ or showed a 20% drop in the TEER from the initial values at the end of the experiment were excluded. These steps ensured the use of an *in-vitro* BBB model that demonstrated the desired structural characteristics with excellent restrictive nature as reflected in the high TEER and low permeability to Lucifer Yellow.

Evaluation of the efflux transporters P-gp and BCRP is a primary objective, and an essential aspect of this study is to confirm the functional activity of those two major efflux transporters. The functional activity of P-gp was confirmed by observing a seven-fold increase in the intracellular accumulation of calcein following inhibition of P-gp. Similarly, the functional activity of BCRP was also confirmed by observing almost a three-fold increase in the intracellular accumulation of Hoechst 33342. These values are comparable to other studies (Cantrill et al., 2012) and provide further validation to the suitability of the *in-vitro* model for conducting TMZ transport studies.

Assessing the stability of compounds in the experimental conditions is another integral part of any transport study. TMZ is a prodrug that undergoes disintegration in a non-enzymatic, pH and temperature dependent manner. In short, TMZ has excellent bioavailability when administered orally, largely due to being robust and stable in the acidic conditions of the stomach. However, once TMZ reaches more basic pH conditions (blood and tissues) it undergoes rapid hydrolysis to its active metabolite MTIC, which in turn yields the reactive methyldiazonium ion (Marchesi et al., 2007).
As reported in literature, TMZ was found to undergo a rapid and exponential degradation in experimental conditions at physiological pH and 37ºC with an estimated half-life of 1.1 hour. This half-life is close to the values reported by Stevens et al, for TMZ in phosphate buffer, and Linz for TMZ in culture medium, with half-lives of 1.24 and 1.3 h respectively (Stevens et al., 1987) (Linz et al., 2015). However, these values are significantly shorter than the observed half-life of 1.8 h in human plasma. Such rapid breakdown is detrimental for *in-vitro* transport studies as these experiments are ideally conducted over a four-hour period.
In an attempt to enhance the stability of TMZ experimental conditions were acidified by adding 8.5% (v/v) phosphoric acid. Acidification of the experimental conditions successfully slowed the degradation but had an additional negative impact. In addition to stabilising TMZ degradation, the addition of 8.5% phosphoric acid resulted in loss of the barrier proprieties of the *in-vitro* BBB model. This was reflected in the significant drop in TEER, which precludes meaningful drug transport studies.

Classical drug transport studies are based on concentration gradient transport assays. These assays use a cellular monolayer to evaluate the affinity of a given efflux transporter for a certain drug. P-gp overexpressing cell lines are commonly employed to enhance the sensitivity of such assays. In short, these assays are based on placing a particular drug in a donor compartment (basal) and assessing transport against a concentration gradient in the receiver compartment (apical). However, this method may still fail to correctly identify true active efflux transportation. This is especially true in compounds with low molecular weight where high permeability and passive diffusion can compensate and obscure active efflux (Luna-Tortos et al., 2008). This is particularly important to our study as TMZ is characterised by being highly lipophilic with low molecular weight (194 Daltons), which in theory should enables it to cross

the BBB freely (Patel et al., 2003). The choice of cell line is also important. For example, most concentration gradient assays employ a cell line that over-expresses the transporter in question (e.g. MDR1-transfected MDCKII cells for P-gp). The utility of such cell lines to enhance the sensitivity of these experiments is controversial. Such cell lines clearly fail to replicate the human *in-vivo* settings, which is a clear and substantial drawback.

To address these limitations, a CETA was employed, where the same concentration of TMZ was added to the basal and apical compartments of the *in-vitro* BBB model. True active drug transport is then decided when an increase in the drug concentration in the apical compartment is detected over time. This type of assay is particularly powerful in measuring transporter-mediated efflux of highly permeable compounds such as antibiotics (Pachot et al., 2003) and antiepileptic drugs (Luna-Tortos et al., 2008).
A major advantage of the CETA is that it unifies the experimental conditions in the apical and basal compartments by adding identical concentrations of a drug. Although drug degradation will not be affected *per se*, adding identical concentrations in both compartments eliminates the effects of TMZ breakdown on the results. This is clearly relevant in our study due to TMZ degradation. Another important advantage for CETA is that it eliminates the concentration gradient and as a result reduces the effects of passive diffusion and improves the detection of active drug transport.

Our findings demonstrate that the efflux transporters P-gp and BCRP weakly transport TMZ. This is best appreciated when analysing the TMZ transport in Transwells® individually. TMZ was detected in higher concentrations in the apical compartments in the absence of P-gp and BCRP inhibition. An important limitation to our study is the limited time window of 60 minutes. Drug transport studies in general, and CETA in particular, needs to be extended over greater time, typically four hours. A recent study found that even for known strong P-gp substrates, such as digoxin and phenytoin, CETA might be negative in the first 60 minutes. Significant transport however, can be detected after the 100 minutes mark (Luna-Tortos et al., 2008). Our finding of weak P-gp and BCRP-mediated transport suggest that TMZ is likely to be a weak substrate and extending the CETA duration could have proved helpful.

A possible solution is to increase the concentration of TMZ in these experiments,

which will prolong the window for TMZ. However, this was avoided as raising the concentration of TMZ above the clinically relevant dose may alter its substrate status as seen with other compounds such as cyclosporin A (Saeki et al., 1993). Additionally, raising the concentration multiple folds above the clinically relevant concentration fails to replicate the clinical settings.

In a recent study, Munoz et al reported that raising the concentration of TMZ (ten times higher than the clinically relevant dose) resulted in an increase in the intracellular accumulation of calcein AM in the multiple drug resistant variant of a lung epithelial cell line (known to overexpress P-gp); the authors concluded that TMZ was a substrate for P-gp (Munoz et al., 2015b). This result was not reproduced in our experimental conditions with the PBEC cell line that resembles the human endothelial cells more closely. Furthermore, in the Munoz study they failed to reproduce P-gp inhibition when using lower concentrations of TMZ or with the original lung epithelial cell line DC3F. This study also noted increased TMZ efficacy in two glioma cell lines in the presence of P-gp inhibitions and used a computer-modelling approach to demonstrate TMZ and P-gp interaction. While these results suggest a role of P-gp in the transport of TMZ, they failed to examine the role of BCRP and did not demonstrate definitive P-gp-mediated TMZ transport directly.

This study set out to establish if TMZ, at clinically relevant concentrations, was transported by P-gp and BCRP using an *in-vitro* BBB model that closely resembles the human *in-vivo* setting. The findings show a trend for TMZ to be weakly transported by P-gp and BCRP and add to the evidence implicating P-gp and BCRP in the active transport of TMZ.

Improving outcomes for patients with high-grade glioma will prove challenging. Inhibition of efflux transporters, such as P-gp and BCRP, may be a valid strategy for enhancing TMZ delivery into brain tumours and overcoming the BBB obstacle. Although these studies increase the evidence demonstrating interaction of TMZ with BBB efflux transporters, more robust evidence is clearly needed before a definite conclusion about TMZ relationship with the efflux transporters can be made, and before treatment strategies can be employed clinically.

Chapter 5 Preclinical *In-vivo* Imaging Study: Temozolomide is Transported by P-glycoprotein and Breast Cancer Resistance Protein Efflux Transporters at the Mouse Blood-Brain Barrier.

5.1. Abstract

Purpose: To confirm the status of TMZ as a substrate for P-gp and BCRP efflux transporters.

Methods: PET scans were performed with [^{11}C]TMZ in female wild type and in mice with genetic knockout of P-gp, BCRP and both transporters. Imaging was also performed in wild type mice before and after the administration of Tariquidar (TQD) to achieve dual P-gp and BCRP transporters inhibition.

Results: Brain-to-plasma ratio of [^{11}C]TMZ were low in wild type mice (0.432 ± 0.042) and slightly higher in mice lacking either transporter (P-gp KO: 0.445 ± 0.031 , BCRP KO: 0.427 ± 0.062) but only significantly higher in mice lacking both transporters (0.575 ± 0.049, p: 0.0045).
Similar results were obtained with the chemical inhibition of both transporters with animals that received TQD showed a higher brain-to-plasma ratio of radioactivity that was significant (vehicle: 0.426 ± 0.039, TQD: 0.524 ± 0.048, p = 0.020).

Conclusions: This study confirms that TMZ is transported by both P-gp and BCRP efflux transporters at the mouse BBB and that dual transporter inhibition is required to significantly enhance TMZ delivery into the brain.

5.2. Introduction

The efficacy of chemotherapy for the treatment of brain tumours relies on the ability of the agent to penetrate the BBB and reach meaningful concentrations in the brain. The BBB restricts the entry of such agents to the brain structurally with tight junctions, leading to low paracellular permeability, and through the expression of various efflux transporters, such as P-gp and BCRP. These transporters are expressed on the luminal membrane of endothelial cells of the BBB. They actively efflux various anticancer drugs into the systemic circulation. Furthermore, the two transporters appear to work together and overlap in their affinity for various anticancer drugs (Szakacs et al., 2006) (de Vries et al., 2007) (Kodaira et al., 2010).

TMZ is an alkylating prodrug that readily crosses the BBB. However, its exact relationship with the efflux transporters P-gp and BCRP remains poorly understood. *In-vitro* studies point to a role for P-gp in the development of chemoresistance to TMZ: long-term treatment with TMZ leads to increased expression of P-gp. Other recent studies have demonstrated that TMZ competes for the P-gp efflux transporters (Munoz et al., 2014) (Munoz et al., 2015b). A preclinical *in-vivo* study using P-gp knockout mouse models has suggested a very limited role for P-gp in the transport of TMZ (Goldwirt et al., 2014). This is the only study to directly demonstrate transport of TMZ by an efflux transporter. Furthermore, Schaich et al. (Schaich et al., 2009) have shown that tumour expression of P-gp could affect the response to TMZ treatment. Interestingly, none of these studies addressed the role of BCRP in the transport of TMZ. Therefore, inaccurate conclusions could have been reached.

The aim of the present study was to confirm the results of previous *in-vitro* studies by demonstrating active efflux of [^{11}C]TMZ by P-gp and BCRP at the mouse BBB. Small animal PET scans were performed in wild-type and transporter knockout mice, and the third-generation P-gp inhibitor tariquidar Tariquidar (TQD) (Fox and Bates, 2007) was used in wild-type mice.

5.3. Materials and Methods

5.3.1. Chemicals

If not stated otherwise, chemicals were purchased from Sigma-Aldrich (Poole, UK), of analytical grade and used without further purification. TQD was obtained from AzaTrius Pharmaceuticals Pvt Ltd (London, UK). For the formulation of the TQD for the *in-vivo* PET experiments, a stock solution of 7.5 mg/mL of TQD free base in 20% ethanol and 80% propylene glycol was diluted with aqueous dextrose solution (5% w/v) to make up the final desired dose of 15mg/kg of TQD in 100 µL. [^{11}C]TMZ was synthesised in-house by broadly following the procedure described by Moseley et al. (Moseley et al., 2012) but with slight modifications to the reaction conditions to improve the yield. Radiochemical purity was in excess of 98%, with specific activity at the end of synthesis of 734.72 ± 344.1 MBq/nmol (n = 22) (figure 5.1).

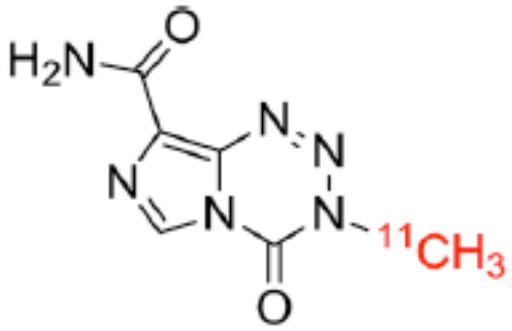

Figure 5.1: Chemical structure of [^{11}C]Temozolomide.

5.3.2. Animals

All animal procedures were approved by the Home Office Inspectorate, carried out under the University of Manchester project license number (40/3268) and conducted according to UK-CCCR guidelines, in compliance with the UK Animal Scientific Procedure Act of 1986. Efforts were made to minimise the number of animals used for each experiment without sacrificing the ability to obtain meaningful results. Animals were maintained with the highest possible standard of care.

The initial female FVB/N (wild type) mice were obtained from Charles River Laboratories (Canterbury UK). The remaining animals, including the female FVB/N (wild type) mice used in the metabolite and PET imaging study, P-gp knockout *Mdr1a/b*$^{(-/-)}$, BCRP knockout *Bcrp*$^{(-/-)}$ and dual P-gp and BCRP knockout *Mdr1a/b*$^{(-/-)}$*Bcrp*$^{(-/-)}$ mice were obtained from Taconic Inc. (Germantown, NY, USA).
All animals used in this study were of the same FVB strain.

The animals were housed in groups with a maximum number of five animals per group with free access to food and water. Environmental conditions were controlled at 45%-65% humidity, a temperature range of 20 − 23ºC and a 12-hour light-dark cycle. The animals used in the experiments reached a minimum weight of 21 g and were between 12 and 16 weeks of age.

5.3.3. Experimental design

Metabolism of [^{11}C]TMZ was evaluated in two groups of wild type (obtained from Charles River, UK and Taconic Inc., USA), P-gp knockout *Mdr1a/b*$^{(-/-)}$, BCRP knockout *Bcrp*$^{(-/-)}$ and dual P-gp and BCRP knockout *Mdr1a/b*$^{(-/-)}$*Bcrp*$^{(-/-)}$ mice. Animals were injected with the radiotracer [^{11}C]TMZ and blood and brain samples were collected for processing and HPLC analysis at the designated time points, as detailed below.

Some mice from the USA based supplier underwent 60-minutes dynamic [^{11}C]TMZ PET scanning. Additionally, to assess the effects of TQD on the brain uptake of [^{11}C]TMZ, a group of wild type animals underwent 60-minute dynamic [^{11}C]TMZ PET scans in which a pharmacological dose of TQD (15 mg/kg) was administered 40 minutes after radiotracer administration. TQD was administered over a time period of one minute via a second tail vein cannula. This particular dose of TQD was chosen based on previous work that showed complete P-gp and significant BCRP inhibition (Wanek et al., 2012). TQD was administered during the PET scan acquisition as previous study showed that IV administration could achieve rapid P-gp inhibition even at low doses (Kreisl et al., 2015). We elected to insert a second tail vein cannula in

order to avoid undesired administration of any residual radiotracer present in the dead space.

5.3.4. Blood, plasma and brain metabolite analysis

Mice were anaesthetised using 1-2% isoflurane in oxygen. The tail vein of each mouse was catheterised under anaesthesia and [^{11}C]TMZ was manually injected intravenously as a bolus injection over 10 seconds.

The injected dose of [^{11}C]TMZ was calculated by measuring the radioactivity in the syringe prior to injection in a dose calibrator followed by subtracting the measured residual radioactivity in the syringe after the injection.

Animals were kept under anaesthesia and upon reaching the desired time point; blood samples were collected by direct cardiac puncture after which the animals were euthanised by cervical dislocation. Brain samples were immediately collected for homogenisation and HPLC analysis.

FVB/N wild type mice sourced from Charles River Laboratories (Canterbury, UK) (n = 10, 21.4 − 26.4 g) were euthanised at 10 (n = 2), 20 (n = 1), 30 (n = 2), 40 (n = 3), 50 (n = 1) and 60 (n = 1) minutes after [^{11}C]TMZ injection.

Similarly, FVB/N wild type animals sourced from Taconic Inc. (Germantown, NY, USA) (n = 12, 22.5 − 29.3 g) were euthanised at 10 (n = 3), 20 (n = 2), 40 (n = 4) and 60 minutes after [^{11}C]TMZ injection. The *Mdr1a/b*$^{(-/-)}$ (n= 4, 24.1 − 26.2 g), *Bcrp*$^{(-/-)}$ (n= 4, 21.6 − 24.1 g) and *Mdr1a/b*$^{(-/-)}$*Bcrp*$^{(-/-)}$ (n= 4, 22.5 − 26.2 g) mice (n= 4 per group) were euthanised at the single time point of 40 minutes. Additional metabolite analysis was performed at the single time point of 60 minutes in the wild type animals (n = 4, 24.6 − 30) sourced from Taconic Inc. (Germantown, NY, USA), which were injected with TQD(15mg/kg) 40 minutes after [^{11}C]TMZ injection.

Details of the UK and USA sourced animals used in the radiolabelled metabolites analysis are provided in Table 5.1 and 5.2 respectively.

Table 5. 1: Characteristics of UK sourced animals that underwent plasma and brain metabolite analysis following injection with [^{11}C]Temozolomide.

Animal ID	Time Point	Injected dose (MBq)	Weight (g)
a01760	10 minutes	25.69	24.1
a01765	10 minutes	53.98	24.2
a01763	20 minutes	47.73	21.4
a01769	30 minutes	43.33	22.0
a01771	30 minutes	44.84	22.9
a01761	40 minutes	18.28	24.2
a01766	40 minutes	29.43	25.2
a01768	40 minutes	49.84	23.7
a01773	50 minutes	32.75	26.0
a01762	60 minutes	33.20	23.7

Table 5. 2: Characteristics of USA sourced animals that underwent plasma and brain metabolite analysis following injection with [^{11}C]Temozolomide.

Animal ID	Group	Time Point	Injected dose (MBq)	Weight (g)	Intervention
a02131	Wild-type	10 minutes	32.92	28.1	-
a02135	Wild-type	10 minutes	44.15	22.5	-
a02139	Wild-type	10 minutes	66.57	24.0	-
a02130	Wild-type	20 minutes	63.42	27.6	-
a02134	Wild-type	20 minutes	46.22	24.8	-
a02132	Wild-type	40 minutes	44.10	26.4	-
a02136	Wild-type	40 minutes	45.39	24.1	-
a02138	Wild-type	40 minutes	63.13	26.4	-
a02140	Wild-type	40 minutes	33.84	27.8	-
a02129	Wild-type	60 minutes	79.80	25.8	-
a02133	Wild-type	60 minutes	62.83	23.7	-
a02137	Wild-type	60 minutes	60.22	29.3	-
a02141	Wild-type	60 minutes	68.40	29.2	TQD 15mg/kg
a02142	Wild-type	60 minutes	42.41	28.5	TQD 15mg/kg
a02143	Wild-type	60 minutes	51.45	24.6	TQD 15mg/kg
a02144	Wild-type	60 minutes	53.53	30.0	TQD 15mg/kg
a01849	P-gp KO	40 minutes	47.86	24.6	-
a01850	P-gp KO	40 minutes	38.41	24.6	-
a01851	P-gp KO	40 minutes	39.10	24.1	-
a01852	P-gp KO	40 minutes	23.38	26.2	-
a01853	BCRP KO	40 minutes	28.44	21.6	-
a01854	BCRP KO	40 minutes	41.81	22.7	-
a01855	BCRP KO	40 minutes	27.82	24.1	-
a01856	BCRP KO	40 minutes	50.76	23.0	-
a01857	Dual KO	40 minutes	51.23	25.7	-
a01858	Dual KO	40 minutes	42.56	26.2	-
a01859	Dual KO	40 minutes	17.11	22.5	-
a01860	Dual KO	40 minutes	54.26	22.6	-

Tariquidar (TQD) was administered by IV bolus 40 minutes after radiotracer injection.

Blood samples collected by direct cardiac puncture were transferred to Eppendorf tubes. The samples were placed on ice until 15 µL was pipetted into an AGC tube containing 1 mL of sterilised water. Plasma was obtained by centrifuging (PK121R centrifuge) the remaining blood samples for 3 minutes at 4ºC with a force of 8050 x g and 15 µL of plasma was added to 1 mL of sterilised water.

Following cardiac puncture, the brain (without cerebellum) was quickly removed from the skull and added to a 10 mL tube containing 1 mL of 50 mM ammonium acetate at an adjusted pH of 6.6. Low pH ensured stability of TMZ and prevented further degradation. The brain was then homogenised using a rotatory blade homogeniser (CAT x 120) at maximum speed for 1 minute. The brain homogenate was subsequently centrifuged for 3 minutes at 4ºC with a force of 8050 x g and 15µL was pipetted and was added to 1 mL of sterilised water.
The total radioactivity concentration in blood, plasma, brain homogenates and supernatants was measured using an automatic gamma counter (AGC, Perkin Elmer Wizard 1470).

Following centrifugation, the remaining plasma samples were injected into the HPLC system (Shimadzu HPLC Prominence) for analysis. The homogenised brain samples were placed on ice whilst HPLC analysis of the plasma samples occurred. Briefly, the HPLC analysis started by manually injecting 150 − 200 µL aliquots of processed plasma and brain samples into the injector. Separation was achieved on an ACE phenyl column (150 x 4.6mm, 5 µm). A guard cartridge was employed for additional column protection. The mobile phase consisted of 50 mM ammonium acetate at a pH of 6.6 and acetonitrile on a gradient method (0 − 10% acetonitrile) with a run time of approximately 20 minutes. Radioactivity detection was achieved via a modified in-house radioactive detector containing a Nal-Well detector with a 1 mL loop.
A universal chromatography interface was used to convert the electronic signal into digital data. For all HPLC chromatograms, the peaks were identified and integrated using Dionex HPLC software (Chromeleon version 6.6). Areas under the curve (AUC) were integrated along with the corresponding peaks from the radioactive trace and then

expressed as percentage of the total peak area. Additionally, all biological samples were spiked with 10µL of unlabelled TMZ as a reference standard to confirm the relative retention time of the parent peak and to track column performance.

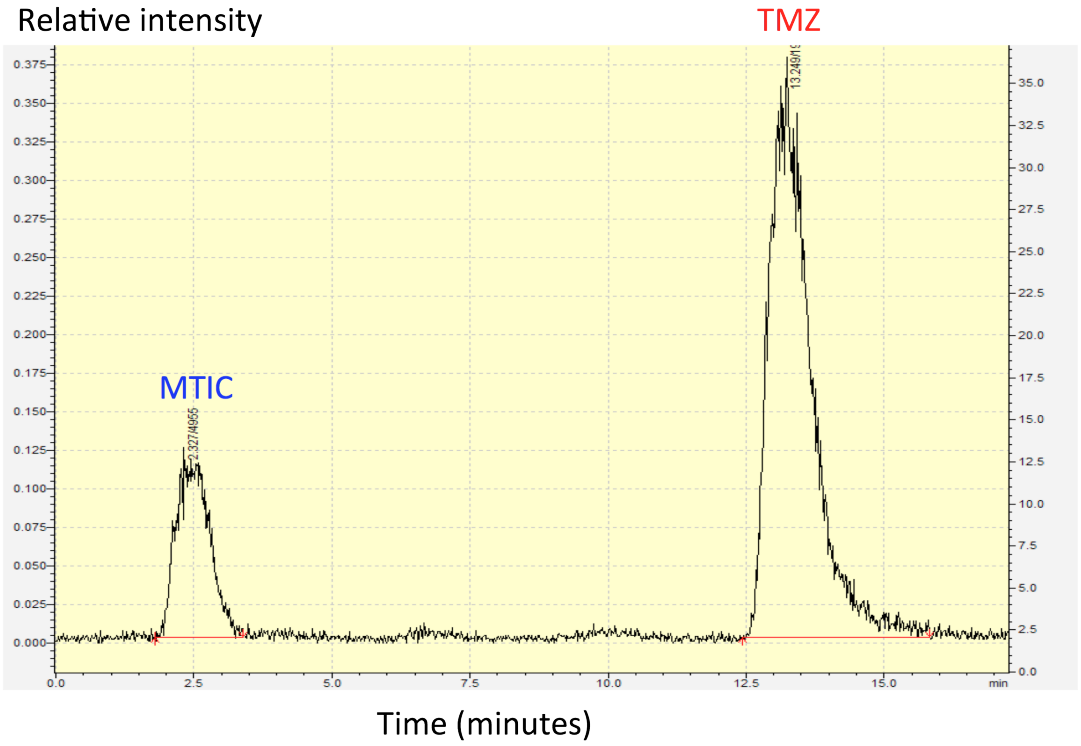

Figure 5. 2: Representative chromatogram of Temozolomide (TMZ) and its active daughter metabolite MTIC in mouse brain 40 minutes post [^{11}C]TMZ injection. Note that Temozolomide elution time is approximately 13.5 minutes with an early MTIC elution time at 2.5 minutes.

5.3.5. Small animal positron emission tomography

Mice were anaesthetised with 1-2% isoflurane in oxygen and the tail vein was catheterised. The animal was then placed into the prone position in the single animal bed (Minerve small animal environment system, Bioscan) with the head restrained on the tooth bar. The mouse was then transferred to an Inveon preclinical PET-CT scanner (Siemens).

Acquisition protocol started with a whole body CT scan prior to PET scan for attenuation and scatter correction. The time coincidence window was set to 3.432 ns and the level of energy discrimination was set to 350 − 650 keV. A reference laser beam was utilised to ensure placement of the brain in the centre of the scanner's field of view in order to enhance sensitivity and spatial resolution.

Anaesthesia was maintained with 1-2% isoflurane in oxygen delivered via a nose cone and adjusted according to the depth of anaesthesia. Respiratory rate and temperature were continuously monitored throughout image acquisition using a pressure sensitive pad and rectal probe. Body temperature was controlled via fan module controlled by BioVet (Inveon) software.

At the start of the scan, the mouse was injected with [^{11}C]TMZ intravenously via the tail vein catheter and list mode data were collected for 60 minutes. Following the scan, the animals recovered in a warmed chamber.

As detailed in section (5.3.4.) the injected dose of [^{11}C]TMZ was calculated by measuring the radioactivity in the syringe prior to injection in a dose calibrator followed by substractiong any measuered residual radioactivity in the syringe after the injection.

Table 5.3 provides the details of the 25 mice used in the PET imaging studies.

Table 5. 3: Characteristics of animals that underwent PET scanning positron emission with [^{11}C]Temozolomide.

Animal ID	Group	Source	Injected dose (MBq)	Weight (g)	Intervention
a01767	Wild-type	UK	55.16	22.6	-
a01768	Wild-type	UK	56.33	23.4	-
a01769	Wild-type	UK	38.86	25.6	-
a01770	Wild-type	UK	61.26	21.7	-
a01772	Wild-type	UK	60.33	24.9	-
a01849*	P-gp KO	USA	38.73	24.7	-
a01850	P-gp KO	USA	37.73	23.4	-
a01851	P-gp KO	USA	42.35	23.9	-
a01852	P-gp KO	USA	43.35	23.7	-
a01853	BCRP KO	USA	31.44	21.6	-
ao1854	BCRP KO	USA	35.95	22.6	-
a01855	BCRP KO	USA	35.20	23.5	-
a01856	BCRP KO	USA	38.89	23.2	-
a01857	Dual KO	USA	33.18	26.5	-
a01858	Dual KO	USA	42.20	25.6	-
a01859	Dual KO	USA	48.15	23.0	-
a01860	Dual KO	USA	46.61	25.2	-
a02129	Wild-type	USA	79.79	25.2	-
a02133	Wild-type	USA	62.83	23.7	-
a02137	Wild-type	USA	60.22	29.3	-
a02139	Wild-type	USA	32.12	23.4	-
a02141	Wild-type	USA	68.40	29.2	TQD 15mg/kg
a02142	Wild-type	USA	42.41	28.5	TQD 15mg/kg
a02143	Wild-type	USA	51.45	24.6	TQD 15mg/kg
a02144	Wild-type	USA	53.53	30.0	TQD 15mg/kg

Tariquidar was administered by IV bolus 40 minutes after radiotracer injection.* scanned twice.

5.3.6. Image reconstruction and analysis

The list mode data were histogrammed with a span of 3 and a maximum ring difference of 79 into 3D sinograms. The list mode data for the emission scans were sorted into 16 dynamic frames (5 x 60 seconds, 5 x 120 seconds, 3 x 300 seconds and 3 x 600 seconds) for image reconstruction. Emission sinograms (individual frames) were corrected for attenuation, dead time, scatter and radioactivity decay, and reconstructed using OSEM3D (16 subsets and 4 iterations). This produced images with the following voxel size of 0.776 x 0.776 x 0.796 mm^3 voxel size. Image quality was inspected for artefact.

Image analysis was performed using the BrainVisa and Anatomist framework setup (http://brainvisa.info/). Automatic segmentation of the PET images was based on the local means analysis (LMA) method (Maroy et al., 2008), with partial volume correction. The LMA method was used because it allows for segmentation of the "functional organ" characterised by particular pharmacokinetics and is not limited by the anatomic boundaries. The geometric transfer matrix (GTM) method and ROIopt method (Maroy et al., 2010) were subsequently used for the correction of partial volume effects.

Briefly, the skeleton is delineated and subtracted from the CT image, this is followed by the application of the GTM method, which relies on the dynamic PET images and spatially segmented domains of the brain, as provided by the LMA method, to generate mean time-activity curves (TAC) for the regions of interest (ROIs). The ROIopt method is used to define the ROI within the LMA segmented domains, and is set to include only 20% of the number of voxels within this region. This improves the GTM method by reducing its susceptibly to manual delineation errors.

5.3.7. Brain uptake of [^{11}C]Temozolomide

The brain uptake of [^{11}C]TMZ was determined by measuring the ratio of the concentration of radioactivity measured in the brain and plasma (brain-to-plasma ratio of radioactivity concentration). The ratio was calculated using two different approaches:

First, the measured brain radioactivity concentration (kBq/mL) was divided by the plasma radioactivity concentration (kBq/mL), both of which were measured with a gamma counter at the 40-minute time point during the metabolites analysis session.

Second, the brain radioactivity concentration from the PET image at 40 minutes was normalised by body weight and injected dose into SUV (standardised uptake value) using the following formula: SUV = (radioactivity per mL / injected radioactivity) x body weight. Since blood sampling was not feasible during the PET scans, plasma radioactivity concentration data were taken from the animals that underwent [^{11}C]TMZ injection for metabolites analysis at the 40-minute time point. Plasma radioactivity data were corrected for radioactive decay to the start of the scan and also expressed as SUV.

Such an approach was deemed feasible as regular cross calibration was performed between the gamma counter, PET camera and dose calibrator on weekly basis by our laboratory technicians.

5.3.8. Statistical analysis

Statistical analysis was performed using Prism6 software (GraphPad Inc., La Jolla, CA, USA). Differences between two groups were analysed by paired t-tests and between multiple groups by one-way analysis of variance (ANOVA) followed by Bonferroni's multiple comparison test. The level of statistical significance was set at $p < 0.05$. All values are expressed as mean ± standard deviation (SD), unless stated otherwise.

5.4. Results

The transport experiments in an *in-vitro* BBB model indicated a role for P-gp and/or BCRP in the transport of TMZ. However, given the limitations of these experiments, a definite conclusion about the substrate status of TMZ for these ABC transporters was not possible and a second approach was needed. In order to investigate whether [^{11}C]TMZ is transported by P-gp and BCRP at the mouse BBB, we performed dynamic small animal PET experiments in wild type and genetically modified transporter knockout mice (P-gp, BCRP and dual transporter knockout). Additional PET studies were conducted in wild type animals with the introduction of the potent third generation P-gp inhibitor TQD (Fox and Bates, 2007).

The use of PET for studying the selectivity of ABC transporters with different PET tracers has proven reliable and is now well established (Bauer et al., 2013a) (Romermann et al., 2013). The relationship between TMZ and P-gp and BCRP has not been assessed previously using this approach.

5.4.1. Plasma and brain radiolabelled metabolite analysis

PET scans measure the total radioactivity in a tissue but cannot distinguish the contribution of different radiolabelled compounds. This is particularly important in this study, as TMZ is a lipophilic compound that is capable of crossing the BBB, while its active metabolite MTIC does not effectively penetrate into the CNS (Farquhar and Benvenuto, 1984) (Meer et al., 1986).

It is therefore essential to elucidate the metabolism of [^{11}C]TMZ and the contribution of the radiolabelled metabolites before determining the efflux mediated transport mechanism of [^{11}C]TMZ.

5.4.1.1. Influence of source of the animals on the metabolism of [^{11}C]Temozolomide

Following the administration of the radiotracer, the parent compound [^{11}C]TMZ and four radiolabelled metabolites were detected in both the plasma and brains of all mice. Interestingly, significant differences were noted between the wild type animals sourced from the two different breeders. The percentage of radioactivity in plasma contributed by the parent compound [^{11}C]TMZ decreased with time, but this effect was more rapid in the wild type animals sourced from UK compared to those sourced from the US. In the wild type animals sourced from the UK, the parent compound contributed approximately 68% of the total radioactivity at 60 minutes, while in the wild type animals sourced from the US this figure was approximately 86% (Figure 5.3). A similar trend was noted in the brain tissue extracts, where the parent compound contributed approximately 60% of the total radioactivity in the UK-sourced animals, and approximately 80% in the US-sourced animals (Figure 5.3).

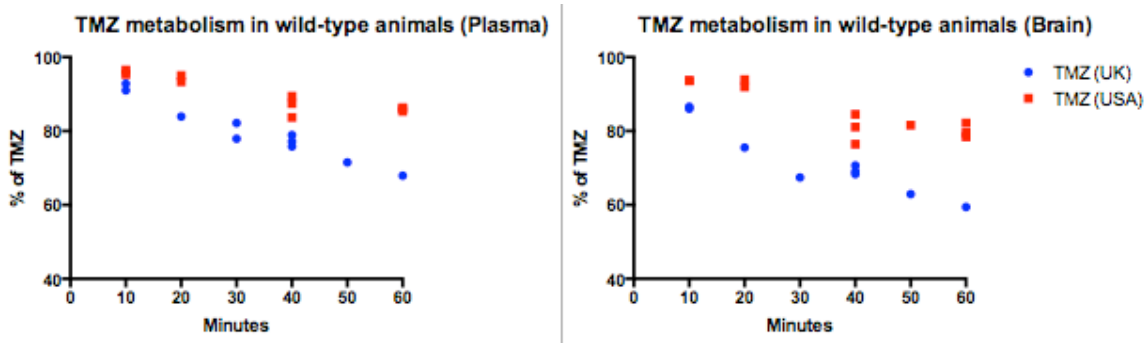

Figure 5. 3: Changes in the relative percentages of the parent compound [^{11}C]TMZ detected in the (A) plasma and (B) brains of wild type animals sourced from UK and US at 10, 20, 30, 40, 50 and 60 minutes following radiotracer administration. For the UK animals, n = 2 at 10, 2 at 20, 3 at 40, and 1 at 50 and 60 minutes. For the US animals, n = 2 at 10 and 20, 4 at 40, and 3 at 60 minutes.

In contrast to the parent compound, the percentage of radioactivity in plasma and brain tissue contributed by the active metabolite MTIC increased with time, an effect that occurred in both wild type groups. In the animals from the UK, MTIC accounted for approximately 5.4% of the total radioactivity in plasma 10 minutes after injection, with the proportion rising to 30% at 60 minutes after injection. Similarly (Figure 5.4), in the US-sourced animals, MTIC accounted for approximately 2.3% of the total

radioactivity in plasma at 10 minutes after injection, with the proportion rising to 11.7% at 60 minutes after injection. A similar pattern was seen in the brain extracts, with MTIC accounting for approximately 40% and 19.9% of the total radioactivity in brain at 60 minutes after injection in the UK and US animals, respectively (rising from 12.1% and 6.7% at 10 minutes after injection, respectively). Overall, the contribution of MTIC to the total radioactivity in the UK-sourced animals was higher than in the US-sourced animals, corroborating the faster degradation of the parent compound in the UK-sourced animals seen earlier (Figure 5.4).

Interestingly, the percentage of radioactivity accounted for by MTIC was higher in the brain than in plasma in both groups. This supports the view that MTIC is mainly converted from TMZ *in-situ* (in the brain), as it cannot effectively cross the BBB. This is a potential reason why other prodrugs, such as Carbazine, that produces MTIC are not effective in the treatment of brain tumours. The possibility that MTIC is a substrate for an efflux transporter is also felt to be less likely as the percentage of MTIC in the brain of KO animals was comparable to the WT animals (section 5.4.12).

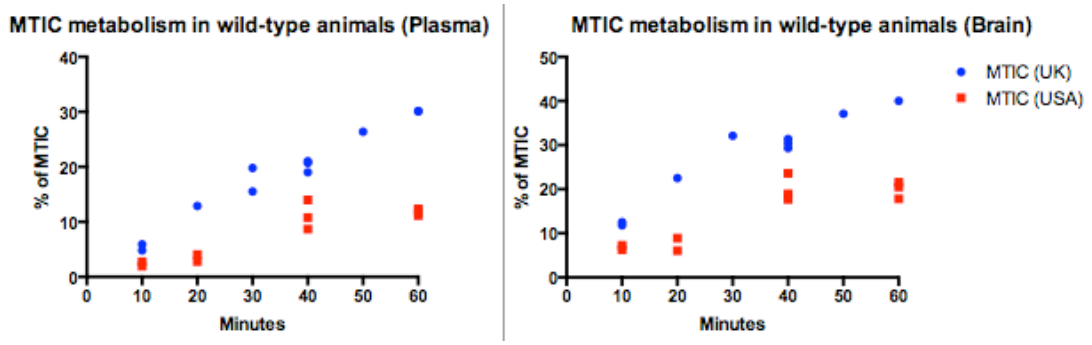

Figure 5. 4: Changes in the relative percentages of the active metabolite MTIC found in the (A) plasma and (B) brains of wild type animals sourced from the UK and the US at 10, 20, 30, 40, 50 and 60 minutes after radiotracer administration. For the UK animals, n = 2 at 10, 2 at 20, 3 at 40, and 1 at 50 and 60 minutes. For the US animals, n = 2 at 10 and 20, 4 at 40, and 3 at 60 minutes.

The percentages of radioactivity in plasma and in brain extracts at various time points that were due to the parent compound [^{11}C]TMZ and the daughter metabolites in both group of animals are presented in Tables 5.4 and 5.5.

Three other unidentified metabolites (M1, M2 and M3) were detected in plasma; however, their contribution to the total measured radioactivity was minimal (approximately 2% in plasma at 60 minutes for both groups of animals), while none of

these metabolites were detected in the brain at 60 minutes. This suggests that these metabolites do not cross the BBB effectively and are not generated *in-situ*.

Table 5. 4: Percentages of parent compound [^{11}C]TMZ and its metabolites found in plasma at 10, 20, 40 and 60 minutes after radiotracer administration in wild type (WT) animals

Compound	HPLC Retention Time (min)	UK WT animals				USA WT animals			
		Time after injection (min)				Time after injection (min)			
		10	20	40	60	10	20	40	60
TMZ	13.9	91.1	83.8	77.2	67.8	95.9	94.4	86.8	85.9
MTIC	2.5	5.4	13.0	20.5	30.1	2.35	3.4	11.1	11.7
M1	4.5	1.0	1.2	1.0	1.2	0.6	1.1	1.0	1.4
M2	8.1	0.2	0.5	0.1	0.0	0.2	0.2	0.2	0.2
M3	10.9	1.4	1.3	1.0	0.9	0.9	0.8	0.7	0.6

For the UK animals, n = 2 at 10, 2 at 20, 3 at 40, and 1 at 60 minutes. For the US animals, n = 2 at 10 and 20, 4 at 40, and 3 at 60 minutes.

Table 5. 5: Relative percentages of parent compound [^{11}C]TMZ and its metabolites found in brain extracts of wild type (WT) animals at 10, 20, 40 and 60 minutes after radiotracer administration in wild type animals.

Compound	HPLC Retention Time (min)	UK WT animals				USA WT animals			
		Time after injection (min)				Time after injection (min)			
		10	20	40	60	10	20	40	60
TMZ	13.9	86.3	75.5	69.3	59.4	92.2	92.5	80.9	80
MTIC	2.5	12.1	22.5	30.3	40.0	6.7	7.5	18.9	19.9
M1	4.5	0.3	0.8	0	0	0	0	0	0
M2	8.1	0.6	0.8	0	0	0.6	0	0	0
M3	10.9	0.6	0.4	0	0.4	0	0	0	0

For the UK animals, n = 2 at 10, 2 at 20, 3 at 40, and 1 at 60 minutes. For the US animals, n = 2 at 10 and 20, 4 at 40, and 3 at 60 minutes).

5.4.1.2. Influence of P-glycoprotein and/or breast cancer resistance protein transporter genetic knockout on the metabolism of [^{11}C]Temozolomide

Blood and brain samples from the knockout animals (all sourced from Taconic Inc. USA) were obtained at the single time point of 40 minutes. The percentages of radioactivity for the wild type animals (UK and USA) and the transporter knockout animals are presented in Table 5.6.

Table 5. 6: Percentages of parent compound [^{11}C]TMZ and its active radiolabelled metabolite MTIC found in plasma and brain extracts at 40 minutes after radiotracer administration.

Animal	Plasma		Brain	
	40 minutes after radiotracer injection			
	TMZ	MTIC	TMZ	MTIC
WT (UK)	77.2	20.5	69.3	30.3
WT (USA)	86.6	11.1	80.9	18.9
P-gp KO	90.4	7.3	86.5	12.7
BCRP KO	87.7	10.0	83.4	15.9
Dual Transporter KO	85.9	10.8	82.5	16.4

$N = 4$, except for the UK wild type, where $n = 3$.

The percentages of radioactivity in plasma contributed by the parent compound [^{11}C]TMZ were 90.4%, 87.7% and 85.9% at 40 minutes post-injection for the P-gp, BCRP and dual transporter knockouts, respectively. MTIC contributed 7.3%, 10% and 10.8% of the total radioactivity in plasma at the same time point for the P-gp, BCRP and dual transporter knockouts, respectively (Figure 5.5).

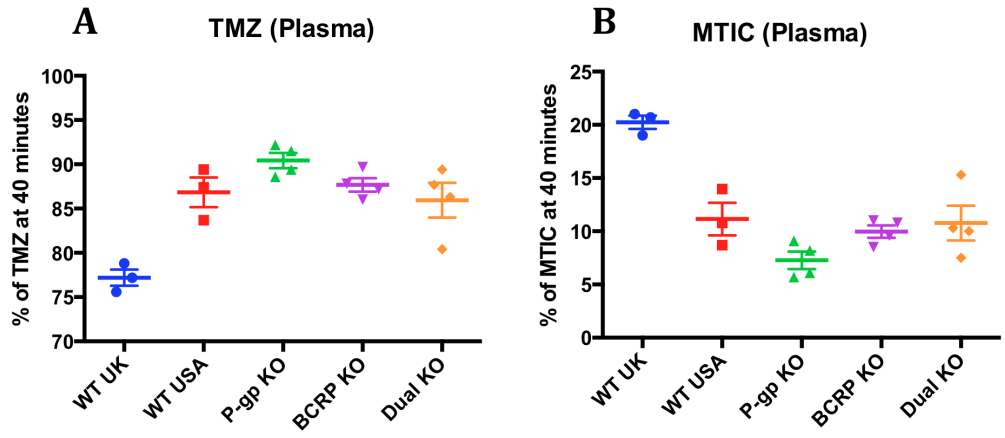

Figure 5. 5: Percentages of (A) parent compound [^{11}C]TMZ and (B) the active radiolabelled metabolite MTIC found in plasma at 40 minutes after radiotracer

administration for wild type (UK), wild type (USA), P-glycoprotein, breast cancer resistance protein and dual transporter knockout mice. $N = 4$ in all groups except for the UK wild type, where $n = 3$.

In the brain, [^{11}C]TMZ contributed 86.5%, 83.4% and 82.5% of the total radioactivity at 40 minutes for the P-gp, BCRP and dual transporter knockouts, respectively, while MTIC's contributions were 12.7%, 15.9% and 16.4% for the same groups at the same time point (Figure 5.6).

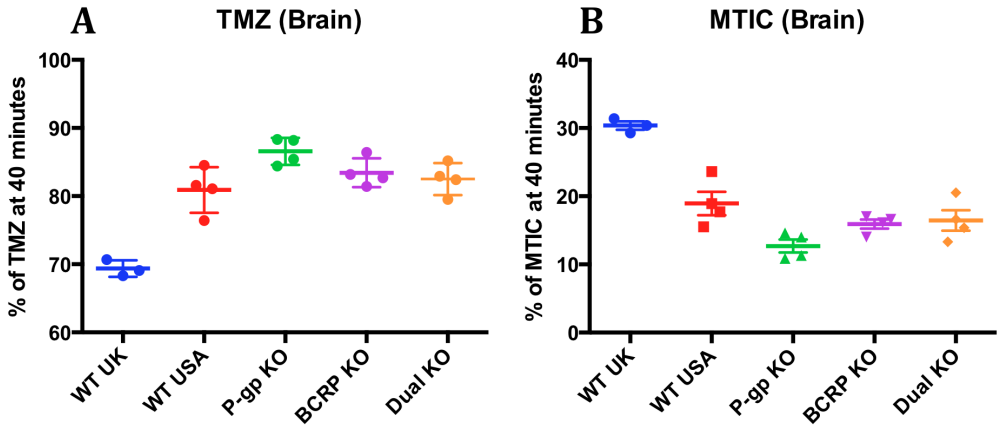

Figure 5. 6: Percentages of (A) parent compound [^{11}C]TMZ and (B) the radiolabelled active metabolite MTIC found in brain extracts at 40 minutes after radiotracer administration for wild type (UK), wild type (USA), P-glycoprotein, breast cancer resistance protein and dual transporter knockout mice. $N = 4$ in all groups except for the UK wild type, where $n = 3$.

The percentages of [^{11}C]TMZ in the knockouts were significantly ($p < 0.0001$) higher than seen in the wild type animals sourced from the UK but were more in line ($p = 0.058$) with the wild type animals sourced from the same breeder in the US. Consequently, the contribution of the active metabolite MTIC in the transporter knockout animals was lower than in the wild type animals sourced from the UK and similar to that of the wild type animals sourced from the same breeder in the US. These data suggest that the differences in the metabolism seen between the animal groups can be attributed to their different source, while genetic knockout of the efflux transporter does not appear to alter metabolism significantly.

5.4.1.3. Influence of TQD on the metabolism of [^{11}C]TMZ in wild type animals

Blood and brain samples from wild type animals (Taconic Inc. USA) that were treated with TQD (15mg/kg) were obtained 60 minutes after [^{11}C]TMZ administration. TQD

was administered 40 minutes after the radiotracer injection via an IV bolus. The percentages of radioactivity in the plasma and brain samples for the treated and untreated animals are presented in Table 5.7.

Table 5. 7: Percentages of parent compound [^{11}C]TMZ and the active radiolabelled metabolite MTIC found in plasma and brain extracts at 60 minutes after radiotracer administration for untreated wild type mice and wild type mice treated with Tariquidar.

Animal	Plasma		Brain	
	60 minutes after radiotracer injection			
	TMZ	MTIC	TMZ	MTIC
Vehicle	85.9	11.9	80.0	18.1
Tariquidar	85.7	11.8	81.4	19.9

Tariquidar (15mg/kg) was administered via an IV bolus 40 minutes after the radiotracer. *n* = 3 for both groups.

TQD administration does not appear to affect the metabolism of TMZ since the percentages of the parent compound and its active radiolabelled metabolite MTIC were very similar between treated and untreated animals, in both the plasma and brain samples (Table 5.4 and Figure 5.7).

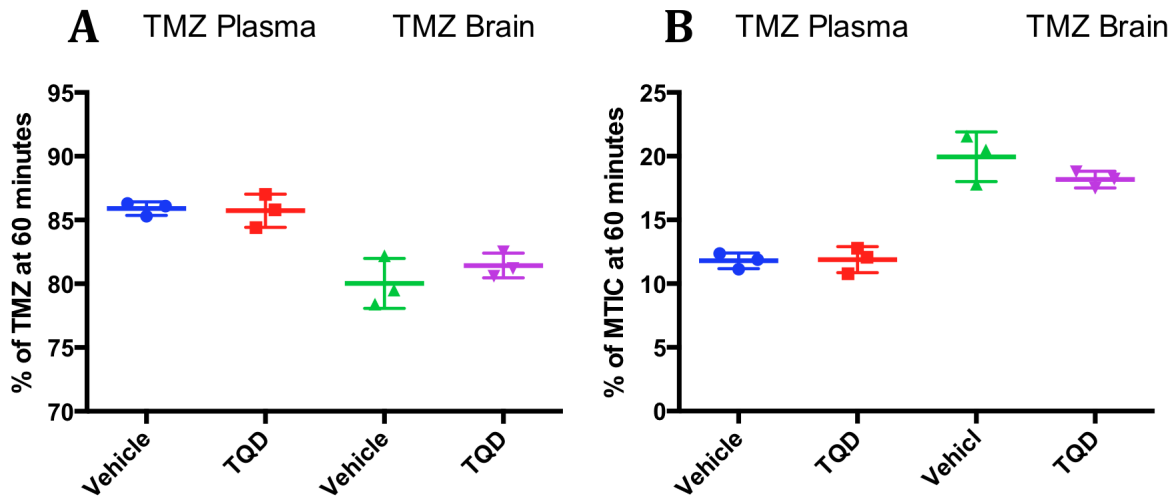

Figure 5. 7: Percentages of (A) parent compound [^{11}C]TMZ and (B) the active radiolabelled metabolite MTIC found in plasma and brain extracts at 60 minutes after radiotracer administration for wild type mice injected with vehicle and Tariquidar (15mg/kg). Tariquidar was administered via a tail vein cannula as a bolus injection 40 minutes after the radiotracer injection. n = 3 for both groups.

5.4.2. *Ex-vivo* brain experiments

5.4.2.1. Effects of P-glycoprotein and/or breast cancer resistance protein transporter knockout on the brain uptake of [^{11}C]Temozolomide

Given the differences in the metabolism of [^{11}C]TMZ between wild type mice from different sources, only animals acquired from the US were used to determine brain uptake of [^{11}C]TMZ. Brain uptake was expressed as the brain-to-plasma ratio of total radioactivity at 40 minutes after injection of [^{11}C]TMZ, as measured with a gamma counter.

The brain-to-plasma ratio was low in the wild type animals and slightly higher in the single transporter knockouts (wild type: 0.133 ± 0.012, P-gp: 0.147 ± 0.024, BCRP: 0.144 ± 0.028, p = 0.108). In the dual transporter knockout, the brain-to-plasma ratio was even higher, although this was still not statistically significant (wild type: 0.133 ± 0.012 and dual transporter knockout: 0.169 ± 0.013, p = 0.062) (Figure 5.8, A). The ratio of 0.133 in wild type mice is slightly lower than the described literature in patients with glioma tumours of approximately 0.2 (Ostermann 2004) (Synold 2009), this is to be expected given the leaky BBB in these patients. This is in keeping with the ability of TMZ to cross the BBB in limited concentrations.

As a second step, and given that MTIC poorly penetrates the BBB, only the contribution of the parent compound in plasma was included in the analysis. The brain-to-plasma ratio of the radioactivity contributed by [^{11}C]TMZ, measured at 40 minutes, were higher in all animal subgroups when compared to measurements prior to the correction. Furthermore, the brain-to-plasma ratios became significantly higher in the dual transporter knockout mice compared to wild type animals (wild type: 0.153 ± 0.013 and dual transporter knockout: 0.200 ± 0.011, p = 0.036). In mice lacking only one of the transporters (either P-gp or BCRP), the brain-to-plasma ratios were only moderately elevated, but this effect was not statistically significant (wild type: 0.153 ± 0.013, P-gp: 0.162 ± 0.025, p = 0.305, BCRP: 0.164 ± 0.033, p = 0.502) (Figure 5.8, B). Raw data is presented in table 1 and 2 in the appendix.

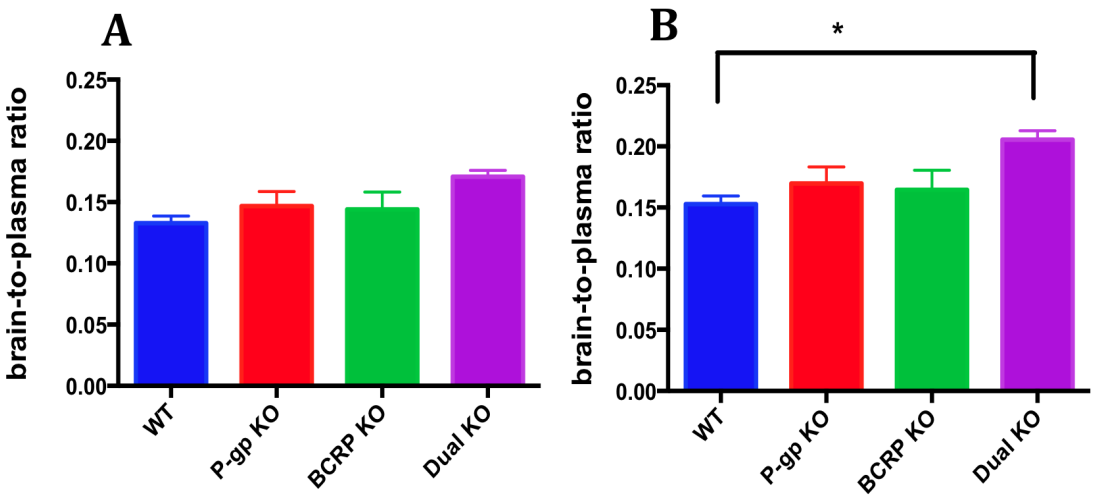

Figure 5. 8: Brain-to-plasma ratios of radioactivity at 40 minutes after radiotracer injection for the different mouse types (A) before and (B) after correcting for the fraction of the parent compound [^{11}C]TMZ in plasma. n = 4 in each group. Data are presented as mean ± SD. Statistical significance was determined by one-way ANOVA with Bonferroni multiple comparison test. * $p < 0.05$.

5.4.2.2 Effects of P-glycoprotein and/or breast cancer resistance protein pharmacological transporter inhibition on the brain uptake of [^{11}C]Temozolomide

In a second approach, pharmacological inhibition of P-gp and BCRP transporters was used. To determine the brain uptake of [^{11}C]TMZ, the brain-to-plasma ratio of radioactivity measured at 60 minutes with a gamma counter were compared between wild type animals that received TQD and a separate group of animals administered with vehicle solution only.

In keeping with the previous result, animals treated with TQD demonstrated significantly higher brain-to-plasma ratios (A) without (vehicle treated: 0.148 ± 0.011, TQD treated: 0.206 ± 0.031, p = 0.030) and (B) with correcting for the fraction of [^{11}C]TMZ in plasma (vehicle treated: 0.172 ± 0.013, TQD treated: 0.241 ± 0.036, p = 0.0294) (Figure 5.9). Raw data from individual animals is presented in the index table 3 and 4.

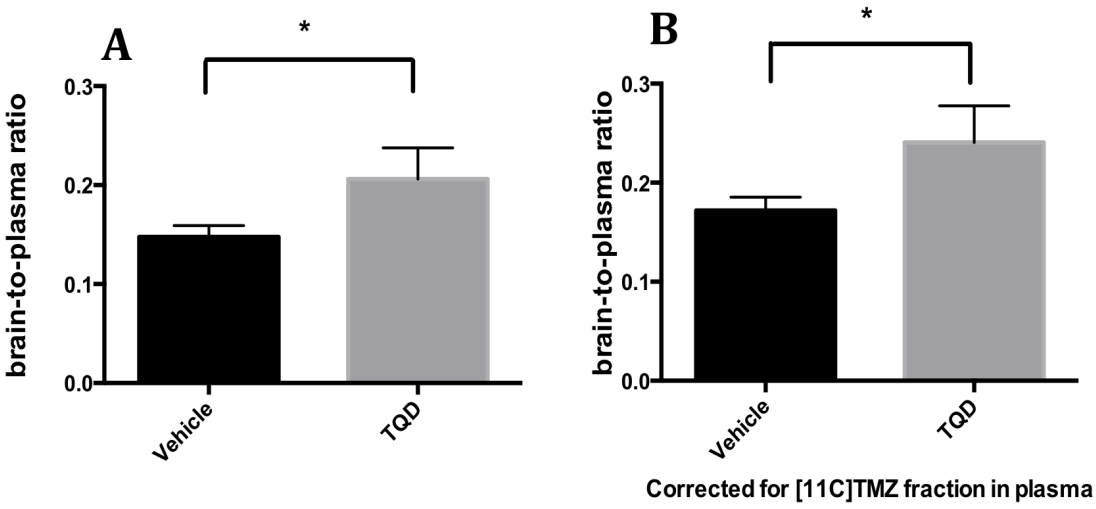

Figure 5. 9: Brain-to-plasma ratios of radioactivity at 60 minutes after [^{11}C]Temozolomide injection in wild type mice injected with vehicle solution with Tariquidar (15mg/kg). Tariquidar was administered by IV bolus 40 minutes after radiotracer injection. (A) Ratios not corrected for the fraction of [^{11}C]TMZ in plasma and (B) ratios after correction. n = 3 for untreated wild type mice and n = 4 for animals treated with Tariquidar. Data are presented as mean ± SD. Statistical significance was determined by unpaired t-test (two-tailed). * $p < 0.05$.

5.4.3. *In-vivo* PET experiments

As a second approach for investigating whether TMZ is a substrate for P-gp and BCRP, we conducted PET scans in wild type and transporter knockout mice. Additional PET experiments were conducted in wild type mice that were injected with 15mg/kg of TQD 40 min after radiotracer administration. TQD at this dose causes almost complete P-gp and some BCRP inhibition in mice (Wanek et al., 2012).

5.4.3.1 Brain segmentation method

The use of a semi-automated segmentation method for delineating the brain in PET images helped to reduce manual delineation variability and resulted in a single ROI with uniform [^{11}C]TMZ uptake corresponding to the brain of the mouse. Additionally, positive correlation of the segmented tumour volume (mm^3) from the dynamic PET image versus the measured brain weight (g) in all mice was observed (n = 19, r^2 = 0.3824, p <0.005) (Figure 5.10, A). It is important to note that this analysis included a mouse whose brain was incompletely excised and therefore had low documented weight (0.36 g). When this particular mouse is excluded from the analysis, the positive correlation is even stronger and more significant (n = 18, r^2 = 0.6714, p < 0.0001) (Figure 5.10, B).

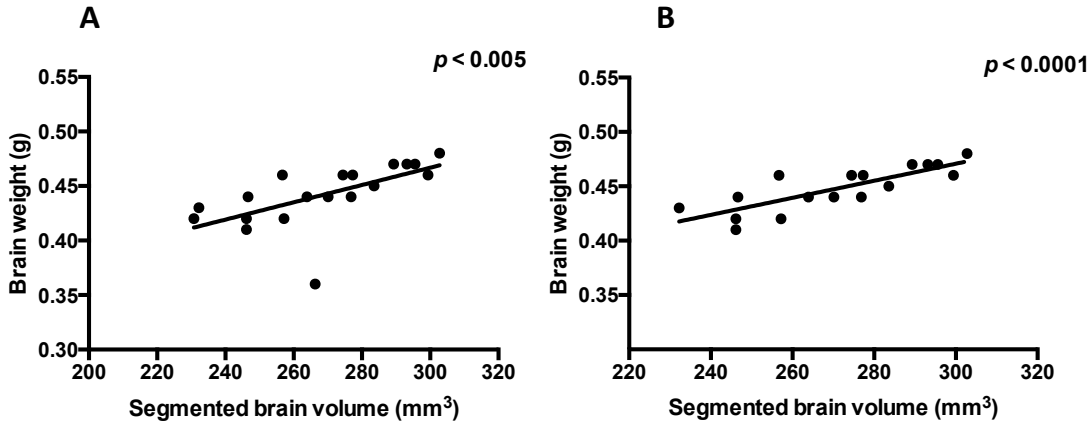

Figure 5. 10: Significant positive correlation between the brain volumes segmented from the dynamic PET image and the brain weights in each mouse across all PET scans with [^{11}C]TMZ. (A) For all animals (n = 19, r^2 = 0.3824, p <0.005) and (B) after the exclusion of the mouse with a partially resected brain (n = 18, r^2 = 0.6714, p < 0.0001).

5.3.3.2. Effects of P-glycoprotein and/or breast cancer resistance protein transporter knockout on the brain uptake of [^{11}C]Temozolomide

As an additional step to investigate whether [^{11}C]TMZ is transported by P-gp and BCRP at the mouse BBB level, we performed PET experiments with [^{11}C]TMZ in wild type, P-gp KO, BCRP KO and dual transporter KO mice.

Brain TAC in wild type mice showed low uptake of [^{11}C]TMZ, and this was only minimally higher in single transporter KO (P-gp or BCRP) mice, with the highest brain uptake seen in the dual transport KO mice (Figure 5.11). Representative maximum intensity projection PET image is presented in Figure 5.12.

Consequently, mice lacking only one of the transporters (P-gp or BCRP) showed only a minimally higher brain area under the curve (AUC) values; while mice with dual transporters KO showed the highest brain AUC values, although this was not statistically significant (wild-type: 8.25 ± 1.3, P-gp KO: 8.56 ± 0.63, BCRP KO: 8.6 ± 0.34 and dual transporter KO: 8.86 ± 0.67).

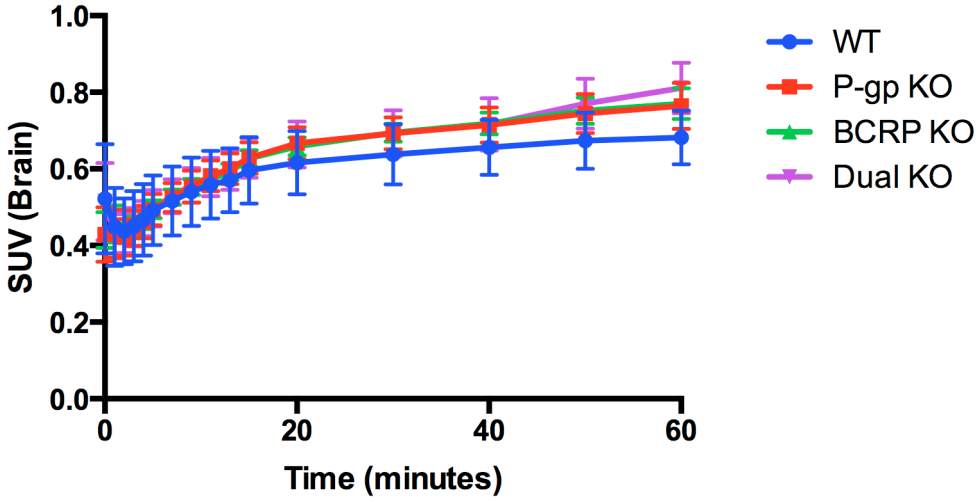

Figure 5. 11: Mean (± SD) whole-brain time-activity curves (SUV) in wild type, P-gp KO, BCRP KO, and dual transporter KO mice (n = 4 in each group, except for the wild type, where n = 3). SUV values represent the mean SUV.

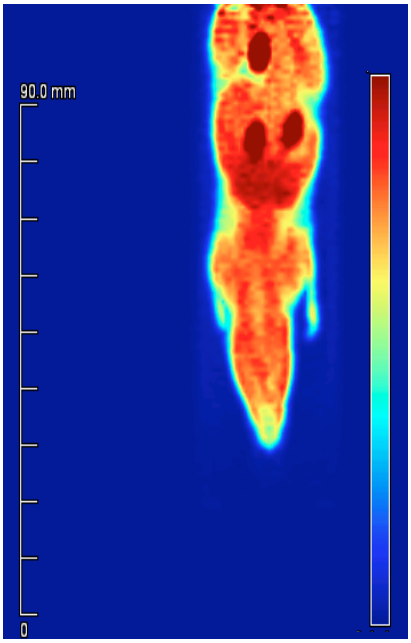

Figure 5.12: Representative maximum intensity projection image (last ten minutes) illustrating brain uptake of [^{11}C]Temozolomide in a dual transporters knockout mice.

Since blood sampling was not feasible during the PET scans, plasma radioactivity data was taken from the animals that underwent [^{11}C]TMZ injection for metabolite analysis. The calculated plasma activity of [^{11}C]TMZ was slightly lower in the BCRP and dual transporter knockout mice; however, there was no statistical significance between the groups (Figure 5.13). This was similar to what was observed when the plasma radioactivity was measured directly by a gamma counter (Figure 5.4).

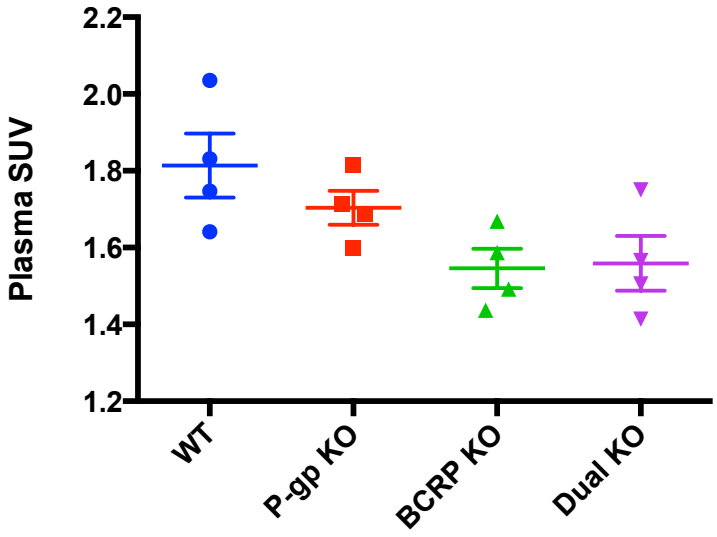

Figure 5. 13: Plasma radioactivity concentrations (SUV) measured at 40 minutes after [^{11}C]TMZ injection in the different groups of mice from the metabolite analysis group. n = 4 in each group. Data are presented as mean ± SD. Statistical significance was determined by one-way ANOVA with Bonferroni multiple comparison.

Brain uptake of [^{11}C]TMZ was expressed as the brain-to-plasma ratio of radioactivity at 40 minutes, calculated by dividing the brain activity concentration measured with PET (mean SUV) by the calculated mean plasma radioactivity concentration of the corresponding mouse group from the metabolites study. Blood radioactivity data were corrected for radioactive decay and expressed as standardised uptake value (SUV = (radioactivity per ml/injected radioactivity) x body weight). This method is well established and has been previously described (Romermann et al., 2013).

In keeping with the earlier results of the metabolites study, the brain-to-plasma ratio of activity was low in wild type animals and slightly higher in the P-gp transporter knockout group, but this difference was not significant (wild type: 0.384 ± 0.019, P-gp KO: 0.407 ± 0.028). In the BCRP and dual transporter knockout mice, the brain-to-plasma ratios of radioactivity were significantly higher than in wild-type animals (wild type: 0.384 ± 0.019, BCRP KO: 0.486 ± 0.022, and dual transporter KO: 0.494 ± 0.042, p = 0.0008) (Figure 5.14).

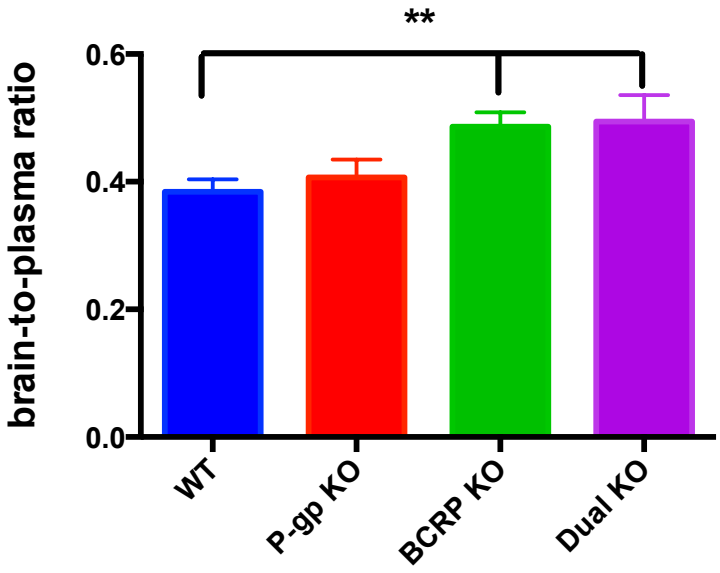

Figure 5. 14: Brain-to-plasma ratios of radioactivity at 40 minutes as measured with positron emission tomography after [^{11}C]Temozolomide injection for the different mouse groups (n = 4 in each group, except wild type, where n = 3). Data are presented as mean ± SD. Statistical significance was determined by one-way ANOVA with Bonferroni multiple comparison test. ** $p < 0.005$.

As discussed earlier, and since MTIC fails to cross the BBB effectively, its contribution to the calculated plasma radioactivity concentration may be ignored. Following a correction for the fraction of the parent compound in plasma, the calculated plasma radioactivity concentrations were similar to the one observed before this correction (Figure 5.15). This was expected, as similar metabolism of [^{11}C]TMZ was demonstrated between the different mouse groups with comparable parent compound percentages at 40 minutes after radiotracer injection (Figure 5.5 and Table 5.3).

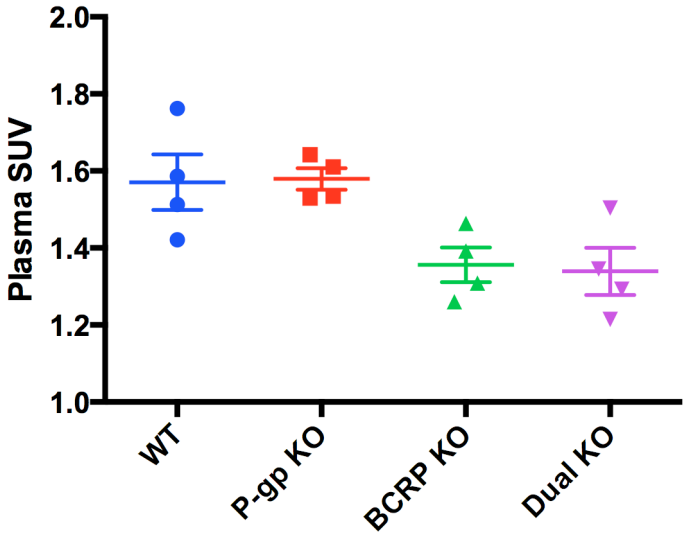

Figure 5. 15: Plasma radioactivity concentrations (SUV) measured at 40 minutes after [^{11}C]TMZ injection in the different mouse groups following correction for the fraction of the parent compound in plasma (n = 4 in each group).

Consequently, the brain-to-plasma ratios of the radioactivity contributed by [^{11}C]TMZ, measured at 40 minutes, were altered. A low brain-to-plasma ratio of radioactivity was again observed in wild type animals, with a significantly higher ratio in the dual transporter knockout mice (wild type: 0.432 ± 0.042 and dual transporter knockout: 0.575 ± 0.049, p: 0.0045). However, in mice lacking only one of the transporters (either P-gp or BCRP), the brain-to-plasma ratios of radioactivity were comparable to the wild type animals, with no statistical difference between the groups (wild type: 0.432 ± 0.042, P-gp KO: 0.445 ± 0.031 , BCRP KO: 0.427 ± 0.062) (Figure 5.16).

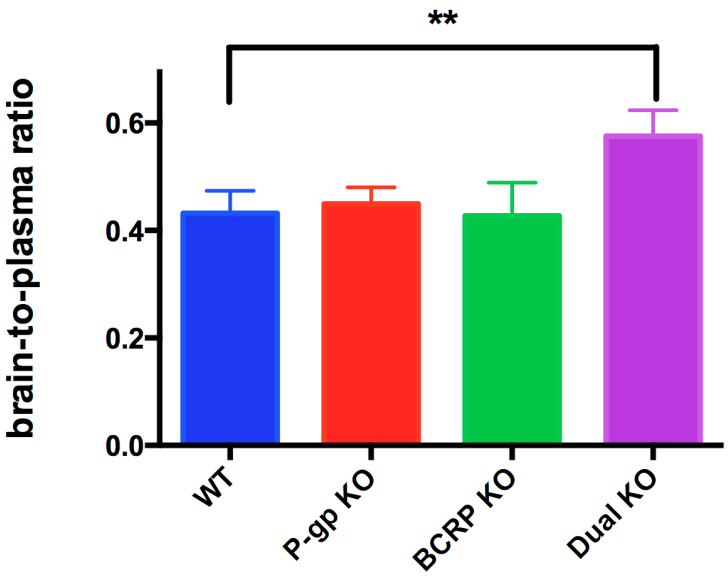

Figure 5.16: Brain-to-plasma ratios of radioactivity as measured with positron emission tomography at 40 minutes after [^{11}C]Temozolomide injection in the different mouse groups, corrected for the fraction of the parent compound in plasma (n = 4 in each group, except for wild type, where n = 3). Data are presented as mean ± SD. Statistical significance was decided by one-way ANOVA with Bonferroni multiple comparison test. ** $p < 0.005$.

5.4.3.3. Effects of P-glycoprotein and/or breast cancer resistance protein pharmacological transporter inhibition on the brain uptake of [^{11}C]Temozolomide

The effect of the dual P-gp and BCRP inhibitor TQD on the brain uptake of [^{11}C]TMZ in wild-type mice was assessed. Animals were injected with TQD (15mg/kg) or vehicle solution at 40 minutes after the radiotracer administration whilst undergoing PET scanning. TQD administration resulted in a visible rise in the brain TACs (Figure 5.17), which was also reflected also in a rise in brain AUC, but this was not statistically significant (vehicle: 36.64 ± 4.5, TQD: 40.15 ± 2.3, $p = 0.234$).

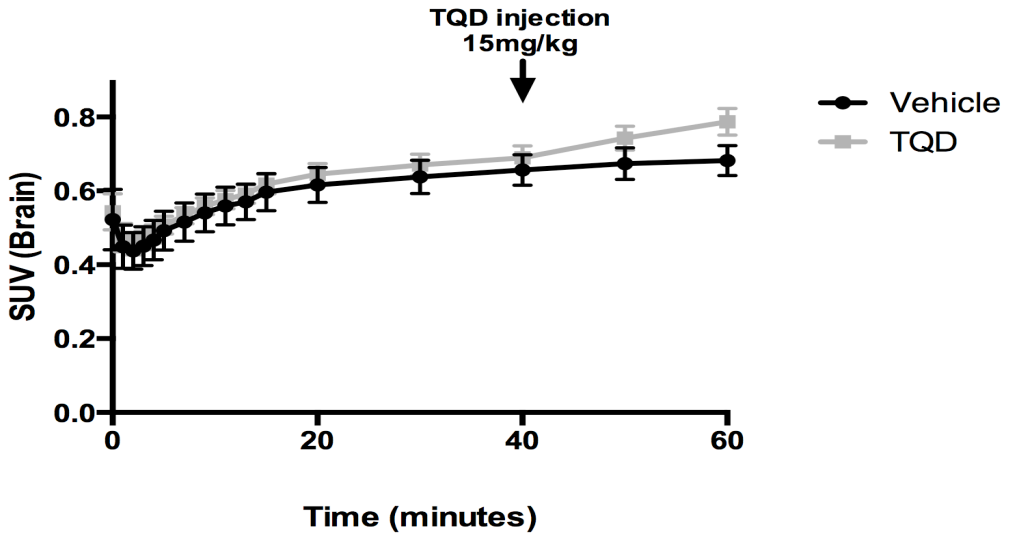

Figure 5. 17: Mean (± SD) whole-brain time-activity curves (SUV) for untreated wild type mice injected with a vehicle and with TQD. TQD (15 mg/kg) was administered as an IV bolus 40 minutes after radiotracer injection and is marked by a black arrow on the graph. ($n = 3$ for untreated wild type mice and $n = 4$ for animals treated with TQD).

As seen in the metabolites study, administration of TQD resulted in a rise in the brain-to-plasma ratio of radioactivity at 60 minutes following radiotracer administration. However, this increase was not significant (vehicle: 0.365 ± 0.045, TQD: 0.439 ± 0.041, $p = 0.072$) (Figure 5.18, A).

Brain uptake of [^{11}C]TMZ was expressed as the brain-to-plasma ratio of radioactivity at 60 minutes, calculated by dividing the brain activity concentration measured with PET (mean SUV) by the calculated mean plasma radioactivity concentration of the corresponding mouse group from the metabolites study. Blood radioactivity data were corrected for radioactive decay and expressed as standardised uptake value (SUV =

(radioactivity per Ml/injected radioactivity) x body weight). This method is well established and has been previously described (Romermann et al., 2013).

As done previously, the calculated plasma radioactivity was corrected for the fraction of the parent compound [^{11}C]TMZ in plasma. Following this correction, animals that received TQD showed a higher brain-to-plasma ratio of radioactivity and this was statically significant (vehicle: 0.426 ± 0.039, TQD: 0.524 ± 0.048, p = 0.020) (Figure 5.18, B).

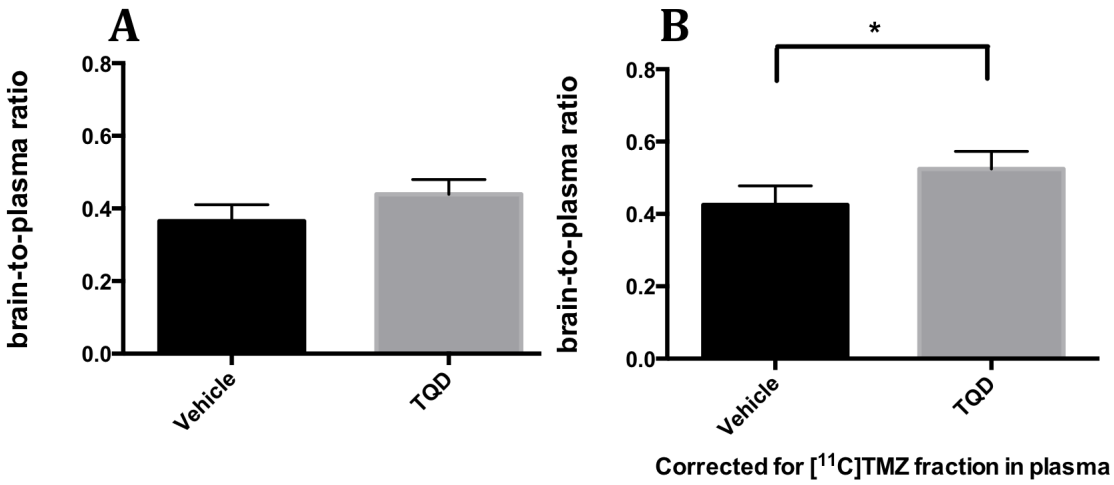

Figure 5. 18: Brain-to-plasma ratios of radioactivity at 60 minutes after [^{11}C]Temozolomide injection in wild type mice injected with a vehicle solution and TQD (15mg/kg). TQD was administered by IV bolus at 40 minutes after radiotracer injection. (A) Brain-to-plasma ratios with no correction for the fraction of the parent compound in plasma and (B) following the correction. (n = 3 for wild type mice injected with a vehicle and n = 4 for animals injected with TQD. Data are presented as mean ± SD. Statistical significance was determined by unpaired t-test (two-tailed). * p < 0.05.

5.5. Discussion and conclusions

The main aim of this study was to investigate the status of TMZ as a substrate for P-gp and BCRP efflux transporters. To the best of our knowledge, brain uptake of [^{11}C]TMZ through ABC transporters has not been assessed. This is the first preclinical *in-vivo* study to confirm, in keeping with our *in-vitro* results, that TMZ entry into the brain is limited by the efflux transporters P-gp and BCRP at the BBB level in mice and that TMZ acts as a dual substrate of P-gp and BCRP. TMZ is excluded from the brain when only one transporter is inhibited. In addition, this study demonstrated that chemical inhibition of P-gp and BCRP with TQD at the BBB level in mice results in an immediate increase in TMZ delivery into the brain.

P-gp and BCRP work in tandem as efflux transporters of many anticancer drugs. Because their affinity for different drugs overlaps significantly, it is essential to evaluate the function of both transporters in one study when investigating the substrate status of a particular agent. One transporter can compensate for loss of function in the other if a drug is a substrate of both transporters (Lagas et al., 2009). For example, Polli et al. demonstrated that P-gp and BCRP double knockout in mice had a synergic effect in increasing brain uptake of a tyrosine kinase inhibitor (lapatinib) when compared to the effects of single transporter knockout (Polli et al., 2009). De Vries et al. reported similar results for the anticancer drug topotecan (de Vries et al., 2007). Several studies have confirmed these findings for various anticancer drugs that are dual P-gp and BCRP substrates (Kodaira et al., 2010) (Agarwal et al., 2011a).

In this study, we used wild-type animals and animals lacking P-gp, BCRP, or both transporters. There are conflicting reports about the use of genetic transporter KO models. Some studies have raised concerns regarding possible compensatory mechanisms in which other efflux transporters such as BCRP are upregulated in P-gp KO models (Cisternino et al., 2004). However, other recent, more comprehensive studies have not substantiated these concerns. For example, Agarwal et al. showed that genetic KO of P-gp, BCRP, or both efflux transporters did not cause compensatory transporter expression and that the differences between the animals were due to simple functional compensation between the two transporters at the BBB, rather than

upregulation of a transporter (Agarwal et al., 2012). We used identical animal models in this study. Additionally, it is clear that animal studies in which only one transporter is inhibited (chemically or genetically) are flawed; they may lead to inaccurate conclusions when evaluating the substrate status of a drug (Lagas et al., 2009) (Bankstahl et al., 2013). It is therefore essential to include animals with dual P-gp and BCRP knockout, as in this study, to abolish any compensatory mediated efflux that could occur should a drug be a dual substrate.

The brain-to-plasma ratio of radioactivity was measured and calculated to estimate brain uptake of [^{11}C]TMZ. The brain-to-plasma ratio of radioactivity was measured directly using a gamma counter and indirectly using PET. The use of radiolabelled compounds and PET in combination with wild-type and efflux transporter knockout (chemical and genetic) animals is well established as a method for investigating the status of a compound as a substrate for particular efflux transporters (Bauer et al., 2013a) (Romermann et al., 2013) (Wanek et al., 2015b). A possible limitation of the use of PET in mice is the extremely small volume of blood. This precludes arterial blood sampling during PET acquisition sampling. To overcome this limitation, the radiotracer was injected into a second group of mice, and blood samples were collected at the 40-minute time point. The measured blood radioactivity was then corrected for radioactive decay and expressed as SUV in order to measure the brain-to-plasma ratio of activity with PET.
Some researchers overcame this by directly collecting small volume blood from the animals during the PET scans (Wu et al., 2007) (Convert et al., 2007). We felt that this approach is not suitable as this it is techniqually challenging and terminal to the animals, which in turn precludes a longuitdunal study design. Furthermore, such an approach would have prevented blood sampling at various time points given the limited blood volume, which can be collected.

Another potential drawback in the use of mice is related to the technical limitations of small animal PET. In this study, we employed a recognised semi-automated brain segmentation method to reduce variability and susceptibly to manual segmentation errors (Maroy et al., 2008) (Maroy et al., 2010). Such a method may result in partial volume effects in volume definition and radioactivity measurement especially when applied to the small brain volume of mice. This may explain why the brain

radioactivity measured with a gamma counter was higher than that measured with PET scans.

Various factors can affect the interpretation of results when using PET to evaluate brain uptake of a radiotracer (Wanek et al., 2015a). In this study, every effort was taken to minimise the impact of such factors by limiting variabilities in experimental settings such as duration and depth of anaesthesia, O_2 flow, injected radiotracer volume, and animal housing conditions.

Other radiotracers such as 99mTc-Sestamibi and [^{64}Cu](DO3A-xy-TPEP) have been employed in evaluating P-gp function in rodents. However, these are mainly utilised in tumour bearing mice and provide limited direct insight into the transport of TMZ itself.

The effect of sourcing animals from two different breeders on the metabolism of the radiotracer [^{11}C]TMZ was also evaluated. Radiolabelled [^{11}C]TMZ metabolites were analysed in the plasma and brain of wild-type mice obtained from two different breeders (UK or USA based) and KO animals. Radiolabelled TMZ and its active radiolabelled metabolite (MTIC) were detected in the plasma and brain for all groups. However, in the plasma and brain, the percentage of [^{11}C]TMZ in WT animals obtained from the USA (86.6%) was higher than in animals obtained from the UK (77.2%) at 40 minutes. The difference was even greater at 60 minutes when the metabolism and breakdown of the radiotracer had increased. Consequently, the percentage of radiolabelled MTIC was lower in the plasma and brain of USA-sourced animals. TMZ breakdown and metabolism were very similar in transporter KO mice (P-gp, BCRP, and both) and WT animals sourced from the USA. This was a main reason why UK-sourced animals were not used in subsequent PET experiments.

The use of chemical inhibition as well as genetic transporter knockout is regarded as good scientific practice when determining the effects of transporter inhibition on the brain uptake of a particular drug. In this study, as an additional step, the potent third-generation P-gp inhibitor TQD (Fox and Bates, 2007) was used to inhibit P-gp and BCRP transporters. A TQD dose of 15 mg/kg was selected because previous studies have shown that it completely abolishes P-gp-mediated efflux and partially inhibits BCRP-mediated efflux (Bankstahl et al., 2013).

TQD has been shown to have a limited effect on the metabolism of radiolabelled verapamil when used in PET experiments (Pauli-Magnus et al., 2000). Similarly, in this study, TQD appeared to have a very limited effect on the breakdown and metabolism of [^{11}C]TMZ: the percentages of the parent compound and the active metabolite MTIC were very similar in plasma and brain samples from treated and untreated animals. The short treatment window of 10 minutes might have been one factor that limited any potential effect on TMZ breakdown (TQD was administered during the PET scan at the 40-minute time point, and sampling was performed at the 60-minute time point).

Because TQD did not affect TMZ metabolism, it is possible to conclude that any results observed following the administration of TQD were due to modulation of efflux transporter function, rather than a change in the metabolism of the radiotracer. A potential caveat for this is the fact the effect of the TQD on cerebral blood flow has not been investigated and therefore remains unknown both in mice and humans.

Such results reinforce the importance of evaluating radiotracer metabolism in PET experiments that aim to assess efflux transporter function. Even subtle differences in the metabolism of a radiotracer can lead to inaccurate conclusions about the substrate status of a compound. Furthermore, this casts doubt over previously reported preclinical and clinical studies that examined P-gp- and BCRP-mediated efflux using PET without evaluating the metabolism of the radiotracer. They may have reached inaccurate conclusions.

Our results provide evidence that both P-gp and BCRP actively efflux [^{11}C]TMZ from the brain to the plasma. A small but not statically significant increase in [^{11}C]TMZ brain delivery was seen in animals lacking only one transporter. However, a significant increase in delivery was observed in animals lacking both transporters. This is the expected finding for a dual substrate: a small increase in brain exposure is seen in mice lacking only one transporter (P-gp or BCRP), but a larger increase in brain exposure is seen in mice lacking both transporters (Kodaira et al., 2010) (Bankstahl et al., 2013). A similar response pattern was noted following the chemical inhibition of P-gp and BCRP. An immediate increase in the brain TAC of animals injected with TQD was

observed during the scanning session. The increase was due to complete inhibition of P-gp function and some inhibition of BCRP function, resulting in an influx of [^{11}C]TMZ into the brains of wild-type animals.

Notably, brain uptake of a majority of dual substrates increases multi-fold when both transporters, rather than a single transporter, are inhibited. This was not the case for [^{11}C]TMZ. In this study, a significant but not multi-fold increase was observed. This finding indicates that TMZ is a dual, but weak, substrate for P-gp and BCRP. Alternatively, TMZ could be a substrate for a third efflux transporter that was not evaluated in this study. This is possible, but unlikely, because one would expect a compensatory efflux mechanism by that particular transporter as seen when only P-gp or BCRP was inhibited.

To date, only one other preclinical *in-vivo* study has shown that TMZ is transported by P-gp (Goldwirt et al., 2014). However, the authors administered high doses of TMZ by intravenous injection and performed pharmacokinetic studies in wild-type mice and mice lacking the P-gp efflux transporter. As in this study, a limited increase in TMZ brain exposure was observed upon transporter knockout: the brain-to-plasma ratio was 1.1 in P-gp-deficient mice and 1.0 in wild-type animals. Other studies have only examined the relationship between TMZ and P-gp indirectly by assessing the transporter's role in the development of chemoresistance and the potential to enhance TMZ efficacy *in-vitro* (Schaich et al., 2009) (Zhang et al., 2014) (Munoz et al., 2015b). None of these studies included drug transporter studies or assessed the impact of TMZ breakdown. Furthermore, no *in-vitro* or *in-vivo* studies have evaluated the role of BCRP in the transport of TMZ.

In conclusion, the results of this study confirm that TMZ is transported by P-gp and BCRP efflux transporters at the mouse BBB and that dual transporter inhibition is required to significantly enhance TMZ delivery into the brain. High-grade gliomas have extremely poor outcomes (Buckner, 2003) (Brodbelt et al., 2015) despite various treatment strategies. TMZ is one of the very few chemotherapy agents to improve outcome significantly in GBM patients when used with concomitant radiotherapy (Stupp et al., 2005). The modulation of P-gp and BCRP efflux function as a strategy for enhancing TMZ efficiency and overcoming chemoresistance in GBM tumours

requires further investigation.

Chapter 6 Preclinical *In-vivo* Glioma Study: P-glycoprotein and Breast Cancer Resistance Protein Inhibition Can Enhance Temozolomide Efficacy in a Glioma Model.

6.1. Abstract

Purpose: To evaluate the role of P-gp and BCRP in limiting TMZ efficacy in brain tumours.

Methods: A human glioma model in mice was derived by intracranial injection of human U87 glioma cells in thirty-three athymic female mice. Animals were treated with TMZ alone (50 mg/kg), TQD alone (40 mg/kg) or combination therapy (TMZ and TQD). Control animals received vehicle solution only. Response to treatment was evaluated by performing volumetric tumour measurement using MRI.
PET imaging with [^{11}C]TMZ was also performed in a subset of animals (n = 8) to assess if TQD inhibited P-gp and BCRP at the BBB level.

Results: Both TMZ alone and combination therapy resulted in a significant tumour response when compared with the control and the TQD alone groups ($p < 0.001$).
Furthermore, the TMZ alone group showed recurrence of glioma tumour growth, detected five weeks after completion of treatment. In contrast, the combination therapy group showed no recurrence of growth, and the tumours continued to shrink throughout the study, with no measurable tumour in three of the five animals.
Moreover, combination therapy resulted in a significantly earlier and sustained response when compared with TMZ alone.
Finally, PET imaging demonstrated increased brain uptake of [^{11}C]TMZ in animals that received combination therapy when compared with the animals that received TMZ alone.

Conclusions: This study demonstrates the effect of combination therapy with TMZ and TQD, a P-gp and BCRP inhibitor, in a human GBM model in mice. TMZ and TQD treatment resulted in more rapid and sustained U87 glioma shrinkage than did treatment with TMZ alone. The study also suggests that oral TQD treatment produced a superior response by inhibiting P-gp and BCRP efflux transporters at the BBB level.

6.2. Introduction

GBM is the most common primary brain tumour in adults (Louis et al., 2007). Despite the availability of various treatment approaches, survival rates are poor (Brodbelt et al., 2015). TMZ treatment with concomitant radiotherapy is the one of the few treatment strategies that significantly improves survival in patients with GBM tumours (Stupp et al., 2005).

A major obstacle to the effective treatment of GBM is the BBB, which restricts the entry of multiple chemotherapy agents into the brain (Agarwal et al., 2011a). The BBB is disrupted in GBM, especially at the tumour core, as demonstrated by contrast enhancement upon imaging. In addition, multiple studies have shown drugs can reach high concentrations in the tumour core and in the enhancing components but reach only limited concentrations in the adjacent non-enhancing part of the tumour (Fine et al., 2006) (Pitz et al., 2011). Such findings suggest that despite disruption of the BBB at the tumour core, the BBB is likely intact at the edges of the tumour where GBM cells may still exist and where efflux transporters can play a significant role in preventing drugs from reaching tumour cells. This is further complicated by the highly invasive nature of GBM tumours, which has been well documented historically. Multiple studies have shown tumoural spread into the contralateral hemisphere (Matsukado et al., 1961) and tumour recurrence following radical surgical approaches such as hemispherectomy (Bell and Karnosh, 1949).

P-gp and BCRP are two of the main efflux transporters present at the BBB. They are thought to play a central role in limiting the effective delivery of chemotherapy agents to the central nervous system (Szakacs et al., 2006) (de Vries et al., 2007) (Kodaira et al., 2010). Furthermore, the P-gp efflux transporter has been implicated in the development of chemoresistance to TMZ. Recent *in-vitro* studies have shown that TMZ treatment causes GBM cells to overexpress P-gp (Munoz et al., 2015b), and a clinical study has shown that the response of brain tumours to TMZ is directly affected by P-gp expression (Schaich et al., 2009). The role of BCRP in brain tumours is less well studied, but two *in-vitro* studies suggest a role for the transporter in the development of chemoresistance to TMZ (Chua et al., 2008) (Bleau et al., 2009). Finally, the previous PET imaging study has confirmed that P-gp and BCRP are efflux

transporters of TMZ that work together to exclude TMZ from the mouse brain at the BBB level.

The aim of this study was to evaluate the role of P-gp and BCRP in limiting TMZ efficacy in brain tumours. Using a xenograft GBM model, we found that chemical inhibition of P-gp- and BCRP-mediated efflux enhanced TMZ efficacy, and we identified a preferential increase in TMZ delivery into brain tumours as a potential mechanism.

6.3. Materials and methods

6.3.1. Materials

All cell culture plasticware was obtained from Greiner Bio-one (Gloucestershire, UK). All cell culture reagents were purchased from Life Technologies (Paisley, UK) except for TQD, which was purchased from MedChemexpress (Stockholm, Sweden). All remaining materials were purchased from Sigma-Aldrich (Poole, UK).

6.3.2. Methods

6.3.2.1. Cell studies

6.3.2.1.1. Cell line and culture

The immortalised human GBM U87 cell line (Ponten and Macintyre, 1968) was used to establish an *in-vivo* orthotopic xenograft model of glioma. The U87 cell line is well established and has been proven to maintain consistent tumourigenicity (Li et al., 2008). Furthermore, the U87 glioma cell line is known to be sensitive to TMZ due to its MGMT methylated status (Sang et al., 2016).

A single vial of the cryopreserved U87 human glioma cell line was removed from liquid nitrogen, thawed in water bath at 37ºC and immediately suspended in 15 mL of warm, freshly prepared U87 growth medium consisting of DMEM with 10% foetal calf serum (FCS), a 1%(v/v) Penicillin/Streptomycin mixture, and 1% L-glutamine. This was subsequently centrifuged at 300 x g for five minutes at 4ºC. The supernatant was removed and the pellet containing the U87 cells was suspended in 10mL of warm, freshly prepared U87 growth media. Media containing the U87 cells was added to a T-75 flask. The flask was maintained in a humidified atmosphere for 24 hours at 37ºC and 5% CO_2. The cells were checked daily by light microscopy and the U87 growth medium was replaced when needed.

6.3.2.1.2. Sub-culture of U87 glioma cells into 96 well-plates

When the U87 glioma cells reached 70-80% confluence (typically 3-6 days post-seeding - Figure 6.1), the media was removed and discarded. The flask was then washed twice with 5 mL of warm sterile PBS. Next, the flask was treated with 2.5 mL of warm trypsin-EDTA (ethylenediaminetetraacetic acid), ensuring that the flask surface was completely covered. The flask was then placed in an incubator in a humidified atmosphere at 37ºC and 5% CO_2 for 3 minutes and checked under microscope for cell detachment. Any remaining attached cells were subsequently detached by gently tapping on the sides of the flask. Next, trypsin was quenched through the addition of U87 growth medium, the cells were suspended in a 15 ml Falcon tube and the contents were centrifuged at 300 x g for 5 minutes. The supernatant was removed and the cell pellet was suspended in 1 ml of fresh U87 media. 20 µL of the cell suspension was added to 20 µL of trypan blue solution and cell density was calculated. The cells were then seeded onto 96-well plates to achieve a cell density of 20,000 cells per well.

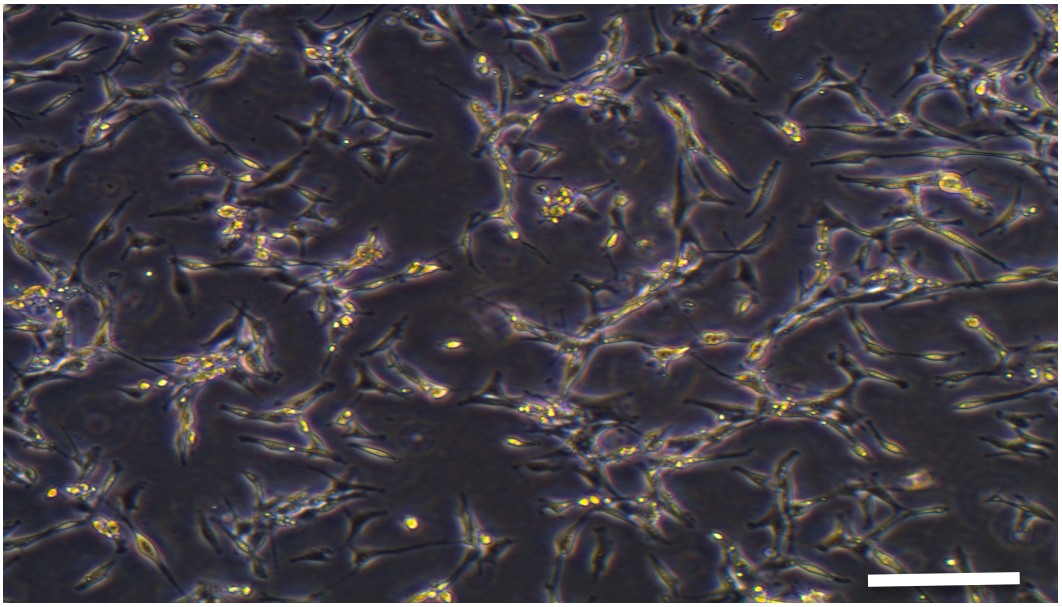

Figure 6. 1: Photomicrograph of U87 glioma cells reaching approximately 70% confluence and revealing classical morphological characteristics. Scale bar indicates 25 µm.

6.3.2.1.3. Determination of the number of viable cells

The number of viable cells was determined using the trypan blue assay (Strober, 2001). The detached cells were suspended in 1 ml culture medium, 20 µl of the cell suspension was transferred to a 1.5 ml Eppendorf tube containing 20 µl of 0.4% (w/v) trypan blue and this was mixed. Following 5 min incubation, a 20 µl aliquot of the cell suspension was placed onto the void of a haemocytometer and covered with a glass cover slip. The number of viable cells was estimated according to the following equation: Viable cells (cells.ml^{-1}) = average unstained cells per grid square x dilution factor x 10^4.

6.3.2.1.4. Measurement of efflux transporter functional activity

U87 glioma cells were seeded in a 96-well plate as detailed above. Measurement of P-gp activity was carried out 2-3 days following seeding the cells when cells reached approximately 80% confluence. On the day of the experiment, the medium was discarded and the wells were washed with 200 µL of warm PBS. Subsequently, 100 µL of phenol red free DMEM supplemented with 1% L-glutamine was added to the wells and the plate was incubated for 30 minutes at 37ºC and 5% CO_2. After this period, either 50 µL of DMEM + 1% L-glutamine (control condition) or 50 µL of P-gp inhibitor verapamil hydrochloride at a concentration of 30 µM (final concentration 10 µM) was added to the cells. Following 30 minutes of incubation, 50 µL of 2 µM calcein–AM (final concentration 0.5 µM) was added to all wells and the plate was incubated for another 30 minutes in a humidified atmosphere at 37ºC and 5% CO_2. After the incubation, the medium was aspirated and the wells were rapidly rinsed twice with 200 µL cold PBS and a further 100 µL cold PBS was added to the wells.

Intracellular calcein accumulation was assessed by fluorescence spectroscopy using a Safire multiplate reader (Tecan, Germany), with an excitation wavelength of 490 nm and an emission wavelength of 530 nm.

The same procedure was followed for measuring BCRP functional activity but the P-gp inhibitor (Verapamil) was substituted with the BCRP inhibitor KO143 (final

concentration 0.5 μM) and calcein–AM was replaced with Hoechst 33342. The intracellular Hoechst 33342 accumulation was assessed by fluorescence spectroscopy with the excitation wavelength of 370 nm and an emission wavelength of 450 nm.

The fluorescence of the treated wells was calculated and expressed as a percentage of the fluorescence of the control wells (% of control). All fluorescence values were corrected for background fluorescence by subtracting the average fluorescence values of eight wells containing 100 μL of PBS.
At least three independent experiments were performed for each transporter functional assay with at least eight replicates in each experiment.

6.3.2.1.5. Preparing U87 cells for intracranial implantation

U87 glioma cells were prepared and cell density was calculated as per Sections 6.3.2.1.2 and 6.3.2.1.3. The total number of cells was calculated and the volume containing the required number of cells (4×10^4 per mouse) was added to a 500 mL Eppendorf tube and centrifuged at 300 x g for five minutes at 18˚C. The supernatant was then removed and cell pellet was suspended with 22 μL/4×10^4 cells of freshly warmed U87 media. The resuspended cells were placed quickly on ice and used immediately for implantation.

6.3.2.2. Animal studies

6.3.2.2.1. Animals

All animals were sourced locally at the Biological Services Facility, University of Manchester. All procedures were approved by the Home Office Inspectorate and carried out under the University of Manchester project license number (70/7760) and conducted according to UK-CCCR guidelines (Workman et al., 2010), in compliance with the UK Animal Scientific Procedure Act, 1986. Efforts were made to minimise the number of animals being used for each experiment without affecting the ability to obtain meaningful results.

Female *nu/nu* CBA mice, 10 − 12 weeks of age, were used in all experiments. Animals

were housed in groups with a maximum number of five animals per group, with free access to food and water. Animals were bred locally and the environmental conditions were controlled at 45% - 65% humidity, a temperature range of 20 − 23ºC and a 12-hour controlled light-dark cycle. All animals were maintained with the highest possible standard of care.

6.3.2.2.2. Animal surgery

Female *nu/nu* CBA mice, 10 −12 weeks of age, were anaesthetised in an induction chamber with 2.5% - 3% isoflurane in O_2 at four L/min. Once under deep anaesthesia, the mice were transferred to a stereotactic head frame apparatus whilst anaesthesia was maintained via a nose cone. Temperature was monitored throughout the procedure via an appropriately placed thermometer probe.

A 1 cm midline scalp incision was made to allow visualisation of the bregma, and a small craniotomy was carried out at a position 2.5 mm posterior and 2 mm right lateral to the bregma. A 10μL Hamilton syringe was advanced via the craniotomy to a 4 mm depth from the cortical brain surface and subsequently withdrawn by 1 mm. This was followed by the injection of the U87 cellular suspension containing 4 x 10^4 cells in 2μL PBS over 3 minutes. Withdrawing the syringe by 1 mm from the 4 mm depth creates a small pocket of space for injecting the cellular suspension, which can reduce cell suspension reflux and prevent the undesired iatrogenic side effect of subcutaneous U87 tumour cell implantation. The craniotomy defect was then sealed with bone wax and the scalp incision was closed with 6.0 polypropylene sutures. The animals received a subcutaneous injection of 100 μg buprenorphine for analgesia and 100 μL normal saline before being transferred to a recovery incubator. The mice were transferred back to their normal housing conditions once full recovery was made.

6.3.2.2.3. Efficacy studies

Seven days following tumour implantation, the animals underwent structural MRI evaluation (protocol detailed in section 6.3.2.2.4) to confirm successful implantation. Tumour bearing animals received one of the four following treatments: TMZ (50 mg/kg), TQD (40 mg/kg), TMZ (50 mg/kg) and TQD (40 mg/kg) or vehicle solution

(5% dextrose in water). All treatment solutions were prepared freshly on the day of administration and delivered within 30 minutes of drug preparation by a single 100 μL oral gavage. Treatment was administered for five days per week for four weeks. TMZ and TQD were suspended in 5% dextrose in water and placed in an ultrasonic bath for 30 minutes.
When administering combination therapy, TQD treatment was always administered 10-15 minutes before TMZ.

The TMZ dose of 50 mg/kg was chosen to ensure no mice received more than 1 g as a total dose. This was particularly important as a decline in the efficacy of TMZ has been reported at higher doses (Hirst et al., 2013).
The TQD dose of 40 mg/kg was selected, as previous studies have indicated that an intravenously administered TQD dose exceeding 15mg/kg would achieve complete P-gp inhibition and significant, but not complete, BCRP inhibition (Wanek et al., 2012).

In the first study, animals were randomised into three different groups: animals that received vehicle solution (n = 4), TMZ (50 mg/kg) (n = 5) or combination therapy of TMZ (50 mg/kg) and TQD (40 mg/kg) (n = 5).
A second study was designed to investigate the effects of TQD alone treatment on the growth of the U87 glioma model. Tumour-bearing animals were randomised into two groups: a control group that received vehicle solution (5% dextrose in water) (n = 5) and a second group that received TQD (40 mg/kg prepared as previously) (n = 5).
Animals in all experiments underwent weekly brain MRI to monitor glioma growth rate. At eight weeks post implantation, the frequency of scanning was reduced to once fortnightly until week 12 when all animals were culled.
The free online software Simple Interactive Statistical Analysis (SISA) was used to calculate the sample size of (n = 5) to detect a 40% volume change, single sided, at week 3 with 80% power and 0.05 significance. This was based on the preliminary study that was used to ensure MRI suitability for monitoring tumour growth.

Outline of the treatment and scanning time line is presented in Figure 6.2 and details of the treatments administered are presented in Table 6.1.

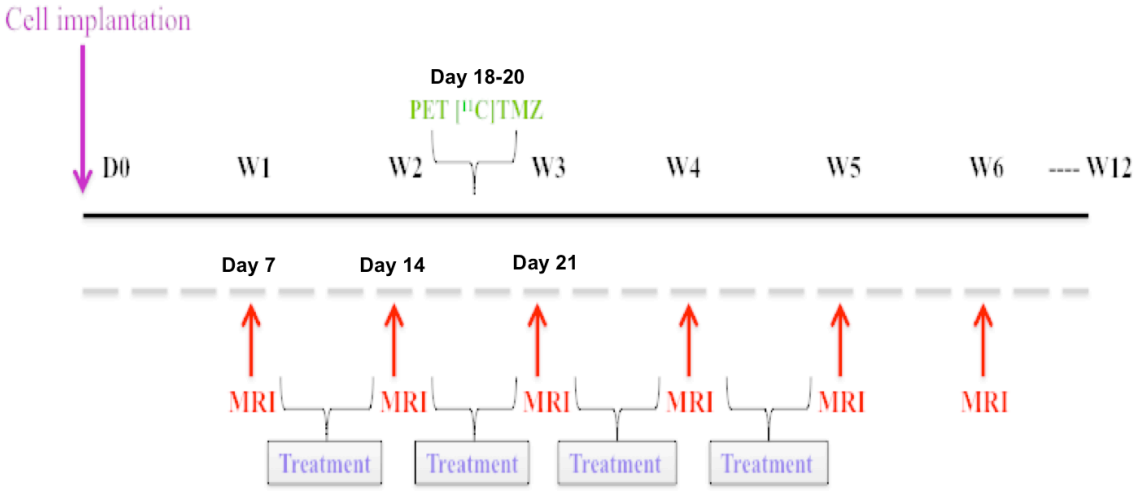

Figure 6. 2: Outline of the first experiment with the human U87 glioma model. Magnetic resonance imaging and treatment time points are shown. Magnetic resonance imaging was performed weekly until week eight after which it was done once every two weeks till week 12 when animals were culled.

Table 6. 1: Treatment groups and dosing regimens

Group	**Treatment**				
	Dose (mg/kg)	**Route**	**Volume**	**Frequency**	**Duration**
Control	Vehicle solution	Oral	100 µL	5 days per week	4 weeks
TMZ	50 mg/kg	Oral	100 µL	5 days per week	4 weeks
TQD	40 mg/kg	Oral	100 µL	5 days per week	4 weeks
Combination therapy	TMZ 50 mg/kg TQD 40 mg/kg	Oral	200 µL	5 days per week	4 weeks

Four different treatment regimens were used in this study: vehicle solution (5% dextrose in water), TMZ (50 mg/kg), TQD (40 mg/kg) and combination therapy (TMZ + TQD, 50 mg/kg and 40 mg/kg respectively). All treatments were prepared freshly on the day of administration. Treatment was administered for five days per week for four weeks.

In both studies, the animals were closely monitored for signs of neurotoxicity, such as deteriorating motor function and balance disturbances. General morbidity was also assessed daily by documenting weight, food intake and changes in breathing patterns, or any other signs of lethargy.

6.3.2.2.4. In-vivo magnetic resonance imaging and tumour volume measurements

Magnetic resonance imaging is a well-established tool for measuring tumour growth rate and therapeutic response in intracranial glioma models (Schmidt et al., 2004) (Cornelissen et al., 2005). An important objective in our first experiment was to confirm the suitability of MRI for detecting U87 glioma tumours and measuring their growth rate.

MR images were acquired using a 3T MRS 3000 (MR solutions, Guildford) with an 88 mm diameter bore system and an 18 mm head surface coil for signal reception. Structural high field MRI was initially optimised in post-mortem control animals for maximum anatomical resolution, with a final acquisition time of approximately 5 minutes for T2-weighted sequences. The sequence was evaluated in tumour bearing mice and showed excellent delineation of the tumour border and a clear demarcation of the tumour-brain interface. MRI was performed at week one post tumour cells implantation and repeated weekly thereafter till week eight. The frequency was then reduced to one MRI fortnightly till week 12 when all animals were culled.

The final structural T2-weighted sequence consisted of the following specifications: coronal image, TE/TR 68/4800, 8 echoes, 16 slices, 1 mm thickness, 256 x 256 matrix and 20 mm field of view.

For MRI scanning, animals were first anaesthetised in an induction chamber with 3% isoflurane in O_2 at 2 L/min. The animals were then transferred to the MRI bed and mounted on a heated pad, with the head secured in an anaesthetic face-mask. The animal's position was secured by light restraint of their limbs with surgical tape. A breathing monitor pad and a temperature probe were placed appropriately for continuous observation during the scanning period. Anaesthesia was maintained via a nasal cone with 1-2% isoflurane in O_2 at 2 L/min.

MRI images were used to manually delineated tumours using the public domain programme ImageJ (http://rsb.info.nih.gov/ij/index.html) and OsiriX 7.0 imaging software (http://www.osirix-viewer.com). T2-weighted images were used to carefully delineate the tumour margins on all adjacent slices. Tumour volume was calculated by

multiplying the tumour surface by the slice thickness. Additionally, particular attention was given to any radiological signs of disease progression, such as tumoural haemorrhage, hydrocephalus, shift of the midline structures and tumour necrosis.

6.3.2.2.5. Impact of treatment on [^{11}C]TMZ uptake and plasma TMZ levels

6.3.2.2.5.1. Study design

A third study was then undertaken to confirm the results observed in study one and to enable treatment-induced effects on brain uptake of [^{11}C]TMZ and plasma TMZ levels to be evaluated.

10 mice were injected with U87 glioma cells and randomised into two separate groups (n = 5 per group). One group received TMZ alone (50 mg/kg) and the second group received TMZ (50 mg/kg) and TQD (40 mg/kg).

Four animals from each group underwent PET scan imaging with [^{11}C]TMZ to assess any differences in the brain uptake of radiolabelled [^{11}C]TMZ after completing two weeks of treatment.

Additional blood sample was collected from all animals as detailed in section 6.3.2.2.5.5.

A summary of all the preclinical *in-vivo* studies is presented in Table 6.2.

Table 6. 2: Summary of animal studies.

Study	Treatment Groups	Number of animals	MRI	[11C]TMZ PET	Blood sample
First	Vehicle Temozolomide Temozolomide and Tariquidar	13*	Yes	No	No
Second	Vehicle Tariquidar	10	Yes	No	No
Third	Temozolomide Temozolomide and Tariquidar	10	Yes	Yes	Yes

Animals underwent weekly MRI scans to evaluate tumour volumes. Animals in the third study underwent additional PET scanning with [^{11}C]TMZ during the second week of treatment, with a blood sample collected at the end of the experiment. * 14 mice were implanted with U87 glioma cells but one failed and was excluded from any future analysis.

6.3.2.2.5.2. Small animal positron emission tomography

In the third preclinical *in-vivo* experiment, eight mice (four from the TMZ alone and four from the combination treatment) underwent PET imaging using [^{11}C]TMZ. All animals were imaged during the second week of treatment. Given the limited time window (three days), an in-house designed dual animal bed was used, which enabled scanning of two animals side by side and therefore maximising the throughput of the imaging studies.

The mice were anaesthetised with 2% isoflurane in O_2 at 2L/min in the induction box. The tail vein was catheterised and the animal was then placed into the prone position in the dual animal bed, with the head restrained on a tooth bar. The mouse was then transferred to the Inveon preclinical PET-CT scanner (Siemens) and anaesthesia was maintained with 1-2% isoflurane in O_2 at 2L/min delivered via a nose cone and adjusted according to the depth of anaesthesia.

Image quality can be affected by multiple factors when using a dual bed, such as positional variation and variations in signal attenuation and scatter that are primarily caused by the differences in the weights of animals. In an effort to minimise the effects of such factors, the position of the animals in the dual bed was alternated with each session so that half the animals from each treatment group were scanned on the right and the other half on the left.
The acquisition protocol started with a whole body CT scan prior to PET scanning to generate an attenuation correction map. The time coincidence window was set to 3.432 ns and the level of energy discrimination was set to 350 − 650 keV. A reference laser beam was utilised to ensure placement of the brains in the centre of the axial field of view.

Respiratory rate and temperature were continuously monitored throughout image acquisition using a pressure sensitive pad and rectal probe. Body temperature was controlled via a fan module controlled by BioVet (Inveon) software. At the start of the scan, each mouse was injected with [^{11}C]TMZ intravenously via the tail vein catheter

and data were collected for 60 minutes. The animals recovered in a warmed chamber. Details of the animals that underwent PET scans are provided in Table 3.

Table 6. 3: Characteristics of animals that underwent PET scans with [^{11}C]TMZ.

Animal ID	Group	Days after tumour implantation	Position	Weight (g)	Injected radioactivity (MBq)
a02199	TMZ	20	Left	22.7	52.2
a02200	TMZ	20	Right	22.8	48.3
a02201	TMZ	19	Left	25.3	22.6
a02202	TMZ	15	Right	22.8	47.0
a02203	TMZ + TQD	19	Right	25.2	24.0
a02204	TMZ + TQD	20	Right	23.3	53.0
a02206	TMZ + TQD	15	Left	22.0	45.2
a02207	TMZ + TQD	20	Left	23.0	51.8

All scans were performed in the second week of treatment using the dual animal bed. The TMZ group (n = 4) received 50 mg/kg and the combination therapy (TMZ + TQD) group (n = 5) received TMZ (50 mg/kg) and TQD (40 mg/kg). All treatments were delivered by oral gavage. Treatments were administered for five days per week for two weeks.

6.3.2.2.5.3. Image reconstruction

The list mode data were histogrammed with a span of 3 and a maximum ring difference of 79 into 3D sinograms. The list mode data of the emission scans were sorted into 16 frames (5 x 60 seconds, 5 x 120 seconds, 3 x 300 seconds and 3 x 600 seconds) for image reconstruction. The emission sinograms (individual frames) were normalised, corrected for attenuation, scatter and radioactivity decay, and reconstructed using OSEM3D (16 subsets and 4 iterations) into 128 x 128 x 159 matrix with a 0.776 x 0.776 x 0.796 mm^3 voxel sizes. No notable artefacts were detected.

6.3.2.2.5.4. Image analysis

As previously detailed (in the previous chapter), semi-automatic segmentation of the PET images and analysis was performed using the BrainVisa and Anatomist framework (http://brainvisa.info/).

Given the relative small tumour volume and the apparent homogenous brain uptake of radiotracer, it was not possible to delineate tumour based on [^{11}C-TMZ] PET scans only. Consequently two approaches were taken: analysing of whole brain or a hemisphere uptake where the two hemispheres in each brain were manually delineated on the summed 60 minutes PET image.

6.3.2.2.5.5. Blood sample collection and Temozolomide analysis

In the third study, blood samples were collected from each animal when they became symptomatic or just before culling.

Mice were anaesthetised using 2% isoflurane in O_2 at 2L/min. oxygen. Blood sample was collected by direct cardiac puncture and transferred to an Eppendorf tube. Plasma was then stored at -80ºC for future analysis.

TMZ concentration in plasma was quantified using a high performance liquid chromatography (HPLC) with a UV detection method. In brief, the plasma samples (78.89 ± 7.469 μL) were spiked with an internal standard (2.3 or 46 μg/ml) and directly injected into the HPLC system (HPLC Prominence, Shimadzu). Separation was achieved on an ACE 5 phenyl column (150 x 4.6 mm, 5 μm). The mobile phase consisted of 58 mM monosodium phosphate at a pH of 2.4 and methanol, with an isocratic elution mode (15% Methanol and 85% monosodium phosphate). Retention time was around 6 minutes for TMZ (5.5 – 6.1 minutes). The analysis run time was set at approximately 20 minutes. The UV wavelength of TMZ was then selected. UV Chromatogram of TMZ is presented in Figure 6.3.

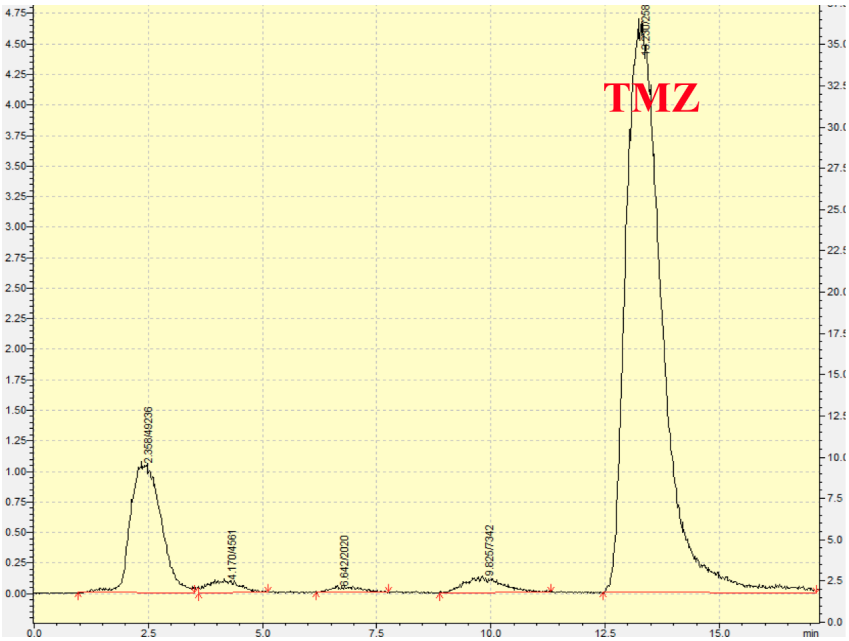

Figure 6. 3: UV Chromatogram of TMZ in a plasma of a mouse 4 hours following administration of TMZ (50 mg/kg) by oral gavage. TMZ peak at the expected retention time of 13.9 minutes.

6.3.2.3. Statistical analysis

Statistical analysis was performed using Prism6 software (GraphPad Inc, La Jolla, CA, USA). The different tests used are detailed in each figure legend. All values are expressed as mean ± standard deviation (SD) unless stated otherwise. No outliers were removed from any set of data. P value of <0.05 were considered to be statistically significant.

6.4. Results

6.4.1. No evidence of functionally active P-glycoprotein transporters in the U87 glioma cells

The activity of P-gp was investigated in U87 cells using an intracellular calcein-AM accumulation assay. Calcein-AM is a molecular probe that, when metabolised by intracellular esterase, produces fluorescent calcein. Calcein-AM is a substrate for P-gp. As a result, intracellular calcein-AM is increased when P-gp function is inhibited (Eneroth et al., 2001). Intracellular calcein was measured by fluorescence and was found to be minimally higher in cells pretreated with P-gp inhibitor verapamil hydrochloride (10μM), compared to vehicle-treated control cells. This effect was not significant ($p = 0.14$) reflecting the lack of functionally active P-gp transporters in the U87 glioma cells (Figure 6.4).

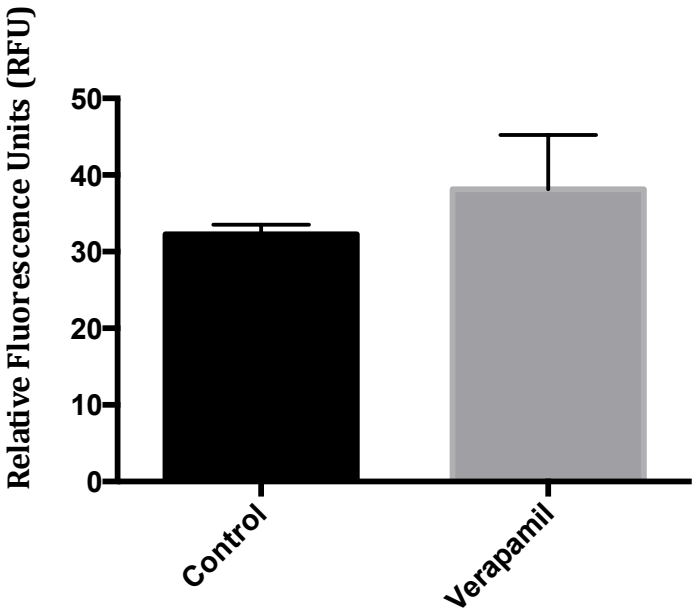

Figure 6. 4: Lack of functional activity of P-glycoprotein in U87 glioma cells. Cells were pre-incubated for 30 min at 37 °C in U87 growth medium alone or U87 growth medium containing 10 μM Verapamil (P-glycoprotein inhibitor). Intracellular accumulation of calcein-AM was measured by spectrofluorometry (excitation λ 490 nm, emission λ 520 nm). Data are expressed as relative fluorescent units and are mean ± SD of eight replicates ($n = 3$). Data analysed using unpaired Student's t-test.

6.4.2. Breast Cancer Resistance Protein is functional in the U87 glioma cells

The functional activity of BCRP was also investigated in U87 glioma cells using the Hoechst 33342 assay. Hoechst 33342 is a molecular probe that is known to be a BCRP substrate and which can easily be measured by fluorescence (Kim et al., 2002). Intracellular retention of Hoechst 33342, as measured by fluorescence, was found to be significantly higher ($p < 0.001$) in cells pretreated with 0.5μM KO143, a selective BCRP inhibitor, compared to vehicle-treated control cells. This finding reflects the presence of functionally active BCRP transporters in the U87 glioma cells (Figure 6.5).

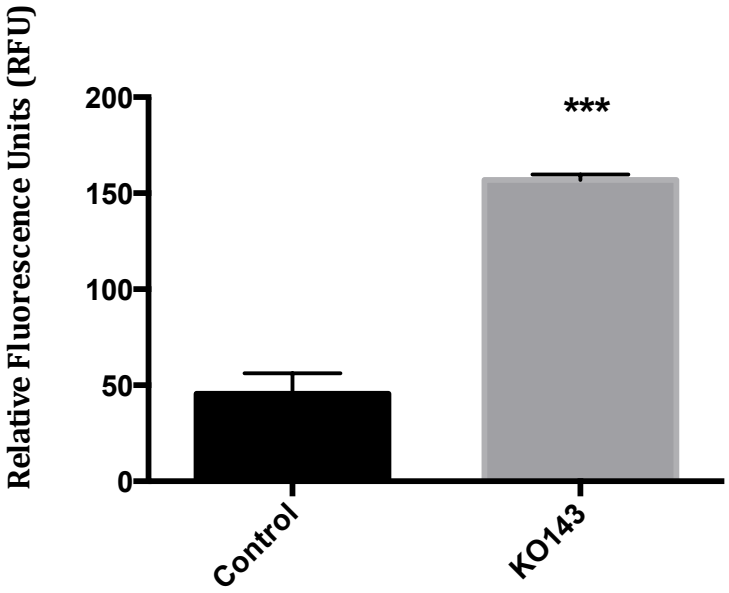

Figure 6. 5: Functional activity of Breast Cancer Resistance Protein in U87 glioma cells. Cells were pre-incubated for 30 min at 37 °C in U87 growth medium alone or U87 growth medium containing 0.5 μM KO143. Intracellular accumulation of Hoechst 33342 was measured by spectrofluorometry (excitation λ 370 nm, emission λ 450 nm). Data are expressed as relative fluorescent units and are mean ± SD of eight replicates ($n = 3$). *** indicates statistical significance of $p<0.001$ compared to respective control by Student's t-test.

6.4.3 Magnetic resonance imaging is a suitable tool for monitoring tumour growth in the U87 glioma model

In the four female *nu/nu* CBA mice that were implanted with $4x10^4$ U87 glioma cells, the glioma tumours demonstrated an exponential growth rate in all animals, with a mean volumetric measurement of 1.2, 4.7 and 45.8 mm^3 at 1, 2 and 3 weeks post tumour implantation, respectively (Figures 6.6).

Figure 6. 6: Representative T2-weighted coronal magnetic resonance images from a single mouse at weeks 1, 2 and 3 (from left to right) following implantation of $4x10^4$ U87 glioma cells. Exponential growth is noted, with a very rapid increase in tumour size in the third week post U87 glioma cell implantation.

Furthermore, the tumours demonstrated diffuse and homogeneous enhancement following gadolinium administration (Figure 6.7).

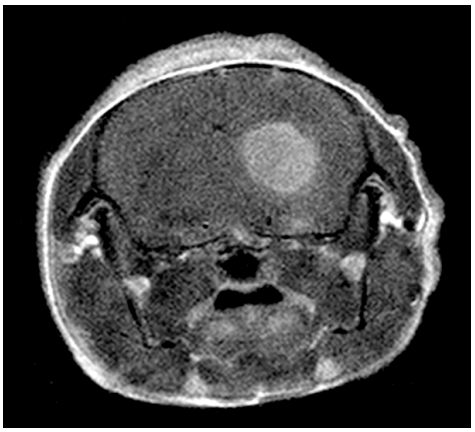

Figure 6. 7: Representative T1-weighted coronal magnetic resonance images following gadolinium administration from a mouse at weeks 2 following implantation of $4x10^4$ U87 glioma cells. Diffuse and homogeneous enhancement is demonstrated.

It is important to note that the MRI protocol was successful in detecting the tumours

and measuring their volume at a very early stage (one week post implantation). This time point was subsequently chosen for administration of treatments.

6.4.4. Combination therapy of Temozolomide and Tariquidar is superior to Temozolomide alone

A summary of the treatment protocol and the 14 Female *nu/nu* CBA mice used is presented in Table 6.4. One of the tumour implantations in the TMZ alone therapy group was unsuccessful, with no evidence of tumour growth upon follow-up MRI. This mouse was excluded from the analysis.

Table 6. 4: Summary of the first *in-vivo* study.

Group	Number of animals	Interval between implantation and initiation of treatment	Interval between treatment initiation and culling	Notes
Vehicle	4	7 days	18 days	-
TMZ	5	7 days	80 days	1 failed implantation
Combination therapy	5	7 days	63 days 71 days 80 days	1 animal 1 animal 3 animals

Analysis of tumour volumes from pre and post-treatment MRI studies (weeks 1 and 5 post U87 implantation) revealed that both treatment approaches (TMZ alone and combination therapy of TMZ and TQD) successfully slowed tumour growth rate in the U87 glioma model when compared with the control animals that received vehicle solution only (Figure 6.8). Additionally, both treatment protocols resulted in statistically significant tumour volume reduction at the end of the treatment period ($p < 0.001$, Figure 6.9).

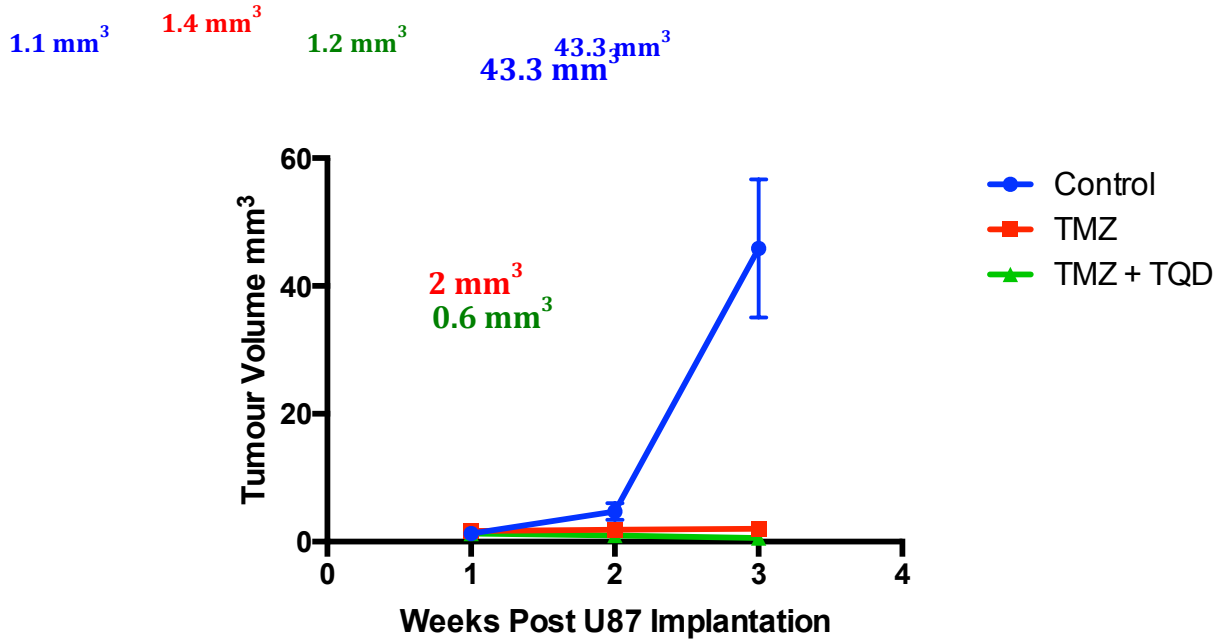

Figure 6. 8: Tumour volume measurements at one, two and three weeks post implantation of 4x10^4 U87 glioma cells. The control group (n = 4) received vehicle solution only (5% dextrose in water), the TMZ group (n = 4) received 50 mg/kg and the combination therapy (TMZ + TQD) group (n = 5) received TMZ (50 mg/kg) and TQD (40 mg/kg). All treatments were delivered by oral gavage.
Data presented as mean ± SD and tumour volume measured as follows at three weeks: (Control) 43.3 ± 3.1, (TMZ) 2.03 ± 0.3, (TMZ + TQD) 0.58 ± 0.1.

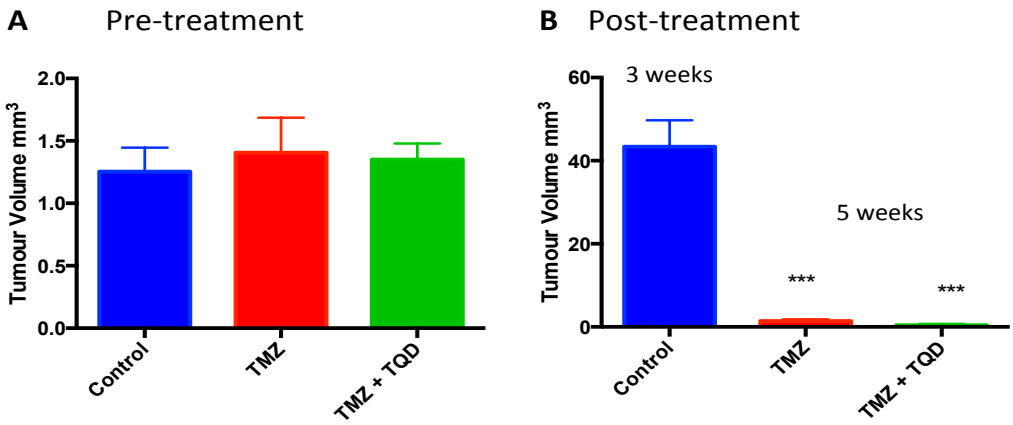

Figure 6. 9: Tumour volume measurements (A) before administration of treatment and (B) after completion of treatment (week 1 and 5 post 4x10^4 U87 glioma cells implantation, respectively). The control group (n = 4) received vehicle solution only (5% dextrose in water), the TMZ group (n = 4) received 50 mg/kg, and the combination therapy (TMZ + TQD) group (n = 5) received TMZ (50 mg/kg) and TQD (40 mg/kg). Data in the post treatment graph is from the last available time point (week 3 post implantation) for the control animals, as they were euthanised due to the development of neurological symptoms and high tumour volume, as measured with MRI. Data were statistically analysed by Kruskal-Wallis test and Dunn's multiple comparison test. *** $p < 0.001$.
Data presented as mean ± SD and tumour volume was measured as follows at three weeks post implantation for (Control) 43.3 ± 3.1, and five weeks post implantation for (TMZ) 1.33 ± 0.2 and (TMZ + TQD) 0.32 ± 0.1.

While treatment with TMZ alone resulted in a slowing of the glioma tumour growth rate, tumour volume regression was only noted after completing three weeks of therapy (Figure 6.10). In contrast, animals that received the combination therapy of TMZ and TQD demonstrated a superior treatment effect, in which tumour regression was evident after only one week of treatment and persisted throughout the duration of the experiment.

Furthermore, the TMZ alone group showed recurrence of glioma tumour growth, detected ten weeks after tumour implantation (five weeks after completion of treatment, Figure 6.10). In contrast, the combination therapy group showed no recurrence of growth, and the tumours continued to shrink throughout the study, with no measurable tumour in 3 of the 5 animals at week 12. Finally, tumour volumes in the combination therapy group were significantly smaller than in the TMZ group at weeks 3, 4, 5, 10, 11 and 12 post U87 glioma implantation.

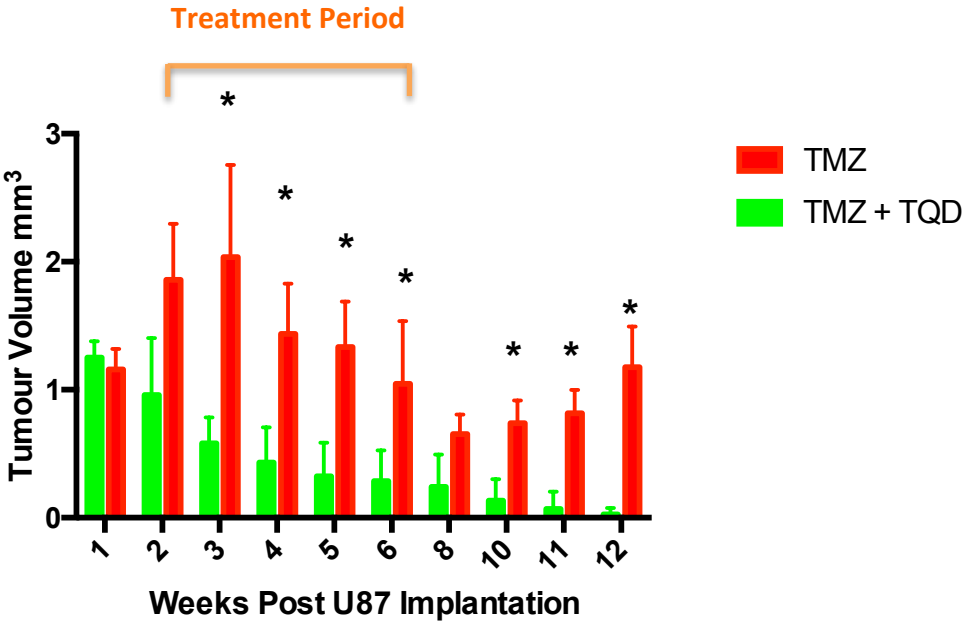

Figure 6. 10: Tumour volume measurements from week 1 to week 12 post implantation of $4x10^4$ U87 glioma cells. The TMZ group (n = 4) received 50 mg/kg and the combination therapy (TMZ + TQD) group (n = 5) received TMZ (50 mg/kg) and TQD (40 mg/kg). Treatment was administered 5 days per week for 4 weeks. Data are presented as mean ± SD. The data were statistically analysed by multiple Mann-Whitney test for each time point. * $p < 0.05$.
Control group was removed for simplification of the graph

Example of tumour response in the different treatment groups after completion of treatment is presented in Figure 6.11.

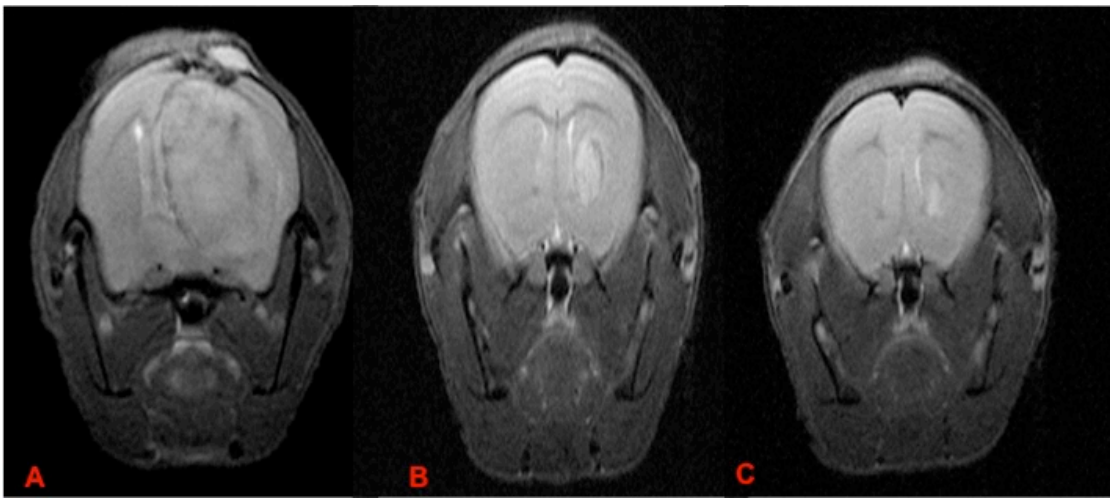

Figure 6. 11: Representative coronal T2-weighted images for each treatment group at completion of treatment for (A) vehicle solution (week three post implantation), (B) TMZ alone (week five post implantation) and (C) combination (TMZ + TQD) treatment (week five post implantation).

6.4.5. Tariquidar alone does not affect glioma growth

In the second study, MRI volumetric measurements revealed no effect for TQD therapy alone when compared with the vehicle treated animals. The growths rate in the control animals was very similar to the growth rate seen in the control animals form the first study (Figure 6.12, A). Furthermore, the TQD group demonstrated a slightly larger tumour volume than control at week three, but this was not statistically significant ($p = 0.81$)(Figure 6.12, B). All animals were sacrificed at the end of week 3 due to loss of physical condition and large tumour volume, as measured with MRI.

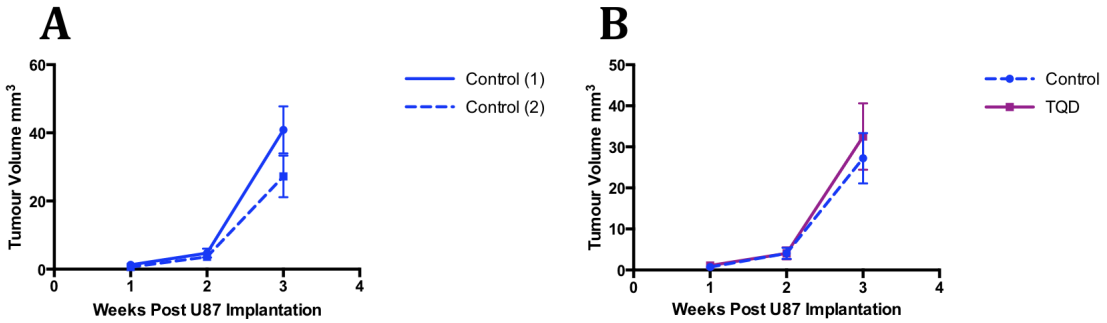

Figure 6. 12: Tumour volume measurements at weeks 1, 2 and 3 post implantation of $4x10^4$ U87 glioma cells in (A) control animals form the first (solid line) and second

(dashed line) studies. (B) In the second study for the control group (n = 5) received vehicle solution only (100 µL of 5% dextrose in water) and the TQD group (n = 5) received treatment solution (40 mg/kg). All treatments were delivered by oral gavage. Treatment was initiated 1 week post tumour cell implantation and administered 5 days per week for two weeks. The data are presented as mean ± SD, n = 5 for both groups. The data were statistically analysed by multiple Mann-Whitney tests for each time point. $p < 0.05$ was considered statistically significant.

6.4.6. Confirmation of the superior effect of combination therapy on glioma growth:

The third animal experiment aimed to investigate whether oral TQD treatment can inhibit the efflux transporters, namely P-gp and BCRP, at the BBB level. 10 U87 tumours were treated with either TMZ or the combination therapy of TMZ and TQD. In contrast to the previous study, treatment was initiated at day 10 following U87 glioma cell implantation, instead of the day 7 time point. This was done to allow for further tumour growth prior to initiation of therapy. As observed in the previous experiment, the combination therapy exhibited a superior effect, both on tumour growth rate and tumour volume. However, this effect was equally evident after one week of treatment ($p < 0.01$), (Figure 6.13).

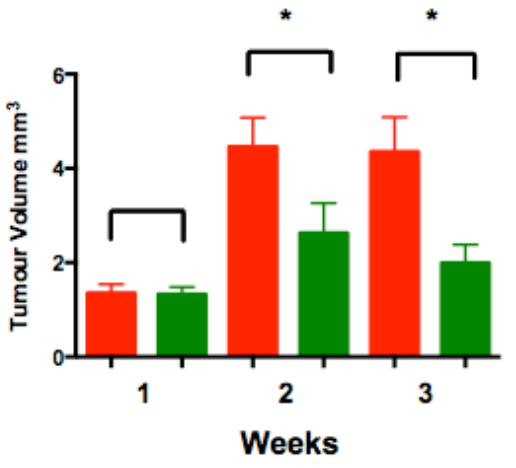

Figure 6. 13: Tumour volume measurements at weeks 1, 2 and 3 post implantation of $4x10^4$ U87 glioma cells. The TMZ group (n = 4 for week 1 and 2, n = 3 for week 3) received 50 mg/kg, and the combination therapy (TMZ + TQD) group (n = 5 for week 1 and 2, n = 4 for week 3) received TMZ (50 mg/kg) and TQD (40 mg/kg). All treatments were delivered by oral gavage. Treatment was administered five days per week for two weeks. Data are presented as mean ± SD. The data were statistically

analysed by multiple Mann-Whitney tests for each time point. $p < 0.05$ was considered statistically significant.

6.4.7. *In-vivo* PET imaging study

6.4.7.1. Brain segmentation from PET images

Use of the semi-automated segmentation software resulted in positive correlation between the segmented brain volumes (mm^3) on the 60 minutes summation PET images and the measured brain weight (g) post mortem in all mice (n = 8, r^2 = 0.826, p = 0.001) (Figure 6.14).

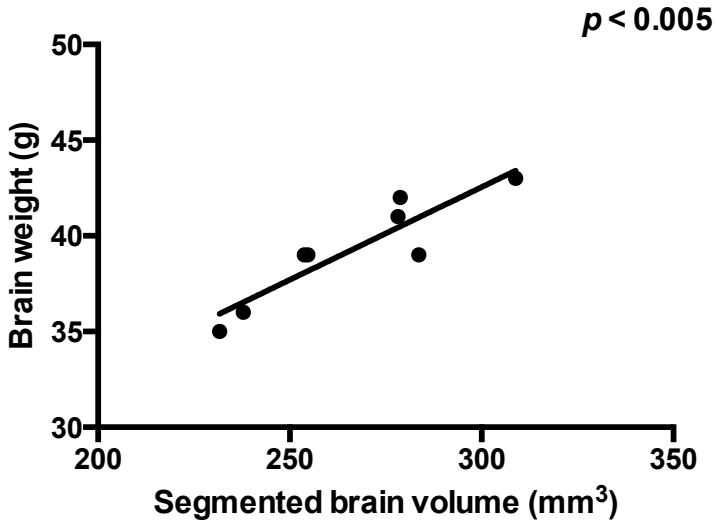

Figure 6. 14: Significant positive correlation was found between the brain volumes segmented using the LMA method and the post mortem brain weights across all PET scans with [^{11}C]TMZ. For all animals, n = 8, r^2 = 0.826, p <0.005. Data were analysed using the Pearson's correlation test.

Furthermore, the segmented brain regions appeared as homogenous regions of activity, with no heterogeneous areas of radiotracer uptake. This finding was also supported by visual inspection of the PET summation images (0 − 60 minutes). Given the relative small tumour volume and the apparent homogeneous brain uptake of radiotracer, it was not possible to delineate tumours based on [^{11}C-TMZ] PET scans only. Consequently two approaches were taken: analysing of whole brain radiotracer uptake and a hemispheric radiotracer uptake where the two hemispheres in each brain were manually delineated on the summed 60 minutes PET image.

6.4.7.2. Small animal PET shows a non-significant increase in whole brain uptake of [^{11}C]TMZ in the combination therapy group in comparison to the TMZ alone group

All PET scans were carried out during the second week of treatment (week 3 post U87 glioma cell implantation) and took place within two hours of treatment administration.

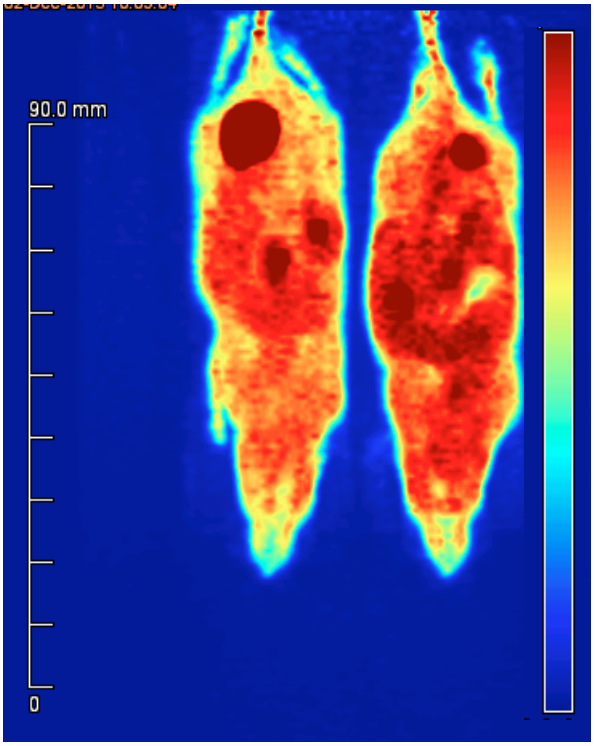

Figure 6.15: Representative maximum intensity projection image (last ten minutes) illustrating brain uptake of [^{11}C]Temozolomide in a dual-bed PET for orthotopic glioma model in the Temozolomide alone (Left) and Temozolomide plus Tariquidar (Right) treatment groups.

Mean TACs of the whole brains from the two different groups are presented in Figure 6.15. Brain radioactivity rose continuously following radiotracer administration in both treatment groups (Figure 6.16, A). The highest point of activity was reached at the end of the scan (60 minutes) and this was slightly higher in the combination therapy group than the TMZ alone treatment group (Figure 6.16, B). However, the calculated areas under the TAC from time 0 to 60 minutes (AUC_{brain}) were similar, with no statistically significant differences seen between combination therapy: 31.9 ± 1.4, TMZ alone: 30.7 ±1.4, $p = 0.56$).

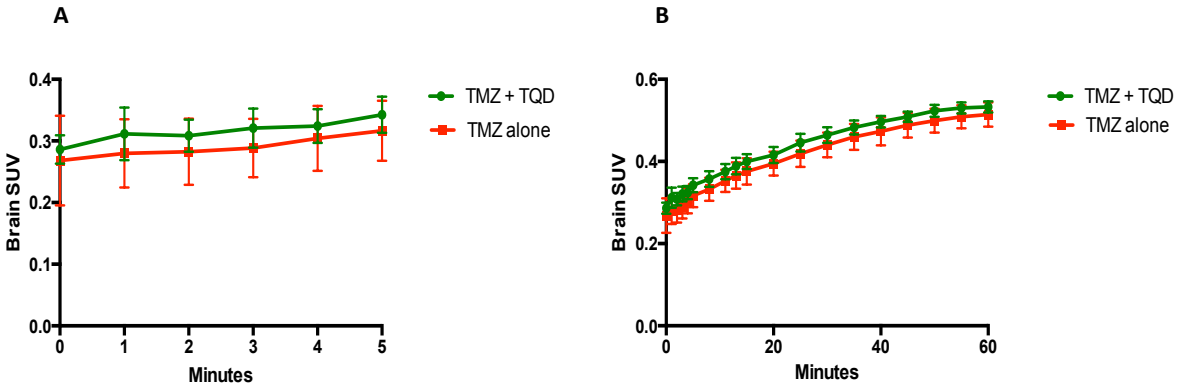

Figure 6. 16: Mean time-activity curves (standardised uptake value (SUV) ± standard error of the mean [SEM]) of [^{11}C]TMZ in the whole brain (A) from 0 to 5 minutes and (B) from 0 to 60 minutes after radiotracer injection. TMZ treatment group (n = 4, 50 mg/kg) and combination therapy (TMZ + TQD) group (n = 4, TMZ 50 mg/kg + TQD 40 mg/kg). Areas under the TAC were statistically compared with Kruskal-Wallis test. SUV indicates SUV mean.

Furthermore, mean TACs from the hemisphere containing the tumour showed higher SUV than the contralateral hemisphere in both treatment groups (Figure 6.17 and table 6.5). However, the AUC_{hemi} calculated for each group were not statistically different (41.6 ± 1.6 and 35.3 ± 5.7 for the combination therapy and 34.1 ± 7.3, 29.6 ± 7.4 for TMZ alone, p = 0.16 in the tumour-bearing and contralateral hemispheres respectively).

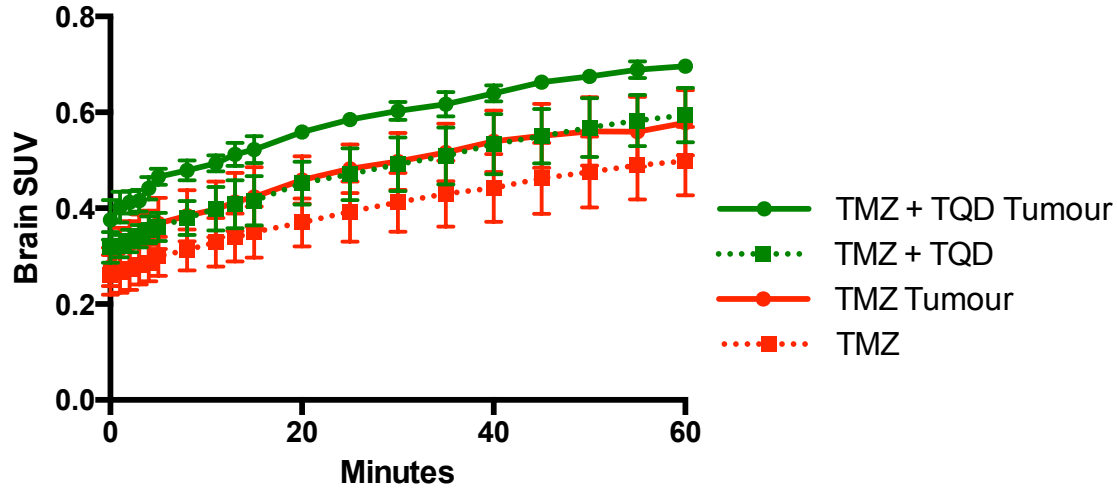

Figure 6. 17: Mean time-activity curves (standardised uptake value (SUV) ± SEM) of [^{11}C]TMZ in the hemispheres from 0 to 60 minutes after radiotracer injection for the combination therapy group in hemispheres containing tumours (solid line) and tumour-free hemispheres (dotted line) (n = 4 for each group, received 50 mg/kg TMZ and 40 mg/kg TQD); and for TMZ alone treatment group, in hemispheres containing tumours (solid line) and in tumour free hemispheres (dotted line) (n = 4 for each group, received 50 mg/kg TMZ only). Areas under the TAC were statistically compared with Kruskal-Wallis test.

Table 6.5: Values of the calculated areas under the curve for [^{11}C]TMZ uptake in each treatment group for the different hemispheres.

	Combination therapy tumour-bearing hemisphere	Combination therapy tumour-free hemisphere	TMZ alone therapy tumour-bearing hemisphere	TMZ alone therapy tumour-free hemisphere
Total area under the curve	35.2	28.9	28.9	24.1
Standard error	0.34	1.08	1.21	1.2

The lack of statistical significance in this study is likely to be attributed to the small number of animals in each group (n = 4). However, this data provide solid foundation of expanding the study in order to provide it with the required statistical power.

As blood sampling is a terminal procedure in mice, further analysis such as the brain-blood ratio of radioactivity was not feasible as animals could not be euthanised to enable volumetric tumour measurements at week three and for collection of blood samples for measurements of cold TMZ levels.

6.4.8. Plasma levels of Temozolomide are not significantly higher in the combination therapy when compared with Temozolomide alone therapy group

Blood sample collection was attempted in 2 mice at the end of week 1 of treatment (two weeks post tumour implantation), as they had demonstrated significant weight loss and needed to be euthanised. One sample was haemolysed and cardiac puncture failed in the other mouse. The remaining blood samples were collected at the end of the second week of treatment with no complications (Table 6.6).

Table 6. 6: Summary of blood collection time points, issues encountered, and Temozolomide concentration in plasma for the different treatment groups.

Animal ID	Group	Time since last dose	TMZ concentration (µg/ml)	Issues
a02199	TMZ	4 hours	12.6	-
a02200	TMZ	2 hours	22.8	-
a02201	TMZ	4 hours	14.2	-
a02202	TMZ	4 hours	13.4	Haemolysed blood sample
a02203	TMZ + TQD	4 hours	17.1	-
a02204	TMZ + TQD	4 hours	18.1	-
a02205	TMZ + TQD	4 hours	-	Unsuccessful cardiac puncture
a02206	TMZ + TQD	4 hours	10.0	Haemolysed blood sample
a02207	TMZ + TQD	2 hours	24.6	-

The TMZ group (n = 4) received 50 mg/kg and the combination therapy (TMZ + TQD) group (n = 5) received TMZ (50 mg/kg) and TQD (50 mg/kg). All treatments were administered by oral gavage. Blood samples were collected at the end of week three, following five days of continuous treatment administration.

TMZ was detected in all plasma samples, with the combination therapy group demonstrating slightly higher TMZ concentration in plasma than the TMZ alone group. However, this was not significant.

As expected, levels were higher at 2h than at 4h, but the 2h data include single animal in each group (samples at the 2 hours post treatment administration time point were inadvertently collected).

Combined data from the 2h time point are shown in Figure 6.18(A) and from the 4h time point only in Figure 6.18(B). While combination therapy demonstrated higher concentration of TMZ in plasma than the TMZ alone treatment group, this effect was not statistically significant either when analysing all blood samples (p = 0.68) or for the 4h post treatment time point only (p = 0.7).

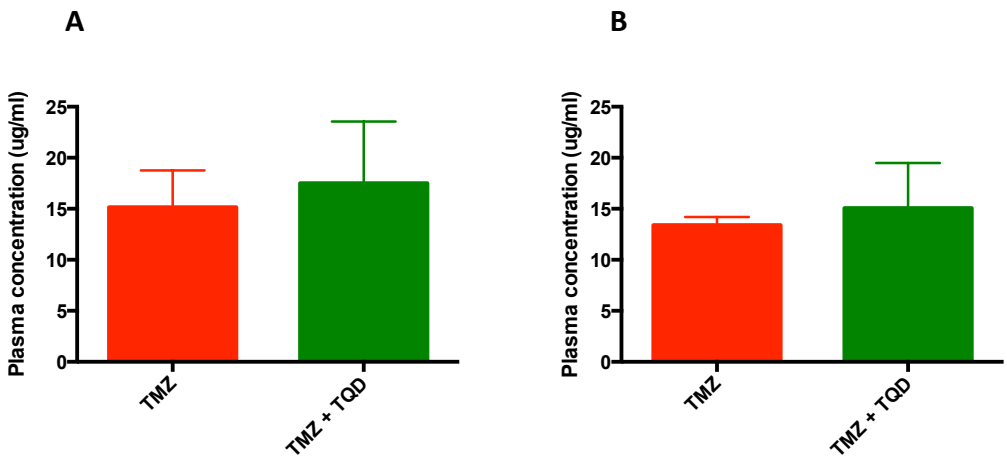

Figure 6. 18: TMZ concentration (µg/mL) in plasma, as measured by high performance liquid chromatography (HPLC) with UV detection for (A) 2h and 4h post treatment time points and (B) for the 4h post treatment time point only. The TMZ group (n = 4) received 50 mg/kg and the combination therapy (TMZ + TQD) group (n = 4) received TMZ (50 mg/kg) and TQD (40 mg/kg). All treatments were delivered by oral gavage. Treatment was administered for five days per week for two weeks. Blood collection was performed by direct cardiac puncture. Data are presented as mean ± SD and include samples in which blood haemolysis was noted. The data were statistically analysed by unpaired Mann-Whitney test.

6.5. Discussion and conclusions:

GBM is the most common and lethal primary brain tumour in adults (Louis et al., 2007). Patients with GBM benefit from a multidisciplinary treatment approach involving surgery, radiotherapy, and chemotherapy (Stupp et al., 2005), but overall survival remains poor (Brodbelt et al., 2015). Despite such treatment approaches, these tumours frequently develop chemoresistance. Various novel therapeutic strategies, such as angiogenic therapy, have been suggested over the years, particularly for patients who develop recurrent or progressive disease, but they have had limited success and have not changed overall survival (Khasraw et al., 2014). Therefore, new, more effective treatments that can overcome the BBB and chemoresistance ,and establish a sustained tumour response are needed.

Because this study assessed the effects of P-gp and BCRP inhibition on tumour response to TMZ, it was important to assess the functional activity of these transporters in U87 glioma cells. We detected limited functional activity for BCRP and no functional activity for P-gp. This is consistent with some of the limited available literature, which reports BCRP expression but no P-gp expression in the U87 cell line (Carcaboso et al., 2010). However, this study evaluated the expression but not the functional activity of BCRP. Furthermore, P-gp and BCRP expression in the rodent brain is well established (Loscher and Potschka, 2005a); such transporters are expected to be highly expressed and functional at the edges of the tumour where the BBB is intact.

TMZ is the primary drug used in the treatment of high-grade glioma, and its efficacy in the treatment of various murine glioma models, including the U87 glioma model, has been established (Hirst et al., 2013). The dosing regimen of 5 days per week was chosen to reflect the strategy used in GBM patients. Treatment was initiated at day 7 post implantation to allow time for tumour growth. This time point as chosen because previous studies have demonstrated that waiting longer than 20 days results in greater tumour response when quantified using volumetric assessment but reduces survival, therefore limiting the ability to assess delayed tumour recurrence (Hirst et al., 2013). Additionally, no mouse received a total dose exceeding 1 g because a decline in the

efficacy of TMZ has been reported at higher doses (Hirst et al., 2013).

TQD is a third-generation P-gp inhibitor (Fox and Bates, 2007) whose inhibitory effect on BCRP function has also been documented (Bankstahl et al., 2013). The dose of 40 mg/kg was chosen to ensure complete P-gp inhibition and significant BCRP inhibition. In an earlier PET imaging study, we demonstrated that TQD causes an immediate increase in TMZ uptake into the brain when administered via IV injection. TQD was administered 15 minutes before TMZ to increase the time window for the initiation of the inhibitory effects and allow for potential delays associated with oral administration.

The U87 glioma model is well established and widely used. The reproducibility of tumour implantation and the rapid growth rates are particularly appealing. However, it is important to remember that animal glioma models derived from immortalised cell lines, such as the model used in this experiment, exhibit relatively homogenous histological and genetic profiles (Jones et al., 1981) (Clark et al., 2010). This is a major difference between the models and human GBMs, which are characterised by histological and genetic heterogeneity.

When compared with standard subcutaneous tumour models, intracranial glioma models are thought to be superior and more clinically relevant because they allow for tumour growth in the brain microenvironment. An important limiting factor in the use of such models is the availability of a non-invasive method with which to accurately quantify tumour burden. Quantification of tumour burden is particularly relevant when selecting appropriate time points for the administration of therapeutic interventions because ideally different treatment cohorts will have comparable tumour burden when initiating therapy. Magnetic resonance imaging is a well-established tool for measuring tumour growth rate and therapeutic response in intracranial glioma models (Schmidt et al., 2004) (Cornelissen et al., 2005). An important objective in our first experiment was to confirm the suitability of MRI in detecting U87 tumours and measuring their growth rate. Consistent with previous studies (Bock et al., 2003) (Schmidt et al., 2004) (Jost et al., 2007), MRI in this study was found to be a reliable tool for localising tumours and performing volumetric measurements, which in turn facilitated our longitudinal study of the therapeutic response in a U87 glioma model.

Consistent with studies reported in the literature, the U87 glioma model demonstrated

a good response to TMZ treatment, evident as a reduction in tumour growth. Although a response to TMZ was expected, the marked potency observed in this study is problematic because it can mask differential responses when comparing combination treatment to treatment with TMZ alone. The observed rapid respond to TMZ is not uncommon; it has been demonstrated in previous studies using the U87 glioma model and TMZ (Corroyer-Dulmont et al., 2013). It might be worth considering reducing the overall dose of TMZ in future studies.

TQD treatment alone did not affect tumour growth. This was expected because TQD, a third-generation P-gp inhibitor that also inhibits BCRP, is not known to have anti-tumour activity.

Combination therapy with TMZ and TQD did not reduce the efficacy of TMZ in the U87 glioma model. In fact, despite the impressive reduction in tumour volume following treatment with TMZ alone, combination therapy resulted in quicker and more significant tumour shrinkage. This was observed at multiple time points in the first study and confirmed in a second study. To the best of our knowledge, this is the first treatment efficacy study to assess the response to TMZ and TQD treatment in a human glioma model in mice.

To understand the mechanisms responsible for the superior tumour response to combination therapy, TMZ plasma levels were analysed in the two treatment groups. Administration of TQD resulted in an increase in plasma levels of TMZ, however this was not significant. TMZ has very high bioavailability when administered orally (Diez et al., 2010). This, in combination with its weak substrate status for P-gp and BCRP, minimises any increase in intestinal absorption by P-gp and BCRP inhibition. This is also reflected in the small 12% increase in plasma levels with P-gp and BCRP inhibition. Furthermore, compounds that are substrates for efflux transporters can demonstrate a dose-dependent transport pattern in which they act as substrates at low (nanomolar) concentrations and as inhibitors at higher concentrations (Bankstahl et al., 2013). It is plausible that TMZ, despite being a weak P-gp and BCRP substrate, caused some efflux transporter inhibition in the gut, given that it was administered at a high concentration, thus further limiting any efflux transporter inhibition contributed by TQD. Notably, a previous *in-vitro* study showed that TMZ decreased the efflux

activity of P-gp (Munoz et al., 2015b). Taken together, it appears that P-gp and/or BCRP inhibition in the gut cannot explain the increase in plasma concentrations of TMZ in the combination treatment group. Additional factors, such as a change in TMZ distribution or elimination, might have contributed.

A potential limitation of this study is that TMZ concentrations in the brain were not directly measured. This is important because it precludes measurement of the brain-to-plasma concentration of TMZ, an indicator of the ability of orally administered TQD to inhibit P-gp and BCRP at the BBB level. PET imaging with radiolabelled TMZ was used as an alternative method to provide insight into the brain uptake of TMZ in the two treatment groups.

When mice received TQD in combination with TMZ therapy, the measured whole-brain radioactivity was higher than in the group treated with TMZ alone. However, this was not statistically significant. The lack of statistical significance may be attributed to the limited number of animals that underwent PET imaging (n = 4 in each group), which prevents the detection of small changes in the brain uptake of TMZ. Nonetheless, the data suggest that oral TQD treatment increased the uptake of radiolabelled TMZ, or its radiolabelled metabolites, at the BBB level and this was particularly higher in the tumour-bearing hemispheres of animals that received combination therapy. Future study should consider increasing the number of animals that undergo PET imaging to enhance the possibility of detecting any statistical significance.

PET scans measure the total radioactivity of a tissue but cannot differentiate the activity contributed by the parent compound from that contributed by its radiolabelled metabolites. However, in this study, TMZ and the active metabolite MTIC were radiolabelled, and the contribution of the other metabolites was minimal, as demonstrated in a previous imaging study. Therefore, despite the limitations of PET, the measured whole-brain radioactivity reflects the active components of the drug.

In this study, U87 tumours demonstrated significant BBB leakage, reflected by the avid enhancement following contrast administration. Furthermore, the hemispheres containing tumours demonstrated higher whole-brain radioactivity than the contralateral, tumour-free hemispheres. These findings are consistent with literature

reporting that high-grade brain tumours disrupt the BBB, enabling anticancer drugs to reach higher concentrations within the tumour core and enhancing components than in the rest of the brain where the BBB is intact (Pitz et al., 2011). This finding was confirmed for TMZ in a previous study (Rosso et al., 2009).

Interestingly, even in hemispheres containing tumours, we found that mice treated with combination therapy demonstrated higher whole-brain radioactivity than mice treated with TMZ alone. However, this again was not statistically significant.
This may reflect the inhibitory effects of TQD on P-gp and BCRP not only on the transporters of the endothelial cells but the U87 glioma cells within the tumours. Similar results have been reported for a different anti-cancer drugs (Agarwal et al., 2013), including erlotinib, a strong P-gp and BCRP substrate (Kodaira et al., 2010). The lack of P-gp expression in U87 glioma cells is unlikely to have significantly altered the results, particularly given that the U87 glioma model is highly leaky, as demonstrated in this study and in others (Liu et al., 2014). Therefore, the results of this study can be attributed to the inhibition of ABC transporters (P-gp and BCRP) at the intact BBB in brain tissues remote from the tumour.

Combination therapy not only hastened tumour shrinkage but also maintained shrinkage for a longer time. A recurrence in tumour growth was observed in the group treated with TMZ alone (five weeks after completion of treatment), but not the combination therapy group. This might reflect the effects of enhanced TMZ delivery when TQD was administered simultaneously, which resulted in more U87 glioma cell death. Additionally, previous *in-vitro* studies have demonstrated that TMZ treatment can increase the expression and activity of P-gp efflux transporters in U87 glioma cells (Munoz et al., 2014), which in turn can increase the cells' resistance to TMZ treatment (Munoz et al., 2015a). Concurrent administration of TQD with TMZ might have prevented U87 glioma cells from developing a "chemoresistant" phenotype by preventing P-gp upregulation, therefore leading to less aggressive tumours.

Although the PET imaging suggests that TQD may have increased TMZ delivery into the brain (in tumour-bearing and tumour-free hemispheres), TQD treatment also increased the plasma concentration of TMZ by approximately 12%. Again this was not statistically significance. Such an increase can be considered minor and may have

resulted from the inhibition of P-gp and/or BCRP in the gastrointestinal tract.
Such a small increase in plasma levels of TMZ is unlikely to account for the differential response between treatment groups. However, as dose-response relationship was not evaluated in this study, it is not possible to completely and categorically discard the effect of such a small increase in drug concentration in plasma, which may have resulted in this superior treatment response. .

In conclusion, this study demonstrates the effect of combination therapy with TMZ and TQD, a P-gp and BCRP inhibitor, in a human GBM model in mice. TMZ and TQD treatment resulted in more rapid and sustained U87 glioma shrinkage than did treatment with TMZ alone. The study also suggests that oral TQD treatment produced a superior response by inhibiting P-gp and BCRP efflux transporters at the BBB level. Finally, concurrent administration of TMZ and TQD may be a viable treatment strategy for enhancing the delivery of TMZ into the brain and brain tumours where P-gp and BCRP expression status is known.

Chapter 7: Imaging P-glycoprotein function in high-grade glioma patients

7.1. Abstract

Purpose: Previous studies confirmed the role of P-gp efflux transporter in the transport of TMZ and highlighted a potential role for P-gp in limiting effective TMZ delivery into the brain. This study investigates the suitability of PET and (R)-[^{11}C]verapamil in the assessment of P-gp function in patients with high-grade gliomas.

Methods: Baseline PET scans with the P-gp substrate (R)-[^{11}C]verapamil were used to assess the functional activity of P-gp in high-grade glioma patients (n = 5) and in healthy controls (n = 9). PET scans with [^{15}O]H_2O were also performed to measure perfusion and enable the generation of brain extraction fractions (E) for (R)-[^{11}C]verapamil. Participants then underwent repeat scans after the i.v administration of the P-gp inhibitor TQD (2mg/kg).

Results: The functional activity of P-gp was successfully demonstrated in patients with high-grade glioma and in healthy controls. Heterogeneous functional activity in P-gp was demonstrated amongst patients and in the different regions of individual tumours. Perfusion measurements were vital to the interpretation of the results in at least one high-grade glioma patient.

Conclusions: This study confirms the feasibility of our non-invasive imaging techniques for direct *in-vivo* visualisation of P-gp function and highlights its heterogeneity in patients with high-grade glioma tumours. It also suggests that perfusion measurements could play an important role in the interpretation of P-gp function.

7.2. Introduction

High-grade glioma tumours are characterised by poor outcome. Three main factors contribute to the dismal prognosis: 1) The highly invasive nature of high-grade glioma tumours; 2) the development of chemoresistance and 3) the difficulty in delivering effective chemotherapy across the BBB (Bai et al., 2011). The efflux transporter P-gp, which is expressed at the luminal side of the BBB, has been implicated in preventing various chemotherapy agents to achieve therapeutic concentrations in the brain (Agarwal et al., 2011a). This explains why many agents, such as doxorubicin, have failed in clinical practice despite demonstrating excellent efficacy against GBM cells *in-vitro* (Hau et al., 2004).

P-gp appears to play an important role in altering TMZ delivery across the BBB and the development of chemoresistance (Schaich et al., 2009) (Munoz et al., 2015b). The relationship between TMZ and P-gp has been clarified in the previous chapters of this thesis. Furthermore, it appears that efflux transporter inhibition in combination with chemotherapy could prove an attractive strategy for enhancing TMZ delivery across the BBB. However, there are conflicting reports on the expression of P-gp in glioma tumours, with variable expression even in tumours of identical grade and histological subtype (Demeule et al., 2001) (Schaich et al., 2009).

PET with the radiolabelled P-gp substrate (R)-[^{11}C]verapamil is a validated non-invasive imaging method for measuring P-gp function in the human (Sasongko et al., 2005). Recently, this method has also been employed in demonstrating increased P-gp functional activity in the temporal lobe in patients with treatment resistant epilepsy (Feldmann et al., 2013). A non-invasive imaging method that allows for measuring P-gp functional activity in patients with brain tumours is an essential step for future translation of studies aiming to enhance drug delivery by modulating P-gp function. The main objective of this study is to establish a non-invasive molecular imaging-based tool to study multi-drug resistance in patients with high-grade gliomas.

7.3. Methods

7.3.1. Patient recruitment

This is a non-randomised unblinded prospective study. Patients with evidence of a supratentorial intracranial mass with radiological features suggestive of a high-grade glioma or a low-grade glioma showing radiological features of higher-grade transformation (WHO grade III and IV) on MRI were recruited from March 2011 to July 2015 when TQD expired. All patients were identified following referral to the neuro-oncology multidisciplinary team meeting at Salford Royal NHS Foundation Trust (Hope Hospital) in Manchester. The Research Ethics Committee, the University of Manchester Research Committee and the UK Administration of Radioactive Substances Advisory Committee approved the study (13/NW0322).

The specific inclusion and exclusion criteria were:

Inclusion criteria

- Age > 18 years and < 70 years, both males and females

Children were excluded due to the dose of injected radiotracer and the need for arterial cannulation. Similarly, patients over 70 years of age are more prone to co-morbid conditions that make it difficult for them to tolerate the study.

- A likely diagnosis of high-grade glioma from MR imaging
- Only patients in whom a surgical intervention (tumour biopsy and/or surgical resection) was planned were approached. This ensured that histological diagnosis was available for all of our cases.
- Currently managed with corticosteroids
- Ability to give full informed consent
- Carer able and willing to participate
- Normal full blood count and liver function test
- Medically able to travel to the Wolfson Molecular Imaging Centre for PET scans
- Able to tolerate lying supine for MRI and PET scans

Patients who required hospitalisation and inpatient care or were systematically unwell

were excluded from the study as participation was deemed an increased burden on them.

Exclusion criteria

- Standard MRI contraindications (e.g. pacemaker, metallic implant or claustrophobia). This also included failure to tolerate MRI examinations in the recent past.

- Pregnancy

Due to the radiation involved in PET scans, female participants were required to demonstrate that they were not pregnant.

- Inability to give full informed consent
- Participation in another trial involving medical products in the preceding three months

Patients whom were planning to participate in another study were excluded to avoid any potential drug–drug interactions with Tariquidar.

- Receiving chemotherapy or radiotherapy
- Abnormal full blood count or liver function test

Tariquidar at high doses can disturb the liver function. As such, patients who had abnormal liver function test results were excluded.

Study subjects were approached by their consultant neurosurgeon during a routine clinical appointment and provided with the relevant information sheets. With subjects' approval, they were subsequently approached by the clinical research fellow who explained the study in more detail and provided the consent from. All subjects were given a minimum of 24 hours to make a decision about participating in the study.

In total, ten patients consented to take part. The study, however, was completed in five patients only. The remaining five patients could not take part in the study for different reasons: failure of the equipment producing and delivering radiolabelled water, failure of arterial cannulation, concerns regarding the sterility of the radiotracer, insufficient staffing levels to conduct the PET study safely and, finally, insufficient time to conduct PET scans prior to surgical intervention.

Overall, five patients (age range 29−64) were included in the study and underwent four PET scans and one MRI examination each prior to surgery. All participants gave

informed consent for MRI and PET imaging, image-guided tumour biopsies and histological analysis of tumour specimens.

Data acquired from previous studies that recruited healthy controls (age range 35−55 years) were also included in this study. These subjects had no known neurological or psychiatric disorders and were not taking medication known to be a P-gp substrate. A total of 10 healthy controls were recruited and underwent both radiolabelled verapamil and [^{15}O]H_2O scans at baseline and after administration of 2 mg/kg of tariquidar.

7.3.2. MRI acquisition

All patients underwent a volumetric MRI scan within a month prior to the PET scanning session (median: 13.5 days, range: 2−27 days). MRI data were acquired 1.5 Tesla whole-body scanners (Philips Achieva, Philips Medical system, Best, NL). The MR imaging protocol consisted of the following sequences:

1) Routine structural imaging:

- High resolution 3D T1-weighted gradient echo sequence
- T1 inversion recovery sequence
- 2D T2-weighted turbo spin echo sequence
- T2 fluid attenuation inversion recovery (FLAIR) sequence
- 3D volumetric post contrast enhanced T1 sequence

2) Advanced MR imaging techniques (data not used in this thesis)

- Diffusion tensor imaging (DTI)
- T1 dynamic contrast enhanced MRI

The standard clinical dose (0.1 mmol per kilogram of body weight) of the contrast agent Gadolinium (Gd, Dotarem, Guerbet Laboratories, Aulunay-sous-Bois, France) was administered intravenously via an automated pressure injector at a fixed injection rate (3 ml/second). This was followed by a bolus of 20 ml saline flush at the same rate to facilitate a standardised entry of the contrast bolus into systemic circulation (Jackson et al., 2002).

The healthy controls were scanned on a 3.0 Tesla GE Excite II scanner (General Electric, Milwaukee, WI,USA)

7.3.3. PET data acquisition

7.3.3.1. (R)-[^{11}C]verapamil and [^{15}O]H_2O Production

Both radiotracers were produced on-site at the WMIC and (R)-[^{11}C]verapamil was synthesised based on a modification of the procedure reported by Luurtsema et al. (Luurtsema et al., 2002). Quality control was performed after radiosynthesis to ensure that the product was within specifications prior to injection. The product characteristics were as follows: (R)-[^{11}C]verapamil: radiochemical purity 98.4%, stable verapamil 4.97 μg/ml and specific activity was 58.4 GB/μmol; and for [^{15}O]H_2O: radiochemical purity 100%.

7.3.3.2. PET scanning procedure

All PET images were acquired in list mode using the High Resolution Research Tomograph (HRRT, CTI/Siemens, Knoxville, TN, USA), the dedicated brain PET scanner at the WMIC in Manchester. The HRRT scanner has an intrinsic spatial resolution of approximately 2.5 mm with a field of view (FOV) of 252 mm axially and 312 mm transaxially. Such high spatial resolution is delivered whilst maintaining sensitivity, which enables the HRRT to image brain structures with details that are beyond the capabilities of other commercially available scanners (Heiss et al., 2004). This is particularly important in our study as subtle functional differences within the tumour itself and between the tumour and the adjacent brain tissue can be more readily appreciated. The high spatial resolution limits the spillover of radioactivity in the (R)-[^{11}C]verapamil images from the chroroid plexus into neighbouring area in the temporal lobe, thalamus and tumour, depending on location.

Head motion was limited by resting on the HRRT head holder and by using additional Velcro straps on the forehead and chin. Furthermore, patients were fitted with an external position tracker (Polaris Vicra, Northen Digital Inc., Waterlook, Canada)

which monitors head motion during the scans.
In order to correct for tissue attenuation of photons, a transmission scan was carried out using a 1.1 GBq ^{137}Cs single-photon emission source (662 keV) where the energy window for the transmission scan was 550−800 keV. Delayed and prompt confidence events were recorded by setting the energy window at 400−650 keV.

To enable continuous arterial blood sampling throughout the scans, a 22-gauge arterial cannula was inserted into the radial artery of the non-dominant hand under local anaesthesia (2% Lidocaine). Following the administration of both radiotracers, arterial blood was sampled continuously for the first 6 minutes for [^{15}O]H_2O and 15 minutes for (R)-[^{11}C]verapamil at a rate of 5 ml/minute using a custom-built bismuth germanium oxide detector (Ranicar et al., 1991). Additional discrete arterial blood samples were collected manually at 4, 5 and 6 minutes for [^{15}O]H_2O and at 5, 10, 15, 20, 30, 40, 50 and 60 minutes for (R)-[^{11}C]verapamil. The first three discrete samples were used to calibrate the radioactivity concentration from the continuously sampled blood.

(R)-[^{11}C]verapamil undergoes peripheral metabolism following its introduction into systemic circulation. Some of its radiolabelled metabolites in plasma cross the BBB and confound the accurate interpretation of the measured radioactivity in the brain using PET. The plasma radioactivity concentrations were also measured and plasma samples (except for the 15- and 50-minute samples) were further analysed to determine the fractions of the parent compound and radiolabelled metabolites using an in-house method based on in-line solid-phase extraction (SPE) and HPLC. In contrast to the method used by Luurtsema et al. (Luurtsema et al., 2005), the in-house method avoids sample acidification and exposure to atmosphere or vacuum where there is potential for loss of polar metabolites (assumed to be [^{11}C]-formaldehyde, [^{11}C]-formate and [^{11}C]-bicarbonate, all volatile at acidic pH) in order to capture these volatile polar metabolites. The lipophilic metabolites are retained on the SPE cartridge and were eluted and analysed by HPLC (Shimadzu Prominence HPLC, instrument control and data acquisition Shimadzu Lab Solutions version 1.11 SP1). The polar metabolites are not retained on the SPE cartridge because of their polarity and were accounted for by measuring the radioactivity in the SPE breakthrough.

For all subjects except three healthy controls, all PET imaging was carried out on the same day. Each scanning session started with a 5-minute [^{15}O]H_2O scan for measuring the regional cerebral blood flow (rCBF). [^{15}O]H_2O was administered as a 15-second intravenous bolus injection. This was followed 10 minutes (five half lives) later by a 60-minute (R)-[^{11}C]verapamil scan, where (R)-[^{11}C]verapamil was administered as a 20-second intravenous bolus injection via the same vascular access point. This was followed by the acquisition of a 6-minute transmission scan.

At the start the second scanning session, patients received an i.v. infusion of the third-generation P-gp inhibitor Tariquidar (TQD) at a dose of 2 mg/kg, which was administered over 30 minutes.. This particular dose was chosen based on previously published literature that showed half-maximum P-gp inhibition can be achieved in healthy control subjects (Wagner et al., 2009) and can highlight areas of different P-gp activity in the brain (Feldmann et al., 2013). Tariquidar infusion was formulated from a stock solution (70 mL) of 7.5 mg/mL of Tariquidar free base in 20% ethanol / 80% propylene glycol (AzaTrius Pharmaceuticals Pvt Ltd, London, UK) and was diluted with aqueous dextrose solution (5%, w/v) to make up the final desired concentration of 2 mg/kg. The full scanning procedure ([^{15}O]H_2O and (R)-[^{11}C]verapamil) was then repeated 60 minutes after the completion of the i.v. infusion of TQD.

7.3.4. PET data processing

7.3.4.1. Image reconstruction

The (R)-[^{11}C]verapamil PET images were reconstructed using the iterative reconstruction algorithm ordinary Poisson ordered-subsets expectation maximisation (OP-OSEM) with resolution modelling (RM-OP-OSEM) (Sureau et al., 2008) with 16 subsets and 5 iterations. A similar approach was followed for the reconstruction of [^{15}O]H_2O PET images using RM-OP-OSEM with 16 subsets and 12 iterations (Walker et al., 2012).

The dynamic images were corrected for head motion using a frame-by-frame approach as previously described (Anton-Rodriguez et al., 2010). In short, the image of linear attenuation coefficients (μ-map) was realigned using the co-registration software in Vinci 2.50 (Max Planck Institute for Neurological Research, Cologne, Germany) to the

non-attenuation corrected (R)-[^{11}C]verapamil image from the first six minutes of acquisition (reference image) prior to final reconstruction. Each subsequent frame of the dynamic emission reconstructed without attenuation correction was also realigned to the reference image. Finally, the realigned frames were reconstructed again with attenuation correction. Correction for head movement was also performed on a frame-by-frame basis, but due to the shorter duration of the dynamic scan, only the first two minutes of acquisition of the [^{15}O]H_2O scan were used as the reference image. Other corrections that are required for quantification were also incorporated in the reconstruction algorithm, including corrections of random and scatter coincidences, attenuation correction, detector normalisation and dead time. The voxel size of reconstructed PET images is 1.22 mm × 1.22 mm × 1.22 mm. A post-reconstruction 3D Gaussian filter was applied to the resulting images with 2 mm (for verapamil) and 4 mm (for [^{15}O]H_2O) full width at half maximum (FWHM) to reduce image noise at the voxel level. Decay correction was incorporated in the pharmacokinetic model.

7.3.4.2. Pharmacokinetic modelling and generation of parametric images

Data were analysed using a single tissue compartment model. The first compartment is the arterial blood. From arterial blood, the radiotracer passes into the second compartment, known as the free compartment (brain tissue in this case). Data obtained by PET camera are a summation of these compartments. The parameters can be estimated by fitting the model to measured PET data with arterial radioactivity concentrate as input function. Pharmacokinetic modeling of (R)-[^{11}C]verapamil PET images used a one-tissue two-rate constant compartment model with the arterial plasma input function corrected for polar radiolabelled metabolites (Lubberink et al., 2007) to derive the transfer rate constant K_1 (ml/min/cm^3) of (R)-[^{11}C]verapamil from plasma to the brain for each voxel; this served as an outcome parameter for P-gp function where low K_1 indicates high P-gp function (Langer et al., 2007). The impact of radiolabelled metabolites of (R)-[^{11}C]verapamil on K_1 estimates was minimised by utilising only the first 10 minutes of the PET data for pharmacokinetic modelling (Kreisl et al., 2010). This enabled the generation of Parametric (R)-[^{11}C]verapamil maps (Feng et al., 1993).

The dynamic [^{15}O]H_2O images were fitted to a one-tissue two-rate constant

compartmental model that included delay (fixed to the whole brain) and dispersion of the blood input function to derive cerebral blood flow (CBF) at the voxel level.

7.3.4.3. Image co-registration

Co-registration of the different MRI sequences and the PET studies is an essential step to enable the use of the variously generated ROIs. Rigid-body co-registration is possible because the brain is structurally unchanged between the different sequences and the two imaging modalities.

The FLAIR, T2-weighted and post-contrast T1-weighted images were co-registered to the post-contrast T1-weighted image using the FLIRT (FMRIB's Linear Image Registration Tool) in FSL (FMRIB's Software Library) 4.1.4 with normalised mutual information and sinc interpolation. Transformation matrixes were then saved.

A similar approach was used for the co-registration between the MRI and PET images where the MRI images were co-registered to the reference summation image of the whole dynamic [^{15}O]H_2O scan after smoothing the image by applying a 4 mm Gaussian filter. Transformation matrixes were saved. Following each co-registration, the quality of co-registration was visually inspected to ensure its reliability and accuracy. Additional co-registration of the (R)-[^{11}C]verapamil images to the MRI image was not required since subjects did not move between radiotracer injections. Example of the co-registration of the MRI images to the summation PET image is presented in Figure 7.1.

For quantitative analysis, MRI images were registered to PET images in order to preserve the original PET data. For image-guided biopsy, PET images were registered to MRI images to facilitate such clinical application, as the latter was the modality used in the operation theatre.

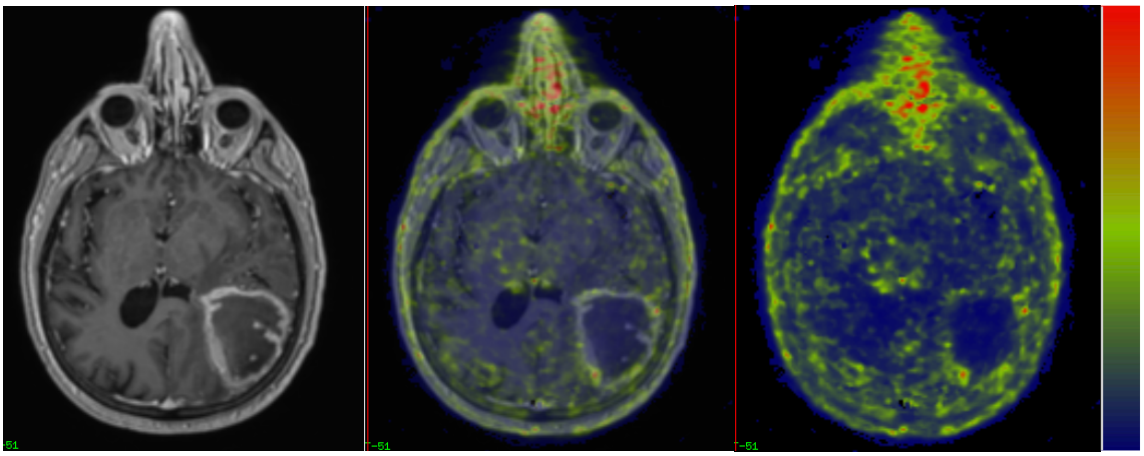

Figure 7. 1: Example of co-registration of PET to MRI (Patient 5). Left panel: post-contrast MRI in native space. Middle panel: co-registered (R)-[^{11}C]verapamil PET superimposed on MRI. Right panel: summed PET image co-registered to MRI; the colour bar indicates radioactivity concentration (kBq/ml).

7.3.4.4. Regions of interest definition and brain segmentation

Regions of interest (ROIs) were manually delineated using the imaging software OsiriX 7.0 (http://www.osirix-viewer.com). ROIs were drawn based on the signal intensity of different sequences, and some overlap between the different ROIs is to be expected. This is particularly important as high-grade gliomas are infiltrating tumours with indistinct borders where tumour cell infiltration extends beyond the radiological abnormalities.

The following ROIs were used:

In all patients:

ROI 1 (perilesional abnormal signal): FLAIR and T2 images were utilised to depict the peri-tumoural abnormal signal (this may possibly include neoplastic infiltration) by tracing around the high signal intensity seen on these sequences.

For patients with a transforming low-grade glioma the following ROI were delineated:

ROI 2 (neoplastic and non-enhancing / presumed low grade): non-necrotic T1 hypointense tumoural tissue and avoiding peritumoural abnormal high T2 signal

ROI 3 (neoplastic and enhancing / presumed high grade): defined on the post-contrast T1 sequences by manually tracing any enhancing component of the tumour.

The following ROIs were delineated in patients with GBM tumours:
ROI 4 (enhancing rim) and ROI 5 (necrotic core): these regions were included in cases where a tumour demonstrated peripheral enhancement with central necrosis. The enhancing rim was delineated by manually tracing along the outer and inner borders of the enhancing wall. Necrosis was then delineated by manually tracing along the inner border of the enhancing rim approximately 1 mm (approximately 1 voxel) central to any enhancing tumoural tissues. This strategy has the added benefit of excluding any enhancing tissue inadvertently included in the delineation as part of the necrotic core.
Finally ROI 6 (haemorrhage) was delineated in one patient (patient 6) in whom intra-tumoural haemorrhage was seen.

For brain tissue segmentation, the brain was initially extracted from the MRI image using the FSL BET toolbox (Smith, 2002). This was followed by subtracting all radiological abnormal brain tissue as identified on MRI images (manually delineated ROIs 1–6). Automatic segmentation was then applied to the remaining brain into cerebrospinal fluid (CSF), grey and white matter using FAST – FMRIB's automated segmentation tool in FSL without the use of spatial priors (Zhang et al., 2001). Grey and white matter regions comprised voxels with probability higher than 75% in their respective maps. Only voxels within the mask of the extracted brain were included in the future analysis. Example of ROI delineation and grey and white matter segmentation is presented in Figure 7.2.

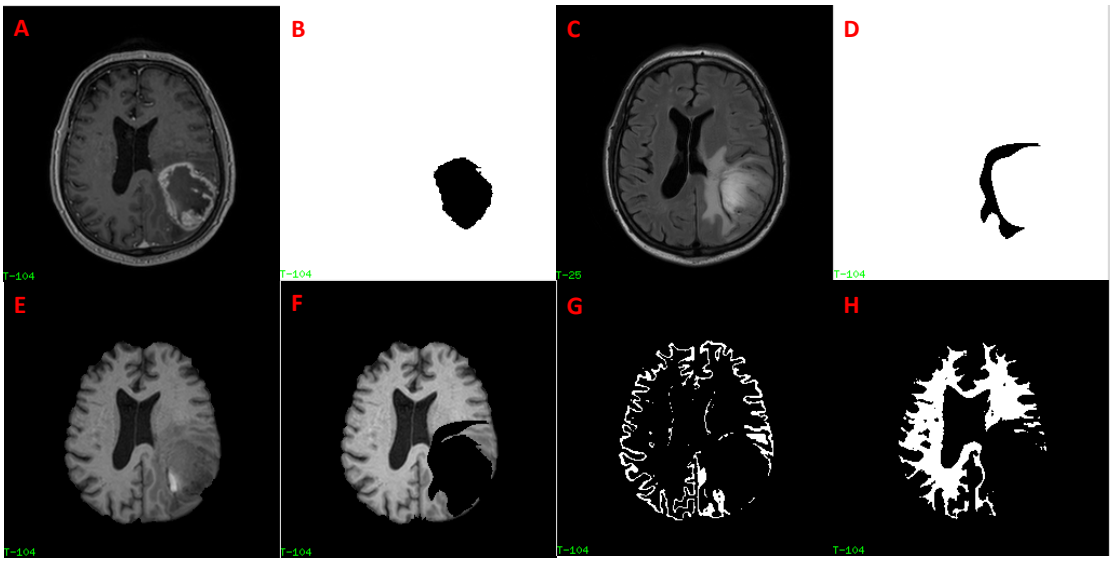

Figure 7. 2: Delineation of regions of interest (ROI) in Patient 5.
Tumour mask was delineated using T1-weighted post-contrast axial MRI (co-registered to PET) for delineation of tumour ROI (A and B). FLAIR images were used for delineating the perileasional abnormal signal changes (C and D). Extracted whole brain (E) before and (F) after applying the tumour mask. This enabled the segmentation of normal (G) grey and (H) white matter in the rest of the brain tissue.

7.3.5. PET/MRI image-guided biopsy

PET images on their own are not suitable for neurological navigation due to their poor anatomical details. Parametric maps of (R)-[^{11}C]verapamil K_1 were co-registered with the MRI scan and the resulting images were presented to the neurosurgical team using Vinci 2.50 software (Max Planck Institute for Neurological Research, Cologne, Germany) to facilitate surgical biopsy and treatment planning. Co-registered PET and MRI images were reviewed and areas of increased P-gp activity on K_1 maps of (R)-[^{11}C]verapamil were identified as biopsy targets. These targets were marked on the volumetric brain MRI and loaded into the BrainLAb neurosurgical navigation system (Munich, Germany) at the time of the operation. Multiple targets were identified but biopsies were performed only in tissue where subsequent resection was intended. Consequently, one potentially interesting target that was located in an eloquent area of the brain was not collected (patient 2).

All image-guided biopsies were performed at Salford Royal NHS Foundation Trust within one week of the subjects undergoing PET scans. As all our subjects underwent tumour resection, an open biopsy technique was preferred to prevent any deviation from the normal surgical approach. Following craniotomy and dural opening, a standard brain biopsy needle was aimed at the targets using the standard clinical neuronavigation system. Biopsy was always performed prior to surgical resection of the tumour. This approach was followed to minimise the effects of brain shift, which can cause tissue-sampling errors.

Biopsy locations were recorded using the screenshot function, while biopsy tissue was placed in a specimen pot and numbered sequentially according to the order in which it was obtained. Specimens were taken and fixed in 10% neutral buffer formalin and transferred for subsequent histopathological examination.

7.3.6. Histopathological assessment

Surgical specimens were processed as per routine clinical settings with paraffin embedding. Sections with a thickness of 5 μm were cut and stained with haematoxylin-eosin (HE) in each block. All samples were filed and kept at the Central Nervous System Tumour Research Tissue Bank at Salford Royal Hospital. An experienced neuropathologist (Dr D. du Plessis, blinded to imaging findings) established the final histological diagnosis based on the current WHO classification (Louis et al., 2007). Routine histopathological assessment was performed and included immuno-staining for Ki67 to assess the cellular proliferation rate, IDH1R132H mutation status and allelic (loss of heterozygosity) of chromosome 1p/19q.

Quantification of P-gp expression in the different histological samples was not performed.

7.3.7. Statistical analysis

Statistical analysis was performed using Prism6 software (GraphPad Inc., La Jolla, CA, USA). Non-parametric Mann-Whitney (for unmatched) and Wilcoxon (for matched) tests were used to compare the groups in terms of age, weights and injected

doses. Further statistical testing for comparison of the brain uptake of the radiotracers was felt to be inappropriate given the limited number of patients. All values were expressed as a mean ± standard deviation unless stated otherwise. No outliers were removed from any set of data.

7.4. Results

Five controls and one patient had mild adverse events, which may be related to TQD. Phlebitis (two controls), hypotension (two controls), nausea (one control) and metallic taste (one control) were all reported. Mild dizziness was experienced by one of the glioma patient during the TQD infusion, but this was self-limiting. Glioma patients included three WHO grade III and two GBM tumours (Table 7.1). The five patients underwent two consecutive PET scans with both [^{15}O]H_2O and (R)-[^{11}C]verapamil at baseline and following a TQD i.v. infusion. However, data from the post-TQD scan in one glioma patient (Patient 1) could not be processed due to incomplete blood data. In total, complete datasets were obtained for four glioma patients. Clinical details of patients are provided in table 7.1.

Table 7. 1: Demographic, clinical and scan details of glioma patients

Number	ID	Gender	Age	Histology	WHO Grade	Tumour location
1	h00455	M	29	Diffuse low-grade astrocytoma with higher-grade transformation	III	Right temporal and parietal lobes
2	h00456	F	39	Anaplastic astrocytoma	III	Right parietal lobe
3	h00472	M	40	Anaplastic astrocytoma	III	Left temporal lobe
4	h00497	M	51	Glioblastoma multiforme with oligodendroglioma elements	IV	Right frontal and temporal lobes
5	h00765	M	63	Glioblastoma multiforme	IV	Left parietal lobe

Data from the post-TQD scan in one glioma patient (Patient 1) were excluded due to incomplete blood data.

Details of the different segmented ROIs within the tumours, including the volumes, are provided in Table 7.2 below.

Table 7. 2: Different segmented ROIs within the tumours.

Number	ID	ROI	Volume cm³
1	h00455	1. Non-enhancing tumour	128.6
		2. Enhancing superior	1.24
		3. Enhancing inferior	4.73
2	h00456	1. Non-enhancing tumour	148.1
		2. Enhancing superior	1.37
		3. Enhancing inferior	1.03
3	h00472	1. Non-enhancing tumour	71.1
		2. Enhancing tumour	1.4
4	h00497	1. Necrotic core	44.4
		2. Enhancing ring	35.3
5	h00765	1. Necrotic core	29.9
		2. Enhancing ring	74.3
		3. Haemorrhage	3.2

Note that the haemorrhage ROI in Patient 5 was excluded from analysis.

Data from the 10 healthy controls who were administered 2mg/kg of TQD were utilised in this study, which included a baseline and a post-inhibition (R)-[^{11}C]verapamil scan from seven controls and [^{15}O]H_2O from eight controls (as detailed in Table 7.3).

Table 7. 3: Demographic and scan details of healthy controls

Number	ID	Gender	Age	Baseline H_2O	Post-inhibition H_2O	Baseline VPM	Post-inhibition VPM
1	h00239	M	47	Yes	Yes	Yes	Yes
2	h00277	F	42	Yes	Yes	Yes	Yes
3	h00339	F	37	Yes	Yes	Yes	Yes
4	h00445	M	36	Yes	Yes	Yes	Yes
5	h00495	M	51	Yes	Yes	Yes	Yes
6	h00227	M	47	Yes	Yes	Yes	No
7	h00259	F	35	Yes	Yes	No	Yes
8	h00273	F	48	Yes	Yes	Yes	No
8	h00268	F	55	Yes	No	Yes	Yes
9	h00463	M	47	No	Yes	Yes	Yes

Subject h00227's second (R)-[^{11}C]verapamil (VPM) data could not be used due to artefact. Subjects h00259 and h00273 had incomplete blood data for the (R)-[^{11}C]verapamil scans 1 and 2, respectively. The first [^{15}O]H_2O scan of subject h00463 and the second [^{15}O]H_2O scan of subject h00268 were not acquired for technical reasons. Complete data set acquired for [^{15}O]H_2O are highlighted in blue box and for (R)-[^{11}C]verapamil in the red boxes.

No difference in age was seen between the glioma patient group and the healthy control group (glioma patients: 44.4 ± 12.9 years, healthy controls: 44.5 ± 6.7 years, p = 0.97), nor difference in weight (glioma patients: 92.6 ± 6.2 kg, healthy controls: 88.2 ± 20.7 kg, p = 0.19).

There was no difference in the injected dose of (R)-[^{11}C]verapamil at baseline (patients: 557 ± 20 MBq, healthy: 556 ± 28 MBq, p = 0.75) or at the post-inhibition scan (patients: 558 ± 6 MBq, healthy: 541 ± 52 MBq, p = 0.68). Similarly, there was no difference in the injected dose of [^{15}O]H_2O per kg of body weight at baseline (patients: 513 ± 68 MBq, healthy: 471 ± 105 MBq, p = 0.61) or at the post-inhibition scan (patients: 555 ± 43 MBq, healthy: 491 ± 111 MBq, p = 0.26).

There was no difference detected in the fraction of non-metabolised (R)-[^{11}C]verapamil between the glioma patients and the healthy controls. TQD did not alter the peripheral metabolism of (R)-[^{11}C]verapamil in healthy controls or in glioma patients.

7.4.1. Cerebral blood flow in glioma patients and healthy controls

At baseline and in comparison to the healthy controls, high-grade glioma patients demonstrated similar CBF values for both grey and white matter (glioma patients GM = 0.38 ± 0.13 mL/min/cm^3, WM = 0.30 ± 0.07 mL/min/cm^3, health controls GM = 0.4 ± 0.04 mL/min/cm^3, and WM = 0.32 ± 0.03 mL/min/cm^3). The lowest CBF values were encountered in the two patients with the highest WHO grade IV (GBM) tumours (CBF GM = 0.36 and 0.23 mL/min/cm^3 and WM = 0.27 and 0.19 mL/min/cm^3 in patients 4 and 5, respectively). This is to be expected given that intracranial tumours cause a rise in intracranial pressure, which in turn causes a reduction in the CBF, and this correlates directly with the tumour grade (Figure 7.3).

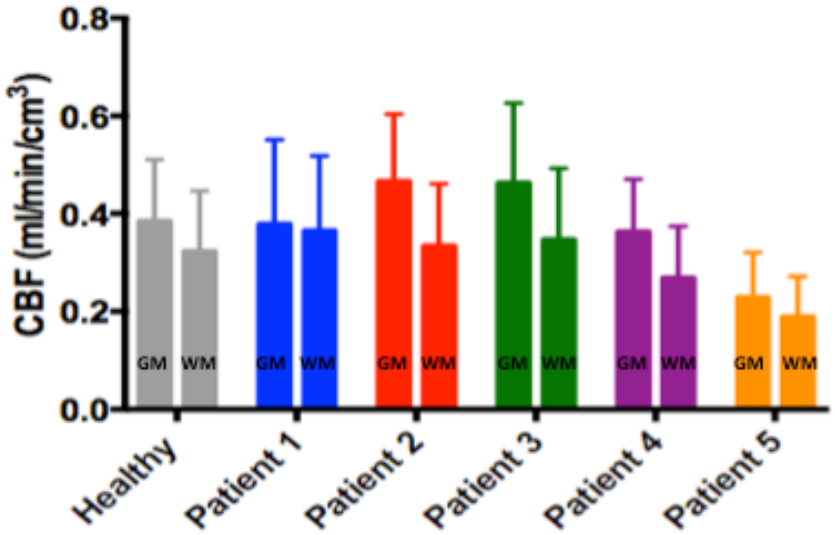

Figure 7. 3: Perfusion (CBF) at baseline in the grey matter (GM) and white matter (WM) for both healthy controls (n = 8) and glioma patients (n = 5). Data presented as mean ± standard deviation for all healthy controls and per individual patient.

Interestingly, glioma patients demonstrated a heterogeneous CBF within the tumours. For example, Patient 1 demonstrated lower CBF values (within the enhancing and non-enhancing component of the tumour) than the grey and white matter. Conversely, Patients 2 and 3 demonstrated higher blood flow in the tumours (enhancing and non-enhancing components of the tumours) when compared to the rest of the brain (Figure 7.4).

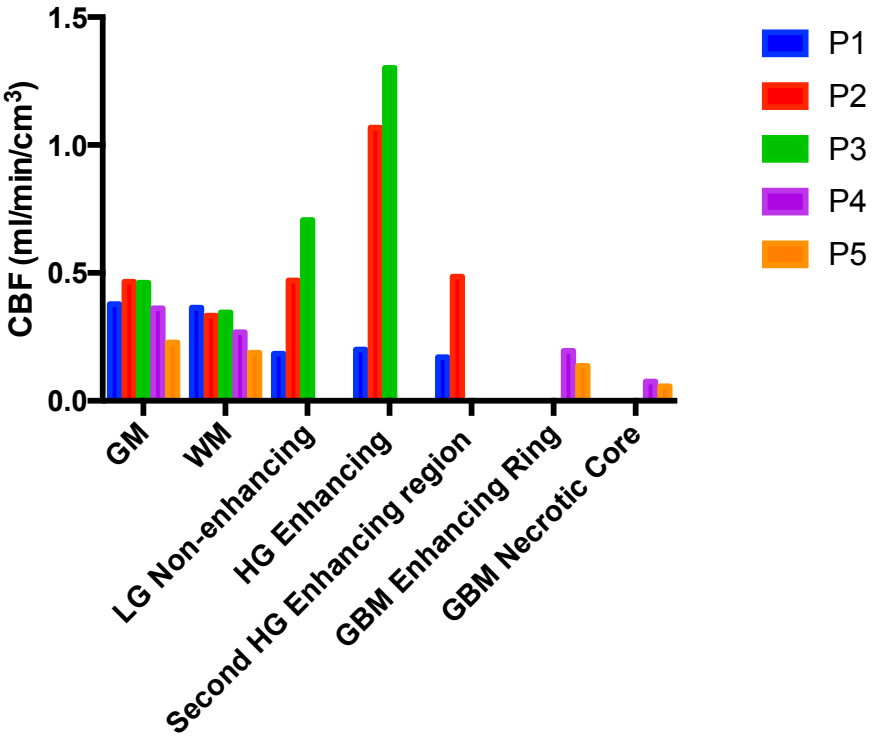

Figure 7. 4: Perfusion (CBF) at baseline in the different region of interests in the five glioma patients. Grey matter (GM), white matter (WM), low-grade (LG), high-grade (HG) and glioblastoma (GBM).

7.4.2. Effects of Tariquidar on cerebral blood flow

The administration of TQD resulted in variable changes in CBF as measured with [^{15}O]H_2O in both healthy controls and glioma patients but these were less than 20% changes in the majority of cases. Only two healthy controls showed an increase of more than 20% whilst patient 4 showed a decrease of approximately 20% (Figure 7.5A and B).

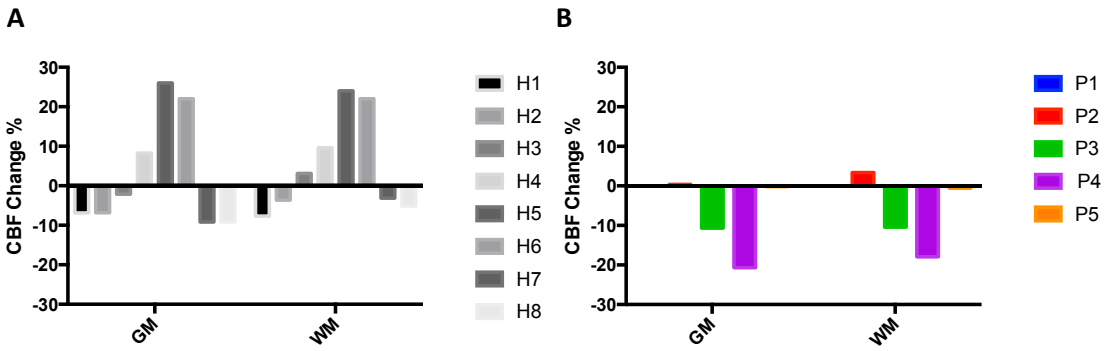

Figure 7. 5: Changes from baseline in perfusion (CBF) after administration of 2 mg/kg of TQD in the grey and white matter for: (A) healthy controls (n = 8) and (B) glioma patients (n = 4). Grey matter (GM) and white matter (WM).

Tumour tissue showed different responses to the grey and white matter (Figure 7.6). Patients with GBM showed a decrease in CBF, which was slightly less pronounced than the grey and white matter changes for patient 4 but higher than in patient 5. Conversely, patients with the transforming gliomas (patients 2 and 3) showed even more heterogeneous changes; Patient 2 demonstrated a >20% increase in CBF of both the enhancing and non-enhancing components of the tumour, which was higher than the grey and white matter changes.

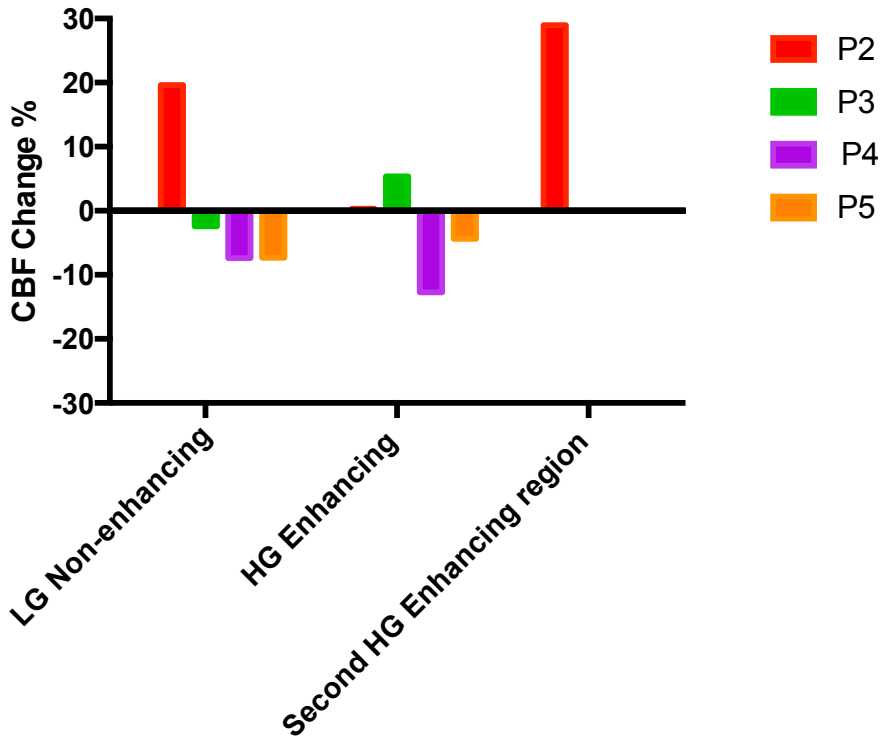

Figure 7. 6: Changes from baseline in perfusion (CBF) after administration of 2 mg/kg of TQD in the different regions of interest in the five glioma patients. Low-grade (LG), high-grade (HG) and glioblastoma (GBM).

In summary, TQD resulted in variable changes in the CBF of both healthy controls and patients with glioma. Furthermore, heterogeneous changes in CBF were noted in individual patients with certain components of the tumours showing different CBF responses to the grey and white matter of the same patient. Finally, all the various CBF changes measured in glioma patients were within the expected range of changes seen in healthy controls (Figure 7.7).

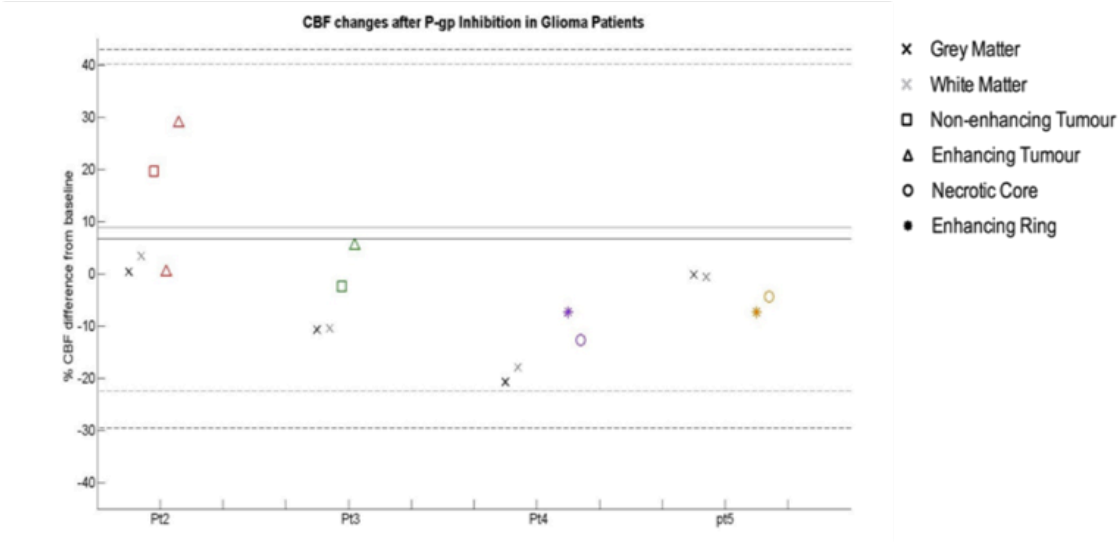

Figure 7. 7: Changes between baseline and Tariquidar scans in four patients (arterial input function not available for scan 2 following TQD administration in patient one) after administration of 2 mg/kg of TQD. Mean CBF changes (solid line) ± 95% confidence intervals (dashed lines) in healthy controls for grey matter (**black**) and white matter (**grey**).

7.3.3. Functional activity of P-glycoprotein

At baseline, glioma patients demonstrated similar grey and white matter (R)-[^{11}C]verapamil K_1, indicating comparative P-glycoprotein functional activity, in comparison to the healthy controls (glioma patients GM = 0.032 ± 0.03 mL/min/cm^3, WM = 0.022 ± 0.01 mL/min/cm^3 , healthy controls GM = 0.037 ± 0.02 mL/min/cm^3, and WM = 0.028 ± 0.02 mL/min/cm^3). The lowest (R)-[^{11}C]verapamil K_1 values were encountered in Patients 1 and 5 (WHO grade III and IV, respectively) with a (R)-[^{11}C]verapamil K_1 (GM = 0.021 and 0.026 mL/min/cm^3 and WM = 0.016 and 0.019 mL/min/cm^3 in patients 1 and 5, respectively). This indicates higher functional activity of P-gp in the grey and white matter of those two particular patients (Figure 7.8).

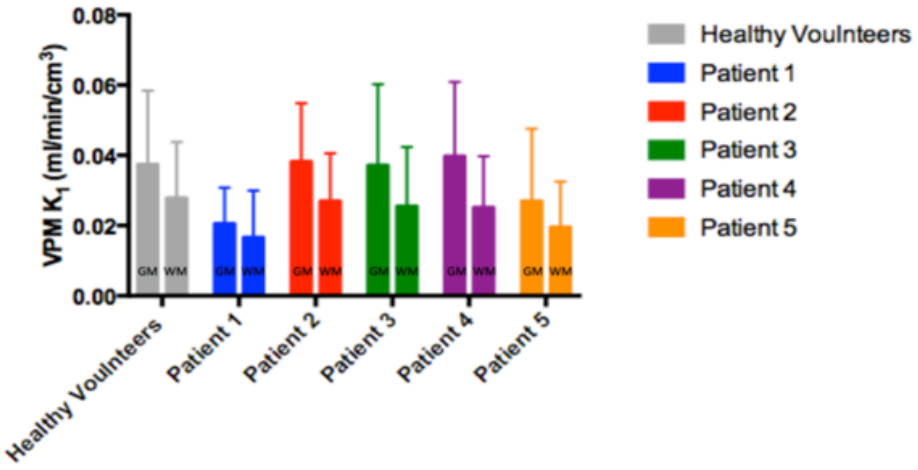

Figure 7. 8: (R)-[^{11}C]verapamil uptake (VPM K_1) at baseline in the grey and white matter (first and second columns, respectively) for both healthy controls (n = 7)and glioma patients (n = 5). Data presented as mean ± standard deviation.

Furthermore, glioma patients showed variable uptake of (R)-[^{11}C]verapamil within the different components of the tumours, reflecting the heterogenous P-gp functional activity within the tumour. In Patient 1, the enhancing and non-enhancing components of the tumour showed lower (R)-[^{11}C]verapamil K_1 in comparison to the grey and white matter (reflecting increased P-gp functional activity). Patients 2 and 3, on the other hand, showed higher (R)-[^{11}C]verapamil K_1 in the tumour, which was even higher in the enhancing part of the tumour (indicating lower P-gp functional activity). Finally, patients four and five showed similar (R)-[^{11}C]verapamil K_1 in the enhancing tumour rim to the grey and white matter (Figure 7.9).

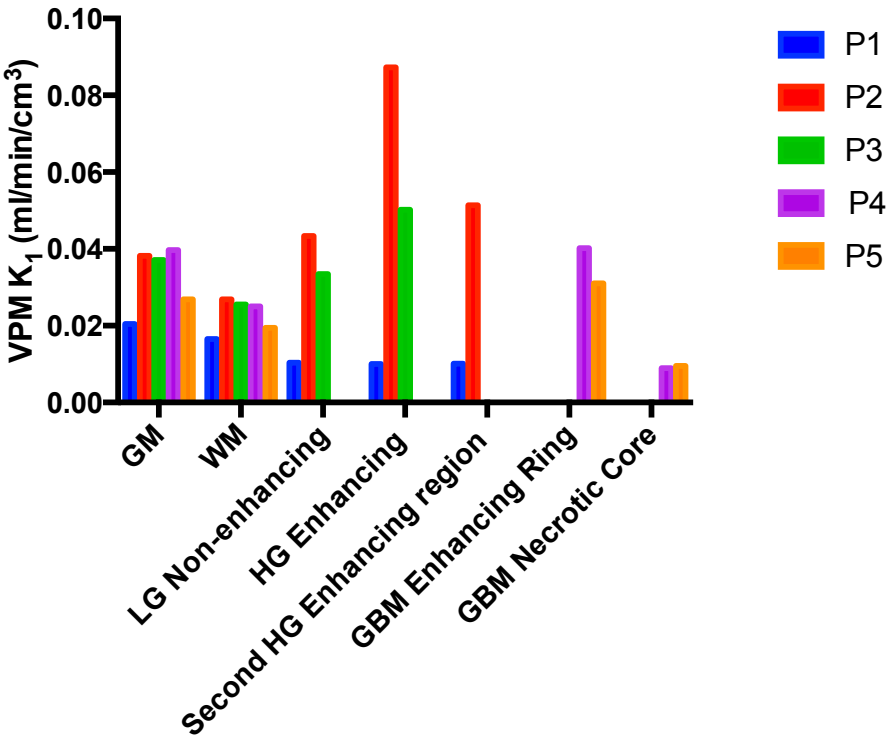

Figure 7. 9: (R)-[^{11}C]verapamil uptake at baseline in the different regions of interest in the five glioma patients. Grey matter (GM), white matter (WM), low-grade (LG), high-grade (HG) and glioblastoma (GBM).

7.4.3.1. Effects of P-gp inhibition

The administration of TQD (2 mg/kg) resulted in a significant increase in the (R)-[^{11}C]verapamil K_1 in the grey and white matter of the healthy controls (54 ± 11% and 57 ± 9.8%, respectively) relative to baseline scans (p = 0.0002) (figure 11). A similar but slightly lower increase in the (R)-[^{11}C]verapamil K_1 was demonstrated in the grey and white matter of the glioma patients (46 ± 21% and 47 ± 20%, respectively) relative to the baseline but this was not significant (p = 0.12) (Figure 7.10A).

The increase in the grey and white matter of (R)-[^{11}C]verapamil K_1 in response to TQD in the glioma patients, however, was more variable, ranging from 26% to 67% in the grey matter and from 27% to 68% in the white matter (healthy controls: from 39% to 72% and from 48% to 75% in the grey and white matter, respectively), Figure 7.10B.

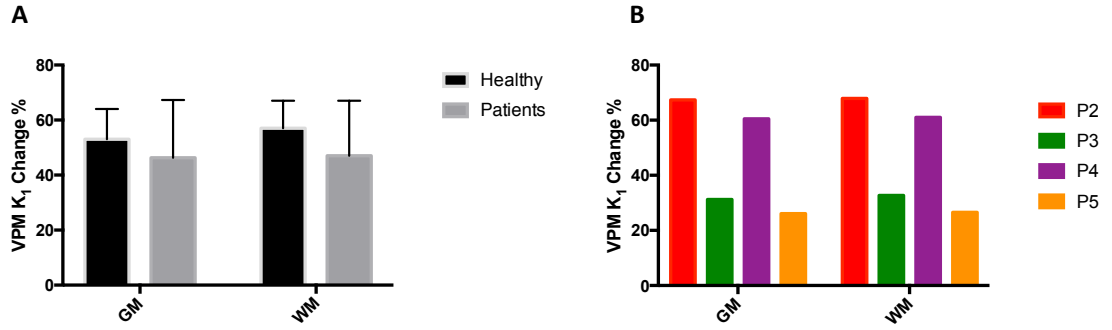

Figure 7. 10: Changes from baseline in (R)-[^{11}C]verapamil K_1 after administration of 2 mg/kg of TQD in the grey and white matter for (A) healthy controls (n = 7) and glioma patients (n = 4) and for (B) individual glioma patients. Grey matter (GM) and white matter (WM).

Finally, the different regions of interest within the tumours also showed variable changes in response to TQD (Figure 12). This is expected given the variability of the functional activity of P-gp in these regions at baseline.

Interestingly, the GBM patients (WHO grade IV) showed a modest increase in the (R)-[^{11}C]verapamil K_1 within the enhancing rim of the tumour, pointing towards increased P-gp functional activity in these tissues. Conversely, Patient two (WHO grade III) showed a higher increase of (R)-[^{11}C]verapamil K_1 in the enhancing component of the tumour (histologically proven grade III) in comparison to the non-enhancing component of the tumour and to the grey and white matter, whilst Patient three showed a very similar increase in (R)-[^{11}C]verapamil K_1 in both the enhancing and non-

enhancing components of the tumour (figure 12).

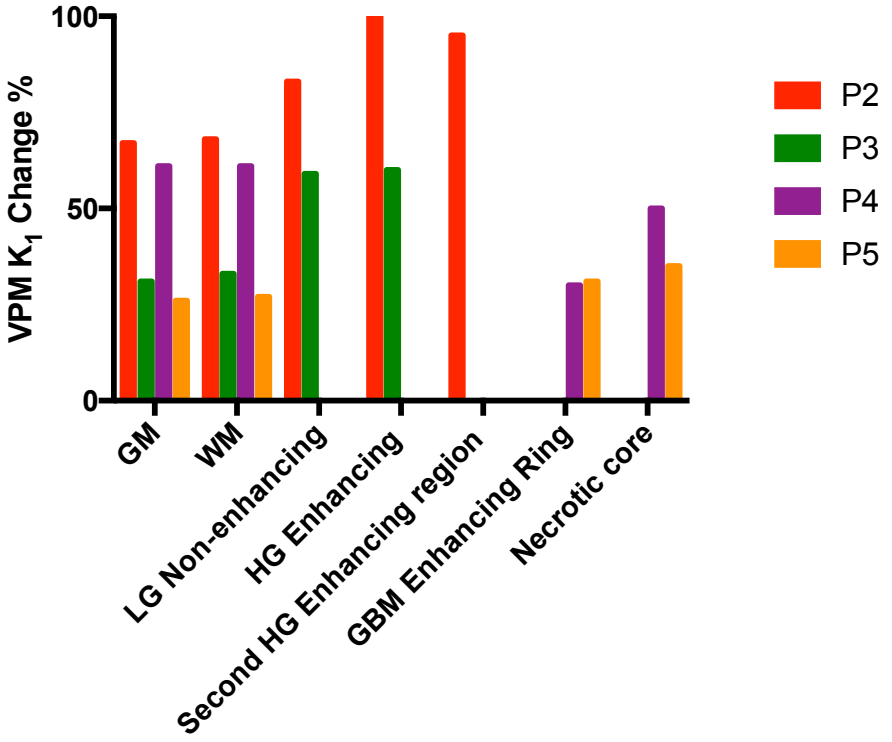

Figure 7. 11: Changes from baseline in (R)-[^{11}C]verapamil K_1 after administration of 2 mg/kg of TQD in the different regions of interest in the four glioma patients. Arterial input function not available for Patient 1 after P-gp inhibition. Grey matter (GM), white matter (WM), low-grade (LG), high-grade (HG) and glioblastoma (GBM).

7.4.3.2. Heterogeneous P-glycoprotein functional activity in brain tumours

(R)-[^{11}C]verapamil K_1 histograms were plotted for the different ROIs with (R)-[^{11}C]verapamil K_1 on the x-axis, with the y-axis expressed as a frequency (%) for each ROI. The histograms for all four glioma patients are presented in Figure 7.12.

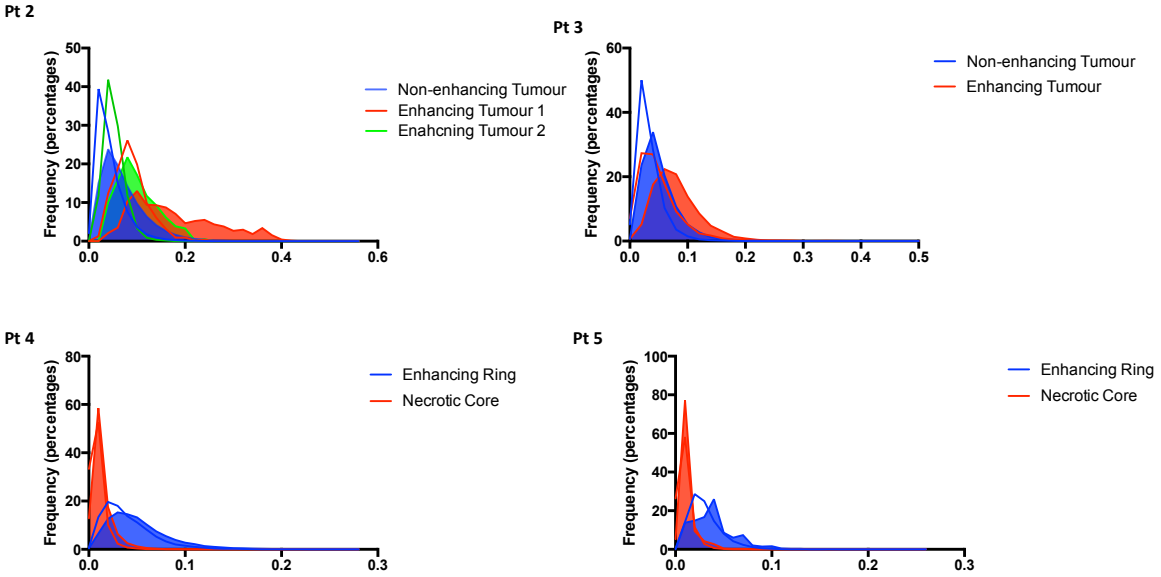

Figure 7. 12: (R)-[^{11}C]verapamil K_1 histograms in Patients two (top left), patient three (top right), patient four (bottom left and patient five (bottom right). Baseline histograms (no fill) and shaded graphs for the post-Tariquidar (P-glycoprotein) inhibition scans are presented for each patient.

All histograms were positively skewed with an elongated tail on the right side of the mean. Following TQD administration, all tumour regions showed a decrease in the frequency with widening of the graphs, reflecting the effects of P-gp inhibition and the heterogeneity of apparent (R)-[^{11}C]verapamil uptake.

The (R)-[^{11}C]verapamil K_1 in the enhancing components of the tumours for all four patients reached a lower relative frequency than the non-enhancing tumoural components (transforming glioma patients 2 and 3) or the necrotic core (glioblastoma patients 4 and 5). However, the (R)-[^{11}C]verapamil K_1 in the enhancing tumoural components were dispersed over a wider range than for those of the non-enhancing components or necrotic core. This indicates the heterogeneous spectrum of the functional activity of P-gp within the entire tumour volume, which also differs amongst the different components of each tumour.

Parametric maps of the baseline and post TQD scans are presented in Figure 7.13.

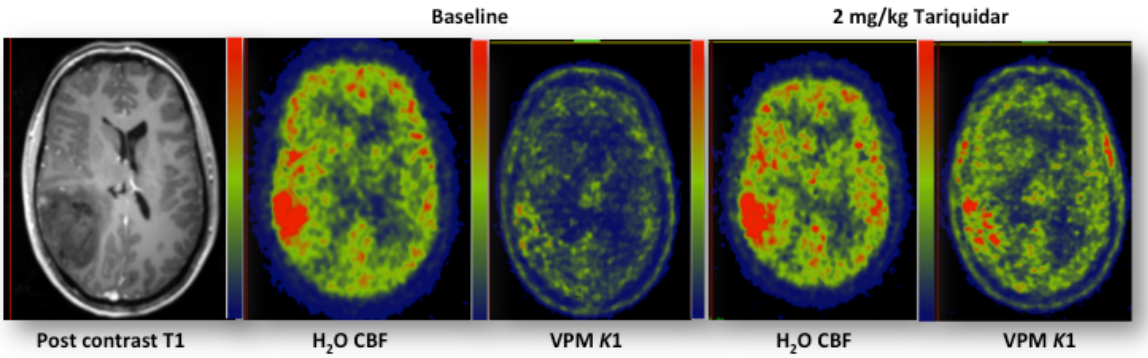

Figure 7. 13: Axial T1-weighted image (column 1) and parametric maps of perfusion (CBF) and (R)-[^{11}C]verapamil brain uptake at baseline (column 2 and 3 respectively) and after P-glycoprotein inhibition (columns 4 and 5 respectively) in patient 2. Note the heterogeneous uptake of (R)-[^{11}C]verapamil in the different regions of the tumour.

7.4.3.3. Extraction fraction

Finally, the extraction fraction (E) of (R)-[^{11}C]verapamil was calculated to factor out the contribution of CBF on the delivery of (R)-[^{11}C]verapamil into the brain using the following formula [E = (R)-[^{11}C]verapamil K_1 divided by CBF] and presented in Figure (14.A) for both healthy controls and glioma patients. Such normalisation of the (R)-[^{11}C]verapamil K_1 to the CBF in the second set of scans did not alter the earlier observed results in patients two and four.

The enhancing rim of the GBM tumours continued to demonstrate a low increase in E of (R)-[^{11}C]verapamil, indicating higher P-gp functional activity. However, in patient five, the reduction in the E of (R)-[^{11}C]verapamil was higher in the enhancing rim of the tumour than that seen in grey and white matter. This suggested that once blood flow is taken into consideration, the functional activity of P-gp is lower than that seen in the rest of the brain. Furthermore, patient three now demonstrated a lower change in E of (R)-[^{11}C]verapamil within the enhancing component of the tumour in comparison to the non-enhancing tumour and to the rest of the grey and white matter. This also suggests that the higher-grade component of the tumour exhibited higher P-gp functional activity when compared to the rest of the tumour and the brain.

Finally, a small change was also seen within the necrotic core of the GBM patients;

this suggests that even in cases where the BBB is completely disrupted, there is some P-gp functional activity (Figure 7.14B).

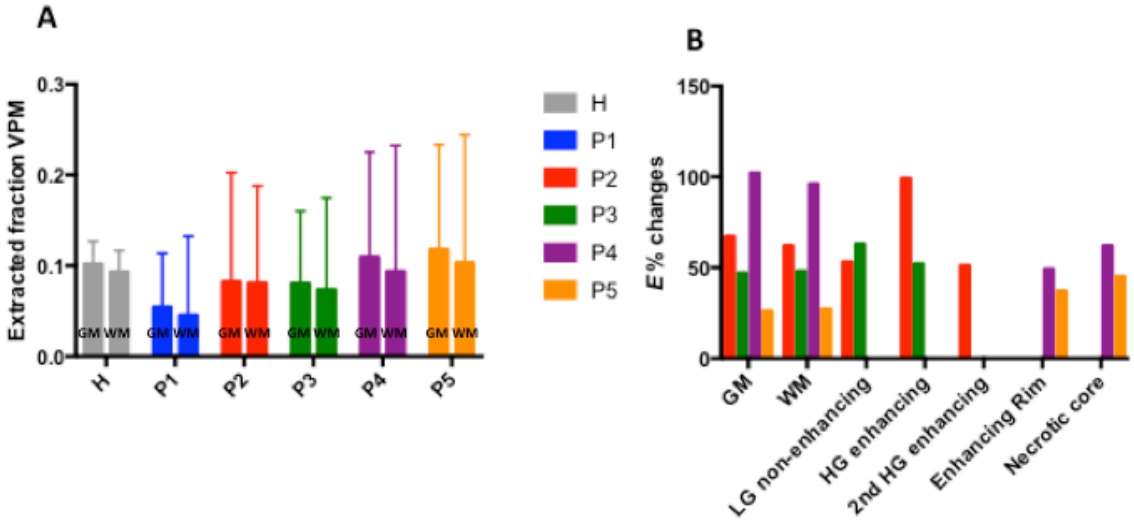

Figure 7. 14: (A) Baseline extraction fraction (*E*) of (R)-[^{11}C]verapamil in the grey and white matter for healthy controls (n = 6) and glioma patients. (B) Changes from baseline in extraction fraction (*E*) of (R)-[^{11}C]verapamil after administration of 2 mg/kg of TQD in the different regions of interest in the four glioma patients. Grey matter (GM), white matter (WM), low-grade (LG), high-grade (HG) and glioblastoma (GBM). Data presented as mean ± standard deviation for all six healthy controls and from each individual patient grey and white matter.

7.5. Discussion and conclusions

This pilot study is the first imaging study to provide direct in-vivo evidence of P-gp functional activity in glioma. The use of PET imaging with (R)-[^{11}C]verapamil, a P-gp substrate, has proven to be a successful approach for studying P-gp function at the human BBB in several human studies involving healthy volunteers (Wagner et al., 2009) (Bauer et al., 2015) and epilepsy patients (Langer et al., 2007) (Feldmann et al., 2013) (Bauer et al., 2014). The PET protocol used in this study involves two consecutive scans: a baseline scan followed by a second scan after P-gp inhibition achieved with a TQD intravenous infusion. Changes in K_1 and extraction fraction (*E*) between the baseline and inhibition scans were used as a surrogate marker for P-gp functional activity (Kreisl et al., 2010).

TQD is a third-generation P-gp inhibitor, which at the used dose of 2 mg/kg is expected to result in P-gp inhibition (Kreisl et al., 2015) but no measurable BCRP inhibition (Bauer et al., 2015). Furthermore, TQD causes inhibition of BCRP at high concentrations (Kannan et al., 2011) but not of multidrug resistance proteins (Mistry et al., 2001). It is important to note that TQD remains an expensive unlicensed drug.

This study shows that high-grade tumours have heterogenous P-gp functional activity, which can differ from grey and white matter in the same patient. The two patients with the grade III transforming glioma (Patients 2 and 3) showed higher changes in K_1 in both the enhancing and non-enhancing components of their tumours than were seen in grey and white matter. This indicates lower P-gp functional activity in the tumours in comparison to the rest of the brain.

In contrast, the enhancing rim of the patients with a GBM tumour showed higher P-gp functional activity than the rest of the brain, whilst Patient 5 showed similar functional activity to the rest of the brain in the enhancing rim. This heterogenous pattern of functional activity for P-gp is in agreement with the limited available literature. Demeule et al. analysed the expression of P-gp in 10 GBM patients using western blot analysis (Demeule et al., 2001). They found that three tumours had higher expression than the normal brain, four showed much lower expression and three showed similar expression. Similar results were also observed for 10 other patients with other high-

grade gliomas. Furthermore, in this study, heterogeneity in the functional activity of P-gp was even observed in individual tumours with variation in the different ROIs in each tumour. This finding further shows that the highly heterogenous nature of high-grade glioma can extend to the functional activity of P-gp.

Multiple studies have demonstrated higher drug concentration in the enhancing part of the tumour and within the tumour core in comparison to the non-enhancing tumour edges (Fine et al., 2006) (Rosso et al., 2009) (Pitz et al., 2011). These studies suggest that chemotherapy may achieve therapeutic concentrations in areas where the BBB is disrupted but is unlikely to do so at its periphery where tumour cells may still reside but there is an intact BBB. In this study, the necrotic core in the two GBM patients demonstrated some P-gp functional activity. This finding, in combination with the functional activity of P-gp demonstrated in the enhancing component of the tumour, suggests that disruption of the BBB should be regarded as incomplete, as P-gp efflux transporters may still play a role in limiting chemotherapy access to the tumour cells. This is particularly important as TMZ is a substrate for P-gp (Chapters 4 and 5). Similarly, active P-gp efflux transporters have also been demonstrated in a preclinical in-vivo study when Agarwal et al. found P-gp functional activity in the tumour core of an orthotopic glioma model implanted in rodents (Agarwal et al., 2013).

An important aspect of this study is the use of radiolabelled [^{15}O]H_2O to quantify CBF. Radiolabelled H_2O is considered the gold-standard method of estimating CBF, which can be significantly altered in patients with high-grade glioma (Hoeffner, 2005). The lowest levels of CBF were seen in patients with the GBM tumours. This can be attributed to raised intracranial pressure that is usually seen in patients with large GBM tumours. Interestingly, in Patients 2 and 3 with the transforming glioma, the enhancing components of the tumour demonstrated much higher CBF values than the rest of the tumour and brain. This was not observed in Patient 1. The exact cause for this is unclear. The administration of TQD resulted in variable changes in CBF, including a decrease, increase or little change in CBF in both healthy controls and patients with glioma (Figure 7.5). This response in CBF following TQD is a novel finding that has not been previously described in glioma patients.

Previous clinical PET imaging studies investigating P-gp function typically assumed brain extraction of (R)-[^{11}C]verapamil as insensitive to changes in CBF (Wagner et al.,

2009) (Bauer et al., 2015). Extraction fractions were then estimated by dividing K_1 by an assumed standardised cerebral blood flow value of 0.5 $mL.g^{-1}.min^{-1}$. Such an assumption was made based on the fact that (R)-[^{11}C]verapamil is a low-extraction radiotracer and TQD was not known to cause CBF changes. In this study, the extraction fraction for each ROI in every individual patient was calculated by dividing K_1 by CBF. This approach ensured that any changes detected in the (R)-[^{11}C]verapamil images could be attributed to P-gp function and not confounded by changes in CBF. The importance of such correction is highlighted by the changes seen in Patient 2, where the functional activity of P-gp was underestimated before accounting for CBF changes. The possibility that previously reported regional differences in P-gp functional activity could at least be partially attributed to changes in CBF cannot be discounted.

The main limitation of this study is the limited number of patients recruited, which precludes meaningful statistical testing and prevents any corrections for other variations such as age, gender (van Assema et al., 2012), race, drug history and tumour molecular markers. It also limits the interpretation of the observed findings.
Another important limiting factor is that detailed histological analysis of the biopsy samples and P-gp quantification in it was not carried out. This precludes direct radiological correlation with P-gp expression and histology in these samples. Difficulty in recruitment was multifactorial, such as the recently introduced guidelines of surgical intervention within seven to ten days for patients with suspected high-grade glioma and the performance status of patients. However, the aim of the study was to assess the feasibility of imaging P-gp function in patients with glioma tumours and this has been demonstrated. Future studies could expand the number of patients to account for these factors.

To date, there have been no clinical trials evaluating the effect of P-gp inhibition on treatment efficacy in brain tumours. Several clinical trials employed third generation P-gp inhibitors in combination with chemotherapy in patients with various cancer types tumours with disappointing results (Pusztai et al., 2005) (Cripe et al., 2010) (Kelly et al., 2011). A potential explanation of these failures is that many of these chemotherapy agents are substrates for other efflux transporters as well as P-gp. This may account for the relative success seen in one clinical trial in patients with acute

myeloid leukaemia that utilised cyclosporine A, which can inhibit multiple efflux transporters (Shaffer et al., 2012). This is important and should be taken into consideration when planning efflux transporter inhibition in combination with TMZ. Despite some clinical data implicating P-gp in determining response of glioma tumours to TMZ (Fromm, 2002) (Marzolini et al., 2004) and even in the development of chemoresistance (Schaich et al., 2009), we have demonstrated that TMZ is a dual P-gp and BCRP substrate. Therefore, single transporter inhibition in combination with TMZ therapy is unlikely to achieve the desired results.

Another major issue with these clinical trials is the lack of insight into the tumour expression of P-gp and other efflux transporters. This is particularly important, as not all of the tumours investigated express P-gp. Furthermore, in the current age of increasingly individualised clinical care, which is tailored according to each patient's need, a non-invasive imaging technique could help guide future treatment and trials by selecting patients with known high levels of transporter activity. Our observational study highlights the heterogeneity of P-gp activity amongst glioma patients.

In conclusion, this is an observational study, which confirms the feasibility of noninvasive imaging techniques enabling direct in-vivo visualisation of P-gp function and highlights its heterogeneity in patients with high-grade glioma tumours. It also suggests that CBF measurements could be important factor in the interpretation of the results. This study will need to be expanded to include more patients to confirm these results. Future clinical trials aiming to assess the effects of P-gp inhibition may benefit from including an imaging component, which helps identify appropriate patients.

Chapter 8 Summary and Future Work

8.1. An overview

The ultimate objective of the work in this thesis was to investigate and develop a non-invasive imaging method that allows measurement of TMZ delivery in brain tumours and assessment of the response to therapeutic manoeuvre designed to improve delivery. As described in chapter two, high-grade glioma continues to represent a major clinical challenge with limited five-year survival rates. MR imaging plays an integral part in the clinical management of these patients with multiple imaging biomarkers providing secondary information on the status of tumours and the response to therapy. The ability to investigate chemotherapy delivery in patients with brain tumours has been severely limited by the available technology and the need for invasive procedures.

In chapter three, the BBB and its status in glial tumours was reviewed and particular emphasis was placed on the role of the efflux transporters P-gp and BCRP in limiting the effectiveness of chemotherapy. At the time this work started, the relationship between TMZ and the efflux transporters P-gp and BCRP was poorly understood.

The study in chapter four aimed to investigate the relationship between TMZ and P-gp and BCRP. In particular the study was designed to assess if this relationship can be evaluated in an environment that closely resembles the *in-vivo* setting. An *in-vitro* BBB model was generated and validated. The BBB model was characterised by high TEER and functionally active P-gp and BCRP efflux transporters. However, TMZ was found to undergo rapid breakdown in the experimental conditions. In an effort to limit the impact of TMZ breakdown a CETA was performed with TMZ being added to both apical and basal compartments of the model at identical and clinically relevant concentrations. The study demonstrated a trend for TMZ to be weakly transported by P-gp and BCRP. Although this study provided the first direct evidence of TMZ transport by P-gp and BCRP, a definite conclusion about TMZ relationship with these efflux transporters could not be reached.

In chapter five, the relationship between TMZ and the efflux transporters P-gp and BCRP was established. PET imaging with radiolabelled TMZ were utilised in wild type and genetic transporter knockout mice. This demonstrated a significant increase in brain uptake of TMZ in animals lacking both transporters whilst animals with single transporter knockout (P-gp or BCRP) showed minimal increases, but this was not statically significant. Similar findings were demonstrated when brain radioactivity was measured directly from brain samples with gamma counter or non-invasively with PET. Similar results were observed when P-gp and BCRP were inhibited chemically with TQD.

Furthermore, the study also highlighted the importance of evaluating metabolism of radiotracers when assessing efflux transporter function as this enabled the correction for the different radiolabelled metabolites in plasma.

The objective of chapter six was to assess the impact of P-gp and BCRP inhibition on the efficacy of TMZ on a glioma model in mice. A glioma model was established in mice using the U87 cell line. Functional activity of BCRP was confirmed prior to implantation but no significant P-gp activity was detected. Glioma growth was monitored with serial MR scans as a surrogate for tumour response. TQD and TMZ therapy resulted in more rapid and sustained U87 glioma shrinkage than did treatment with TMZ alone.

PET imaging with radiolabelled TMZ was then employed to assess TMZ delivery across the BBB. Results suggested that oral TQD treatment produced a superior response by inhibiting P-gp and BCRP efflux transporters at the BBB level, however, this was not confirmed.

This study suggests that the concurrent administration of TMZ and TQD may be a viable treatment strategy for enhancing the delivery of TMZ into the brain and brain tumours, especially where P-gp and BCRP expression status is known.

Chapter seven the final experimental chapter aimed to assess the feasibility of measuring treatment induced changes in drug delivery in response to P-gp inhibition in patients with glioma. PET scans with radiolabelled water and Verapamil were performed pre and post TQD administration.
The study confirmed the feasibility of non-invasive PET imaging in enabling direct *in-vivo* visualisation of P-gp function and highlighted the heterogeneity of the functional activity of P-gp in patients with high-grade glioma tumours. Furthermore, CBF measurements appear to confound measurement of the true extraction fraction of Verapamil and therefore the interpretation of P-gp function. This study will need to be expanded to include more patients before these results can be confirmed.

8.2. Critical appraisal of the work presented

The novel experimental work presented in this thesis further adds to the increasing body of knowledge investigating the role of the BBB and its efflux transporters in limiting the delivery of effective chemotherapy in patients with brain tumours. The use of *in-vitro*, preclinical *in-vivo* and clinical studies enabled the collection of comprehensive data on the roles of P-gp and BCRP as efflux transporters at the BBB and in glioma cells in limiting TMZ delivery. The work in this thesis establishes the previously unknown relationship between TMZ and the efflux transporters P-gp and BCRP, and allows, for the first time, to directly visualise P-gp efflux function in patients with glioma tumours. It also suggests a possible role of P-gp and BCRP inhibition in enhancing TMZ efficacy in the treatment of high-grade glioma tumours.

8.2.1. Strength of experimental design

This experimental work is a solid example of stepwise investigative research where various *in-vitro*, preclinical *in-vivo*, and clinical experiments were employed to provide a comprehensive answer to a research question. This work simultaneously assessed the transport of TMZ by P-gp and BCRP efflux transporters. This is particularly important, as those two transporters are known to work closely together as efflux transporters for multiple anticancer drugs (Polli et al., 2009) (de Vries et al., 2007) (Agarwal et al.,

2011c) (Kodaira et al., 2010).

The use of an *in-vitro* BBB model that closely resembles the human BBB with high TEER and active P-gp and BCRP transporters, in combination with clinically relevant TMZ concentrations compares favourably with the commonly employed approach of using a cellular monolayer and high drug concentrations.

The preclinical *in-vivo* imaging studies utilised a suitable number of animals and combined both genetic and chemical transporter knockout. Furthermore, the assessment of TMZ metabolism in the different groups allowed for appropriate conclusions as the effect of radiolabelled metabolites was excluded. The relationship between TMZ and the efflux transporters P-gp and BCRP was evaluated using PET imaging and direct radioactivity measurements of brain and plasma samples. The PET analysis approach was semi-automated whilst a second operator measured the radioactivity concentrations in an attempt to reduce operator bias.

In the preclinical *in-vivo* glioma model studies, appropriate numbers of animals were used to detect a 40% change in tumour volume at week three between the treatment groups. The positive results observed were confirmed in a repeated experiment.

Also the study attempted to explain the mechanism for the response observed by performing PET imaging with radiolabelled TMZ and measuring TMZ concentrations in plasma. The number of animals used in the PET imaging component were limited to four per group. This probably account for the lack of statistical significance in the observed result despite their consistency. Data from this study will provide the needed information for appropriate powering of future studies.

In the final imaging study, P-gp functional activity was demonstrated in four patients with high-grade glioma. The use of radiolabelled H_2O to measure CBF proved particularly important as it allowed for measuring the extraction fraction of radiolabelled Verapamil, which proved important even for such a low-extraction radiotracer.

8.2.2. Weakness of experimental design

The use of an *in-vitro* BBB model to investigate the effects of P-gp and BCRP inhibition on the transport of TMZ proved challenging. This was mainly due to the rapid breakdown of TMZ in the experimental conditions, which limits the time

duration to one hour. This is suboptimal because even high affinity substrates can take up to 120 minutes (Luna-Tortos et al., 2008). The subsequent PET imaging with radiolabelled TMZ in rodents confirmed results of the *in-vitro* experiment.

Another important limitation is that although combination therapy of TQD and TMZ appears to enhance TMZ efficacy, the exact mechanism for this has not been clarified. There was an attempt to investigate this by performing PET imaging with radiolabelled TMZ, which indicated increased TMZ uptake in animals receiving TQD, especially in the hemispheres where glioma model was implanted. However, this was not statistically significant. A potential explanation of lack of statistical significance is the limited number of tumour-bearing mice that were imaged. This resulted in a slightly underpowered study, which may have prevented the detection of subtle but significant changes.

Furthermore, as blood sampling was not feasible, these results cannot be confirmed due to lack of a suitable arterial input function data.

With regards to the PET imaging study in patients with high-grade glioma, the limited number of patients remains the main weakness. Such numbers preclude any meaningful statistical analysis and prevent definite conclusions. However, as a proof of concept, this preliminary study demonstrates the feasibility of P-gp imaging in patients with glioma tumours. Future studies could expand the number of patients to enable more robust conclusions.

8.2.3. Potential clinical applications of the work presented

The translation of this research into clinical practice will prove challenging. Despite extensive literature in the preclinical settings reporting on the increased delivery of various anticancer drugs across the BBB when combined with efflux transporter inhibition, there has been no clinical study evaluating the effects of efflux transporter inhibition in patients with glioma. There are multiple factors that can account for this. Firstly, there are significant interspecies differences in the relative expression of P-gp and BCRP at the BBB. In humans BCRP appears to be the dominant efflux transporter with a BCRP/P-gp expression ratio of 1.3, this is in contrast to the lower ratio of 0.3 seen in rodents where the majority of the preclinical studies have been performed

(Uchida et al., 2011). This is also confounded by the variable and unknown expression of P-gp and BCRP in the glioma cells.

Moreover, TMZ is a substrate for both P-gp and BCRP. Consequently, meaningful increased delivery across the BBB can only be achieved when using dual P-gp and BCRP inhibitors. Currently, there are no known BCRP inhibitors that have been approved for clinical use. TQD is a third generation P-gp inhibitor that at high doses has shown some inhibitory effects on BCRP in the preclinical setup, but in humans when dosing exceeds 6 mg/kg significant side effects were encountered(Bauer et al., 2013b). Elacridar is a dual P-gp and BCRP inhibitor that was developed to overcome multidrug resistant in cancer but its development has been stopped (Hyafil et al., 1993). Recently, Elacridar was used as a dual P-gp and BCRP inhibitors in non-human primates only (Tournier et al., 2016). If the use of Elacridar expands into humans, PET imaging with radiolabelled TMZ will provide the ideal imaging method for measuring TMZ delivery in brain tumours and studying the effects of dual transporter inhibition.

Finally, the use of PET imaging to non invasively assess P-gp function in patients with glioma can be incorporated into clinical trials aiming to investigate the effects of P-gp inhibition on delivery of any chemotherapy agent. This is particularly relevant in the age of individualised clinical care. PET imaging can help identify patients with high levels of transporter expression, which are more likely to benefit from transporter inhibition.

8.3. Suggestions for future work

There are a number of projects that can expand the work presented here. The relationship between TMZ and the efflux transporters P-gp and BCRP has been clearly defined. As a proof of concept, combination TMZ and dual efflux transporter (P-gp and BCRP) inhibition has demonstrated superior efficacy in comparison to TMZ alone in a preclinical glioma model. This effect should be evaluated further in more clinically robust glioma models before consideration for clinical translation. Both novel *in-vitro* (Gomez-Roman et al., 2016) and preclinical but patient derived *in-vivo* glioma models have been recently introduced and appear to replicate the human GBM more closely, especially when compared with the simplified U87 glioma model.

The future use of larger rodents, such as a rat instead of mouse is also favoured. The small size of the mouse brain was a limiting factor in imaging the glioma model with PET and radiolabelled TMZ. A larger brain, such as in rats, may prove superior as it can allow for more tumour growth, which could be visualised with PET imaging. A study combining more relevant glioma model and PET imaging with radiolabelled TMZ will also provide a direct proof of enhanced TMZ delivery in these tumours.

Lack of clinically approved BCRP inhibitors for use in humans is another important factor in limiting the clinical translation of the work presented. TMZ is dual P-gp and BCRP substrate; therefore effective dual transporters inhibition is essential to establish significant enhancement in TMZ delivery in patients with brain tumours. Third generation P-gp inhibitors, such as TQD and Elacridar, have demonstrated some inhibitory effects on BCRP but none are currently suitable for clinical use.

Finally, the preliminary P-gp imaging study in patients with high-grade glioma will need to be expanded in order to confirm the results observed such as heterogeneity of P-gp expression which was seen between different patients and within the individual tumours.

References

ABBOTT, N. J. 2002. Astrocyte-endothelial interactions and blood-brain barrier permeability. *J Anat,* 200, 629-38.

ABBOTT, N. J., PATABENDIGE, A. A., DOLMAN, D. E., YUSOF, S. R. & BEGLEY, D. J. 2010. Structure and function of the blood-brain barrier. *Neurobiol Dis,* 37, 13-25.

ACHTEN, E., JACKSON, G. D., CAMERON, J. A., ABBOTT, D. F., STELLA, D. L. & FABINYI, G. C. 1999. Presurgical evaluation of the motor hand area with functional MR imaging in patients with tumors and dysplastic lesions. *Radiology,* 210, 529-38.

AGARWAL, S., HARTZ, A. M., ELMQUIST, W. F. & BAUER, B. 2011a. Breast cancer resistance protein and P-glycoprotein in brain cancer: two gatekeepers team up. *Curr Pharm Des,* 17, 2793-802.

AGARWAL, S., MANCHANDA, P., VOGELBAUM, M. A., OHLFEST, J. R. & ELMQUIST, W. F. 2013. Function of the blood-brain barrier and restriction of drug delivery to invasive glioma cells: findings in an orthotopic rat xenograft model of glioma. *Drug Metab Dispos,* 41, 33-9.

AGARWAL, S., SANE, R., OBEROI, R., OHLFEST, J. R. & ELMQUIST, W. F. 2011b. Delivery of molecularly targeted therapy to malignant glioma, a disease of the whole brain. *Expert Rev Mol Med,* 13, e17.

AGARWAL, S., SANE, R., OHLFEST, J. R. & ELMQUIST, W. F. 2011c. The role of the breast cancer resistance protein (ABCG2) in the distribution of sorafenib to the brain. *J Pharmacol Exp Ther,* 336, 223-33.

AGARWAL, S., UCHIDA, Y., MITTAPALLI, R. K., SANE, R., TERASAKI, T. & ELMQUIST, W. F. 2012. Quantitative proteomics of transporter expression in brain capillary endothelial cells isolated from P-glycoprotein (P-gp), breast cancer resistance protein (Bcrp), and P-gp/Bcrp knockout mice. *Drug Metab Dispos,* 40, 1164-9.

AHN, S. S., SHIN, N. Y., CHANG, J. H., KIM, S. H., KIM, E. H., KIM, D. W. & LEE, S. K. 2014. Prediction of methylguanine methyltransferase promoter methylation in glioblastoma using dynamic contrast-enhanced magnetic resonance and diffusion tensor imaging. *J Neurosurg,* 121, 367-73.

ALLT, G. & LAWRENSON, J. G. 2001. Pericytes: cell biology and pathology. *Cells*

Tissues Organs, 169, 1-11.

ANDRONESI, O. C., KIM, G. S., GERSTNER, E., BATCHELOR, T., TZIKA, A. A., FANTIN, V. R., VANDER HEIDEN, M. G. & SORENSEN, A. G. 2012. Detection of 2-hydroxyglutarate in IDH-mutated glioma patients by in vivo spectral-editing and 2D correlation magnetic resonance spectroscopy. *Sci Transl Med,* 4, 116ra4.

ARAKAWA, R., ITO, H., OKUMURA, M., MORIMOTO, T., SEKI, C., TAKAHASHI, H., TAKANO, A. & SUHARA, T. 2010. No inhibitory effect on P-glycoprotein function at blood-brain barrier by clinical dose of clarithromycin: a human PET study with [(1)(1)C]verapamil. *Ann Nucl Med,* 24, 83-7.

ARITA, H., KINOSHITA, M., KAGAWA, N., FUJIMOTO, Y., KISHIMA, H., HASHIMOTO, N. & YOSHIMINE, T. 2012. (1)(1)C-methionine uptake and intraoperative 5-aminolevulinic acid-induced fluorescence as separate index markers of cell density in glioma: a stereotactic image-histological analysis. *Cancer,* 118, 1619-27.

ARTURSSON, P. 1990. Epithelial transport of drugs in cell culture. I: A model for studying the passive diffusion of drugs over intestinal absorptive (Caco-2) cells. *J Pharm Sci,* 79, 476-82.

ARTZI, M., BLUMENTHAL, D. T., BOKSTEIN, F., NADAV, G., LIBERMAN, G., AIZENSTEIN, O. & BEN BASHAT, D. 2015. Classification of tumor area using combined DCE and DSC MRI in patients with glioblastoma. *J Neurooncol,* 121, 349-57.

ARTZI, M., BOKSTEIN, F., BLUMENTHAL, D. T., AIZENSTEIN, O., LIBERMAN, G., CORN, B. W. & BEN BASHAT, D. 2014. Differentiation between vasogenic-edema versus tumor-infiltrative area in patients with glioblastoma during bevacizumab therapy: a longitudinal MRI study. *Eur J Radiol,* 83, 1250-6.

BAI, R. Y., STAEDTKE, V. & RIGGINS, G. J. 2011. Molecular targeting of glioblastoma: Drug discovery and therapies. *Trends Mol Med,* 17, 301-12.

BAKER, S.D., WIRTH, M., STATKEVICH, P., REINDENBERG, P., ALTON, K., SARTORIUS, S.E., DUGAN, M., CUTLER, D., BARTRA, V., GCROCHOW, L.B., 1999. Absorption, metabolism, and excertion of 14C temozolomie following oral administration to patients with advanced cancer. *Clin Cancer*

Res, 5. 309-317.

BAKHSHI, S. & NORTH, R. B. 1995. Implantable pumps for drug delivery to the brain. *J Neurooncol,* 26, 133-9.

BANKS, W. A. 2009. Characteristics of compounds that cross the blood-brain barrier. *BMC Neurol,* 9 Suppl 1, S3.

BANKSTAHL, J. P., BANKSTAHL, M., KUNTNER, C., STANEK, J., WANEK, T., MEIER, M., DING, X. Q., MULLER, M., LANGER, O. & LOSCHER, W. 2011. A novel positron emission tomography imaging protocol identifies seizure-induced regional overactivity of P-glycoprotein at the blood-brain barrier. *J Neurosci,* 31, 8803-11.

BANKSTAHL, J. P., BANKSTAHL, M., ROMERMANN, K., WANEK, T., STANEK, J., WINDHORST, A. D., FEDROWITZ, M., ERKER, T., MULLER, M., LOSCHER, W., LANGER, O. & KUNTNER, C. 2013. Tariquidar and elacridar are dose-dependently transported by P-glycoprotein and Bcrp at the blood-brain barrier: a small-animal positron emission tomography and in vitro study. *Drug Metab Dispos,* 41, 754-62.

BARAZZUOL, L., JENA, R., BURNET, N. G., JEYNES, J. C., MERCHANT, M. J., KIRKBY, K. J. & KIRKBY, N. F. 2012. In vitro evaluation of combined temozolomide and radiotherapy using X rays and high-linear energy transfer radiation for glioblastoma. *Radiat Res,* 177, 651-62.

BAUER, M., KARCH, R., ZEITLINGER, M., LIU, J., KOEPP, M. J., ASSELIN, M. C., SISODIYA, S. M., HAINFELLNER, J. A., WADSAK, W., MITTERHAUSER, M., MULLER, M., PATARAIA, E. & LANGER, O. 2014. In vivo P-glycoprotein function before and after epilepsy surgery. *Neurology,* 83, 1326-31.

BAUER, M., KARCH, R., ZEITLINGER, M., PHILIPPE, C., ROMERMANN, K., STANEK, J., MAIER-SALAMON, A., WADSAK, W., JAGER, W., HACKER, M., MULLER, M. & LANGER, O. 2015. Approaching complete inhibition of P-glycoprotein at the human blood-brain barrier: an (R)-[11C]verapamil PET study. *J Cereb Blood Flow Metab,* 35, 743-6.

BAUER, M., KARCH, R., ZEITLINGER, M., STANEK, J., PHILIPPE, C., WADSAK, W., MITTERHAUSER, M., JAGER, W., HASLACHER, H., MULLER, M. & LANGER, O. 2013a. Interaction of 11C-tariquidar and 11C-elacridar with P-glycoprotein and breast cancer resistance protein at the human

blood-brain barrier. *J Nucl Med,* 54, 1181-7.

BAUER, M., ZEITLINGER, M., KARCH, R., MATZNELLER, P., STANEK, J., JAGER, W., BOHMDORFER, M., WADSAK, W., MITTERHAUSER, M., BANKSTAHL, J. P., LOSCHER, W., KOEPP, M., KUNTNER, C., MULLER, M. & LANGER, O. 2012. Pgp-mediated interaction between (R)-[11C]verapamil and tariquidar at the human blood-brain barrier: a comparison with rat data. *Clin Pharmacol Ther,* 91, 227-33.

BAUER, M., ZEITLINGER, M., TODORUT, D., BOHMDORFER, M., MULLER, M., LANGER, O. & JAGER, W. 2013b. Pharmacokinetics of single ascending doses of the P-glycoprotein inhibitor tariquidar in healthy subjects. *Pharmacology,* 91, 12-9.

BELL, E., JR. & KARNOSH, L. J. 1949. Cerebral hemispherectomy; report of a case 10 years after operation. *J Neurosurg,* 6, 285-93.

BLAKELEY, J. 2008. Drug delivery to brain tumors. *Curr Neurol Neurosci Rep,* 8, 235-41.

BLEAU, A. M., HAMBARDZUMYAN, D., OZAWA, T., FOMCHENKO, E. I., HUSE, J. T., BRENNAN, C. W. & HOLLAND, E. C. 2009. PTEN/PI3K/Akt pathway regulates the side population phenotype and ABCG2 activity in glioma tumor stem-like cells. *Cell Stem Cell,* 4, 226-35.

BOCK, N. A., ZADEH, G., DAVIDSON, L. M., QIAN, B., SLED, J. G., GUHA, A. & HENKELMAN, R. M. 2003. High-resolution longitudinal screening with magnetic resonance imaging in a murine brain cancer model. *Neoplasia,* 5, 546-54.

BORST, P. & ELFERINK, R. O. 2002. Mammalian ABC transporters in health and disease. *Annu Rev Biochem,* 71, 537-92.

BOXERMAN, J. L., ZHANG, Z., SAFRIEL, Y., LARVIE, M., SNYDER, B. S., JAIN, R., CHI, T. L., SORENSEN, A. G., GILBERT, M. R. & BARBORIAK, D. P. 2013. Early post-bevacizumab progression on contrast-enhanced MRI as a prognostic marker for overall survival in recurrent glioblastoma: results from the ACRIN 6677/RTOG 0625 Central Reader Study. *Neuro Oncol,* 15, 945-54.

BREEDVELD, P., BEIJNEN, J. H. & SCHELLENS, J. H. 2006. Use of P-glycoprotein and BCRP inhibitors to improve oral bioavailability and CNS penetration of anticancer drugs. *Trends Pharmacol Sci,* 27, 17-24.

BRANDES, A,A., FRANCESCHI, E., TOSONI, A., BLATT, V., PESSION, A.,

TALLINI, G., BERTORELLE, R., BARTOLINI, S., CALBUCCI, F., ANDEROLI, A., FREZZA, G., LEONARDI, M., SPANGOLLI, F., ERMANI, M,J. 2008. MGMT promoter methylation status can predict the incidence and outcome of pseudoprogression after concomitant radiochemotheraoy in newly diagnosed glioblastoma patients. 2008. *Clin Oncol*. 2008, 26, 2192-7.

BREM, H., PIANTADOSI, S., BURGER, P. C., SELKER, R., VICK, N. A., BLACK, K., SISTI, M., BREM, S., MOHER, G. 1995. Placebo-controlled trial of safety and efficacy of intraoperative controlled delivery by biodegradable polymers of chemotherapy for recurrent gliomas. The polymer-brain tumour treatment group. *Lancet*, 345, 1008-12.

BRIGHTMAN, M. W. & REESE, T. S. 1969. Junctions between intimately apposed cell membranes in the vertebrate brain. *J Cell Biol,* 40, 648-77.

BRODBELT, A., GREENBERG, D., WINTERS, T., WILLIAMS, M., VERNON, S. & COLLINS, V. P. 2015. Glioblastoma in England: 2007-2011. *Eur J Cancer,* 51, 533-42.

BROWN, R., ZLATESCU, M., SIJBEN, A., ROLDAN, G., EASAW, J., FORSYTH, P., PARNEY, I., SEVICK, R., YAN, E., DEMETRICK, D., SCHIFF, D., CAIRNCROSS, G. & MITCHELL, R. 2008. The use of magnetic resonance imaging to noninvasively detect genetic signatures in oligodendroglioma. *Clin Cancer Res,* 14, 2357-62.

BRUEHLMEIER, M., ROELCKE, U., SCHUBIGER, P. A. & AMETAMEY, S. M. 2004. Assessment of hypoxia and perfusion in human brain tumors using PET with 18F-fluoromisonidazole and 15O-H2O. *J Nucl Med,* 45, 1851-9.

BUCKNER, J. C. 2003. Factors influencing survival in high-grade gliomas. *Semin Oncol,* 30, 10-4.

BUCKNER, J. C., Giannin, C., Eckel-Passow, J., Lanchance, D., Parney, I., Laack, N. & Jenkins, R. 2017. Management of diffuse low-grade gliomas in adults – use of molecular diagnostics. 2017. *Nat Rev Neurol*, 54.

BULAKBASI, N., KOCAOGLU, M., ORS, F., TAYFUN, C. & UCOZ, T. 2003. Combination of single-voxel proton MR spectroscopy and apparent diffusion coefficient calculation in the evaluation of common brain tumors. *AJNR Am J Neuroradiol,* 24, 225-33.

CANTRILL, C. A., SKINNER, R. A., ROTHWELL, N. J. & PENNY, J. I. 2012. An immortalised astrocyte cell line maintains the in vivo phenotype of a primary

porcine in vitro blood-brain barrier model. *Brain Res,* 1479, 17-30.

CARCABOSO, A. M., ELMELIEGY, M. A., SHEN, J., JUEL, S. J., ZHANG, Z. M., CALABRESE, C., TRACEY, L., WATERS, C. M. & STEWART, C. F. 2010. Tyrosine kinase inhibitor gefitinib enhances topotecan penetration of gliomas. *Cancer Res,* 70, 4499-508.

CARRILLO, J. A., LAI, A., NGHIEMPHU, P. L., KIM, H. J., PHILLIPS, H. S., KHARBANDA, S., MOFTAKHAR, P., LALAEZARI, S., YONG, W., ELLINGSON, B. M., CLOUGHESY, T. F. & POPE, W. B. 2012. Relationship between tumor enhancement, edema, IDH1 mutational status, MGMT promoter methylation, and survival in glioblastoma. *AJNR Am J Neuroradiol,* 33, 1349-55.

CHA, S., TIHAN, T., CRAWFORD, F., FISCHBEIN, N. J., CHANG, S., BOLLEN, A., NELSON, S. J., PRADOS, M., BERGER, M. S. & DILLON, W. P. 2005. Differentiation of low-grade oligodendrogliomas from low-grade astrocytomas by using quantitative blood-volume measurements derived from dynamic susceptibility contrast-enhanced MR imaging. *AJNR Am J Neuroradiol,* 26, 266-73.

CHA, S., YANG, L., JOHNSON, G., LAI, A., CHEN, M. H., TIHAN, T., WENDLAND, M. & DILLON, W. P. 2006. Comparison of microvascular permeability measurements, K(trans), determined with conventional steady-state T1-weighted and first-pass T2*-weighted MR imaging methods in gliomas and meningiomas. *AJNR Am J Neuroradiol,* 27, 409-17.

CHAMBERLAIN, M. C., KORMANIK, P. A. & BARBA, D. 1997. Complications associated with intraventricular chemotherapy in patients with leptomeningeal metastases. *J Neurosurg,* 87, 694-9.

CHAWLA, S., KREJZA, J., VOSSOUGH, A., ZHANG, Y., KAPOOR, G. S., WANG, S., O'ROURKE, D. M., MELHEM, E. R. & POPTANI, H. 2013. Differentiation between oligodendroglioma genotypes using dynamic susceptibility contrast perfusion-weighted imaging and proton MR spectroscopy. *AJNR Am J Neuroradiol,* 34, 1542-9.

CHEN, W., SILVERMAN, D. H., DELALOYE, S., CZERNIN, J., KAMDAR, N., POPE, W., SATYAMURTHY, N., SCHIEPERS, C. & CLOUGHESY, T. 2006. 18F-FDOPA PET imaging of brain tumors: comparison study with 18F-FDG PET and evaluation of diagnostic accuracy. *J Nucl Med,* 47, 904-11.

CHUA, C., ZAIDEN, N., CHONG, K. H., SEE, S. J., WONG, M. C., ANG, B. T. & TANG, C. 2008. Characterization of a side population of astrocytoma cells in response to temozolomide. *J Neurosurg,* 109, 856-66.

CISTERNINO, S., MERCIER, C., BOURASSET, F., ROUX, F. & SCHERRMANN, J. M. 2004. Expression, up-regulation, and transport activity of the multidrug-resistance protein Abcg2 at the mouse blood-brain barrier. *Cancer Res,* 64, 3296-301.

CLAES, A., WESSELING, P., JEUKEN, J., MAASS, C., HEERSCHAP, A. & LEENDERS, W. P. 2008. Antiangiogenic compounds interfere with chemotherapy of brain tumors due to vessel normalization. *Mol Cancer Ther,* 7, 71-8.

CLARK, C. A., BARRICK, T. R., MURPHY, M. M. & BELL, B. A. 2003. White matter fiber tracking in patients with space-occupying lesions of the brain: a new technique for neurosurgical planning? *Neuroimage,* 20, 1601-8.

CLARK, M. J., HOMER, N., O'CONNOR, B. D., CHEN, Z., ESKIN, A., LEE, H., MERRIMAN, B. & NELSON, S. F. 2010. U87MG decoded: the genomic sequence of a cytogenetically aberrant human cancer cell line. *PLoS Genet,* 6, e1000832.

COHEN, A. L., HOLMEN, S. L. & COLMAN, H. 2013. IDH1 and IDH2 mutations in gliomas. *Curr Neurol Neurosci Rep,* 13, 345.

COHEN-KASHI MALINA, K., COOPER, I. & TEICHBERG, V. I. 2009. Closing the gap between the in-vivo and in-vitro blood-brain barrier tightness. *Brain Res,* 1284, 12-21.

COLLINS, J. M. & DEDRICK, R. L. 1983. Distributed model for drug delivery to CSF and brain tissue. *Am J Physiol,* 245, R303-10.

CONVERT, L., Morin-Brassard, G., Cardorette, J., Archambault, M., Bentourika, M., Lecomte, R. 2007. A new tool for molecular imaging: The microvolumteric B Blood counter. *J Nuc Med*, 48:1197-1206

COORAY, H. C., BLACKMORE, C. G., MASKELL, L. & BARRAND, M. A. 2002. Localisation of breast cancer resistance protein in microvessel endothelium of human brain. *Neuroreport,* 13, 2059-63.

CORDON-CARDO, C., O'BRIEN, J. P., CASALS, D., RITTMAN-GRAUER, L., BIEDLER, J. L., MELAMED, M. R. & BERTINO, J. R. 1989. Multidrug-resistance gene (P-glycoprotein) is expressed by endothelial cells at blood-

brain barrier sites. *Proc Natl Acad Sci U S A,* 86, 695-8.

CORNELISSEN, B., KERSEMANS, V., JANS, L., STAELENS, L., OLTENFREITER, R., THONISSEN, T., ACHTEN, E. & SLEGERS, G. 2005. Comparison between 1 T MRI and non-MRI based volumetry in inoculated tumours in mice. *Br J Radiol,* 78, 338-42.

CORROYER-DULMONT, A., PERES, E. A., PETIT, E., GUILLAMO, J. S., VAROQUEAUX, N., ROUSSEL, S., TOUTAIN, J., DIVOUX, D., MACKENZIE, E. T., DELAMARE, J., IBAZIZENE, M., LECOCQ, M., JACOBS, A. H., BARRE, L., BERNAUDIN, M. & VALABLE, S. 2013. Detection of glioblastoma response to temozolomide combined with bevacizumab based on muMRI and muPET imaging reveals [18F]-fluoro-L-thymidine as an early and robust predictive marker for treatment efficacy. *Neuro Oncol,* 15, 41-56.

CRIPE, L. D., UNO, H., PAIETTA, E. M., LITZOW, M. R., KETTERLING, R. P., BENNETT, J. M., ROWE, J. M., LAZARUS, H. M., LUGER, S. & TALLMAN, M. S. 2010. Zosuquidar, a novel modulator of P-glycoprotein, does not improve the outcome of older patients with newly diagnosed acute myeloid leukemia: a randomized, placebo-controlled trial of the Eastern Cooperative Oncology Group 3999. *Blood,* 116, 4077-85.

DANCHAIVIJITR, N., WALDMAN, A. D., TOZER, D. J., BENTON, C. E., BRASIL CASEIRAS, G., TOFTS, P. S., REES, J. H. & JAGER, H. R. 2008. Low-grade gliomas: do changes in rCBV measurements at longitudinal perfusion-weighted MR imaging predict malignant transformation? *Radiology,* 247, 170-8.

DARDIS, C., MILTON, K., ASHBY, L. & SHAPIRO, W. 2014. Leptomeningeal metastases in high-grade adult glioma: development, diagnosis, management, and outcomes in a series of 34 patients. *Front Neurol,* 5, 220.

DE CARLI, E., WANG, X. & PUGET, S. 2009. IDH1 and IDH2 mutations in gliomas. *N Engl J Med,* 360, 2248; author reply 2249.

DE VRIES, N. A., ZHAO, J., KROON, E., BUCKLE, T., BEIJNEN, J. H. & VAN TELLINGEN, O. 2007. P-glycoprotein and breast cancer resistance protein: two dominant transporters working together in limiting the brain penetration of topotecan. *Clin Cancer Res,* 13, 6440-9.

DEAN, M., FOJO, T. & BATES, S. 2005. Tumour stem cells and drug resistance. *Nat Rev Cancer,* 5, 275-84.

DEAN, M., HAMON, Y. & CHIMINI, G. 2001. The human ATP-binding cassette (ABC) transporter superfamily. *J Lipid Res,* 42, 1007-17.

DECLEVES, X., FAJAC, A., LEHMANN-CHE, J., TARDY, M., MERCIER, C., HURBAIN, I., LAPLANCHE, J. L., BERNAUDIN, J. F. & SCHERRMANN, J. M. 2002. Molecular and functional MDR1-Pgp and MRPs expression in human glioblastoma multiforme cell lines. *Int J Cancer,* 98, 173-80.

DEL ZOPPO, G. J., MILNER, R., MABUCHI, T., HUNG, S., WANG, X. & KOZIOL, J. A. 2006. Vascular matrix adhesion and the blood-brain barrier. *Biochem Soc Trans,* 34, 1261-6.

DEMEULE, M., SHEDID, D., BEAULIEU, E., DEL MAESTRO, R. F., MOGHRABI, A., GHOSN, P. B., MOUMDJIAN, R., BERTHELET, F. & BELIVEAU, R. 2001. Expression of multidrug-resistance P-glycoprotein (MDR1) in human brain tumors. *Int J Cancer,* 93, 62-6.

DENNY, B. J., WHEELHOUSE, R. T., STEVENS, M. F., TSANG, L. L. & SLACK, J. A. 1994. NMR and molecular modeling investigation of the mechanism of activation of the antitumor drug temozolomide and its interaction with DNA. *Biochemistry,* 33, 9045-51.

DHERMAIN, F. G., HAU, P., LANFERMANN, H., JACOBS, A. H. & VAN DEN BENT, M. J. 2010. Advanced MRI and PET imaging for assessment of treatment response in patients with gliomas. *Lancet Neurol,* 9, 906-20.

DI COSTANZO, A., SCARABINO, T., TROJSI, F., GIANNATEMPO, G. M., POPOLIZIO, T., CATAPANO, D., BONAVITA, S., MAGGIALETTI, N., TOSETTI, M., SALVOLINI, U., D'ANGELO, V. A. & TEDESCHI, G. 2006. Multiparametric 3T MR approach to the assessment of cerebral gliomas: tumor extent and malignancy. *Neuroradiology,* 48, 622-31.

DIEZ, B. D., STATKEVICH, P., ZHU, Y., ABUTARIF, M. A., XUAN, F., KANTESARIA, B., CUTLER, D., CANTILLON, M., SCHWARZ, M., PALLOTTA, M. G. & OTTAVIANO, F. H. 2010. Evaluation of the exposure equivalence of oral versus intravenous temozolomide. *Cancer Chemother Pharmacol,* 65, 727-34.

DOHMAN, B. M., SHIELDS, A. F. & GREIRSON, J. R. 2000. The use of PET in evaluating patients with primary brain tumours: is it useful ? *J Neurol Neurosurg Psychiatry.* 41, 966.

BENDALY, E. A., SLOAN, A. E. & DOHMAN, B. M. 2002. Use of [^{18}F]-FLT-PET

to assess the metabolic activity of primary and metastatic brain tumours. *J Nucl Med.* 42, 401.

DOYLE, L. & ROSS, D. D. 2003. Multidrug resistance mediated by the breast cancer resistance protein BCRP (ABCG2). *Oncogene,* 22, 7340-58.

DOYLE, L. A., YANG, W., ABRUZZO, L. V., KROGMANN, T., GAO, Y., RISHI, A. K. & ROSS, D. D. 1998. A multidrug resistance transporter from human MCF-7 breast cancer cells. *Proc Natl Acad Sci U S A,* 95, 15665-70.

DRABYCZ, S., ROLDAN, G., DE ROBLES, P., ADLER, D., MCINTYRE, J. B., MAGLIOCCO, A. M., CAIRNCROSS, J. G. & MITCHELL, J. R. 2010. An analysis of image texture, tumor location, and MGMT promoter methylation in glioblastoma using magnetic resonance imaging. *Neuroimage,* 49, 1398-405.

ELLINGSON, B. M., CLOUGHESY, T. F., POPE, W. B., ZAW, T. M., PHILLIPS, H., LALEZARI, S., NGHIEMPHU, P. L., IBRAHIM, H., NAEINI, K. M., HARRIS, R. J. & LAI, A. 2012. Anatomic localization of O6-methylguanine DNA methyltransferase (MGMT) promoter methylated and unmethylated tumors: a radiographic study in 358 de novo human glioblastomas. *Neuroimage,* 59, 908-16.

ELLINGSON, B. M., MALKIN, M. G., RAND, S. D., CONNELLY, J. M., QUINSEY, C., LAVIOLETTE, P. S., BEDEKAR, D. P. & SCHMAINDA, K. M. 2010. Validation of functional diffusion maps (fDMs) as a biomarker for human glioma cellularity. *J Magn Reson Imaging,* 31, 538-48.

ENEROTH, A., ASTROM, E., HOOGSTRAATE, J., SCHRENK, D., CONRAD, S., KAUFFMANN, H. M. & GJELLAN, K. 2001. Evaluation of a vincristine resistant Caco-2 cell line for use in a calcein AM extrusion screening assay for P-glycoprotein interaction. *Eur J Pharm Sci,* 12, 205-14.

EOLI, M., MENGHI, F., BRUZZONE, M. G., DE SIMONE, T., VALLETTA, L., POLLO, B., BISSOLA, L., SILVANI, A., BIANCHESSI, D., D'INCERTI, L., FILIPPINI, G., BROGGI, G., BOIARDI, A. & FINOCCHIARO, G. 2007. Methylation of O6-methylguanine DNA methyltransferase and loss of heterozygosity on 19q and/or 17p are overlapping features of secondary glioblastomas with prolonged survival. *Clin Cancer Res,* 13, 2606-13.

FAN, G. G., DENG, Q. L., WU, Z. H. & GUO, Q. Y. 2006. Usefulness of diffusion/perfusion-weighted MRI in patients with non-enhancing supratentorial brain gliomas: a valuable tool to predict tumour grading? *Br J*

Radiol, 79, 652-8.

FANDINO, J., KOLLIAS, S. S., WIESER, H. G., VALAVANIS, A. & YONEKAWA, Y. 1999. Intraoperative validation of functional magnetic resonance imaging and cortical reorganization patterns in patients with brain tumors involving the primary motor cortex. *J Neurosurg,* 91, 238-50.

FARID, N., ALMEIDA-FREITAS, D. B., WHITE, N. S., MCDONALD, C. R., MULLER, K. A., VANDENBERG, S. R., KESARI, S. & DALE, A. M. 2013. Restriction-Spectrum Imaging of Bevacizumab-Related Necrosis in a Patient with GBM. *Front Oncol,* 3, 258.

FARQUHAR, D. & BENVENUTO, J. 1984. 1-Aryl-3,3-dimethyltriazenes: potential central nervous system active analogues of 5-(3,3-dimethyl-1-triazeno)imidazole-4-carboxamide (DTIC). *J Med Chem,* 27, 1723-7.

FATTORI, S., BECHERINI, F., CIANFRIGLIA, M., PARENTI, G., ROMANINI, A. & CASTAGNA, M. 2007. Human brain tumors: multidrug-resistance P-glycoprotein expression in tumor cells and intratumoral capillary endothelial cells. *Virchows Arch,* 451, 81-7.

FELDMANN, M., ASSELIN, M. C., LIU, J., WANG, S., MCMAHON, A., ANTON-RODRIGUEZ, J., WALKER, M., SYMMS, M., BROWN, G., HINZ, R., MATTHEWS, J., BAUER, M., LANGER, O., THOM, M., JONES, T., VOLLMAR, C., DUNCAN, J. S., SISODIYA, S. M. & KOEPP, M. J. 2013. P-glycoprotein expression and function in patients with temporal lobe epilepsy: a case-control study. *Lancet Neurol,* 12, 777-85.

FELSBERG, J., ERKWOH, A., SABEL, M. C., KIRSCH, L., FIMMERS, R., BLASCHKE, B., SCHLEGEL, U., SCHRAMM, J., WIESTLER, O. D. & REIFENBERGER, G. 2004. Oligodendroglial tumors: refinement of candidate regions on chromosome arm 1p and correlation of 1p/19q status with survival. *Brain Pathol,* 14, 121-30.

FENG, D., WANG, Z. & HUANG, S. C. 1993. A study on statistically reliable and computationally efficient algorithms for generating local cerebral blood flow parametric images with positron emission tomography. *IEEE Trans Med Imaging,* 12, 182-8.

FINE, H. A., DEAR, K. B., LOEFFLER, J. S., BLACK, P. M. & CANELLOS, G. P. 1993. Meta-analysis of radiation therapy with and without adjuvant chemotherapy for malignant gliomas in adults. *Cancer,* 71, 2585-97.

FINE, R. L., CHEN, J., BALMACEDA, C., BRUCE, J. N., HUANG, M., DESAI, M., SISTI, M. B., MCKHANN, G. M., GOODMAN, R. R., BERTINO, J. S., JR., NAFZIGER, A. N. & FETELL, M. R. 2006. Randomized study of paclitaxel and tamoxifen deposition into human brain tumors: implications for the treatment of metastatic brain tumors. *Clin Cancer Res,* 12, 5770-6.

FISCHER, I., GAGNER, J. P., LAW, M., NEWCOMB, E. W. & ZAGZAG, D. 2005. Angiogenesis in gliomas: biology and molecular pathophysiology. *Brain Pathol,* 15, 297-310.

FOLKMAN, J. 1992. The role of angiogenesis in tumor growth. *Semin Cancer Biol,* 3, 65-71.

FORSYTH, P. A., WONG, H., LAING, T. D., REWCASTLE, N. B., MORRIS, D. G., MUZIK, H., LECO, K. J., JOHNSTON, R. N., BRASHER, P. M., SUTHERLAND, G. & EDWARDS, D. R. 1999. Gelatinase-A (MMP-2), gelatinase-B (MMP-9) and membrane type matrix metalloproteinase-1 (MT1-MMP) are involved in different aspects of the pathophysiology of malignant gliomas. *Br J Cancer,* 79, 1828-35.

FOX, E. & BATES, S. E. 2007. Tariquidar (XR9576): a P-glycoprotein drug efflux pump inhibitor. *Expert Rev Anticancer Ther,* 7, 447-59.

FRANKE, H., GALLA, H. J. & BEUCKMANN, C. T. 1999. An improved low-permeability in vitro-model of the blood-brain barrier: transport studies on retinoids, sucrose, haloperidol, caffeine and mannitol. *Brain Res,* 818, 65-71.

FROMM, M. F. 2002. The influence of MDR1 polymorphisms on P-glycoprotein expression and function in humans. *Adv Drug Deliv Rev,* 54, 1295-310.

FRUEHAUF, J. P., BREM, H., BREM, S., SLOAN, A., BARGER, G., HUANG, W. & PARKER, R. 2006. In vitro drug response and molecular markers associated with drug resistance in malignant gliomas. *Clin Cancer Res,* 12, 4523-32.

GERSTNER, E. R., CHEN, P. J., WEN, P. Y., JAIN, R. K., BATCHELOR, T. T. & SORENSEN, G. 2010. Infiltrative patterns of glioblastoma spread detected via diffusion MRI after treatment with cediranib. *Neuro Oncol,* 12, 466-72.

GIESE, A., BJERKVIG, R., BERENS, M. E. & WESTPHAL, M. 2003. Cost of migration: invasion of malignant gliomas and implications for treatment. *J Clin Oncol,* 21, 1624-36.

GILBERT, M. R., DIGNAM, J. J., ARMSTRONG, T. S., WEFEL, J. S., BLUMENTHAL, D. T., VOGELBAUM, M. A., COLMAN, H.,

CHAKRAVARTI, A., PUGH, S., WON, M., JERAJ, R., BROWN, P. D., JAECKLE, K. A., SCHIFF, D., STIEBER, V. W., BRACHMAN, D. G., WERNER-WASIK, M., TREMONT-LUKATS, I. W., SULMAN, E. P., ALDAPE, K. D., CURRAN, W. J., JR. & MEHTA, M. P. 2014. A randomized trial of bevacizumab for newly diagnosed glioblastoma. *N Engl J Med,* 370, 699-708.

GILBERTSON, R. J. & RICH, J. N. 2007. Making a tumour's bed: glioblastoma stem cells and the vascular niche. *Nat Rev Cancer,* 7, 733-6.

GLAUDEMANS, A. W., ENTING, R. H., HEESTERS, M. A., DIERCKX, R. A., VAN RHEENEN, R. W., WALENKAMP, A. M. & SLART, R. H. 2013. Value of 11C-methionine PET in imaging brain tumours and metastases. *Eur J Nucl Med Mol Imaging,* 40, 615-35.

GOLDEN, P. L. & PARDRIDGE, W. M. 1999. P-Glycoprotein on astrocyte foot processes of unfixed isolated human brain capillaries. *Brain Res,* 819, 143-6.

GOLDWIRT, L., BECCARIA, K., CARPENTIER, A., FARINOTTI, R. & FERNANDEZ, C. 2014. Irinotecan and temozolomide brain distribution: a focus on ABCB1. *Cancer Chemother Pharmacol,* 74, 185-93.

GOMEZ-ROMAN, N., STEVENSON, K., GILMOUR, L., HAMILTON, G. & CHALMERS, A. J. 2016. A novel 3D human glioblastoma cell culture system for modeling drug and radiation responses. *Neuro Oncol*.

GROFT, L. L., MUZIK, H., REWCASTLE, N. B., JOHNSTON, R. N., KNAUPER, V., LAFLEUR, M. A., FORSYTH, P. A. & EDWARDS, D. R. 2001. Differential expression and localization of TIMP-1 and TIMP-4 in human gliomas. *Br J Cancer,* 85, 55-63.

GUDINAVICIENE, I., PRANYS, D. & JUOZAITYTE, E. 2004. Impact of morphology and biology on the prognosis of patients with gliomas. *Medicina (Kaunas),* 40, 112-20.

GUPTA, A., PRAGER, A., YOUNG, R. J., SHI, W., OMURO, A. M. & GRABER, J. J. 2013. Diffusion-weighted MR imaging and MGMT methylation status in glioblastoma: a reappraisal of the role of preoperative quantitative ADC measurements. *AJNR Am J Neuroradiol,* 34, E10-1.

GUPTA, A., YOUNG, R. J., KARIMI, S., SOOD, S., ZHANG, Z., MO, Q., GUTIN, P. H., HOLODNY, A. I. & LASSMAN, A. B. 2011. Isolated diffusion restriction precedes the development of enhancing tumor in a subset of patients

with glioblastoma. *AJNR Am J Neuroradiol,* 32, 1301-6.

HAMSTRA, D. A., CHENEVERT, T. L., MOFFAT, B. A., JOHNSON, T. D., MEYER, C. R., MUKHERJI, S. K., QUINT, D. J., GEBARSKI, S. S., FAN, X., TSIEN, C. I., LAWRENCE, T. S., JUNCK, L., REHEMTULLA, A. & ROSS, B. D. 2005. Evaluation of the functional diffusion map as an early biomarker of time-to-progression and overall survival in high-grade glioma. *Proc Natl Acad Sci U S A,* 102, 16759-64.

HAMSTRA, D. A., GALBAN, C. J., MEYER, C. R., JOHNSON, T. D., SUNDGREN, P. C., TSIEN, C., LAWRENCE, T. S., JUNCK, L., ROSS, D. J., REHEMTULLA, A., ROSS, B. D. & CHENEVERT, T. L. 2008. Functional diffusion map as an early imaging biomarker for high-grade glioma: correlation with conventional radiologic response and overall survival. *J Clin Oncol,* 26, 3387-94.

HARRIS, R. J., CLOUGHESY, T. F., POPE, W. B., NGHIEMPHU, P. L., LAI, A., ZAW, T., CZERNIN, J., PHELPS, M. E., CHEN, W. & ELLINGSON, B. M. 2012. 18F-FDOPA and 18F-FLT positron emission tomography parametric response maps predict response in recurrent malignant gliomas treated with bevacizumab. *Neuro Oncol,* 14, 1079-89.

HAU, P., FABEL, K., BAUMGART, U., RUMMELE, P., GRAUER, O., BOCK, A., DIETMAIER, C., DIETMAIER, W., DIETRICH, J., DUDEL, C., HUBNER, F., JAUCH, T., DRECHSEL, E., KLEITER, I., WISMETH, C., ZELLNER, A., BRAWANSKI, A., STEINBRECHER, A., MARIENHAGEN, J. & BOGDAHN, U. 2004. Pegylated liposomal doxorubicin-efficacy in patients with recurrent high-grade glioma. *Cancer,* 100, 1199-207.

HAWKINS, B. T. & DAVIS, T. P. 2005. The blood-brain barrier/neurovascular unit in health and disease. *Pharmacol Rev,* 57, 173-85.

HEGI, M. E., DISERENS, A. C., GODARD, S., DIETRICH, P. Y., REGLI, L., OSTERMANN, S., OTTEN, P., VAN MELLE, G., DE TRIBOLET, N. & STUPP, R. 2004. Clinical trial substantiates the predictive value of O-6-methylguanine-DNA methyltransferase promoter methylation in glioblastoma patients treated with temozolomide. *Clin Cancer Res,* 10, 1871-4.

HEISS, W. D., HABEDANK, B., KLEIN, J. C., HERHOLZ, K., WIENHARD, K., LENOX, M. & NUTT, R. 2004. Metabolic rates in small brain nuclei determined by high-resolution PET. *J Nucl Med,* 45, 1811-5.

HERRMANN, K., CZERNIN, J., CLOUGHESY, T., LAI, A., POMYKALA, K. L., BENZ, M. R., BUCK, A. K., PHELPS, M. E. & CHEN, W. 2014. Comparison of visual and semiquantitative analysis of 18F-FDOPA-PET/CT for recurrence detection in glioblastoma patients. *Neuro Oncol,* 16, 603-9.

HESSELINK, J. R., BARKOVICH, M. J., SEIBERT, T. M., FARID, N., MULLER, K. A., MURPHY, K. T. & KESARI, S. 2014. Bevacizumab: radiation combination produces restricted diffusion on brain MRI. *CNS Oncol,* 3, 329-35.

HIRAI, T., MURAKAMI, R., NAKAMURA, H., KITAJIMA, M., FUKUOKA, H., SASAO, A., AKTER, M., HAYASHIDA, Y., TOYA, R., OYA, N., AWAI, K., IYAMA, K., KURATSU, J. I. & YAMASHITA, Y. 2008. Prognostic value of perfusion MR imaging of high-grade astrocytomas: long-term follow-up study. *AJNR Am J Neuroradiol,* 29, 1505-10.

HIRANO, A. & MATSUI, T. 1975. Vascular structures in brain tumors. *Hum Pathol,* 6, 611-21.

HIRST, T. C., VESTERINEN, H. M., SENA, E. S., EGAN, K. J., MACLEOD, M. R. & WHITTLE, I. R. 2013. Systematic review and meta-analysis of temozolomide in animal models of glioma: was clinical efficacy predicted? *Br J Cancer,* 108, 64-71.

HOEFFNER, E. G. 2005. Cerebral perfusion imaging. *J Neuroophthalmol,* 25, 313-20.

HOLLAND, E. C. 2000. Glioblastoma multiforme: the terminator. *Proc Natl Acad Sci U S A,* 97, 6242-4.

HOURANI, R., BRANT, L. J., RIZK, T., WEINGART, J. D., BARKER, P. B. & HORSKA, A. 2008. Can proton MR spectroscopic and perfusion imaging differentiate between neoplastic and nonneoplastic brain lesions in adults? *AJNR Am J Neuroradiol,* 29, 366-72.

HOWE, F. A., BARTON, S. J., CUDLIP, S. A., STUBBS, M., SAUNDERS, D. E., MURPHY, M., WILKINS, P., OPSTAD, K. S., DOYLE, V. L., MCLEAN, M. A., BELL, B. A. & GRIFFITHS, J. R. 2003. Metabolic profiles of human brain tumors using quantitative in vivo 1H magnetic resonance spectroscopy. *Magn Reson Med,* 49, 223-32.

HSIAO, P., SASONGKO, L., LINK, J. M., MANKOFF, D. A., MUZI, M., COLLIER, A. C. & UNADKAT, J. D. 2006. Verapamil P-glycoprotein transport across the rat blood-brain barrier: cyclosporine, a concentration inhibition analysis, and

comparison with human data. *J Pharmacol Exp Ther,* 317, 704-10.

HUANG, Y., ALKINS, R., SCHWARTZ, M. L. & HYNYNEN, K. 2016. Opening the Blood-Brain Barrier with MR Imaging-guided Focused Ultrasound: Preclinical Testing on a Trans-Human Skull Porcine Model. *Radiology*, 152154.

HYAFIL, F., VERGELY, C., DU VIGNAUD, P. & GRAND-PERRET, T. 1993. In vitro and in vivo reversal of multidrug resistance by GF120918, an acridonecarboxamide derivative. *Cancer Res,* 53, 4595-602.

IMBESI, F., MARCHIONI, E., BENERICETTI, E., ZAPPOLI, F., GALLI, A., CORATO, M. & CERONI, M. 2006. A randomized phase III study: comparison between intravenous and intraarterial ACNU administration in newly diagnosed primary glioblastomas. *Anticancer Res,* 26, 553-8.

JACKSON, A., KASSNER, A., ANNESLEY-WILLIAMS, D., REID, H., ZHU, X. P. & LI, K. L. 2002. Abnormalities in the recirculation phase of contrast agent bolus passage in cerebral gliomas: comparison with relative blood volume and tumor grade. *AJNR Am J Neuroradiol,* 23, 7-14.

JAIN, R. K., DI TOMASO, E., DUDA, D. G., LOEFFLER, J. S., SORENSEN, A. G. & BATCHELOR, T. T. 2007. Angiogenesis in brain tumours. *Nat Rev Neurosci,* 8, 610-22.

JANZER, R. C. & RAFF, M. C. 1987. Astrocytes induce blood-brain barrier properties in endothelial cells. *Nature,* 325, 253-7.

JELLISON, B. J., FIELD, A. S., MEDOW, J., LAZAR, M., SALAMAT, M. S. & ALEXANDER, A. L. 2004. Diffusion tensor imaging of cerebral white matter: a pictorial review of physics, fiber tract anatomy, and tumor imaging patterns. *AJNR Am J Neuroradiol,* 25, 356-69.

JENKINSON, M. D., DU PLESSIS, D. G., SMITH, T. S., JOYCE, K. A., WARNKE, P. C. & WALKER, C. 2006a. Histological growth patterns and genotype in oligodendroglial tumours: correlation with MRI features. *Brain,* 129, 1884-91.

JENKINSON, M. D., SMITH, T. S., JOYCE, K. A., FILDES, D., BROOME, J., DU PLESSIS, D. G., HAYLOCK, B., HUSBAND, D. J., WARNKE, P. C. & WALKER, C. 2006b. Cerebral blood volume, genotype and chemosensitivity in oligodendroglial tumours. *Neuroradiology,* 48, 703-13.

JONES, T. R., BIGNER, S. H., SCHOLD, S. C., JR., ENG, L. F. & BIGNER, D. D. 1981. Anaplastic human gliomas grown in athymic mice. Morphology and glial fibrillary acidic protein expression. *Am J Pathol,* 105, 316-27.

JOSSERAND, V., PELERIN, H., DE BRUIN, B., JEGO, B., KUHNAST, B., HINNEN, F., DUCONGE, F., BOISGARD, R., BEUVON, F., CHASSOUX, F., DAUMAS-DUPORT, C., EZAN, E., DOLLE, F., MABONDZO, A. & TAVITIAN, B. 2006. Evaluation of drug penetration into the brain: a double study by in vivo imaging with positron emission tomography and using an in vitro model of the human blood-brain barrier. *J Pharmacol Exp Ther,* 316, 79-86.

JOST, S. C., WANEBO, J. E., SONG, S. K., CHICOINE, M. R., RICH, K. M., WOOLSEY, T. A., LEWIS, J. S., MACH, R. H., XU, J. & GARBOW, J. R. 2007. In vivo imaging in a murine model of glioblastoma. *Neurosurgery,* 60, 360-70; discussion 370-1.

JULIANO, R. L. & LING, V. 1976. A surface glycoprotein modulating drug permeability in Chinese hamster ovary cell mutants. *Biochim Biophys Acta,* 455, 152-62.

KANNAN, P., JOHN, C., ZOGHBI, S. S., HALLDIN, C., GOTTESMAN, M. M., INNIS, R. B. & HALL, M. D. 2009. Imaging the function of P-glycoprotein with radiotracers: pharmacokinetics and in vivo applications. *Clin Pharmacol Ther,* 86, 368-77.

KANNAN, P., TELU, S., SHUKLA, S., AMBUDKAR, S. V., PIKE, V. W., HALLDIN, C., GOTTESMAN, M. M., INNIS, R. B. & HALL, M. D. 2011. The "specific" P-glycoprotein inhibitor Tariquidar is also a substrate and an inhibitor for breast cancer resistance protein (BCRP/ABCG2). *ACS Chem Neurosci,* 2, 82-9.

KELLY, R. J., DRAPER, D., CHEN, C. C., ROBEY, R. W., FIGG, W. D., PIEKARZ, R. L., CHEN, X., GARDNER, E. R., BALIS, F. M., VENKATESAN, A. M., STEINBERG, S. M., FOJO, T. & BATES, S. E. 2011. A pharmacodynamic study of docetaxel in combination with the P-glycoprotein antagonist tariquidar (XR9576) in patients with lung, ovarian, and cervical cancer. *Clin Cancer Res,* 17, 569-80.

KHASRAW, M., AMERATUNGA, M. S., GRANT, R., WHEELER, H. & PAVLAKIS, N. 2014. Antiangiogenic therapy for high-grade glioma. *Cochrane Database Syst Rev*, CD008218.

KIM, M., TURNQUIST, H., JACKSON, J., SGAGIAS, M., YAN, Y., GONG, M., DEAN, M., SHARP, J. G. & COWAN, K. 2002. The multidrug resistance

transporter ABCG2 (breast cancer resistance protein 1) effluxes Hoechst 33342 and is overexpressed in hematopoietic stem cells. *Clin Cancer Res,* 8, 22-8.

KINOSHITA, M., ARITA, H., GOTO, T., OKITA, Y., ISOHASHI, K., WATABE, T., KAGAWA, N., FUJIMOTO, Y., KISHIMA, H., SHIMOSEGAWA, E., HATAZAWA, J., HASHIMOTO, N. & YOSHIMINE, T. 2012. A novel PET index, 18F-FDG-11C-methionine uptake decoupling score, reflects glioma cell infiltration. *J Nucl Med,* 53, 1701-8.

KITIS, O., ALTAY, H., CALLI, C., YUNTEN, N., AKALIN, T. & YURTSEVEN, T. 2005. Minimum apparent diffusion coefficients in the evaluation of brain tumors. *Eur J Radiol,* 55, 393-400.

KLEIHUES, P., BURGER, P. C. & SCHEITHAUER, B. W. 1993. The new WHO classification of brain tumours. *Brain Pathol,* 3, 255-68.

KOCHII, M., KITAMURA, I., GOTO, T., NISHI, T., TAKESHIMA, H., SAITO, Y., YAMAMOTO, K., KIMURA, T., KINO, T., TADA, K., SHIRAISHI, S., UEMURA, S., IWASAKI, T., KURATSU, J. & USHIO, Y. 2000. Randomized comparison of intra-arterial versus intravenous infusion of ACNU for newly diagnosed patients with glioblastoma. *J Neurooncol,* 49, 63-70.

KODAIRA, H., KUSUHARA, H., USHIKI, J., FUSE, E. & SUGIYAMA, Y. 2010. Kinetic analysis of the cooperation of P-glycoprotein (P-gp/Abcb1) and breast cancer resistance protein (Bcrp/Abcg2) in limiting the brain and testis penetration of erlotinib, flavopiridol, and mitoxantrone. *J Pharmacol Exp Ther,* 333, 788-96.

KONO, K., INOUE, Y., NAKAYAMA, K., SHAKUDO, M., MORINO, M., OHATA, K., WAKASA, K. & YAMADA, R. 2001. The role of diffusion-weighted imaging in patients with brain tumors. *AJNR Am J Neuroradiol,* 22, 1081-8.

KREISL, W. C., BHATIA, R., MORSE, C. L., WOOCK, A. E., ZOGHBI, S. S., SHETTY, H. U., PIKE, V. W. & INNIS, R. B. 2015. Increased permeability-glycoprotein inhibition at the human blood-brain barrier can be safely achieved by performing PET during peak plasma concentrations of tariquidar. *J Nucl Med,* 56, 82-7.

KREISL, W. C., LIOW, J. S., KIMURA, N., SENECA, N., ZOGHBI, S. S., MORSE, C. L., HERSCOVITCH, P., PIKE, V. W. & INNIS, R. B. 2010. P-glycoprotein function at the blood-brain barrier in humans can be quantified with the substrate radiotracer 11C-N-desmethyl-loperamide. *J Nucl Med,* 51, 559-66.

KROLL, R. A. & NEUWELT, E. A. 1998. Outwitting the blood-brain barrier for therapeutic purposes: osmotic opening and other means. *Neurosurgery,* 42, 1083-99; discussion 1099-100.

KUNTNER, C., BANKSTAHL, J. P., BANKSTAHL, M., STANEK, J., WANEK, T., STUNDNER, G., KARCH, R., BRAUNER, R., MEIER, M., DING, X., MULLER, M., LOSCHER, W. & LANGER, O. 2010. Dose-response assessment of tariquidar and elacridar and regional quantification of P-glycoprotein inhibition at the rat blood-brain barrier using (R)-[(11)C]verapamil PET. *Eur J Nucl Med Mol Imaging,* 37, 942-53.

KUSUHARA, H. & SUGIYAMA, Y. 2007. ATP-binding cassette, subfamily G (ABCG family). *Pflugers Arch,* 453, 735-44.

LAGAS, J. S., VLAMING, M. L. & SCHINKEL, A. H. 2009. Pharmacokinetic assessment of multiple ATP-binding cassette transporters: the power of combination knockout mice. *Mol Interv,* 9, 136-45.

LAM, W. W., POON, W. S. & METREWELI, C. 2002. Diffusion MR imaging in glioma: does it have any role in the pre-operation determination of grading of glioma? *Clin Radiol,* 57, 219-25.

LANGER, O. 2016. Use of PET Imaging to Evaluate Transporter-Mediated Drug-Drug Interactions. *Journal of Clinical Pharmacology,* 56, S143-S156.

LANGER, O., BAUER, M., HAMMERS, A., KARCH, R., PATARAIA, E., KOEPP, M. J., ABRAHIM, A., LUURTSEMA, G., BRUNNER, M., SUNDER-PLASSMANN, R., ZIMPRICH, F., JOUKHADAR, C., GENTZSCH, S., DUDCZAK, R., KLETTER, K., MULLER, M. & BAUMGARTNER, C. 2007. Pharmacoresistance in epilepsy: a pilot PET study with the P-glycoprotein substrate R-[(11)C]verapamil. *Epilepsia,* 48, 1774-84.

LARNER, J. M., PHILLIPS, C. D., DION, J. E., JENSEN, M. E., NEWMAN, S. A. & JANE, J. A. 1995. A phase 1-2 trial of superselective carboplatin, low-dose infusional 5-fluorouracil and concurrent radiation for high-grade gliomas. *Am J Clin Oncol,* 18, 1-7.

LARSEN, V. A., SIMONSEN, H. J., LAW, I., LARSSON, H. B. & HANSEN, A. E. 2013. Evaluation of dynamic contrast-enhanced T1-weighted perfusion MRI in the differentiation of tumor recurrence from radiation necrosis. *Neuroradiology,* 55, 361-9.

LARSSON, H. B., STUBGAARD, M., FREDERIKSEN, J. L., JENSEN, M.,

HENRIKSEN, O. & PAULSON, O. B. 1990. Quantitation of blood-brain barrier defect by magnetic resonance imaging and gadolinium-DTPA in patients with multiple sclerosis and brain tumors. *Magn Reson Med,* 16, 117-31.

LAW, M., YANG, S., BABB, J. S., KNOPP, E. A., GOLFINOS, J. G., ZAGZAG, D. & JOHNSON, G. 2004. Comparison of cerebral blood volume and vascular permeability from dynamic susceptibility contrast-enhanced perfusion MR imaging with glioma grade. *AJNR Am J Neuroradiol,* 25, 746-55.

LAW, M., YANG, S., WANG, H., BABB, J. S., JOHNSON, G., CHA, S., KNOPP, E. A. & ZAGZAG, D. 2003. Glioma grading: sensitivity, specificity, and predictive values of perfusion MR imaging and proton MR spectroscopic imaging compared with conventional MR imaging. *AJNR Am J Neuroradiol,* 24, 1989-98.

LAW, M., YOUNG, R. J., BABB, J. S., PECCERELLI, N., CHHEANG, S., GRUBER, M. L., MILLER, D. C., GOLFINOS, J. G., ZAGZAG, D. & JOHNSON, G. 2008. Gliomas: predicting time to progression or survival with cerebral blood volume measurements at dynamic susceptibility-weighted contrast-enhanced perfusion MR imaging. *Radiology,* 247, 490-8.

LAZAROVA, N., ZOGHBI, S. S., HONG, J., SENECA, N., TUAN, E., GLADDING, R. L., LIOW, J. S., TAKU, A., INNIS, R. B. & PIKE, V. W. 2008. Synthesis and evaluation of [N-methyl-11C]N-desmethyl-loperamide as a new and improved PET radiotracer for imaging P-gp function. *J Med Chem,* 51, 6034-43.

LEE, C. C., WARD, H. A., SHARBROUGH, F. W., MEYER, F. B., MARSH, W. R., RAFFEL, C., SO, E. L., CASCINO, G. D., SHIN, C., XU, Y., RIEDERER, S. J. & JACK, C. R., JR. 1999. Assessment of functional MR imaging in neurosurgical planning. *AJNR Am J Neuroradiol,* 20, 1511-9.

LEE, W. J., CHOI, S. H., PARK, C. K., YI, K. S., KIM, T. M., LEE, S. H., KIM, J. H., SOHN, C. H., PARK, S. H. & KIM, I. H. 2012. Diffusion-weighted MR imaging for the differentiation of true progression from pseudoprogression following concomitant radiotherapy with temozolomide in patients with newly diagnosed high-grade gliomas. *Acad Radiol,* 19, 1353-61.

LI, A., WALLING, J., KOTLIAROV, Y., CENTER, A., STEED, M. E., AHN, S. J., ROSENBLUM, M., MIKKELSEN, T., ZENKLUSEN, J. C. & FINE, H. A.

2008. Genomic changes and gene expression profiles reveal that established glioma cell lines are poorly representative of primary human gliomas. *Mol Cancer Res,* 6, 21-30.

LIEBNER, S., FISCHMANN, A., RASCHER, G., DUFFNER, F., GROTE, E. H., KALBACHER, H. & WOLBURG, H. 2000. Claudin-1 and claudin-5 expression and tight junction morphology are altered in blood vessels of human glioblastoma multiforme. *Acta Neuropathol,* 100, 323-31.

LINZ, U., HUPERT, M., SANTIAGO-SCHUBEL, B., WIEN, S., STAB, J. & WAGNER, S. 2015. Transport of treosulfan and temozolomide across an in-vitro blood-brain barrier model. *Anticancer Drugs,* 26, 728-36.

LIOW, J. S., KREISL, W., ZOGHBI, S. S., LAZAROVA, N., SENECA, N., GLADDING, R. L., TAKU, A., HERSCOVITCH, P., PIKE, V. W. & INNIS, R. B. 2009. P-glycoprotein function at the blood-brain barrier imaged using 11C-N-desmethyl-loperamide in monkeys. *J Nucl Med,* 50, 108-15.

LIU, H. L., HUANG, C. Y., CHEN, J. Y., WANG, H. Y., CHEN, P. Y. & WEI, K. C. 2014. Pharmacodynamic and therapeutic investigation of focused ultrasound-induced blood-brain barrier opening for enhanced temozolomide delivery in glioma treatment. *PLoS One,* 9, e114311.

LONG, D. M. 1970. Capillary ultrastructure and the blood-brain barrier in human malignant brain tumors. *J Neurosurg,* 32, 127-44.

LOSCHER, W. & POTSCHKA, H. 2005a. Blood-brain barrier active efflux transporters: ATP-binding cassette gene family. *NeuroRx,* 2, 86-98.

LOSCHER, W. & POTSCHKA, H. 2005b. Drug resistance in brain diseases and the role of drug efflux transporters. *Nat Rev Neurosci,* 6, 591-602.

LOUIS, D. N., OHGAKI, H., WIESTLER, O. D., CAVENEE, W. K., BURGER, P. C., JOUVET, A., SCHEITHAUER, B. W. & KLEIHUES, P. 2007. The 2007 WHO classification of tumours of the central nervous system. *Acta Neuropathol,* 114, 97-109.

LOUIS, D. N., PERRY, A., REIFENBERGER, G., VON DEIMLING, A., FIGARELLA-BRANGER, D., CAVENEE, W. K., OHGAKI, H., WIESTLER, O. D., KLEIHUES, P. & ELLISON, D. W. 2016. The 2016 World Health Organization Classification of Tumors of the Central Nervous System: a summary. *Acta Neuropathologica,* 131, 803-820.

LUBBERINK, M., LUURTSEMA, G., VAN BERCKEL, B. N., BOELLAARD, R.,

TOORNVLIET, R., WINDHORST, A. D., FRANSSEN, E. J. & LAMMERTSMA, A. A. 2007. Evaluation of tracer kinetic models for quantification of P-glycoprotein function using (R)-[11C]verapamil and PET. *J Cereb Blood Flow Metab,* 27, 424-33.

LUNA-TORTOS, C., FEDROWITZ, M. & LOSCHER, W. 2008. Several major antiepileptic drugs are substrates for human P-glycoprotein. *Neuropharmacology,* 55, 1364-75.

LUO, Y., ELLIS, L. Z., DALLAGLIO, K., TAKEDA, M., ROBINSON, W. A., ROBINSON, S. E., LIU, W., LEWIS, K. D., MCCARTER, M. D., GONZALEZ, R., NORRIS, D. A., ROOP, D. R., SPRITZ, R. A., AHN, N. G. & FUJITA, M. 2012. Side population cells from human melanoma tumors reveal diverse mechanisms for chemoresistance. *J Invest Dermatol,* 132, 2440-50.

LUTZ, K., WIESTLER, B., GRAF, M., BAUMER, P., FLOCA, R., SCHLEMMER, H. P., HEILAND, S., WICK, W., BENDSZUS, M. & RADBRUCH, A. 2014. Infiltrative patterns of glioblastoma: Identification of tumor progress using apparent diffusion coefficient histograms. *J Magn Reson Imaging,* 39, 1096-103.

LUURTSEMA, G., MOLTHOFF, C. F., SCHUIT, R. C., WINDHORST, A. D., LAMMERTSMA, A. A. & FRANSSEN, E. J. 2005. Evaluation of (R)-[11C]verapamil as PET tracer of P-glycoprotein function in the blood-brain barrier: kinetics and metabolism in the rat. *Nucl Med Biol,* 32, 87-93.

LUURTSEMA, G., WINDHORST, A. D., MOOIJER, M. P. J., HERSCHEID, J. D. M., LAMMERTSMA, A. A. & FRANSSEN, E. J. F. 2002. Fully automated high yield synthesis of (R)- and (S)-[C-11]verapamil for measuring P-glycoprotein function with positron emission tomography. *Journal of Labelled Compounds & Radiopharmaceuticals,* 45, 1199-1207.

MA, J., MURPHY, M., O'DWYER, P. J., BERMAN, E., REED, K. & GALLO, J. M. 2002. Biochemical changes associated with a multidrug-resistant phenotype of a human glioma cell line with temozolomide-acquired resistance. *Biochem Pharmacol,* 63, 1219-28.

MACDONALD, D. R., CASCINO, T. L., SCHOLD, S. C., JR. & CAIRNCROSS, J. G. 1990. Response criteria for phase II studies of supratentorial malignant glioma. *J Clin Oncol,* 8, 1277-80.

MAIA, A. C., JR., MALHEIROS, S. M., DA ROCHA, A. J., DA SILVA, C. J., GABBAI, A. A., FERRAZ, F. A. & STAVALE, J. N. 2005. MR cerebral blood volume maps correlated with vascular endothelial growth factor expression and tumor grade in nonenhancing gliomas. *AJNR Am J Neuroradiol,* 26, 777-83.

MANGLA, R., SINGH, G., ZIEGELITZ, D., MILANO, M. T., KORONES, D. N., ZHONG, J. & EKHOLM, S. E. 2010. Changes in relative cerebral blood volume 1 month after radiation-temozolomide therapy can help predict overall survival in patients with glioblastoma. *Radiology,* 256, 575-84.

MARCHESI, F., TURRIZIANI, M., TORTORELLI, G., AVVISATI, G., TORINO, F. & DE VECCHIS, L. 2007. Triazene compounds: mechanism of action and related DNA repair systems. *Pharmacol Res,* 56, 275-87.

MARK, K. S. & MILLER, D. W. 1999. Increased permeability of primary cultured brain microvessel endothelial cell monolayers following TNF-alpha exposure. *Life Sci,* 64, 1941-53.

MAROY, R., BOISGARD, R., COMTAT, C., FROUIN, V., CATHIER, P., DUCHESNAY, E., DOLLE, F., NIELSEN, P. E., TREBOSSEN, R. & TAVITIAN, B. 2008. Segmentation of rodent whole-body dynamic PET images: an unsupervised method based on voxel dynamics. *IEEE Trans Med Imaging,* 27, 342-54.

MAROY, R., BOISGARD, R., COMTAT, C., JEGO, B., FONTYN, Y., JAN, S., DUBOIS, A., TREBOSSEN, R. & TAVITIAN, B. 2010. Quantitative organ time activity curve extraction from rodent PET images without anatomical prior. *Med Phys,* 37, 1507-17.

MARZOLINI, C., PAUS, E., BUCLIN, T. & KIM, R. B. 2004. Polymorphisms in human MDR1 (P-glycoprotein): recent advances and clinical relevance. *Clin Pharmacol Ther,* 75, 13-33.

MATSUKADO, Y., MACCARTY, C. S. & KERNOHAN, J. W. 1961. The growth of glioblastoma multiforme (astrocytomas, grades 3 and 4) in neurosurgical practice. *J Neurosurg,* 18, 636-44.

MATSUSUE, E., FINK, J. R., ROCKHILL, J. K., OGAWA, T. & MARAVILLA, K. R. 2010. Distinction between glioma progression and post-radiation change by combined physiologic MR imaging. *Neuroradiology,* 52, 297-306.

MCBRIDE, D. Q., MILLER, B. L., NIKAS, D. L., BUCHTHAL, S., CHANG, L., CHIANG, F. & BOOTH, R. A. 1995. Analysis of brain tumors using 1H

magnetic resonance spectroscopy. *Surg Neurol,* 44, 137-44.

MCCARTY, J. H. 2009. Cell adhesion and signaling networks in brain neurovascular units. *Curr Opin Hematol,* 16, 209-14.

MCKNIGHT, T. R., LAMBORN, K. R., LOVE, T. D., BERGER, M. S., CHANG, S., DILLON, W. P., BOLLEN, A. & NELSON, S. J. 2007. Correlation of magnetic resonance spectroscopic and growth characteristics within Grades II and III gliomas. *J Neurosurg,* 106, 660-6.

MEER, L., JANZER, R. C., KLEIHUES, P. & KOLAR, G. F. 1986. In vivo metabolism and reaction with DNA of the cytostatic agent, 5-(3,3-dimethyl-1-triazeno)imidazole-4-carboxamide (DTIC). *Biochem Pharmacol,* 35, 3243-7.

METELLUS, P., COULIBALY, B., COLIN, C., DE PAULA, A. M., VASILJEVIC, A., TAIEB, D., BARLIER, A., BOISSELIER, B., MOKHTARI, K., WANG, X. W., LOUNDOU, A., CHAPON, F., PINEAU, S., OUAFIK, L., CHINOT, O. & FIGARELLA-BRANGER, D. 2010. Absence of IDH mutation identifies a novel radiologic and molecular subtype of WHO grade II gliomas with dismal prognosis. *Acta Neuropathol,* 120, 719-29.

MILLER, A. B., HOOGSTRATEN, B., STAQUET, M. & WINKLER, A. 1981. Reporting results of cancer treatment. *Cancer,* 47, 207-14.

MILLER, G. 2002. Drug targeting. Breaking down barriers. *Science,* 297, 1116-8.

MINAMI, M. 2011. [Neuro-glio-vascular interaction in ischemic brains]. *Yakugaku Zasshi,* 131, 539-44.

MISTRY, P., STEWART, A. J., DANGERFIELD, W., OKIJI, S., LIDDLE, C., BOOTLE, D., PLUMB, J. A., TEMPLETON, D. & CHARLTON, P. 2001. In vitro and in vivo reversal of P-glycoprotein-mediated multidrug resistance by a novel potent modulator, XR9576. *Cancer Res,* 61, 749-58.

MOFFAT, B. A., CHENEVERT, T. L., MEYER, C. R., MCKEEVER, P. E., HALL, D. E., HOFF, B. A., JOHNSON, T. D., REHEMTULLA, A. & ROSS, B. D. 2006. The functional diffusion map: an imaging biomarker for the early prediction of cancer treatment outcome. *Neoplasia,* 8, 259-67.

MONG, S., ELLINGSON, B. M., NGHIEMPHU, P. L., KIM, H. J., MIRSADRAEI, L., LAI, A., YONG, W., ZAW, T. M., CLOUGHESY, T. F. & POPE, W. B. 2012. Persistent diffusion-restricted lesions in bevacizumab-treated malignant gliomas are associated with improved survival compared with matched controls. *AJNR Am J Neuroradiol,* 33, 1763-70.

MOON, W. J., CHOI, J. W., ROH, H. G., LIM, S. D. & KOH, Y. C. 2012. Imaging parameters of high grade gliomas in relation to the MGMT promoter methylation status: the CT, diffusion tensor imaging, and perfusion MR imaging. *Neuroradiology,* 54, 555-63.

MOSELEY, C. K., CARLIN, S. M., NEELAMEGAM, R. & HOOKER, J. M. 2012. An efficient and practical radiosynthesis of [11C]temozolomide. *Org Lett,* 14, 5872-5.

MUNOZ, J. L., RODRIGUEZ-CRUZ, V., GRECO, S. J., NAGULA, V., SCOTTO, K. W. & RAMESHWAR, P. 2014. Temozolomide induces the production of epidermal growth factor to regulate MDR1 expression in glioblastoma cells. *Mol Cancer Ther,* 13, 2399-411.

MUNOZ, J. L., RODRIGUEZ-CRUZ, V., RAMKISSOON, S. H., LIGON, K. L., GRECO, S. J. & RAMESHWAR, P. 2015a. Temozolomide resistance in glioblastoma occurs by miRNA-9-targeted PTCH1, independent of sonic hedgehog level. *Oncotarget,* 6, 1190-201.

MUNOZ, J. L., WALKER, N. D., SCOTTO, K. W. & RAMESHWAR, P. 2015b. Temozolomide competes for P-glycoprotein and contributes to chemoresistance in glioblastoma cells. *Cancer Lett,* 367, 69-75.

MURPHY, M., LOOSEMORE, A., CLIFTON, A. G., HOWE, F. A., TATE, A. R., CUDLIP, S. A., WILKINS, P. R., GRIFFITHS, J. R. & BELL, B. A. 2002. The contribution of proton magnetic resonance spectroscopy (1HMRS) to clinical brain tumour diagnosis. *Br J Neurosurg,* 16, 329-34.

NABORS, M. W., GRIFFIN, C. A., ZEHNBAUER, B. A., HRUBAN, R. H., PHILLIPS, P. C., GROSSMAN, S. A., BREM, H. & COLVIN, O. M. 1991. Multidrug resistance gene (MDR1) expression in human brain tumors. *J Neurosurg,* 75, 941-6.

NEGENDANK, W. G., SAUTER, R., BROWN, T. R., EVELHOCH, J. L., FALINI, A., GOTSIS, E. D., HEERSCHAP, A., KAMADA, K., LEE, B. C., MENGEOT, M. M., MOSER, E., PADAVIC-SHALLER, K. A., SANDERS, J. A., SPRAGGINS, T. A., STILLMAN, A. E., TERWEY, B., VOGL, T. J., WICKLOW, K. & ZIMMERMAN, R. A. 1996. Proton magnetic resonance spectroscopy in patients with glial tumors: a multicenter study. *J Neurosurg,* 84, 449-58.

NEWLANDS, E. S., STEVENS, M. F., WEDGE, S. R., WHEELHOUSE, R. T. &

BROCK, C. 1997. Temozolomide: a review of its discovery, chemical properties, pre-clinical development and clinical trials. *Cancer Treat Rev,* 23, 35-61.

NICO, B. & RIBATTI, D. 2012. Morphofunctional aspects of the blood-brain barrier. *Curr Drug Metab,* 13, 50-60.

NIES, A. T. 2007. The role of membrane transporters in drug delivery to brain tumors. *Cancer Lett,* 254, 11-29.

NOBUSAWA, S., WATANABE, T., KLEIHUES, P. & OHGAKI, H. 2009. IDH1 mutations as molecular signature and predictive factor of secondary glioblastomas. *Clin Cancer Res,* 15, 6002-7.

NOELL, S., WOLBURG-BUCHHOLZ, K., MACK, A. F., RITZ, R., TATAGIBA, M., BESCHORNER, R., WOLBURG, H. & FALLIER-BECKER, P. 2012. Dynamics of expression patterns of AQP4, dystroglycan, agrin and matrix metalloproteinases in human glioblastoma. *Cell Tissue Res,* 347, 429-41.

OHGAKI, H. & KLEIHUES, P. 2005. Population-based studies on incidence, survival rates, and genetic alterations in astrocytic and oligodendroglial gliomas. *J Neuropathol Exp Neurol,* 64, 479-89.

OLDENDORF, W. H., CORNFORD, M. E. & BROWN, W. J. 1977. The large apparent work capability of the blood-brain barrier: a study of the mitochondrial content of capillary endothelial cells in brain and other tissues of the rat. *Ann Neurol,* 1, 409-17.

OMURO, A. M., FAIVRE, S. & RAYMOND, E. 2007. Lessons learned in the development of targeted therapy for malignant gliomas. *Mol Cancer Ther,* 6, 1909-19.

OSTERMANN, S., CSAJKA, C., BUCLIN, T., LEYVRAZ, S., LEJEUNE, F., DECOSTERD, L. A. & STUPP, R. 2004. Plasma and cerebrospinal fluid population pharmacokinetics of temozolomide in malignant glioma patients. *Clin Cancer Res,* 10, 3728-36.

PACHOT, J. I., BOTHAM, R. P., HAEGELE, K. D. & HWANG, K. 2003. Experimental estimation of the role of P-Glycoprotein in the pharmacokinetic behaviour of telithromycin, a novel ketolide, in comparison with roxithromycin and other macrolides using the Caco-2 cell model. *J Pharm Pharm Sci,* 6, 1-12.

PAPADOPOULOS, M. C., KRISHNA, S. & VERKMAN, A. S. 2002. Aquaporin water channels and brain edema. *Mt Sinai J Med,* 69, 242-8.

PAPADOPOULOS, M. C., SAADOUN, S., DAVIES, D. C. & BELL, B. A. 2001. Emerging molecular mechanisms of brain tumour oedema. *Br J Neurosurg,* 15, 101-8.

PARDRIDGE, W. M. 2005. The blood-brain barrier: bottleneck in brain drug development. *NeuroRx,* 2, 3-14.

PATANKAR, T. F., HAROON, H. A., MILLS, S. J., BALERIAUX, D., BUCKLEY, D. L., PARKER, G. J. & JACKSON, A. 2005. Is volume transfer coefficient (K(trans)) related to histologic grade in human gliomas? *AJNR Am J Neuroradiol,* 26, 2455-65.

PAULEIT, D., FLOETH, F., HAMACHER, K., RIEMENSCHNEIDER, M. J., REIFENBERGER, G., MULLER, H. W., ZILLES, K., COENEN, H. H. & LANGEN, K. J. 2005. O-(2-[18F]fluoroethyl)-L-tyrosine PET combined with MRI improves the diagnostic assessment of cerebral gliomas. *Brain,* 128, 678-87.

PAULI-MAGNUS, C., VON RICHTER, O., BURK, O., ZIEGLER, A., METTANG, T., EICHELBAUM, M. & FROMM, M. F. 2000. Characterization of the major metabolites of verapamil as substrates and inhibitors of P-glycoprotein. *J Pharmacol Exp Ther,* 293, 376-82.

PERRIERE, N., DEMEUSE, P., GARCIA, E., REGINA, A., DEBRAY, M., ANDREUX, J. P., COUVREUR, P., SCHERRMANN, J. M., TEMSAMANI, J., COURAUD, P. O., DELI, M. A. & ROUX, F. 2005. Puromycin-based purification of rat brain capillary endothelial cell cultures. Effect on the expression of blood-brain barrier-specific properties. *J Neurochem,* 93, 279-89.

PERSIDSKY, Y., RAMIREZ, S. H., HAORAH, J. & KANMOGNE, G. D. 2006. Blood-brain barrier: structural components and function under physiologic and pathologic conditions. *J Neuroimmune Pharmacol,* 1, 223-36.

PETRELLA, J. R., SHAH, L. M., HARRIS, K. M., FRIEDMAN, A. H., GEORGE, T. M., SAMPSON, J. H., PEKALA, J. S. & VOYVODIC, J. T. 2006. Preoperative functional MR imaging localization of language and motor areas: effect on therapeutic decision making in patients with potentially resectable brain tumors. *Radiology,* 240, 793-802.

PIERALLINI, A., BONAMINI, M., BOZZAO, A., PANTANO, P., STEFANO, D. D., FERONE, E., RAGUSO, M., BOSMAN, C. & BOZZAO, L. 1997. Supratentorial diffuse astrocytic tumours: proposal of an MRI classification.

Eur Radiol, 7, 395-9.

PIKE, V. W. 2009. PET radiotracers: crossing the blood-brain barrier and surviving metabolism. *Trends Pharmacol Sci,* 30, 431-40.

PINKEL, D. & WOO, S. 1994. Prevention and treatment of meningeal leukemia in children. *Blood,* 84, 355-66.

PIROTH, M. D., HOLY, R., PINKAWA, M., STOFFELS, G., KAISER, H. J., GALLDIKS, N., HERZOG, H., COENEN, H. H., EBLE, M. J. & LANGEN, K. J. 2011. Prognostic impact of postoperative, pre-irradiation (18)F-fluoroethyl-l-tyrosine uptake in glioblastoma patients treated with radiochemotherapy. *Radiother Oncol,* 99, 218-24.

PIROTH, M. D., PINKAWA, M., HOLY, R., KLOTZ, J., SCHAAR, S., STOFFELS, G., GALLDIKS, N., COENEN, H. H., KAISER, H. J., LANGEN, K. J. & EBLE, M. J. 2012. Integrated boost IMRT with FET-PET-adapted local dose escalation in glioblastomas. Results of a prospective phase II study. *Strahlenther Onkol,* 188, 334-9.

PITZ, M. W., DESAI, A., GROSSMAN, S. A. & BLAKELEY, J. O. 2011. Tissue concentration of systemically administered antineoplastic agents in human brain tumors. *J Neurooncol,* 104, 629-38.

PLATE, K. H., BREIER, G., WEICH, H. A. & RISAU, W. 1992. Vascular endothelial growth factor is a potential tumour angiogenesis factor in human gliomas in vivo. *Nature,* 359, 845-8.

POLLI, J. W., OLSON, K. L., CHISM, J. P., JOHN-WILLIAMS, L. S., YEAGER, R. L., WOODARD, S. M., OTTO, V., CASTELLINO, S. & DEMBY, V. E. 2009. An unexpected synergist role of P-glycoprotein and breast cancer resistance protein on the central nervous system penetration of the tyrosine kinase inhibitor lapatinib (N-{3-chloro-4-[(3-fluorobenzyl)oxy]phenyl}-6-[5-({[2-(methylsulfonyl)ethyl]amino }methyl)-2-furyl]-4-quinazolinamine; GW572016). *Drug Metab Dispos,* 37, 439-42.

PONTEN, J. & MACINTYRE, E. H. 1968. Long term culture of normal and neoplastic human glia. *Acta Pathol Microbiol Scand,* 74, 465-86.

POPE, W. B., CHEN, J. H., DONG, J., CARLSON, M. R., PERLINA, A., CLOUGHESY, T. F., LIAU, L. M., MISCHEL, P. S., NGHIEMPHU, P., LAI, A. & NELSON, S. F. 2008. Relationship between gene expression and enhancement in glioblastoma multiforme: exploratory DNA microarray

analysis. *Radiology,* 249, 268-77.

POPE, W. B., LAI, A., MEHTA, R., KIM, H. J., QIAO, J., YOUNG, J. R., XUE, X., GOLDIN, J., BROWN, M. S., NGHIEMPHU, P. L., TRAN, A. & CLOUGHESY, T. F. 2011. Apparent diffusion coefficient histogram analysis stratifies progression-free survival in newly diagnosed bevacizumab-treated glioblastoma. *AJNR Am J Neuroradiol,* 32, 882-9.

POPE, W. B., PRINS, R. M., ALBERT THOMAS, M., NAGARAJAN, R., YEN, K. E., BITTINGER, M. A., SALAMON, N., CHOU, A. P., YONG, W. H., SOTO, H., WILSON, N., DRIGGERS, E., JANG, H. G., SU, S. M., SCHENKEIN, D. P., LAI, A., CLOUGHESY, T. F., KORNBLUM, H. I., WU, H., FANTIN, V. R. & LIAU, L. M. 2012. Non-invasive detection of 2-hydroxyglutarate and other metabolites in IDH1 mutant glioma patients using magnetic resonance spectroscopy. *J Neurooncol,* 107, 197-205.

POPE, W. B., SAYRE, J., PERLINA, A., VILLABLANCA, J. P., MISCHEL, P. S. & CLOUGHESY, T. F. 2005. MR imaging correlates of survival in patients with high-grade gliomas. *AJNR Am J Neuroradiol,* 26, 2466-74.

PROVENZALE, J. M., MUKUNDAN, S. & DEWHIRST, M. 2005. The role of blood-brain barrier permeability in brain tumor imaging and therapeutics. *AJR Am J Roentgenol,* 185, 763-7.

PUSZTAI, L., WAGNER, P., IBRAHIM, N., RIVERA, E., THERIAULT, R., BOOSER, D., SYMMANS, F. W., WONG, F., BLUMENSCHEIN, G., FLEMING, D. R., ROUZIER, R., BONIFACE, G. & HORTOBAGYI, G. N. 2005. Phase II study of tariquidar, a selective P-glycoprotein inhibitor, in patients with chemotherapy-resistant, advanced breast carcinoma. *Cancer,* 104, 682-91.

QI, S., YU, L., LI, H., OU, Y., QIU, X., DING, Y., HAN, H. & ZHANG, X. 2014. Isocitrate dehydrogenase mutation is associated with tumor location and magnetic resonance imaging characteristics in astrocytic neoplasms. *Oncol Lett,* 7, 1895-1902.

RANICAR, A. S., WILLIAMS, C. W., SCHNORR, L., CLARK, J. C., RHODES, C. G., BLOOMFIELD, P. M. & JONES, T. 1991. The on-line monitoring of continuously withdrawn arterial blood during PET studies using a single BGO/photomultiplier assembly and non-stick tubing. *Med Prog Technol,* 17, 259-64.

RASCHER, G., FISCHMANN, A., KROGER, S., DUFFNER, F., GROTE, E. H. & WOLBURG, H. 2002. Extracellular matrix and the blood-brain barrier in glioblastoma multiforme: spatial segregation of tenascin and agrin. *Acta Neuropathol,* 104, 85-91.

REESE, T. S. & KARNOVSKY, M. J. 1967. Fine structural localization of a blood-brain barrier to exogenous peroxidase. *J Cell Biol,* 34, 207-17.

RIBATTI, D., NICO, B., CRIVELLATO, E. & ARTICO, M. 2006. Development of the blood-brain barrier: a historical point of view. *Anat Rec B New Anat,* 289, 3-8.

RICCI, P. E. 1999. Imaging of adult brain tumors. *Neuroimaging Clin N Am,* 9, 651-69.

RIEGER, J., BAHR, O., MULLER, K., FRANZ, K., STEINBACH, J. & HATTINGEN, E. 2010. Bevacizumab-induced diffusion-restricted lesions in malignant glioma patients. *J Neurooncol,* 99, 49-56.

ROBERTS, H. C., ROBERTS, T. P., BOLLEN, A. W., LEY, S., BRASCH, R. C. & DILLON, W. P. 2001. Correlation of microvascular permeability derived from dynamic contrast-enhanced MR imaging with histologic grade and tumor labeling index: a study in human brain tumors. *Acad Radiol,* 8, 384-91.

ROELCKE, U., RADU, E., AMETAMEY, S., PELLIKKA, R., STEINBRICH, W. & LEENDERS, K. L. 1996. Association of rubidium and C-methionine uptake in brain tumors measured by positron emission tomography. *J Neurooncol,* 27, 163-71.

ROMERMANN, K., WANEK, T., BANKSTAHL, M., BANKSTAHL, J. P., FEDROWITZ, M., MULLER, M., LOSCHER, W., KUNTNER, C. & LANGER, O. 2013. (R)-[(11)C]verapamil is selectively transported by murine and human P-glycoprotein at the blood-brain barrier, and not by MRP1 and BCRP. *Nucl Med Biol,* 40, 873-8.

ROSSO, L., BROCK, C. S., GALLO, J. M., SALEEM, A., PRICE, P. M., TURKHEIMER, F. E. & ABOAGYE, E. O. 2009. A new model for prediction of drug distribution in tumor and normal tissues: pharmacokinetics of temozolomide in glioma patients. *Cancer Res,* 69, 120-7.

ROTTENBERG, D. A., GINOS, J. Z., KEARFOTT, K. J., JUNCK, L. & BIGNER, D. D. 1984. In vivo measurement of regional brain tissue pH using positron emission tomography. *Ann Neurol,* 15 Suppl, S98-102.

ROUX, F. E., BOULANOUAR, K., LOTTERIE, J. A., MEJDOUBI, M., LESAGE, J. P. & BERRY, I. 2003. Language functional magnetic resonance imaging in preoperative assessment of language areas: correlation with direct cortical stimulation. *Neurosurgery,* 52, 1335-45; discussion 1345-7.

RUBIN, L. L., HALL, D. E., PORTER, S., BARBU, K., CANNON, C., HORNER, H. C., JANATPOUR, M., LIAW, C. W., MANNING, K., MORALES, J. & ET AL. 1991. A cell culture model of the blood-brain barrier. *J Cell Biol,* 115, 1725-35.

RYOO, I., CHOI, S. H., KIM, J. H., SOHN, C. H., KIM, S. C., SHIN, H. S., YEOM, J. A., JUNG, S. C., LEE, A. L., YUN, T. J., PARK, C. K. & PARK, S. H. 2013. Cerebral blood volume calculated by dynamic susceptibility contrast-enhanced perfusion MR imaging: preliminary correlation study with glioblastoma genetic profiles. *PLoS One,* 8, e71704.

SAEKI, T., UEDA, K., TANIGAWARA, Y., HORI, R. & KOMANO, T. 1993. Human P-glycoprotein transports cyclosporin A and FK506. *J Biol Chem,* 268, 6077-80.

SALEEM. A., BROWN. G., BRADY. F., ABOAGYE. E., OSMAN. S., LUTHRA. S., RANICAR. A .S.O., BROCK. C. S., STEVENS. M. F. G., NEWLANDS. E., JONES. T. & PRICE. P. 2003. Metabolic activation of Temozolomide measuersd in vivo using positron emission tomography. *Cancer Res*. Volume 15; issue 63, 2409-2415.

SANG Y. Lee. 2016.

Temozolomide resistance in glioblastoma multiforme. *Gene and diseases*, volume 3, issue 3, 198-210.

SASONGKO, L., LINK, J. M., MUZI, M., MANKOFF, D. A., YANG, X., COLLIER, A. C., SHONER, S. C. & UNADKAT, J. D. 2005. Imaging P-glycoprotein transport activity at the human blood-brain barrier with positron emission tomography. *Clin Pharmacol Ther,* 77, 503-14.

SATO, N., SUZUKI, M., KUWATA, N., KURODA, K., WADA, T., BEPPU, T., SERA, K., SASAKI, T. & OGAWA, A. 1999. Evaluation of the malignancy of glioma using 11C-methionine positron emission tomography and proliferating cell nuclear antigen staining. *Neurosurg Rev,* 22, 210-4.

SAUNDERS, N. R., DREIFUSS, J. J., DZIEGIELEWSKA, K. M., JOHANSSON, P. A., HABGOOD, M. D., MOLLGARD, K. & BAUER, H. C. 2014. The rights

and wrongs of blood-brain barrier permeability studies: a walk through 100 years of history. *Front Neurosci,* 8, 404.

SAWLANI, R. N., RAIZER, J., HOROWITZ, S. W., SHIN, W., GRIMM, S. A., CHANDLER, J. P., LEVY, R., GETCH, C. & CARROLL, T. J. 2010. Glioblastoma: a method for predicting response to antiangiogenic chemotherapy by using MR perfusion imaging--pilot study. *Radiology,* 255, 622-8.

SCHAICH, M., KESTEL, L., PFIRRMANN, M., ROBEL, K., ILLMER, T., KRAMER, M., DILL, C., EHNINGER, G., SCHACKERT, G. & KREX, D. 2009. A MDR1 (ABCB1) gene single nucleotide polymorphism predicts outcome of temozolomide treatment in glioblastoma patients. *Ann Oncol,* 20, 175-81.

SCHERER, H. J. 1940. A Critical Review: The Pathology of Cerebral Gliomas. *J Neurol Psychiatry,* 3, 147-77.

SCHINKEL, A. H. & JONKER, J. W. 2003. Mammalian drug efflux transporters of the ATP binding cassette (ABC) family: an overview. *Adv Drug Deliv Rev,* 55, 3-29.

SCHMAINDA, K. M., ZHANG, Z., PRAH, M., SNYDER, B. S., GILBERT, M. R., SORENSEN, A. G., BARBORIAK, D. P. & BOXERMAN, J. L. 2015. Dynamic susceptibility contrast MRI measures of relative cerebral blood volume as a prognostic marker for overall survival in recurrent glioblastoma: results from the ACRIN 6677/RTOG 0625 multicenter trial. *Neuro Oncol*.

SCHMIDT, K. F., ZIU, M., SCHMIDT, N. O., VAGHASIA, P., CARGIOLI, T. G., DOSHI, S., ALBERT, M. S., BLACK, P. M., CARROLL, R. S. & SUN, Y. 2004. Volume reconstruction techniques improve the correlation between histological and in vivo tumor volume measurements in mouse models of human gliomas. *J Neurooncol,* 68, 207-15.

SCHWARZENBERG, J., CZERNIN, J., CLOUGHESY, T. F., ELLINGSON, B. M., POPE, W. B., GROGAN, T., ELASHOFF, D., GEIST, C., SILVERMAN, D. H., PHELPS, M. E. & CHEN, W. 2014. Treatment response evaluation using 18F-FDOPA PET in patients with recurrent malignant glioma on bevacizumab therapy. *Clin Cancer Res,* 20, 3550-9.

SCOTT, J. N., BRASHER, P. M., SEVICK, R. J., REWCASTLE, N. B. & FORSYTH, P. A. 2002. How often are nonenhancing supratentorial gliomas

malignant? A population study. *Neurology,* 59, 947-9.

SHAFFER, B. C., GILLET, J. P., PATEL, C., BAER, M. R., BATES, S. E. & GOTTESMAN, M. M. 2012. Drug resistance: still a daunting challenge to the successful treatment of AML. *Drug Resist Updat,* 15, 62-9.

SHAPIRO, W. R., GREEN, S. B., BURGER, P. C., SELKER, R. G., VANGILDER, J. C., ROBERTSON, J. T., MEALEY, J., JR., RANSOHFF, J. & MAHALEY, M. S., JR. 1992. A randomized comparison of intra-arterial versus intravenous BCNU, with or without intravenous 5-fluorouracil, for newly diagnosed patients with malignant glioma. *J Neurosurg,* 76, 772-81.

SHELEG, S. V., KOROTKEVICH, E. A., ZHAVRID, E. A., MURAVSKAYA, G. V., SMEYANOVICH, A. F., SHANKO, Y. G., YURKSHTOVICH, T. L., BYCHKOVSKY, P. B. & BELYAEV, S. A. 2002. Local chemotherapy with cisplatin-depot for glioblastoma multiforme. *J Neurooncol,* 60, 53-9.

SHEN, S. & ZHANG, W. 2010. ABC transporters and drug efflux at the blood-brain barrier. *Rev Neurosci,* 21, 29-53.

SIDDHARTHAN, V., KIM, Y. V., LIU, S. & KIM, K. S. 2007. Human astrocytes/astrocyte-conditioned medium and shear stress enhance the barrier properties of human brain microvascular endothelial cells. *Brain Res,* 1147, 39-50.

SIEGAL, T. & ZYLBER-KATZ, E. 2002. Strategies for increasing drug delivery to the brain: focus on brain lymphoma. *Clin Pharmacokinet,* 41, 171-86.

SIJENS, P. E. & OUDKERK, M. 2002. 1H chemical shift imaging characterization of human brain tumor and edema. *Eur Radiol,* 12, 2056-61.

SKINNER, R. A., GIBSON, R. M., ROTHWELL, N. J., PINTEAUX, E. & PENNY, J. I. 2009. Transport of interleukin-1 across cerebromicrovascular endothelial cells. *Br J Pharmacol,* 156, 1115-23.

SMITH, E. A., CARLOS, R. C., JUNCK, L. R., TSIEN, C. I., ELIAS, A. & SUNDGREN, P. C. 2009. Developing a clinical decision model: MR spectroscopy to differentiate between recurrent tumor and radiation change in patients with new contrast-enhancing lesions. *AJR Am J Roentgenol,* 192, W45-52.

SMITH, S. M. 2002. Fast robust automated brain extraction. *Hum Brain Mapp,* 17, 143-55.

SORENSEN, A. G., BATCHELOR, T. T., ZHANG, W. T., CHEN, P. J., YEO, P.,

WANG, M., JENNINGS, D., WEN, P. Y., LAHDENRANTA, J., ANCUKIEWICZ, M., DI TOMASO, E., DUDA, D. G. & JAIN, R. K. 2009. A "vascular normalization index" as potential mechanistic biomarker to predict survival after a single dose of cediranib in recurrent glioblastoma patients. *Cancer Res,* 69, 5296-300.

SPIEGL-KREINECKER, S., BUCHROITHNER, J., ELBLING, L., STEINER, E., WURM, G., BODENTEICH, A., FISCHER, J., MICKSCHE, M. & BERGER, W. 2002. Expression and functional activity of the ABC-transporter proteins P-glycoprotein and multidrug-resistance protein 1 in human brain tumor cells and astrocytes. *J Neurooncol,* 57, 27-36.

STADLBAUER, A., GRUBER, S., NIMSKY, C., FAHLBUSCH, R., HAMMEN, T., BUSLEI, R., TOMANDL, B., MOSER, E. & GANSLANDT, O. 2006. Preoperative grading of gliomas by using metabolite quantification with high-spatial-resolution proton MR spectroscopic imaging. *Radiology,* 238, 958-69.

STEINHOFF, H., GRUMME, T., KAZNER, E., LANGE, S., LANKSCH, W., MEESE, W. & WULLENWEBER, R. 1978. Axial transverse computerized tomography in 73 glioblastomas. *Acta Neurochir (Wien),* 42, 45-56.

STEVENS, M. F., HICKMAN, J. A., LANGDON, S. P., CHUBB, D., VICKERS, L., STONE, R., BAIG, G., GODDARD, C., GIBSON, N. W., SLACK, J. A. & ET AL. 1987. Antitumor activity and pharmacokinetics in mice of 8-carbamoyl-3-methyl-imidazo[5,1-d]-1,2,3,5-tetrazin-4(3H)-one (CCRG 81045; M & B 39831), a novel drug with potential as an alternative to dacarbazine. *Cancer Res,* 47, 5846-52.

STIPPICH, C., RAPPS, N., DREYHAUPT, J., DURST, A., KRESS, B., NENNIG, E., TRONNIER, V. M. & SARTOR, K. 2007. Localizing and lateralizing language in patients with brain tumors: feasibility of routine preoperative functional MR imaging in 81 consecutive patients. *Radiology,* 243, 828-36.

STRASSER, J. F., FUNG, L. K., ELLER, S., GROSSMAN, S. A. & SALTZMAN, W. M. 1995. Distribution of 1,3-bis(2-chloroethyl)-1-nitrosourea and tracers in the rabbit brain after interstitial delivery by biodegradable polymer implants. *J Pharmacol Exp Ther,* 275, 1647-55.

STROBER, W. 2001. Trypan blue exclusion test of cell viability. *Curr Protoc Immunol,* Appendix 3, Appendix 3B.

STUPP, R., MASON, W. P., VAN DEN BENT, M. J., WELLER, M., FISHER, B.,

TAPHOORN, M. J., BELANGER, K., BRANDES, A. A., MAROSI, C., BOGDAHN, U., CURSCHMANN, J., JANZER, R. C., LUDWIN, S. K., GORLIA, T., ALLGEIER, A., LACOMBE, D., CAIRNCROSS, J. G., EISENHAUER, E. & MIRIMANOFF, R. O. 2005. Radiotherapy plus concomitant and adjuvant temozolomide for glioblastoma. *N Engl J Med,* 352, 987-96.

SUGAHARA, T., KOROGI, Y., KOCHI, M., IKUSHIMA, I., SHIGEMATU, Y., HIRAI, T., OKUDA, T., LIANG, L., GE, Y., KOMOHARA, Y., USHIO, Y. & TAKAHASHI, M. 1999. Usefulness of diffusion-weighted MRI with echo-planar technique in the evaluation of cellularity in gliomas. *J Magn Reson Imaging,* 9, 53-60.

SUREAU, F. C., READER, A. J., COMTAT, C., LEROY, C., RIBEIRO, M. J., BUVAT, I. & TREBOSSEN, R. 2008. Impact of image-space resolution modeling for studies with the high-resolution research tomograph. *J Nucl Med,* 49, 1000-8.

SWANSON, K. R., CHAKRABORTY, G., WANG, C. H., ROCKNE, R., HARPOLD, H. L., MUZI, M., ADAMSEN, T. C., KROHN, K. A. & SPENCE, A. M. 2009. Complementary but distinct roles for MRI and 18F-fluoromisonidazole PET in the assessment of human glioblastomas. *J Nucl Med,* 50, 36-44.

PORNOW, J., BADIE, B., CHEN, M., BLANCHARD, S. & SYNOLD, T.W. 2009. The neuropharmacokinetics of temozolomide in patients with resctable brain tumours: potential implications for the current approach to chemoradiation. *Clin Cancer Res.* 15, 7092-7098.

SYVANEN, S., LINDHE, O., PALNER, M., KORNUM, B. R., RAHMAN, O., LANGSTROM, B., KNUDSEN, G. M. & HAMMARLUND-UDENAES, M. 2009. Species differences in blood-brain barrier transport of three positron emission tomography radioligands with emphasis on P-glycoprotein transport. *Drug Metab Dispos,* 37, 635-43.

SZAKACS, G., PATERSON, J. K., LUDWIG, J. A., BOOTH-GENTHE, C. & GOTTESMAN, M. M. 2006. Targeting multidrug resistance in cancer. *Nat Rev Drug Discov,* 5, 219-34.

TATTER, S. B. 1999. Neurosurgical management of brain tumors. *Neuroimaging Clin N Am,* 9, 779-99.

(TCGA) CANCER GENOME ATLAS RESEARCH NETWORK. (2008).

Comprehsnive genomic characterization defines human glioblastoma genes and core pathways. *Nature*. 455, 1061-1068.

TISDALE, M. J. 1987. Antitumor imidazotetrazines--XV. Role of guanine O6 alkylation in the mechanism of cytotoxicity of imidazotetrazinones. *Biochem Pharmacol,* 36, 457-62.

TOTH, K., VAUGHAN, M. M., PERESS, N. S., SLOCUM, H. K. & RUSTUM, Y. M. 1996. MDR1 P-glycoprotein is expressed by endothelial cells of newly formed capillaries in human gliomas but is not expressed in the neovasculature of other primary tumors. *Am J Pathol,* 149, 853-8.

TOURNIER, N., GOUTAL, S., AUVITY, S., TRAXL, A., MAIRINGER, S., WANEK, T., HELAL, O. B., BUVAT, I., SOUSSAN, M., CAILLE, F. & LANGER, O. 2016. Strategies to inhibit ABCB1- and ABCG2-mediated efflux transport of erlotinib at the blood-brain barrier: a PET study in non-human primates. *J Nucl Med*.

TOZER, D. J., JAGER, H. R., DANCHAIVIJITR, N., BENTON, C. E., TOFTS, P. S., REES, J. H. & WALDMAN, A. D. 2007. Apparent diffusion coefficient histograms may predict low-grade glioma subtype. *NMR Biomed,* 20, 49-57.

TSUJI, A. 1998. P-glycoprotein-mediated efflux transport of anticancer drugs at the blood-brain barrier. *Ther Drug Monit,* 20, 588-90.

UCHIDA, Y., OHTSUKI, S., KATSUKURA, Y., IKEDA, C., SUZUKI, T., KAMIIE, J. & TERASAKI, T. 2011. Quantitative targeted absolute proteomics of human blood-brain barrier transporters and receptors. *J Neurochem,* 117, 333-45.

UPADHYAY, N & WALDMAN A. D. 2011. Conventional MRI evaluation of gliomas. *Br J Radiol,* 2, 107-111.

UPTON, R. N. 2007. Cerebral uptake of drugs in humans. *Clin Exp Pharmacol Physiol,* 34, 695-701.

VAN ASSEMA, D. M., LUBBERINK, M., BOELLAARD, R., SCHUIT, R. C., WINDHORST, A. D., SCHELTENS, P., LAMMERTSMA, A. A. & VAN BERCKEL, B. N. 2012. P-glycoprotein function at the blood-brain barrier: effects of age and gender. *Mol Imaging Biol,* 14, 771-6.

VAUPEL, P., KALLINOWSKI, F. & OKUNIEFF, P. 1989. Blood flow, oxygen and nutrient supply, and metabolic microenvironment of human tumors: a review. *Cancer Res,* 49, 6449-65.

VILLANO, J. L., SEERY, T. E. & BRESSLER, L. R. 2009. Temozolomide in

malignant gliomas: current use and future targets. *Cancer Chemother Pharmacol,* 64, 647-55.

VOGES, J., HERHOLZ, K., HOLZER, T., WURKER, M., BAUER, B., PIETRZYK, U., TREUER, H., SCHRODER, R., STURM, V. & HEISS, W. D. 1997. 11C-methionine and 18F-2-fluorodeoxyglucose positron emission tomography: a tool for diagnosis of cerebral glioma and monitoring after brachytherapy with 125I seeds. *Stereotact Funct Neurosurg,* 69, 129-35.

VON BOSSANYI, P., DIETE, S., DIETZMANN, K., WARICH-KIRCHES, M. & KIRCHES, E. 1997. Immunohistochemical expression of P-glycoprotein and glutathione S-transferases in cerebral gliomas and response to chemotherapy. *Acta Neuropathol,* 94, 605-11.

VUKELJA, S. J., ANTHONY, S. P., ARSENEAU, J. C., BERMAN, B. S., CUNNINGHAM, C. C., NEMUNAITIS, J. J., SAMLOWSKI, W. E. & FOWERS, K. D. 2007. Phase 1 study of escalating-dose OncoGel (ReGel/paclitaxel) depot injection, a controlled-release formulation of paclitaxel, for local management of superficial solid tumor lesions. *Anticancer Drugs,* 18, 283-9.

WAGGENER, J. D. & BEGGS, J. L. 1976. Vasculature of Neural Neoplasms. *Adv Neurol,* 15, 27-49.

WAGNER, C. C., BAUER, M., KARCH, R., FEURSTEIN, T., KOPP, S., CHIBA, P., KLETTER, K., LOSCHER, W., MULLER, M., ZEITLINGER, M. & LANGER, O. 2009. A pilot study to assess the efficacy of tariquidar to inhibit P-glycoprotein at the human blood-brain barrier with (R)-11C-verapamil and PET. *J Nucl Med,* 50, 1954-61.

WALKER, C., DU PLESSIS, D. G., JOYCE, K. A., FILDES, D., GEE, A., HAYLOCK, B., HUSBAND, D., SMITH, T., BROOME, J. & WARNKE, P. C. 2005. Molecular pathology and clinical characteristics of oligodendroglial neoplasms. *Ann Neurol,* 57, 855-65.

WALKER, D. G. & KAYE, A. H. 2003. Low grade glial neoplasms. *J Clin Neurosci,* 10, 1-13.

WALKER, M. D., FELDMANN, M., MATTHEWS, J. C., ANTON-RODRIGUEZ, J. M., WANG, S., KOEPP, M. J. & ASSELIN, M. C. 2012. Optimization of methods for quantification of rCBF using high-resolution [(1)(5)O]H(2)O PET images. *Phys Med Biol,* 57, 2251-71.

WANEK, T., KUNTNER, C., BANKSTAHL, J. P., MAIRINGER, S., BANKSTAHL, M., STANEK, J., SAUBERER, M., FILIP, T., ERKER, T., MULLER, M., LOSCHER, W. & LANGER, O. 2012. A novel PET protocol for visualization of breast cancer resistance protein function at the blood-brain barrier. *J Cereb Blood Flow Metab,* 32, 2002-11.

WANEK, T., ROMERMANN, K., MAIRINGER, S., STANEK, J., SAUBERER, M., FILIP, T., TRAXL, A., KUNTNER, C., PAHNKE, J., BAUER, F., ERKER, T., LOSCHER, W., MULLER, M. & LANGER, O. 2015a. Factors Governing P-Glycoprotein-Mediated Drug-Drug Interactions at the Blood-Brain Barrier Measured with Positron Emission Tomography. *Mol Pharm,* 12, 3214-25.

WANEK, T., TRAXL, A., BANKSTAHL, J. P., BANKSTAHL, M., SAUBERER, M., LANGER, O. & KUNTNER, C. 2015b. [(18)F]FDG is not transported by P-glycoprotein and breast cancer resistance protein at the rodent blood-brain barrier. *Nucl Med Biol,* 42, 585-9.

WANG, F., CHENG, Y., MEI, J., SONG, Y., YANG, Y. Q., LIU, Y. & WANG, Z. 2009. Focused ultrasound microbubble destruction-mediated changes in blood-brain barrier permeability assessed by contrast-enhanced magnetic resonance imaging. *J Ultrasound Med,* 28, 1501-9.

WARREN, M. S., ZERANGUE, N., WOODFORD, K., ROBERTS, L. M., TATE, E. H., FENG, B., LI, C., FEUERSTEIN, T. J., GIBBS, J., SMITH, B., DE MORAIS, S. M., DOWER, W. J. & KOLLER, K. J. 2009. Comparative gene expression profiles of ABC transporters in brain microvessel endothelial cells and brain in five species including human. *Pharmacol Res,* 59, 404-13.

WARTH, A., KROGER, S. & WOLBURG, H. 2004. Redistribution of aquaporin-4 in human glioblastoma correlates with loss of agrin immunoreactivity from brain capillary basal laminae. *Acta Neuropathol,* 107, 311-8.

WEISS, N., MILLER, F., CAZAUBON, S. & COURAUD, P. O. 2009. The blood-brain barrier in brain homeostasis and neurological diseases. *Biochim Biophys Acta,* 1788, 842-57.

WEN, P. Y. & KESARI, S. 2008. Malignant gliomas in adults. *N Engl J Med,* 359, 492-507.

WEN, P. Y., MACDONALD, D. R., REARDON, D. A., CLOUGHESY, T. F., SORENSEN, A. G., GALANIS, E., DEGROOT, J., WICK, W., GILBERT, M. R., LASSMAN, A. B., TSIEN, C., MIKKELSEN, T., WONG, E. T.,

CHAMBERLAIN, M. C., STUPP, R., LAMBORN, K. R., VOGELBAUM, M. A., VAN DEN BENT, M. J. & CHANG, S. M. 2010. Updated response assessment criteria for high-grade gliomas: response assessment in neuro-oncology working group. *J Clin Oncol,* 28, 1963-72.

WEYBRIGHT, P., SUNDGREN, P. C., MALY, P., HASSAN, D. G., NAN, B., ROHRER, S. & JUNCK, L. 2005. Differentiation between brain tumor recurrence and radiation injury using MR spectroscopy. *AJR Am J Roentgenol,* 185, 1471-6.

WHITE, M. L., ZHANG, Y., KIRBY, P. & RYKEN, T. C. 2005. Can tumor contrast enhancement be used as a criterion for differentiating tumor grades of oligodendrogliomas? *AJNR Am J Neuroradiol,* 26, 784-90.

WIENHARD, K., HERHOLZ, K., COENEN, H. H., RUDOLF, J., KLING, P., STOCKLIN, G. & HEISS, W. D. 1991. Increased amino acid transport into brain tumors measured by PET of L-(2-18F)fluorotyrosine. *J Nucl Med,* 32, 1338-46.

WILLIS, C. L., LEACH, L., CLARKE, G. J., NOLAN, C. C. & RAY, D. E. 2004a. Reversible disruption of tight junction complexes in the rat blood-brain barrier, following transitory focal astrocyte loss. *Glia,* 48, 1-13.

WILLIS, C. L., NOLAN, C. C., REITH, S. N., LISTER, T., PRIOR, M. J., GUERIN, C. J., MAVROUDIS, G. & RAY, D. E. 2004b. Focal astrocyte loss is followed by microvascular damage, with subsequent repair of the blood-brain barrier in the apparent absence of direct astrocytic contact. *Glia,* 45, 325-37.

WINKLER, F., KOZIN, S. V., TONG, R. T., CHAE, S. S., BOOTH, M. F., GARKAVTSEV, I., XU, L., HICKLIN, D. J., FUKUMURA, D., DI TOMASO, E., MUNN, L. L. & JAIN, R. K. 2004. Kinetics of vascular normalization by VEGFR2 blockade governs brain tumor response to radiation: role of oxygenation, angiopoietin-1, and matrix metalloproteinases. *Cancer Cell,* 6, 553-63.

WITWER, B. P., MOFTAKHAR, R., HASAN, K. M., DESHMUKH, P., HAUGHTON, V., FIELD, A., ARFANAKIS, K., NOYES, J., MORITZ, C. H., MEYERAND, M. E., ROWLEY, H. A., ALEXANDER, A. L. & BADIE, B. 2002. Diffusion-tensor imaging of white matter tracts in patients with cerebral neoplasm. *J Neurosurg,* 97, 568-75.

WOLBURG, H. & LIPPOLDT, A. 2002. Tight junctions of the blood-brain barrier:

development, composition and regulation. *Vascul Pharmacol,* 38, 323-37.

WOLBURG, H., NEUHAUS, J., KNIESEL, U., KRAUSS, B., SCHMID, E. M., OCALAN, M., FARRELL, C. & RISAU, W. 1994. Modulation of tight junction structure in blood-brain barrier endothelial cells. Effects of tissue culture, second messengers and cocultured astrocytes. *J Cell Sci,* 107 (Pt 5), 1347-57.

WORKMAN, P., ABOAGYE, E. O., BALKWILL, F., BALMAIN, A., BRUDER, G., CHAPLIN, D. J., DOUBLE, J. A., EVERITT, J., FARNINGHAM, D. A., GLENNIE, M. J., KELLAND, L. R., ROBINSON, V., STRATFORD, I. J., TOZER, G. M., WATSON, S., WEDGE, S. R. & ECCLES, S. A. 2010. Guidelines for the welfare and use of animals in cancer research. *Br J Cancer,* 102, 1555-77.

WU, H. M., ASUI, G., LEE, C. C., PRINS, M. L., LANDO, W., LIN, H. D., YU, A. S., PHELPES, M. E. & HUANG, S. C. 2007. In vivo quantification of glucose metabolism in mice using small-animal PET and microfluiudic device. *J Nucl Med*, 48, 11a-12a.

YAMADA, K., USHIO, Y., HAYAKAWA, T., ARITA, N., HUANG, T. Y., NAGATANI, M., YAMADA, N. & MOGAMI, H. 1987. Distribution of radiolabeled 1-(4-amino-2-methyl-5-pyrimidinyl)methyl-3-(2-chloroethyl)-3-nitros ourea hydrochloride in rat brain tumor: intraarterial versus intravenous administration. *Cancer Res,* 47, 2123-8.

YAMASAKI, T., FUJINAGA, M., KAWAMURA, K., HATORI, A., YUI, J., NENGAKI, N., OGAWA, M., YOSHIDA, Y., WAKIZAKA, H., YANAMOTO, K., FUKUMURA, T. & ZHANG, M. R. 2011. Evaluation of the P-glycoprotein- and breast cancer resistance protein-mediated brain penetration of 11C-labeled topotecan using small-animal positron emission tomography. *Nucl Med Biol,* 38, 707-14.

Yan H, Parsons DW, Jin G et-al. IDH1 and IDH2 mutations in gliomas. *N. Engl. J. Med*. 2009;360 (8): 765-73.

YAN, H., BIGNER, D. D., VELCULESCU, V. & PARSONS, D. W. 2009. Mutant metabolic enzymes are at the origin of gliomas. *Cancer Res,* 69, 9157-9.

YANG, D., KOROGI, Y., SUGAHARA, T., KITAJIMA, M., SHIGEMATSU, Y., LIANG, L., USHIO, Y. & TAKAHASHI, M. 2002. Cerebral gliomas:

prospective comparison of multivoxel 2D chemical-shift imaging proton MR spectroscopy, echoplanar perfusion and diffusion-weighted MRI. *Neuroradiology,* 44, 656-66.

YOON, J. H., KIM, J. H., KANG, W. J., SOHN, C. H., CHOI, S. H., YUN, T. J., EUN, Y., SONG, Y. S. & CHANG, K. H. 2014. Grading of cerebral glioma with multiparametric MR imaging and 18F-FDG-PET: concordance and accuracy. *Eur Radiol,* 24, 380-9.

ZAGZAG, D., ESENCAY, M., MENDEZ, O., YEE, H., SMIRNOVA, I., HUANG, Y., CHIRIBOGA, L., LUKYANOV, E., LIU, M. & NEWCOMB, E. W. 2008. Hypoxia- and vascular endothelial growth factor-induced stromal cell-derived factor-1alpha/CXCR4 expression in glioblastomas: one plausible explanation of Scherer's structures. *Am J Pathol,* 173, 545-60.

ZENG, Q., LIU, H., ZHANG, K., LI, C. & ZHOU, G. 2011. Noninvasive evaluation of cerebral glioma grade by using multivoxel 3D proton MR spectroscopy. *Magn Reson Imaging,* 29, 25-31.

ZHANG, J., STEVENS, M. F. & BRADSHAW, T. D. 2012. Temozolomide: mechanisms of action, repair and resistance. *Curr Mol Pharmacol,* 5, 102-14.

ZHANG, J., STEVENS, M. F., LAUGHTON, C. A., MADHUSUDAN, S. & BRADSHAW, T. D. 2010. Acquired resistance to temozolomide in glioma cell lines: molecular mechanisms and potential translational applications. *Oncology,* 78, 103-14.

ZHANG, W., MOJSILOVIC-PETROVIC, J., ANDRADE, M. F., ZHANG, H., BALL, M. & STANIMIROVIC, D. B. 2003. The expression and functional characterization of ABCG2 in brain endothelial cells and vessels. *FASEB J,* 17, 2085-7.

ZHANG, X., GUO, M., SHEN, L. & HU, S. 2014. Combination of photodynamic therapy and temozolomide on glioma in a rat C6 glioma model. *Photodiagnosis Photodyn Ther,* 11, 603-12.

ZHANG, Y., BRADY, M. & SMITH, S. 2001. Segmentation of brain MR images through a hidden Markov random field model and the expectation-maximization algorithm. *IEEE Trans Med Imaging,* 20, 45-57.

ZHANG, Y., LI, C. S., YE, Y., JOHNSON, K., POE, J., JOHNSON, S., BOBROWSKI, W., GARRIDO, R. & MADHU, C. 2006. Porcine brain microvessel endothelial cells as an in vitro model to predict in vivo blood-brain

barrier permeability. *Drug Metab Dispos,* 34, 1935-43.

ZHOU, Q. & GALLO, J. M. 2005. In vivo microdialysis for PK and PD studies of anticancer drugs. *AAPS J,* 7, E659-67.

ZHOU, S., SCHUETZ, J. D., BUNTING, K. D., COLAPIETRO, A. M., SAMPATH, J., MORRIS, J. J., LAGUTINA, I., GROSVELD, G. C., OSAWA, M., NAKAUCHI, H. & SORRENTINO, B. P. 2001. The ABC transporter Bcrp1/ABCG2 is expressed in a wide variety of stem cells and is a molecular determinant of the side-population phenotype. *Nat Med,* 7, 1028-34.

ZLOKOVIC, B. V. & APUZZO, M. L. 1998. Strategies to circumvent vascular barriers of the central nervous system. *Neurosurgery,* 43, 877-8.

ZONARI, P., BARALDI, P. & CRISI, G. 2007. Multimodal MRI in the characterization of glial neoplasms: the combined role of single-voxel MR spectroscopy, diffusion imaging and echo-planar perfusion imaging. *Neuroradiology,* 49, 795-803.

Appendix

Table 1: Raw data for Figure 5.8 (A)

Animal number	Wild Type	P-gp KO	BCRP KO	Dual KO
1	0.134505	0.139052	0.107405	0.160761
2	0.116864	0.181121	0.142415	0.179005
3	0.145087	0.127265	0.175787	0.168664
4	0.135236	0.140419	0.151056	0.178555

Brain-to-plasma ratios of radioactivity at 40 minutes after radiotracer injection for the different mouse types before correcting for the fraction of the parent compound [^{11}C]TMZ in plasma.

Table 2: Raw data for Figure 5.8 (B)

Animal number	Wild Type	P-gp KO	BCRP KO	Dual KO
1	0.1553171	0.1534764	0.1224683	0.1955062
2	0.1349464	0.1999119	0.1623886	0.2083881
3	0.1675374	0.1404688	0.2004412	0.1995291
4	0.1558892	0.1549878	0.1722422	0.2078644

Brain-to-plasma ratios of radioactivity at 40 minutes after radiotracer injection for the different mouse types after correcting for the fraction of the parent compound [^{11}C]TMZ in plasma.

Table 3: Raw data for Figure 5.9 (A)

Animal Number	Vehicle treated	TQD treated
1	0.1609359	0.2163965
2	0.1413205	0.2446441
3	0.1408629	0.1714812
4		0.1917637

Brain-to-plasma ratios of radioactivity at 60 minutes after [^{11}C]Temozolomide injection in wild type mice injected with vehicle solution and with Tariquidar (TQD 15mg/kg) without correting for the fraction of Temozolomide in plasma. Tariquidar was administered by IV bolus 40 minutes after radiotracer injection.

Table 4: Raw data for Figure 5.9 (B)

Animal Number	Vehicle treated	TQD treated
1	0.1873526	0.2527996
2	0.1645175	0.2857992
3	0.1639847	0.2003283
4		0.2240232

Brain-to-plasma ratios of radioactivity at 60 minutes after [^{11}C]Temozolomide injection in wild type mice injected with vehicle solution and with Tariquidar (TQD 15mg/kg) after correting for the fraction of Temozolomide in plasma. Tariquidar was administered by IV bolus 40 minutes after radiotracer injection.